# DIMETHYLSULFIDE IN THE MARINE ATMOSPHERE
# —
# FROM THE CRADLE TO THE GRAVE

A DISSERTATION SUBMITTED TO THE GRADUATE DIVISION OF THE UNIVERSITY OF HAWAI‘I IN PARTIAL FULFILLMENT OF THE REQUIREMENTS FOR THE DEGREE OF

DOCTOR OF PHILOSOPHY

IN

OCEANOGRAPHY

December 2010

By

Mingxi Yang

Dissertation Committee:

Barry Huebert, Chairperson
Antony Clarke
Christopher Fairall
Kevin Hamilton
David Ho

We certify that we have read this dissertation and that, in our opinion, it is satisfactory in scope and quality as a dissertation for the degree of Doctor of Philosophy in Oceanography.

DISSERTATION COMMITTEE

_____
Chairperson

_____

_____

_____

_____

# ACKNOWLEDGEMENTS

I would like to first acknowledge the funding agencies (NSF and NOAA) for their support in all of our field projects, as well as the Graduate Student Organization (GSO) at University of Hawai‘i for awarding me a travel grant. In an attempt to more completely describe the surface ocean and lower atmosphere, besides analyzing data we collected ourselves, I have pooled results from many different sources. For the Vamos Ocean-Cloud-Atmosphere-Land Study Regional Experiment (VOCALS-REx), in particular, observations sampled on multiple platforms by different research groups were utilized in my analysis. These include aerosol measurements from Lelia Hawkins and Lynn Russell of Scripps Institute of Oceanography, Timothy Bates, Patricia Quinn, James Johnson, and Derek Coffman of NOAA Pacific Marine Environmental Laboratory, sulfur gas measurements from Alan Bandy and Nenad Zagorac of Drexel University, liquid water path and drizzle from Paquita Zuidema of University of Miami, Sara Tucker, Alan Brewer, Simon deSzoeke, and Daniel Wolfe of NOAA Earth System Research Laboratory, among others. For the Southern Ocean Gas Exchange Experiment (SO GasEx), I greatly appreciate Christopher Fairall and Daniel Wolfe of NOAA Earth System Research Laboratory and Steven Archer of Plymouth Marine Laboratory for their meteorological and seawater measurements. Christopher also taught me much about air-sea exchange and the theories behind the NOAA COARE 3.0 bulk air-sea flux model. I also want to thank Antony Clarke and his group at University of Hawai‘i for not only their aircraft aerosol measurements, but also invaluable

insights and provocative questions. I truly appreciate the continuing guidance in instrumental operation, data evaluation, and in-depth analysis from Byron Blomquist and Steven Howell from University of Hawai‘i. I feel extremely fortunate to have worked with Byron and Steve, as their ingenuity and dedication have had a great influence on me as a person and as a starting up scientist. David Ho and Kevin Hamilton, members of my PhD committee, have stimulated me with many ideas that are now parts of this dissertation. I cannot imagine a better PhD adviser personally than Barry Huebert, who at a very early stage placed a tremendous amount of trust and responsibility on me. I am grateful to have been given the chance to work independently most of the time and also receive immediate help from him when needed. Barry has also been very supportive of me in exploring activities outside of research, including ceramics, photography, and traveling. Last but definitely not least, I would like to thank my friends and family for their unwavering encouragement and support; they are the sources of my motivation and inspiration.

# ABSTRACT

Air-sea exchange has profound implications for biogeochemical cycling and climate. Sea-to-air transfer of the biologically produced dimethylsulfide (DMS) is of particular interest because the gas is a precursor to sulfate aerosols, which affect atmospheric chemistry and earth's radiative balance. In my dissertation, I discuss the air-sea exchange of DMS and the oxidation of DMS in the marine atmosphere. Chapter 1 provides background information on the formation of seawater DMS, theories behind air-sea exchange, oxidative destruction of DMS in the atmosphere, and the climatic impacts of sulfate aerosols. I also briefly describe our method for measuring DMS sea-to-air flux and provide an example of elevated DMS field near a front between two water masses. In Chapter 2, I compare air-sea transfer velocity measurements from the Southern Ocean to previous observations in temperate and tropical regions. I show that DMS transfer is suppressed in cold waters at high latitudes, not only due to reduced diffusivity, but also increased solubility. The transfer velocity of DMS is lower than those of the less soluble gases also because of this solubility effect. I shift my focus to biogeochemistry in the stratocumulus clouds topped Southeast Pacific in Chapter 3 and 4. In Chapter 3, based on shipboard and aircraft measurements, I estimate an average effective hydroxyl radical concentration from the budget analysis of DMS. In Chapter 4, I use a similar budget approach to analyze the diel cycles of sulfur dioxide and sulfate aerosols. I find that the dynamics of the boundary layer, which alternates from being coupled at night to decoupled during the day, significantly affects observed

chemical concentrations. I also provide examples of recent particle formation observed on the ship and aircraft, which were often associated with drizzle events and open cell structures in the clouds. Along with results from Chapter 3, I summarize the atmospheric sulfur cycling in the Southeast Pacific. While oxidized sulfur species from pollution emissions dominate the near shore region, DMS still supplies most of the sulfur mass, and at times new particle number, to the remote marine boundary layer.

# TABLE OF CONTENTS

# List of Tables

# List of Figures

# Chapter 1. Background

Over the past few decades, there have been numerous studies on the marine gas dimethylsulfide (DMS) from various disciplines, including biological regulation, atmospheric oxidation, air-sea exchange, and climatic feedback, etc. What initially spurred these interdisciplinary studies was the idea that the Earth is a self-regulating entity, where living constituents help maintain conditions favorable for life on the planet through feedback cycles in biogeochemistry and climate (Lovelock and Margulis, 1974). Such a feedback loop involving DMS was first hypothesized by Charlson et al. (1987) and coined the 'CLAW' hypothesis. Biologically produced in the upper ocean, DMS is ventilated to the atmosphere across the air-sea interface and constitutes ~90% of the global biogenic sulfur flux (Andreae, 1985). The oxidation of DMS in the marine atmosphere leads to sulfate aerosols that can serve as cloud condensation nuclei (CCN), which affect the formation, reflectivity, and lifetime of clouds. In the CLAW hypothesis, warmer climate leads to enhanced marine primary production, higher DMS concentration, more sulfate aerosols, and more CCN in the atmosphere. With amount of water vapor unchanged, more CCN leads to brighter and more persistent clouds, which reflect more incoming radiation back to space and induce cooling, thereby reducing biological production and completing the negative feedback loop (Falkowski et al., 1992). Verifying this hypothesis, however, has proven to be extremely challenging because it requires quantifying the biological production of DMS and the amount ventilated to the atmosphere, as well as understanding the complex chemical reactions of sulfur species in the marine air and the modifications of clouds due to sulfate aerosols on a large scale. The rest of this chapter consists of brief introductions on these various

aspects of DMS-related research. I draw particular attention to important and open questions in air-sea gas exchange and atmospheric sulfur cycling, which I attempt to address through observational and simple modeling works in Chapters 2, 3, and 4 of my dissertation.

### 1.1 Seawater DMS

DMS is produced by the enzymatic cleavage of dimethylsulfoniopropionate (DMSP) in the upper ocean, with typical DMSP to DMS turnover rates in the range of < 0.1~10 nM per day (Kiene and Service, 1991). Produced mostly by plankton, DMSP makes up the bulk of the reduced sulfur pool in marine systems (Simó et al, 2002). DMSP content is highly species-specific, with micro- and macro-algae among the most abundant sources. In the open ocean, phytoplankton containing the highest levels of DMSP include dinoflagellates and coccolithophores, with intracellular concentrations exceeding 100 mM (Sunda et al, 2002). In addition to a postulated osmotic role inside of phytoplankton cells (Keller et al, 1989), DMSP and its breakdown product DMS are thought to be antioxidants and protect algal cells from ultraviolet radiation (UVR) because they readily scavenge hydroxyl radicals and other reactive oxygen species (Sunda et al., 2002).

DMSP and DMS are released from phytoplankton to the water column via direct discharge and cell rupture. Direct discharge can be accelerated by stress, such as elevated UVR, high sea surface temperature (SST), and low nutrient availability (Kloster et al., 2006). Cell rupture occurs as a result of zooplankton grazing, bacterial, and viral attacks (Dacey and Wakeham, 1986; Sunda et al, 2002). Intracellular DMSP in phytoplankton is

found to be physically separated from the enzyme capable of catalyzing the DMSP cleavage reaction, suggesting healthy algal populations produce little DMS (Stefels and Boekel, 1993). Bacteria catalyze the degradation of dissolved DMSP in the water column to DMS.

The major sinks for DMS in the upper water column are bacterial degradation and photolysis, while ventilation to the atmosphere only removes a few percent of DMS (Kiene and Service, 1991; Toole et al., 2004; Bailey et al., 2008). Even though DMS is produced from algae, its concentration does not always correlate well with primary productivity or even the concentration of its precursor – DMSP. In bloom regions such as the Southern Ocean and the North Sea, mono-species phytoplankton blooms determine the DMS stocks and DMS appears to have a positive correlation with DMSP (Simó and Dachs, 2002). In contrast, in oligotrophic regions such as the Sargasso Sea, DMS appears to be uncoupled to DMSP or chlorophyll-a. Instead, SST and UVR account for most of the variability in DMS (Toole and Siegel, 2004). For such nutrient limited waters, the conversion from DMSP to DMS tends to peak during the decline of a bloom as opposed to during the active growing phase; the highest concentration of DMS is often observed in the summer despite lower levels of chlorophyll-a and DMSP than in the spring (Dacey et al, 1998).

To measure DMS in seawater, the gas is usually taken out of the water phase by either a purge-and-trap or equilibration method and then quantified in the gas phase by gas chromatography (GC) or mass spectrometry (MS). The purge and trap technique involves complete stripping of DMS from the water sample using an inert gas and trapping on an adsorbant (e.g. Bates et al. 2000). The equilibration method requires

establishing a Henry's law equilibrium between the water and the headspace gas. Given the complexity in the cycling of seawater DMS, it is no surprise that surface observations show high degrees of variability both spatially and temporally (Bates et al., 1987), presenting a challenge to numerical models. Diagnostic approaches to predict seawater DMS concentration rely on some combination of chlorophyll-a (Anderson et al., 2001; Aumont et al., 2002), mixed layer depth (Simó and Dachs, 2002), and solar radiation dose (Vallina and Simó, 2007). While these algorithms capture some of the large-scale patterns in seawater DMS, they do not reproduce local variability very well, necessitating further in situ measurements. Updating the database assembled by Kettle et al. (1999), Kettle and Andreae (2000) interpolated a global, monthly 1° x 1° climatology of surface seawater DMS concentration. Significant differences between these two related climatological datasets are found in high latitude regions, where observations are limited. In Chapter 2, I report seawater DMS concentration measured during a cruise in March and April of 2008 in the Southern Ocean.

### 1.2 Air-Sea Exchange of DMS

In order to understand the impact of DMS on climate, we first need to quantify its sea-to-air flux. Transfer of gases across the air-sea interface has profound implications on biogeochemical cycling and climate. The dissolution of carbon dioxide ($CO_2$) in the surface ocean has increased the acidity of seawater and slowed down the build up of this Greenhouse Gas in the atmosphere. Future prediction of climate change requires knowing how fast the ocean can take up more $CO_2$. Chlorofluorocarbons, sulfur hexafluoride, bomb $^{14}C$, and other anthropogenically produced gases dissolve in the

ocean have been used as tracers for water mass movements. DMS is ubiquitous in the surface ocean and is always emitted to the atmosphere. Previous estimates for the global sea-to-air flux of DMS range from 15 to 33 Tg $yr^{-1}$ (Kettle and Andreae, 2000; Simó and Dachs, 2002). A more recent review by Elliot (2009) suggested an annual flux of 17~19 Tg S, with discrepancies mainly stemming from the uncertainties in the transfer velocity parameterization as a function of wind speed. In Chapter 2, I provide a comprehensive assessment on the measurements of DMS air-sea exchange in distinct oceanographic environments and over a wide range of wind speeds.

*1.21 Theoretical Backgrounds in Gas Exchange*

The air-water flux of a gas ($F$) is typically parameterized as the transfer velocity ($k$) multiplied by the concentration difference across the air-sea interface:

$$F = k(C_w - \alpha C_a) \quad (1.1)$$

A positive $F$ denotes an upward flux out of the ocean; $k$ is in units of velocity and is by definition always positive; $C_w$ and $C_a$ are bulk waterside and airside concentrations, respectively; $\alpha$ is the dimensionless Ostwald solubility of the gas and is related to the Henry's law equilibrium (larger $\alpha$, more soluble). Gases in the atmosphere have $\alpha$ spanning several orders of magnitude, exemplified by the extremely insoluble sulfur hexafluoride ($SF_6$) and helium (He) to the very soluble amines and alcohols. Formulated from the perspective of the liquid phase, the term $\alpha C_a$ represents the waterside concentration that would be in equilibrium with the airside.

Gas transfer velocity is limited by molecular diffusion and turbulent transport on both sides of the air-water interface. Quiescent molecular sub-layers form just above and

below the interface in which turbulent transports diminish and molecular diffusions dominate (Liss and Slater, 1974). We may conceptualize this system as an electrical circuit, with molecular diffusive sub-layers on both sides of the interface analogous to two resistors in series, concentration difference as the voltage potential, and $F$ as the current. Inversely related to resistance, total transfer velocity ($k$) is a function of transfer velocities in both the waterside and the airside ($k_w$ and $k_a$, respectively):

$$k = [\frac{1}{k_w} + \frac{\alpha}{k_a}]^{-1} \quad (1.2)$$

Transfer velocity does not depend on the concentration difference, just as the resistance of the resistors is independent of the voltage potential. If the interfacial concentration difference reverses in sign, so will the direction of the flux (i.e. into the water vs. out of the water). For gases with very low solubility, few molecules need to be transported across the interface before solubility equilibrium is achieved. Thus transport through the waterside molecular sub-layer is limiting to $k$ (i.e. $k \approx k_w$). Such gases, including carbon dioxide ($CO_2$) and $SF_6$, are said to be waterside controlled. The contribution to total resistance from the airside is only on the order of 0.2% for $CO_2$ at 20 °C. In contrast, exchange of highly soluble gases are controlled by airside resistance because reaching Henry's equilibrium is the slow, rate-limiting step (i.e. $k \approx k_a/\alpha$), with water vapor ($H_2O$) representing complete airside control. Gases that are consumed rapidly in the surface water via chemical reactions, such as ozone ($O_3$) and sulfur dioxide ($SO_2$), can also be airside controlled. DMS is a largely waterside controlled gas, with the airside providing ~5% of the total resistance at 20 °C (McGillis et al., 2000). As solubility increases with decreasing temperature, airside resistance becomes more important. In Chapter 2, I

address the variance in DMS transfer velocity measurement due to the temperature dependence in airside resistance.

The Schmidt number is the ratio between kinematic viscosity of a medium and molecular diffusivity of the gas in that medium. To remove variance due to the temperature dependence in waterside diffusivity or to relate one relatively insoluble gas to another, measured $k_w$ is often normalized to a reference waterside Schmidt number ($S_{cw}$) of 600 or 660 following a $S_{cw}^{n}$ relationship. The exponent $n$ is shown both theoretically and in the laboratory to vary from -2/3 for a rigid boundary to -1/2 for a non-rigid surface, agreeing with the measurement from Nightingale et al. (2000) in the North Sea. The reference 600 and 660 correspond to $S_{cw}$ of $CO_2$ at 20°C in freshwater and seawater, respectively.

*1.22 Transfer Velocity Parameterizations*

Wind stress ($\tau$) at the surface generates turbulence, which disrupts molecular sub-layers on both side of the interface and increases $k$. Most gas exchange parameterizations are functions of wind speed at 10 meters ($U_{10}$), but with significant differences in both magnitude and functionality, especially in high winds. Based on lake measurements of $SF_6$ and wind tunnel observations, Liss and Merlivat (1986) (LM86) modeled $k_w$ as three piece-wise linear functions of wind speed with increasing slope towards higher winds [cm $hr^{-1}$]:

LM86 $k_w = 0.17U_{10}(S_{cw}/600)^{-2/3}$ $U_{10} \le 3.6$ (1.3a)

$k_w = (2.85U_{10} - 9.65)(S_{cw}/600)^{-1/2}$ $3.6 < U_{10} \le 13$ (1.3b)

$k_w = (5.9U_{10} - 49.3)(S_{cw}/600)^{-1/2}$ $U_{10} > 13$ (1.3c)

Based on natural $^{14}C$ disequilibrium and the bomb $^{14}C$ inventory, Wanninkhof (1992) (Wa92) fitted a quadratic relationship between $k$ and ship-based $U_{10}$ [cm hr$^{-1}$]:

Wa92 $$k = 0.31U_{10}^{\ 2}\ (S_{cw}/660)^{-1/2} \quad (1.4)$$

From artificial injections of two volatile tracers ($^3He$ and $SF_6$) and a non-volatile tracer (spores) in the North Sea, Nightingale et al. (2000) (N00) parameterized $k$ with both a linear and a quadratic term with respect to $U_{10}$ [cm hr$^{-1}$]:

N00 $$k = (0.222U_{10}^{\ 2} + 0.333U_{10})\ (S_{cw}/600)^{-1/2} \quad (1.5)$$

Ho et al. (2006) (Ho06) decided on a quadratic dependence on $U_{10}$ based on $^3He/SF_6$ measurements in the Southern Ocean [cm hr$^{-1}$]:

Ho06 $$k = 0.266U_{10}^{\ 2}\ (S_{cw}/600)^{-1/2} \quad (1.6)$$

Based on eddy covariance observations of $CO_2$ in the North Atlantic, Wanninkhof and McGillis (1999) (WM99) suggested a cubic fit between $k$ and $U_{10}$ [cm hr$^{-1}$]:

WM99 $$k = 0.0283U_{10}^{\ 3}\ (S_{cw}/660)^{-1/2} \quad (1.7)$$

Using the same approach during a subsequent cruise in the Equatorial Pacific, McGillis et al. 2004 (M04) reported a weaker wind speed dependence in $k$ and a large positive intercept at $U_{10} = 0$ [cm hr$^{-1}$]:

M04 $$k = 8.2 + 0.014U_{10}^{\ 3}\ (S_{cw}/660)^{-1/2} \quad (1.8)$$

The authors attributed this discrepancy to a limited wind speed range and strong diurnal heating. From recent observations of the transfer velocity of DMS in the Northeast Atlantic, Huebert et al., 2010 (Hu10) found near linear dependences in $k$ with $U_{10}$ as well as with the friction velocity ($u_*$) in the wind speed range of 4~12 m s$^{-1}$ [cm hr$^{-1}$]:

Hu10 $$k = (-5.0 + 2.4U_{10})\ (S_{cw}/660)^{-1/2} \quad (1.9a)$$

$$k = (-1.5 + 58.9u_*)(S_{cw}/660)^{-1/2} \quad (1.9b)$$

The linear dependence with $u_*$ is consistent with air-sea exchange theory from Csanady (1990). The friction velocity relates to 10-m wind speed ($U_{10}$) through the drag coefficient ($C_D$): $u_*^2 = C_D|U_{10}|U_{10} = \tau/\rho_a$, and more directly represents wind stress, with $\rho_a$ being the air density. The above wind speed parameterizations are plotted in Fig. 1.1. Except for M04, the formulations agree fairly well up to a wind speed of ~8 m $s^{-1}$, above which they diverge significantly (by a factor of ~2 in high winds). The large differences in high winds can be partly explained by the different solubility of the gases, which affect how much they can be transferred by bubbles.

Waves break and whitecaps form on the sea surface in high winds. The added surface area from injected air bubbles (Woolf, 1997) and the turbulence from breaking waves (Monahan and Spillane, 1984) can cause additional bubble-mediated gas transport ($k_b$). Scaling up from a single bubble model, Woolf (1997) (Wo97) parameterized $k_b$ for $CO_2$ [cm $hr^{-1}$]:

Wo97 $$k_b = 2450 f_{wh} \alpha^{-1} [1 + (14 \alpha S_{cw}^{-1/2})^{-1/1.2}]^{-1.2} \quad (1.10)$$

Here $f_{wh} = 3.84 \times 10^{-6} U_{10}^{3.41}$ is the whitecap fraction (Monahan and O'Muircheartaigh, 1980). Assuming the solubility dependence in (1.10) holds for other gases, we see that $k_b$ is larger for an insoluble gas than for a soluble gas. Total transfer velocity at high wind speed is the sum of direct transfer and $k_b$. However, the fractional contributions to gas exchange at high winds from direct and bubble-mediated transfer are still poorly quantified in the field. I attempt to separate these two mechanisms in Chapter 2 from DMS transfer velocity observations.

Exchange of airside controlled gases is traditionally studied by looking at water vapor transfer. Based on wind tunnel measurements, Liss (1973) (L73) proposed a linear relationship between airside transfer velocity ($k_a$) and $U_{10}$ that is not gas specific [cm $s^{-1}$]:

L73 $$k_a = 0.005 + 0.21U_{10} \quad (1.11)$$

Liss and Slater (1974) subsequently suggested an estimate of $k_a$ for any gas from that of $H_2O$ by multiplying by the square root of the ratio of the molecular weights (MW). From resistance theory, Duce et al. (1991) (D91) estimated $k_a$ using an $MW^{1/3}$ dependence; a linear relationship with wind speed was assumed by choosing a fixed $C_D$ [cm $s^{-1}$]:

D91 $$k_a = \frac{100U_{10}}{700 + 45MW^{1/3}} \quad (1.12)$$

Derived from water vapor transfer models, the parameterization of $k_a$ from McGillis et al. (2000) (M00) is [cm $s^{-1}$]:

M00 $$k_a = 0.183U_{10}(MW / MW_{H_2O})^{-1/2} \quad (1.13)$$

*1.23 NOAA COARE Gas Transfer Model*

While wind-speed dependent parameterizations might be adequate for estimating transfer velocities of specified gases in certain environments, they tend to oversimplify complex physical mechanisms that drive gas exchange. In comparison, models that attempt to approximate the physical processes at the air-water interface are more likely to be applicable to a wider range of gases and distinct environments. Originally developed to estimate bulk heat and moisture fluxes, the NOAA COARE 3.0 air-sea bulk flux model (Fairall et al., 2003) predicts waterside and airside gas transfers separately by estimating the thickness of the respective diffusion sub-layers. Total transfer velocity is then

calculated following (1.2). The waterside transfer velocity contains terms for direct transfer and bubble-mediated transfer in breaking waves [cm $hr^{-1}$]:

$$\text{COARE} \quad k_w = 360000 u_* (\rho_w / \rho_a)^{-1/2} [h_w S_{cw}^{1/2} + \kappa^{-1} \ln(0.5/\delta_w)]^{-1} + B(k_b) \qquad (1.14)$$

Here $\rho_w$ is the density of water, $\delta_w$ the waterside molecular sublayer thickness (~1 mm), $\kappa$ the von Karman constant (0.4), and $h_w = 13.3/(A\phi)$. The second term inside the bracket on the RHS of (1.14) is small compared to the first term. In $h_w$, $A$ is an empirical constant and tuned to 1.3 by Blomquist et al. (2006) using early eddy covariance measurements of DMS; $\varphi$ accounts for surface buoyancy flux enhancement of the transfer and only becomes important in low wind speed. The term $B(k_b)$ refers to the Wo97 parameterization for bubble-mediated exchange in high winds (1.10), with B provisionally set to 1.0. Figure 1.2 shows $k_w$ predicted by COARE for $CO_2$, DMS, acetaldehyde, acetone, and methanol without the bubble effect ($A$=1.0; $B$=1.3) at 20 °C. Normalized to $S_{cw}^{-0.5}$, direct waterside transfer of these gases would be essentially identical.

The airside transfer velocity in COARE is formulated analogously to direct transfer on the waterside, but with the molecular sublayer thickness empirically estimated from $C_D$ [cm $s^{-1}$]:

$$\text{COARE} \quad k_a = 100 u_* [13.3 S_{ca}^{1/2} + C_D^{-1/2} - 5 + 0.5\kappa^{-1} \ln(S_{ca})]^{-1} \qquad (1.15)$$

Figure 1.3 shows $k_a$ of acetaldehyde, acetone, and methanol predicted by COARE. A heavier molecule has a lower diffusivity in air, higher airside Schmidt number ($S_{ca}$), and thus lower $k_a$. Compared to (1.11), (1.12), and (1.13), the COARE formulation of $k_a$ has a nonlinear wind speed dependence, though the magnitudes from different models for a particular gas are fairly similar. The total transfer velocity of $CO_2$, DMS, acetaldehyde,

acetone, and methanol normalized to the respective temperature at which $S_{cw}$ = 660 ($k_{660}$) are shown in Fig. 1.4 ($A$=1.0; $B$=1.3). The large divergences in $k_{660}$ among these gases are principally due to their different solubility, which affects transfer velocity both through (1.2) and (1.10) in high winds. Methanol is by far the most soluble gas out of this group and has the lowest $k_{660}$. Since $CO_2$ and DMS are both largely waterside controlled, their $k_{660}$ are similar in low-to-mid winds before the onset of whitecapping. COARE 3.0 qualitatively captures the diverging curvatures of their transfer velocities in higher winds due to bubbles (Hare et al., 2004; Blomquist et al., 2006), suggesting that this physics-based model is more universal than any simple wind speed parameterization. However, quantitatively how well does the COARE model predict DMS transfer over a wide range of wind speeds? Southern Ocean Gas Exchange Experiment (SO GasEx) provided us for the first time with a large sample size of DMS transfer velocity observations up to a wind speed of 16 m $s^{-1}$, which I use to assess the performance of COARE. I also compare the DMS transfer velocity to previous observations from $CO_2$ and $^3He/SF_6$.

*1.24 Measurements of DMS Flux and Transfer Velocity*

Global DMS flux estimates rely on climatology of waterside concentration and empirical parameterizations of transfer velocity; both are coarse in spatial resolution and subject to substantial errors. We measure the sea-to-air flux of DMS directly with eddy covariance (EC) on a ship in the open ocean. Dividing flux by the concurrent air-sea concentration difference in DMS, which is largely dictated by the seawater concentration, yields the transfer velocity.

Equating turbulent flux typically measured at 10~20 m above the ocean surface with the true surface flux requires the assumption of a small vertical gradient in flux associated with near-steady state and horizontal homogeneity. With DMS emitted from the ocean surface and diluted by entrainment of free troposphere air, there is a decreasing trend in DMS concentration with height in the marine boundary layer. Blomquist (2010) showed that for typical seawater DMS fields and an 800 m deep boundary layer, measuring at 18 m only underestimates true surface flux by ~1%. The steady state assumption is justified over the ocean because the lifetime of DMS (~1 day) is much longer than the averaging time required by EC (~1 hr).

On a ship, we measure the atmospheric DMS concentration at a frequency of 20 Hz using an Atmospheric Pressure Ionization Mass Spectrometer with isotopically labeled standard (APIMS-ILS). Determination of the ambient DMS mixing ratio is based on the ratio of ambient DMS and a triply deuterated $d_3$DMS standard that is continuously added to the sample air at the inlet. The use of the labeled standard ensures that the accuracy of the measurement is largely unaffected by changes in the sensitivity of the instrument (Bandy et al. 2002). A high turbulent flow is used to preserve high frequency variability during the transit from the inlet to the detector. However, an air drier, necessary for a high ionization efficiency of DMS, adsorbs DMS slightly and limits the half-power response frequency to 1~2 Hz.

We measure winds and ship's three-dimensional motion at the same frequency as DMS using a co-located sonic anemometer and motion sensor. Following Edson et al. (1998), we subtract ship's motion from measured winds to obtain wind velocities along the ship ($U$), across the ship ($V$), and in the vertical ($W$). To account for mean flow

distortions caused by ship's superstructure, the wind velocity coordinates are rotated so that both *V* and *W* average to zero on hourly-basis. An arbitrary ~100 s segment of DMS and motion corrected *W* is shown in Fig. 1.5, with covariance between the two variables visible at time scales ranging from a few seconds to over a minute. The lag correlation between DMS and *W* usually shows a maximum at ~1.5 s that corresponds to the time it takes for air to travel from the inlet through the air drier to the APIMS. Accounting for the lag time, turbulent flux is calculated as $\overline{D\mathrm{MS}'W'}$ in 10-minute intervals and reduced to hourly averages. The primes denote instantaneous deviations from the means, with the overbar indicating time averaging. Figure 1.6 shows a typical DMS:*W* cospectrum, with most of the flux found in the frequency range of 0.5~0.005 Hz. The quadrature spectrum, or the imaginary component of cross correlation, fluctuates around zero, as expected for two variables directly correlated. When winds are clearly out-of-sector (i.e., from a stern quadrant) or when the ship is turning, flow distortion at the inlet is increased, which results in an absence of a clear peak in the DMS:*W* lag correlation and a non-zero mean in the quadrature spectrum; those periods are excluded from the hourly averages. An empirical inlet attenuation correction is applied to the DMS:*W* cospectra for signal loss at high frequencies. An estimate for additional losses at high and low frequencies is obtained by fitting observation with a theoretical cospectral function for neutral conditions (Kaimal et al., 1972). Together, these corrections on flux are generally less than 10%.

In addition to sensor resolution, ambient variability (stochastic nature of eddies) contributes to the random noise of EC flux, which may be reduced through averaging (noise $\propto N^{-1/2}$, where *N* is the number of independent measurements). At a wind speed of

~8 m $s^{-1}$ and in a near-neutral atmosphere, Blomquist et al. (2010) showed that relative uncertainty in DMS flux is on the order of ~30% for an integration time of one hour, and further increases when the boundary layer is stable. The instrumentation details of APIMS-ILS and the measurement of DMS flux by EC are described in Blomquist et al. (2010).

There are significant deviations among transfer velocity parameterizations as functions of wind speed (e.g. Fig. 1.1). EC measurements also show amplifying scatter in high winds, which, in addition to the aforementioned sampling uncertainty, may be due to environmental variability. A number of potential controlling factors that could affect gas exchange have been proposed, including surfactants, wave properties, and boundary layer dynamics. From the Deep Ocean Gas Exchange Experiment (DOGEE) in the Northeast Atlantic, artificial surfactant patches were laid out over areas of several squared kilometers. DMS transfer velocity measured in the presence of surfactants by EC appears to be slightly suppressed compared to observations outside surfactant patches (M. Salter personal communication, 2010), though the reduction is much smaller than previously demonstrated in laboratory (e.g. Frew et al. 2004). From the same experiment, DMS transfer velocity is seen to increase with wave steepness and decrease with wave age. But because both wave steepness and age are correlated with wind speed, their effects on the DMS transfer velocity are, to first order, captured in the wind speed dependence.

The stability of the marine boundary layer, as related to the air-sea temperature difference, can also affect the precision of EC measurements. When the sea surface is warmer than the overlying air, as typical of tropical and temperate environments, the

boundary layer is statically unstable. In the surface water, besides wind shear, buoyancy-driven convection provides another mechanism for turbulence production. In contrast, when the boundary layer is statically stable (air warmer than water), shear-generated turbulence becomes intermittent or suppressed and the boundary layer tends to be shallow. With sea-to-air and entrainment fluxes unchanged, a shallower boundary layer implies a greater systematic underestimate of the true surface flux as a result of measuring at 10~20 m above the surface. In the Southern Ocean Gas Exchange Experiment (SO GasEx) near South Georgia Island, the air temperature frequently exceeded SST. In Chapter 2, I examine the effects of marine boundary layer stability on EC measurements.

*1.25 Example of DMS Flux Measurement in a Region of Elevated Seawater DMS*

Elevated concentration of seawater DMS was often found on the edge of an eddy or near a front between distinct water masses (T. Bates and P. Matrai, unpublished data). We encountered such a vastly enhanced DMS field during Leg 1 of the Vamos Ocean-Cloud-Atmosphere-Land Study Regional Experiment (VOCALS-REx) in October 2008. The ship sailed southward at 11 knots from Panama City, past Ecuador, to the Southeast Pacific. At ~2°S latitude, the sea surface temperature decreased by ~6°C and salinity increased by ~2.5 psu over a distance of 100 km (1.7(a)). At the interface between the warm equatorial water and the cold, nutrient-rich, upwelled water, biological productivity must have been much higher. At the southern edge of this front, seawater DMS concentration (shown every 30 minutes) increased from a typical level of ~2 nM to ~80 nM in a space of just ~20 km. The atmospheric DMS concentration (every minute) and

sea-to-air flux (every 10 minutes) also increased from ~200 pptv and ~3 μmoles $m^2$ $day^{-1}$ to ~1700 pptv and ~150 μmoles $m^2$ $day^{-1}$, respectively (1.7(b)). Because the ship was sailing into surface wind from the south, enhanced atmospheric DMS and DMS flux were detected before the seawater DMS peak and their signals appeared to be somewhat smeared out. The high correspondence between atmospheric DMS concentration and flux was aided by the fact that the front passing occurred in the nighttime, when DMS was not photochemically destroyed by OH. The temporal resolution of the semi-automated seawater DMS measurement by purge-and-trap/GC was limited to every half an hour. A much faster measurement, such as by membrane equilibration/MS, would have afforded better spatial resolution near the edges of such fronts or eddies.

### 1.3 Atmospheric Sulfur Cycle

In the atmosphere, the oxidation of DMS yields, among other products, sulfur dioxide ($SO_2$) and non-sea-salt sulfate aerosols ($SO_4^{2-}$). These water-soluble and acidic $SO_4^{2-}$ aerosols affect atmospheric chemistry (Charlson and Rodhe, 1982) and also influence the global radiative balance directly by scattering of incoming radiation and indirectly through their effects on cloud microphysics (Charlson et al., 1992; Charlson et al., 1987).

When ambient water vapor content reaches supersaturation, aerosols larger than a critical size act as cloud condensation nuclei (CCN) and activate to form cloud droplets (Hoppel et al., 1986). Given the same amount of liquid water, more CCN leads to a greater cloud droplet number concentration and reduced mean droplet size, which results in more reflective and possibly longer lived clouds. The impact of naturally derived

$SO_4^{2-}$ on clouds should be the most noticeable in regions lacking anthropogenic CCN (Twomey, 1991), such as over the remote ocean. Gunson et al. (2006) modeled a 1.6 ºC warming / 0.8 ºC cooling for a decrease / increase of DMS emission by a factor of two. Moreover, their modeled DMS flux out of the ocean responds to warming (cooling) by slightly increasing (decreasing) over time, consistent with a negative feedback. Other studies suggest less pronounced climatic effects from DMS with increasing input of anthropogenic $SO_2$ and $SO_4^{2-}$ to the atmosphere. From the modeling work of Boucher and Lohmann (1995) and Woodhouse et al. (2010), the indirect radiative forcing by $SO_4^{2-}$ aerosols is found to be much more sensitive to total $SO_4^{2-}$ and cloud droplet number concentration than to the spatial distribution of DMS flux and background $SO_4^{2-}$ level. The apparent insensitivity to DMS is in part related to the difficulty in separating the natural and anthropogenic contributions to $SO_4^{2-}$ aerosols. The climatic effect of DMS might be more apparent locally. Boucher et al. (2003) showed high spatial heterogeneity in their modeled indirect radiative forcing, varying from close to zero to -5 $Wm^{-2}$. More accurately constraining the climatic effects of DMS-derived $SO_4^{2-}$ aerosols requires being able to model their regional distributions. The complex formation and removal pathways of sulfur species in the atmosphere, however, are still not well-understood and are subject to ongoing research. Using observations from a ship and an aircraft, I closely examine the budgets of DMS-derived $SO_2$ and $SO_4^{2-}$ aerosols in the marine atmosphere of the Southeast Pacific in Chapters 3 and 4.

*1.31 DMS Oxidation*

About 95% of atmospheric DMS oxidation takes place in the gas phase, with the hydroxyl radical (OH) being the most important oxidant, resulting in a DMS lifetime of ~1 day (Lucas and Prinn, 2002; Chen et al., 1999). The principle oxidizing free radical towards trace gases in the atmosphere (Levy, 1971), OH is formed from the reaction between $O(^1D)$, a product of ozone ($O_3$) photolysis, and water vapor. The tropospheric concentration of OH peaks in midday and becomes non-existent at night due to its high reactivity and low selectivity. Globally, the highest OH levels are found in the tropics characterized by high humidity and strong actinic fluxes (Seinfeld and Pandis, 2006).

DMS is oxidized by OH through two distinctive pathways: H-atom abstraction and direct OH-addition (Hynes et al., 1996). The abstraction pathway dominates at high temperatures and leads to $SO_2$, which can be further oxidized to $SO_4^{2-}$. The addition pathway, in contrast, speeds up at low temperatures and leads to dimethylsulfoxide (DMSO), dimethylsulfone ($DMSO_2$), methanesulfonic acid (MSA), $SO_2$, and other minor products. At 298 K, about 80% of the oxidation of DMS goes through the abstraction pathway; at 285 K the two pathways are about equal (Wallington et al., 1993). A simplified DMS oxidation scheme in the remote marine atmosphere is illustrated in Fig. 1.8, as simplified from Davis et al. (1999). Studies from Christmas Island in the remote Central Pacific have shown a pronounced diel cycle in DMS that is dictated by the reaction with OH (Bandy et al., 1996). As DMS is emitted from the ocean to the atmosphere continuously, its concentration builds up overnight in the absence of OH and reaches a maximum by sunrise. During the daytime, DMS is oxidized by OH and its concentration declines to a minimum by sunset.

At night in a polluted marine environment, DMS can also be lost through the reaction with the nitrate radical ($NO_3$), which is formed from the reaction between $NO_2$ and $O_3$. Because $NO_3$ rapidly photolyzes during the daytime, its concentration is only significant in the nighttime. The oxidation of DMS by $NO_3$ proceeds through the H-atom abstraction pathway and has a rate constant ~4 times lower than that of the overall OH reaction at 298 K (Sander et al., 2006). Because of its localized production and short residence time (1~4 days), $NO_3$ is estimated to remove more DMS in the heavily industrial Northern Hemisphere (8.7%) than in the cleaner Southern Hemisphere (6.5%), where $NO_2$ input is lower (Kloster et al., 2006). In the remote tropical Pacific, $NO_3$ accounts for only a few percent of the total DMS oxidative loss (Davis et al., 1999; Chen et al., 2000). The oxidation of DMS by $NO_3$ becomes more important at high latitudes where sunlight is limited in the winter, allowing for the build up of the radical.

Other oxidants of DMS that have been studied include $O_3$ and halogen radicals. Since the mixing ratio of $O_3$ generally increases with altitude, the DMS oxidation by $O_3$ is thought to be more important in the upper troposphere (on the order of 5%, Boucher et al., 2003). Halogen radicals produced from sea-salt aerosols, in particular bromine oxide (BrO), can catalytically oxidize DMS (Seinfeld and Pandis, 2006). The oxidation of DMS by BrO follows the addition pathway and leads to DMSO. Some authors (Sciare et al., 2000; Boucher et al. 2003) have suggested that the removal of DMS by BrO can be significant, which is supported by recent measurements of high concentrations of BrO in the tropical Atlantic (Read et al., 2008). However, techniques for measuring BrO at concentrations typically encountered in the open ocean (differential optical absorption spectroscopy and mass spectrometry) are still challenged with detection limits. Until

halogen radical concentrations can be measured accurately and routinely at ambient levels, their importance towards DMS remains mostly speculative.

What dictates the diel variability in DMS in the Southeast Pacific, in a marine region that is also influenced by pollution transport from the continent? Is OH still the main oxidant, or do pollution-derived nitrate radicals and halogen radicals play important roles in DMS oxidation? In Chapter 3, from the mass balance of DMS measured in VOCALS-REx, I estimate an effective concentration of OH in the stratocumulus-topped marine boundary layer of the Southeast Pacific. This OH-equivalent oxidant concentration is compared to estimates from complex photochemical models. By examining the diel cycles of DMS as well as the oxidants, I place constraints on the oxidation of DMS due to $NO_3$ and BrO radicals.

*1.32 Products of DMS Oxidation*

Bandy et al. (1996) first reported from measurements at Christmas Island that $SO_2$ increased during the day when DMS decreased due to OH oxidation. The anti-correlation suggested that DMS is indeed the main source for $SO_2$ in the remote marine atmosphere. The conversion efficiency from DMS to $SO_2$ has been found to be 70~90% (Davis et al., 1999; Chen et al., 2000; Shon et al., 2001; Faloona 2009). Among oxidation products of DMS, only $SO_2$ has the potential to make more new particles, while the others increase aerosol mass by condensing upon preexisting surfaces.

$SO_2$ is oxidized in both the gas phase and the aqueous phase. The gas phase reaction between $SO_2$ and OH forms sulfuric acid vapor ($H_2SO_{4(g)}$):

$$SO_2 + OH \rightarrow HOSO_2 \xrightarrow{O_2} SO_3 + HO_2 \qquad (1.16a)$$

$$SO_3 + H_2O \rightarrow H_2SO_4(g) \quad (1.16b)$$

In most circumstances, the non-volatile $H_2SO_{4(g)}$ condenses upon preexisting aerosol surfaces and grows them to larger sizes, thereby increasing $SO_4^{2-}$ aerosol mass. Under specific conditions, $H_2SO_{4(g)}$ molecules undergo gas-to-particle conversion and form new nm-sized particles, resulting in sudden and dramatic increase in the particle number concentration (Weber et al., 1999). Environments favorable for such nucleation processes typically have high $H_2SO_{4(g)}$ and humidity, as well as low aerosol surface areas and temperatures. New particle formation events have been observed in clean air high in the free troposphere (Clarke 1998b), near cloud outflow regions (Hegg et al., 1990; Perry and Hobbs, 1994), in the remote marine boundary layer (Hoppel et al., 1994), and adjacent to a region of precipitation (Clarke et al., 1998a). Clouds remove aerosol surface area by scavenging and inject moisture into the surroundings. In the outflow region, elevated actinic flux enhances OH and so $H_2SO_{4(g)}$ production. Mixing of air is that cleaned of particles by clouds and air rich in reactive vapors creates an ideal condition for nucleation (Clarke et al, 1998a). Rainfall similarly creates favorable conditions for nucleation by removing aerosols through precipitation scavenging. Freshly nucleated particles grow by condensation of vapor and coagulation by Brownian motion to a detectable size of ~3 nm in minutes to an hour (Weber et al., 1999) and to 10 nm with in a few hours (Hegg et al., 1992). From shipboard measurements, Covert et al. (1992) observed a ~3 hr time lag between a recent nucleation event and the increase in concentration of 20~24 nm particles. In the Southeast Pacific, we observed frequent occurrences of recent new particle formation from an aircraft as well as from a ship. Where in the atmosphere and under what conditions did the nucleation take place? Was

the source of volatile vapors in the gas-to-particle conversion natural or anthropogenic? In Chapter 4, I provide examples of new particle formation observed on both sampling platforms and discuss their correspondence to drizzle events and open cell structures in clouds.

The oxidation of $SO_2$ in the aqueous phase is much faster than in the gas phase. In an aqueous solution, $SO_2$ is equilibrated to $SO_2.H_2O$, $HSO_3^-$, and $SO_3^{2-}$ (together S(IV)) in an analogous fashion to $CO_2$. The equilibrium reactions are pH dependent with $HSO_3^-$ being the predominant species at typical atmospheric pH. Aqueous phase oxidation of $SO_2$ can take place in cloud water mostly by $H_2O_2$, or in sea-salt aerosols by $O_3$, leading to $SO_4^{2-}$ aerosols (S(IV)):

$$S(IV) + H_2O_2 \rightarrow S(VI) + H_2O \quad (1.17a)$$

$$S(IV) + O_3 \rightarrow S(VI) + O_2 \quad (1.17b)$$

These secondary $SO_4^{2-}$ typically make up the bulk of the submicron (fine) aerosol mass, whereas sea-salt from wave breaking account for the majority of the supermicron (coarse) number as well as total aerosol mass. Due to the dissolution of $CO_2$ and other acidic species, cloud water typically has a pH under 5 (Chameides, 1984), which makes $H_2O_2$ the principal oxidant of $SO_2$ in cloud. Hegg (1985) suggested cloud processing to be the most important mechanism for the conversion from $SO_2$ to $SO_4^{2-}$.

The S(IV)-$H_2O_2$ reaction is largely pH insensitive because the pH dependences in the equilibrium of $HSO_3^-$ and in the $H_2O_2$ reaction cancel. The S(IV)-$O_3$ reaction, on the other hand, is extremely pH-sensitive. The reaction rate approximately varies inversely with the square of $[H^+]$ and is greatly enhanced at high pH. Sea-salt tends to be more basic than the fine mode aerosols because of the initial alkalinity of seawater (pH~8.1)

and the carbonate buffering capacity. Some authors postulated oxidation in sea-salt aerosols by $O_3$ to be a major sink of $SO_2$ and source of $SO_4^{2-}$ mass (Sievering et al., 1991; Faloona et al., 2010). However, both the uptake of $SO_2$ and the production of $SO_4^{2-}$ increase the acidity of the sea-salt, making the $O_3$ reaction self-limiting.

Aside from oxidation reactions, $SO_2$ is removed from the MBL by dry deposition to the ocean surface. The rate of dry deposition of aerosols strongly depends on particle size. Deposition velocity is very slow for the accumulation mode, which is the reason why aerosols in that size range accumulate in the atmosphere. Dry deposition is much faster for coarse particles due to gravitational settling and has been proposed to be a significant mechanism for the removal of non-sea-salt $SO_4^{2-}$ (Sievering et al., 1991; Faloona et al., 2010). However, given that little non-sea-salt $SO_4^{2-}$ mass is usually present in the coarse mode, it appears unlikely for dry deposition to be a major sink for $SO_4^{2}$. Because of its relatively low solubility in precipitating droplets, $SO_2$ is not significantly affected by wet deposition. In contrast, the highly soluble MSA and $SO_4^{2-}$ are efficiently removed from the MBL by wet deposition. The efficiency of wet scavenging is a complex function of precipitation droplet size, rain rate, and aerosol size distribution.

In a marine atmosphere covered by stratocumulus clouds, what fractions of $SO_2$ are removed due to cloud processing and sea salt oxidation? I estimate the heterogeneous reaction rates of $SO_2$ in the Southeast Pacific in Chapter 4. I also constrain the dry and wet deposition fluxes of $SO_4^{2-}$ based on observations using a mass balance approach. In addition to being produced in situ, $SO_2$ and $SO_4^{2-}$ aerosols may be transported over a long distance in the free troposphere and mixed into the marine boundary layer via

entrainment. I use the aircraft observations to estimate the entrainment of these two sulfur species. To further examine the sources and sinks of $SO_2$ and $SO_4^{2-}$, a simple one-layer model is used to calculate their expected diurnal cycles. Along with results from Chapter 3, I summarize the atmospheric cycling of DMS, $SO_2$, and $SO_4^{2-}$ in the Southeast Pacific in Chapter 4.

**Figures**

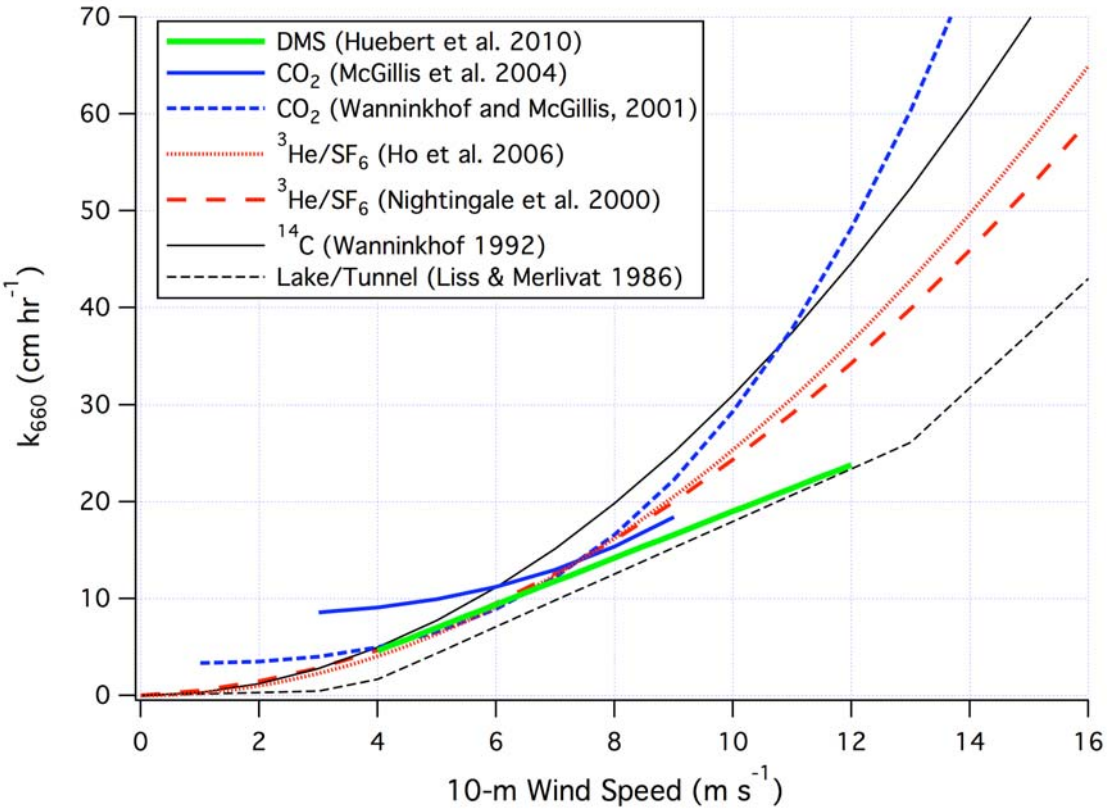


Figure 1.1 Transfer velocity parameterizations of waterside controlled gases at $S_c$ = 660 as functions of wind speed. While most models agree fairly well in low to moderate winds, they diverge significantly in high winds. Transfer of DMS appears to be lower than those derived from sparingly soluble tracer gases, including $CO_2$ and $^3He/SF_6$.

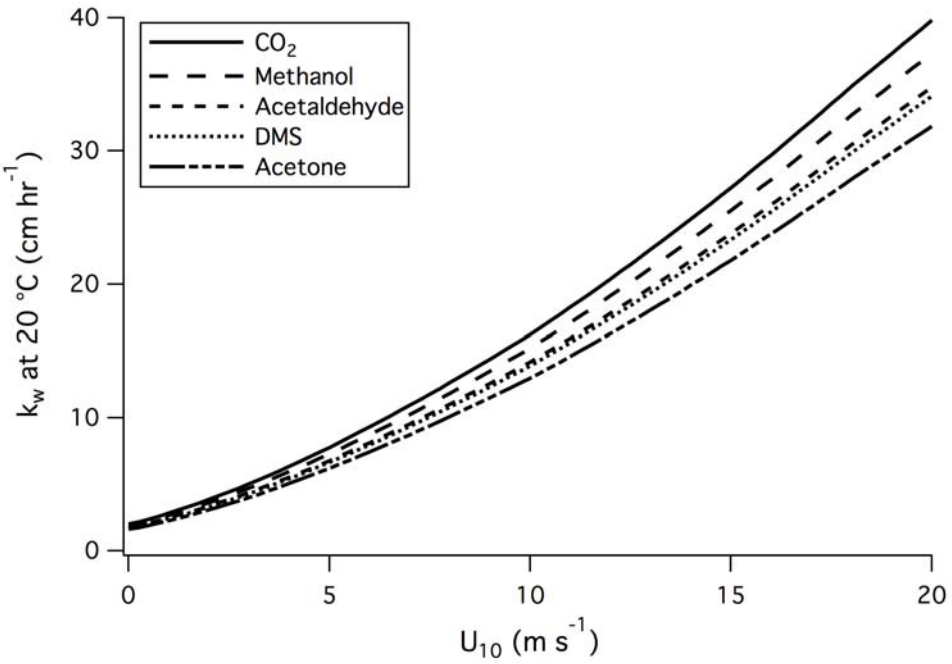


Figure 1.2 Waterside transfer velocity ($k_w$) of $CO_2$, DMS, acetaldehyde, acetone, and methanol without the bubble effect predicted by the NOAA COARE 3.0 air-sea bulk flux model at 20 °C. $k_w$ of different gases can be related by the relationship $S_{cw}^{-0.5}$.

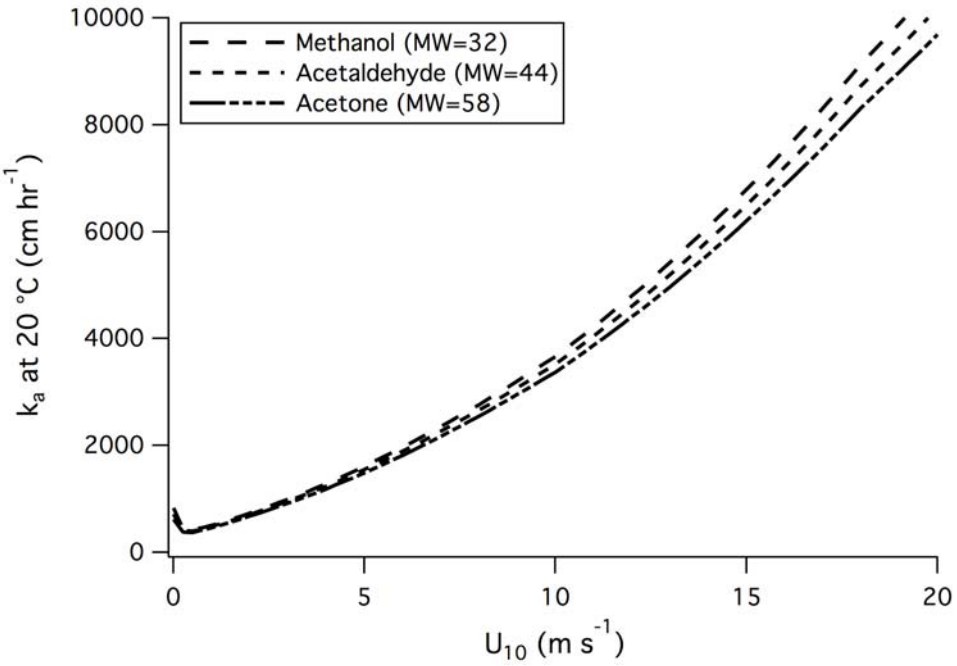


Figure 1.3 Airside transfer velocity ($k_a$) predicted by the NOAA COARE 3.0 air-sea bulk flux model at 20 °C. $k_a$ decreases as the molecular weight (MW) of the gas increases.

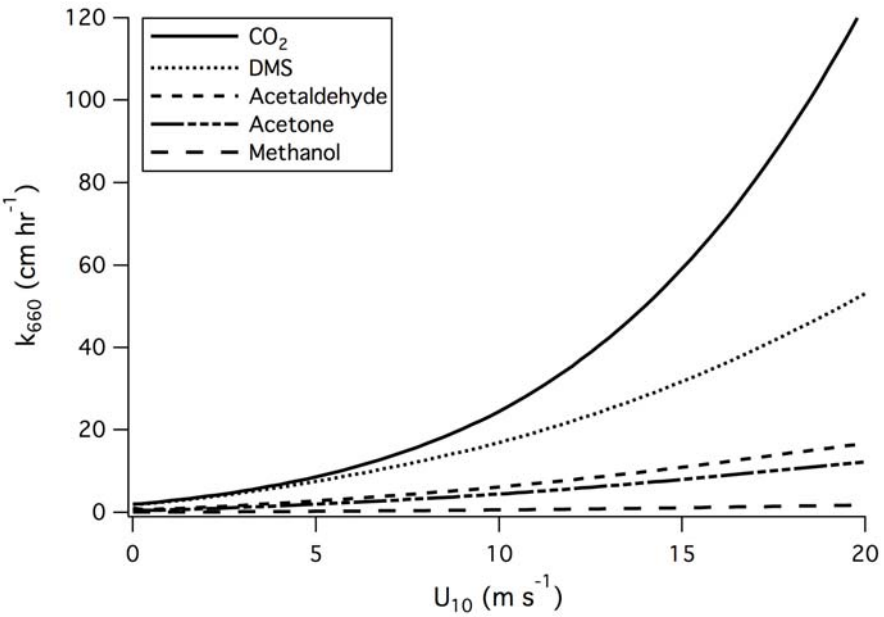


Figure 1.4 Total transfer velocity ($k_{660}$) predicted by the NOAA COARE 3.0 air-sea bulk flux model. Soluble gases having much lower transfer velocity than insoluble gases due to both increased airside control and less partition in air bubbles.

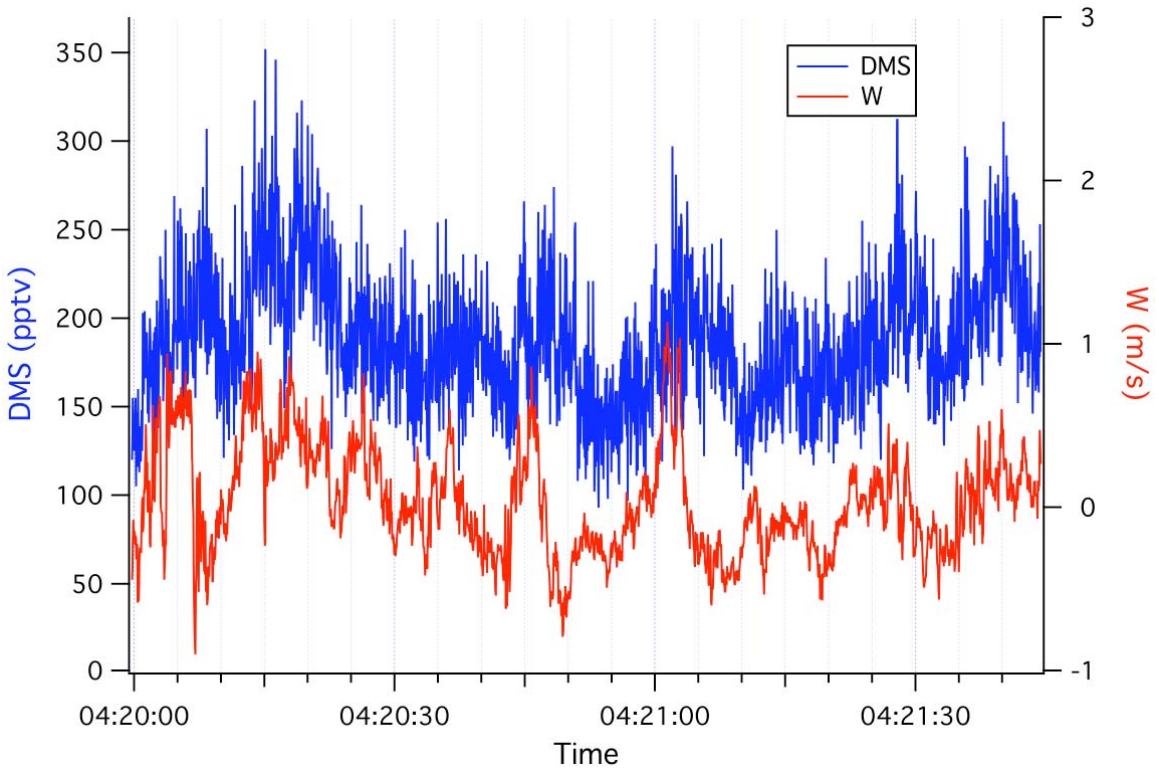


Figure 1.5 A ~100 s time series of DMS and motion-corrected *W* showing covariance on different time scales, from a few seconds to over a minute. Due to the time it takes for air to travel from the inlet to the mass spectrometer, DMS usually lags behind *W* by ~1.5 seconds, a time accurately determined from the lag correlation analysis between these two variables.

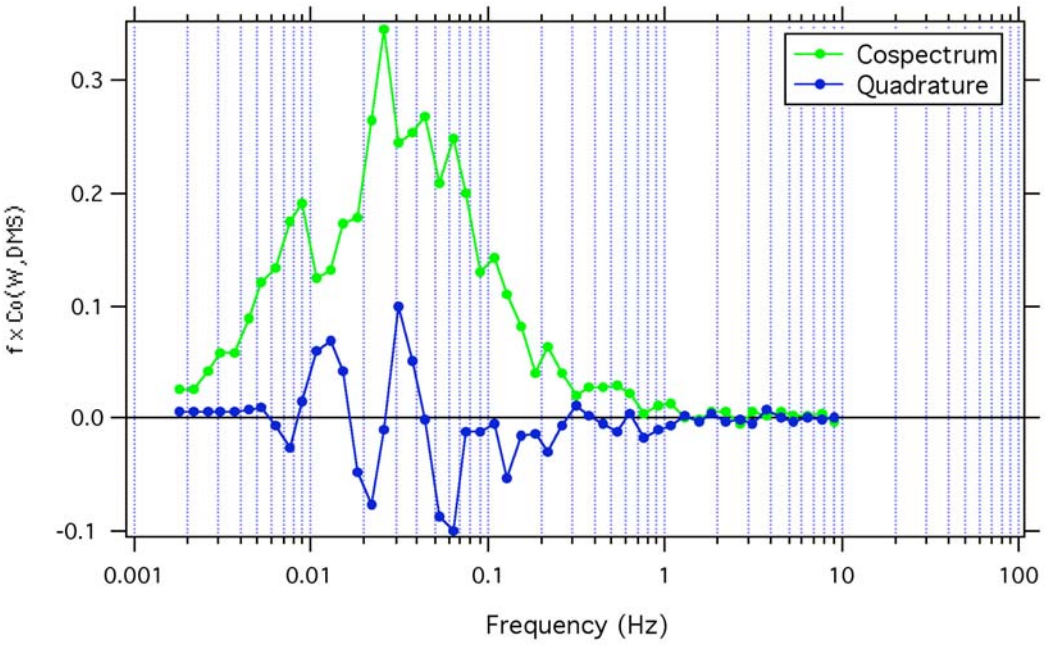


Figure 1.6 Typical hourly cospectrum (flux) and quadrature between DMS and *W*. Most of the flux is found between 0.005~0.5 Hz. The loss of flux at very high and very low frequencies is usually only a few percent. Quadrature (the imaginary component of the cross correlation) fluctuates around zero, as expected for a high degree of correlation between two variables.

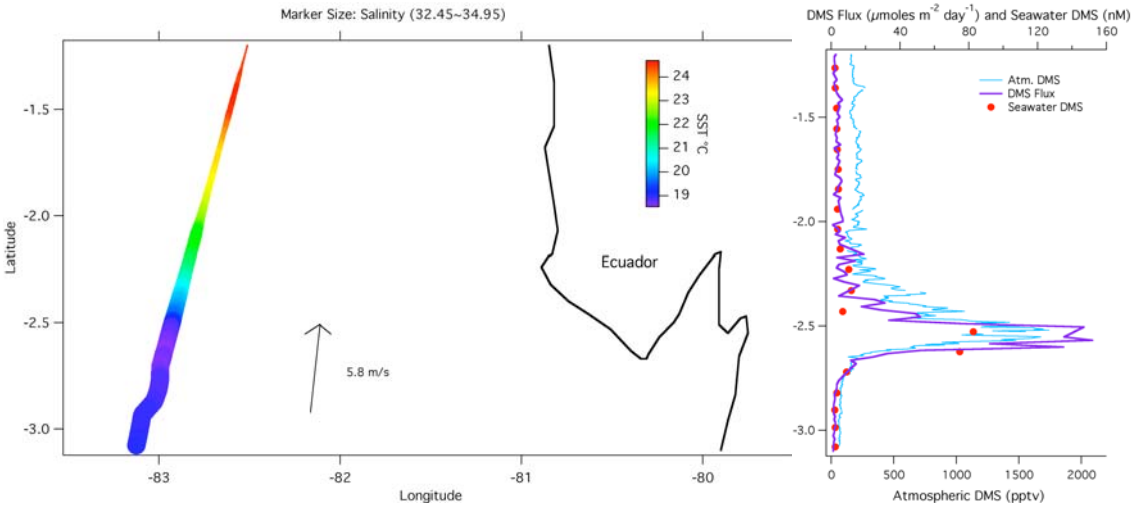


(a) (b)

Figure 1.7 (a) Crossing of a front from the warm and fresh equatorial water to the cool and salty water in the south during the 1st Leg of the VOCALS-REx cruise; the mean wind was perpendicular to the front (b) A large enhancement in seawater DMS (30 min), atmospheric DMS (1 min), and sea-to-air flux (10 min) on the southern side of the front crossing. As the ship sailed into the wind, elevated atmospheric DMS and flux were observed slightly before the peak in seawater concentration. A faster seawater DMS measurement would have afforded better resolution near the edges of similar fronts and eddies.

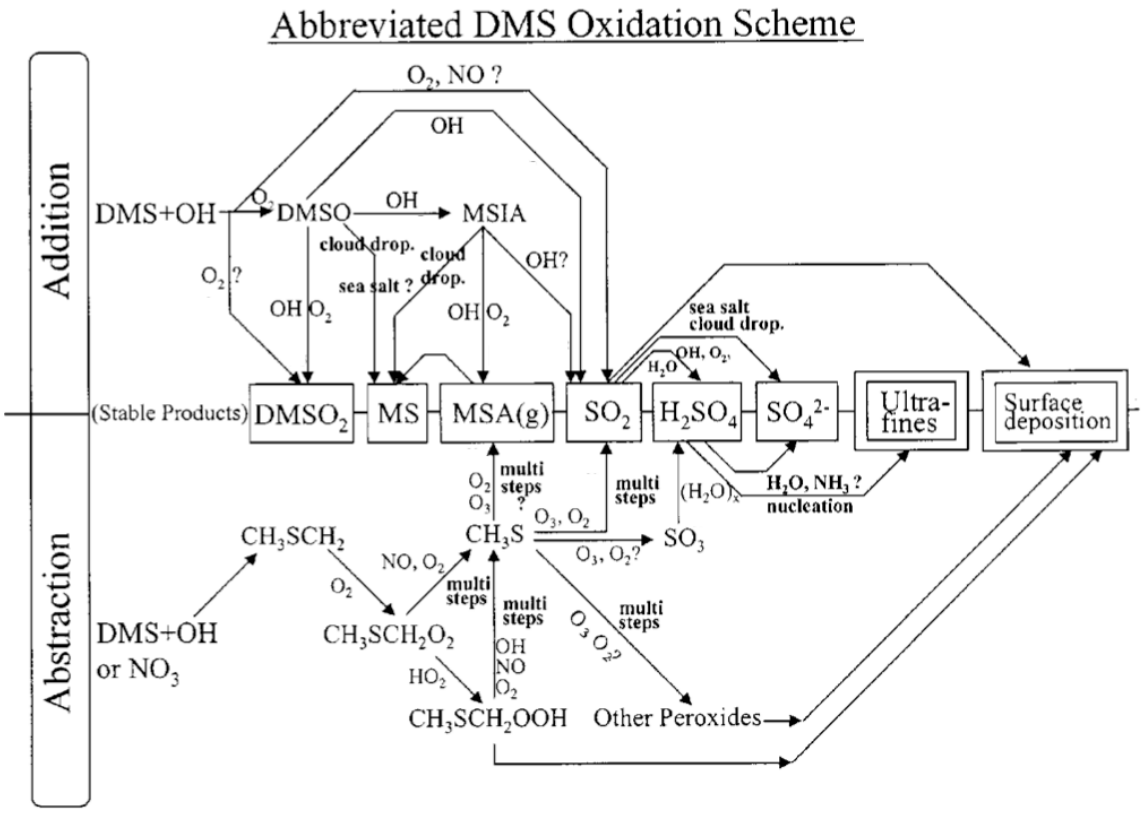


Figure 1.8. Sulfur oxidation scheme in the remote marine atmosphere simplified from Davis et al., (1999). DMS oxidization by OH has two pathways, addition and abstraction. The abstraction pathway leads to $SO_2$, which is further oxidized to $SO_4^{2-}$. The addition channel leads to DMSO, $DMSO_2$, MSA, and also $SO_2$. The symbol '?' denotes proposed reaction steps with no supporting kinetic or field data.

## References


Anderson, T.R., Spall, S. A., Yool, A., Cipollini, P., Challenor, P. G., and Fasham, M. J. R.: Global fields of sea surface dimethylsulfide predicted from chlorophyll, nutrients and light, J. Marine Syst., 30, 1–20, 2001.

Andreae, M.O.: The biogeochemical cycling of sulfur and nitrogen in the remote atmosphere, J.N. Galloway et al., Eds., p. 5-25. 1985.

Aumont, O., Belviso, S., and Monfray, P.: Dimethylsulfoniopropionate (DMSP) and dimethylsulfide (DMS) sea surface distributions simulated from a global three-dimensional ocean carbon cycle model, J. Geophys. Res.-Oceans, 107, C4, doi:10.1029/1999JC000111, 2002.

Bailey, K.E., Toole, D., Blomquist, B., Najjar, R., Huebert, B., Kieber, D., Kiene, R., Matrai, P., Westby, G., del Valle, D.: Dimethylsulfide production in Sargasso Sea eddies, Deep Sea Research Part II: Topical Studies in Oceanography, Volume 55, Issues 10-13, Mesoscale Physical-Biological-Biogeochemical Linkages in the Open Ocean: Results from the E-FLUX and EDDIES Programs, 1491-1504, ISSN 0967-0645, DOI: 10.1016/j.dsr2.2008.02.011, 2008.

Bandy, A.R., Thornton, D.C., Blomquist, B.W., Chen, S., Wade, T.P., Ianni, J.C., Mitchell, G.M., and Nadler, W.: Chemistry of dimethyl sulfide in the equatorial Pacific atmosphere, Geophys. Res. Lett. 23, 741-744, 1996.

Bandy, A.R., Thornton, D.C., Tu, F.H., Blomquist, B.W., Nadler, W., Mitchell, G.M., and Lenchow D.H.: Determination of the vertical flux of dimethylsulfide by eddy correlation and atmospheric pressure ionization mass spectrometry (APIMS), J. Geophys. Res., 107(D24), 4743, doi:10.1029/2002JD002472, 2002.

Bates, T.S., Cline, J.D., Gammon, R.H., and Kelly-Hansen, S.R.: Regional and seasonal variations in the flux of oceanic dimethylsulfide to the atmosphere, J.Geophys. Res., 92, 2930-2938, 1987.

Bates, T.S., Quinn, P.K., Covert, D.S., Coffman, D.J., Johnson, J.E., and Wiedensohler, A.: Aerosol physical properties and processes in the lower marine boundary layer: A comparison of shipboard sub-micron data from ACE-1 and ACE-2, Tellus, Ser. B, 52, 258 – 272, 2000.

Blomquist, B., Fairall, C.W., Huebert, B., Kieber D., and Westby, G.: DMS sea-air transfer velocity: Direct measurements by eddy covariance and parameterization based on the NOAA/COARE gas transfer model, Geophys. Res. Lett., 33(1.7), 10.1029/2006GL025735, 2006.

Blomquist, B. W., Huebert, B. J., Fairall, C. W., and Faloona, I. C.: Determining the sea-air flux of dimethylsulfide by eddy correlation using mass spectrometry, Atmos. Meas. Tech., 3, 1-20, doi:10.5194/amt-3-1-2010, 2010.

Boucher, O. and Lohmann, U.: The sulface-CCN-cloud albedo effect: A sensitivity study with two general circulation models, Tellus, 47B, 281-300, 1995.

Boucher, B., Moulin, C., Belviso, S., Aumont, O., Bopp, L., Cosme, E., von Kuhlmann R., Lawrence, M.G., Pham, M., Reddy, M.S., Sciare, J., and Venkataraman, C.,: DMS atmospheric concentrations and sulphate aerosol indirect radiative forcing: a sensitive study to the DMS source representation and oxidation. Atmos. Chem. and Phys, 3, 49-65, 2003.

Chameides, W.L.: The photochemistry of a remote marine stratiform cloud, J. Geophys. Res. 89(D3), 4739–4755, doi:10.1029/JD089iD03p04739, 1984.

Charlson, R.J., and H. Rodhe: Factors controlling the acidity of rainwater, Nature, 295, 683-685, 1982.

Charlson, R.J., Lovelock, J.E., Andreae, M.O., and Warren S.G.: Oceanic phytoplankton, atmospheric sulfur, cloud albedo and climate, Nature, 326, 655-661, 1987.

Chen G., Davis, D., Kasibhatla, P., Bandy, A., Thornton, D., Blake, D.: A mass-balance/photochemical assessment of DMS sea-to-air flux as inferred from NASA GTE PEM – West A and B observations. J. Geophys. Res., vol. 104, NO. D5, 5471-5482, 1999.

Chen, G., Davis, D.D., Kasibhatla, P., Bandy, A.R., Thornton D.C., Huebert, B.J., Clarke, A.D., Blomquist, B.W.: A study of DMS oxidation in the tropics: comparison of Christmas Island field observations of DMS, $SO_2$, and DMSO with model simulations. Journal of Atmos. Chem., 37, 137-160, 2000.

Clarke, A.D., Davis, D., Kapustin, V.N., Eisele, F., Chen, G., Paluch, I., Lenschow D., Bandy, A.R., Thornton D., Moore, K., Mauldin, L., Tanner, D., Litchy, M., Carroll, M.A., Collins, J., Albercook, G.: Particle nucleation in the tropical boundary layer and its coupling to marine sulfur sources. Science Vol 282, 89-92, 1998a.

Clarke, A. D., Varner, J. L., Eisele, F., Mauldin, R. L., Tanner, D., and Litchy, M.: Particle production in the remote marine atmosphere: Cloud outflow and subsidence during ACE 1, J. Geophys. Res., 103(D13), 16,397–16,409, doi:10.1029/97JD02987, 1998b.

Csanady, G.T.: The role of breaking wavelets in air-sea gas transfer, J. Geophys. Res., 95, 749–759, 1990.

Covert, D.S., Kapustin, V.N., Quinn, P.K., and Bates T.S., New particle formation in the marine boundary layer, J. Geophys. Res., 92, 20, 581-589, 1992.

Dacey J.W., Wakeham S.G.: Oceanic dimethylsulfide: production during zooplankton grazing on phytoplankton. Science, Vol. 233, p.1314-1316, 1986.

Dacey, J.W.H., Howse, F.A., Michaels, A.F., and Wakeham, S.G.: Temporal variability of dimethylsulfide and dimethylsulfoniopropionate in the Sargasso Sea, Deep Sea Res., 45, 2085-2104, 1998.

Davis, D., Chen, G., Bandy, A., Thornton D., Eisele, F., Mauldin, L., Tanner, D., Lenschow, D., Fuelberg, H., Huebert B., Heath, J., Clarke, A., and Blake, D.,: Dimethylsulfide oxidation in the equatorial Pacific: comparison of model simulations with field observations for DMS, $SO_2$, $H_2SO_4$(g), MSA(g), MS, and NSS. J. Geophys. Res., Vol 104, NO. D5, 5765-5784,1999.

Duce, R. A., Liss, P., Merrill, J.T. et al.:, The Atmospheric Input of Trace Species to the World Ocean, Global Biogeochem. Cycles, 5, 193259, 1991.

Edson, J.B., Hinton, A.A., Prada, K.E., Hare, J.E., and Fairall C.W.: Direct covariance flux estimates from mobile platforms at sea, J. Atmos. Oceanic Technol., 15, 547–562, 1998.

Elliott, S.:, Dependence of DMS global sea-air flux distribution on transfer velocity and concentration field type, J. Geophys. Res., 114, G02001, doi:10.1029/2008JG000710. 2009.

Fairall, C.W., Bradley, E.F., Hare, J.E., Grachev, A.A., and Edson, J.B.: Bulk parameterization of air-sea fluxes: Updates and verification for the COARE algorithm, J. Climate, 16, 571–591, 2003.

Faloona, I. Sulfur processing in the marine atmospheric boundary layer: A review and critical assessment of modeling uncertainties, Atmos. Environ., 43, 18, 2841-2854, ISSN 1352-2310, DOI: 10.1016/j.atmosenv.2009.02.043 2009.

Faloona, I., Conley, S., Blomquist, B., Clarke, A., Kapustin, V., Howell, S., Lenschow, D.H., Bandy, A.: Sulfur dioxide in the tropical marine boundary layer: dry deposition and heterogeneous oxidation observed during the Pacific Atmospheric Sulfur Experiment. J. Atmos. Chem., doi: 10.1007/s10874-010-9155-0,

2010.

Falkowski, P.G., Kim, Y., Kolber, Z., Wilson, C., Wirick, C., and Cess, R.: Natural versus anthropogenic factors affecting low-level cloud albedo over the North Atlantic, Science, 256, 1311-1313, 1992.

Frew, N. M., et al., Air-sea gas transfer: Its dependence on wind stress, small-scale roughness, and surface films, J. Geophys. Res., 109, C08S17, doi:10.1029/2003JC002131, 2004.

Gunson, J. R., Spall, S. A., Anderson, T. R., Jones, A., Totterdell, I. J., and Woodage, M. J.: Climate sensitivity to ocean dimethylsulphide emissions, Geophys. Res. Lett., 33, L07701, doi:10.1029/2005GL024982, 2006.

Hare, J.E., Fairall, C.W., McGillis, W.R., Edson, J.B., Ward, B., and Wanninkhof R.: Evaluation of the National Oceanic and Atmospheric Administration/Coupled-Ocean Atmospheric Response Experiment (NOAA/COARE) air-sea gas transfer parameterization using GasEx data, J. Geophys. Res., 109, C08S11, doi:10.1029/2003JC001831, 2004.

Hegg, D.A.: The importance of liquid-phase oxidation of $SO_2$ in the troposphere. J. Geophys. Res., 20, 3773-377, 1985.

Hegg, D.A., Covert, D.S., and Kapustin, V.N.: Modeling a case of particle nucleation in the marine boundary layer, J. Geophys. Res., 97, 9851-9857, 1992.

Hegg, D.A., L.F. Radke, and P.V. Hobbs, Particle production associated with marine clouds, J. Geophys. Res., 95, 13917-13926, 1990.

Ho, D., Law, C.S., Smith, M.J., Schlosser, P., Harvey, M., and Hill, P.: Measurements of air-sea gas exchange at high wind speeds in the Southern Ocean: Implications for global parameterizations. Geophys. Res. Lett., Vol. 33, L16611, doi:10.1029/2006GL026817, 2006.

Hoppel, W.A., Frick, G.M., Larson, R.E.: Effect of nonprecipitating clouds on the aerosol size distribution in the marine boundary layer. Geophys. Res. Lett., 13(1.2), 125–128, doi:10.1029/GL013i002p00125, 1986.

Hoppel, W. A., Frick, G. M., Fitzgerald, J. W., and Larson, R. E.: Marine boundary layer measurements of new particle formation and the effects nonprecipitating clouds have on aerosol size distribution, J. Geophys. Res., 99(D7), 14,443–14,459, doi:10.1029/94JD00797, 1994.

Huebert, B., Blomquist, B., Hare, J., Fairall, C., Johnson, J., and Bates, T.: Measurement of the sea-air DMS flux and transfer velocity using eddy correlation, Geophys. Res. Lett., 31, L23113, doi:10.1029/2004GL021567, 2004.

Huebert, B., Blomquist, B., Yang, M., Archer, S., Nightingale, P., Yelland, M., Stephens, J., Pascal, R., and Moat, B.: Linearity of DMS Transfer Coefficient with Both Friction Velocity and Wind Speed in the Moderate Wind Speed Range, Geophys. Res. Lett., 37, L01605, doi:10.1029/2009GL041203, 2010.

Hynes, A.J., Wine, P.H., and Semmes, D.H.: Kinetics and mechanism of OH reactions with organic sulfides, J. Phys. Chem., 90, 4148-4156, 1986.

Kaimal, J., Wyngaard, J., Izumi, Y., and Cot ´e O.: Spectral characteristics of surface layer turbulence, Q. J. Roy. Metor. Soc., 98, 563–589, 1972.

Keller, M.D., et al,: Dimethylsulfide production in marine phytoplankton. Biogenic Sulfur in the Environment (Saltzman, E. and Cooper, W.J., eds), p. 167-182, American Chemical Society, 1989.

Kettle, A. J., et al.: A global database of sea surface dimethylsulfide (DMS) measurements and a procedure to predict sea surface DMS as a function of latitude, longitude, and month, Global Biogeochem. Cycles, 13(1.2), 399–444, doi:10.1029/1999GB900004, 1989.

Kettle, A.J. and Andreae, M.O.: Flux of dimethylsulfide from the oceans: a comparison of updated data sets and flux models. J.Geophys. Res., 105, 26, 793-26, 808, 2000.

Kiene, R.P., and Service, S.K.: Decomposition of dissolved DMSP and DMS in estuarine waters: dependence on temperature and substrate concentration, Mar. Ecol. Prog. Ser., 76, p.1-11, 1991.

Kloster S., Feichter, J., Maier-Reimer, E., Six K.D., Stier P., and Wetzel, P.: DMS cycle in the marine ocean-atmosphere system – a global model study. Biogeosciences, 3, 29-51, 2006.

Levy, H.I.: Normal Atmosphere: Large Radical and Formaldehyde Concentrations Predicted, Science, 173, 141-143, 1971.

Liss, P.S.: Processes of gas exchange across an air-water interface, Deep Sea Research and Oceanographic Abstracts, Volume 20, Issue 3, March 1973, Pages 221-238, ISSN 0011-7471, DOI: 10.1016/0011-7471(73)90013-2, 1973.

Liss, P.S., and Merlivat, L.: Air-sea gas exchange rates: Introduction and synthesis, in The Role of Air-Sea Interactions in Geochemical Cycling, edited by p.Buat-Menard, pp. 113-129, D.Reidel, Hingham, MA, 1986.

Liss, P.S., and Slater P.G.: Flux of Gases across the air-sea interface, Nature, 247, 181–184, 1974.

Lovelock, J.E., and Margulis L.: Atmospheric homeostasis by and for biosphere – Gaia hypothesis, Tellus, 26(102), 2-10, 1974.

Lucas, D. and Prinn, R.G.: Mechanistic studies of dimethylsulfide oxidation products using an observationally constrained model. J. Geophys. Res., Vol. 107, NO. D14, 4201, 2002.

McGillis, W.R., Dacey, J.W.H., Frew, N.M., Bock, E.J., and Nelson, R.K.: Water-air flux of dimethylsulfide, J. Geophys. Res., 105, NO. C1, 1187–1193, 2000.

McGillis, W. R., et al.: Air-sea CO2 exchange in the equatorial Pacific, J. Geophys. Res., 109, C08S02, doi:10.1029/2003JC002256, 2004.

Monahan, E.C., and O'Muircheartaigh I.G.: Optimal power-law description of oceanic whitecap coverage on wind speed, J. Phys. Ocean., 10, 2094–2099, 1980.

Monahan, E.C., and Spillane M.C.: The role of whitecaps in air-sea gas exchange, in Gas Transfer at Water Surfaces, edited by G.H. Jirka and W. Brutsaert, pp. 495–504, D. Reidel, Norwell, MA, 1984.

Nightingale, P.D., Malin, G., Law, C.S., Watson, A.J., Liss, P.S., Liddicoat, M.J., Boutin J., and Upstill-Goddard R.C.: In situ evaluation of air-sea gas exchange using novel conservative and volatile tracers, Global Biogeochem. Cycles, 14, 373–387, 2000.

Perry, K.D., and Hobbs P.V.: Further evidence for particle nucleation in clear air adjacent to marine cumulus clouds, J. Geophys. Res., 99, 22803-22818, 1994.

Read, K.A., Mahajan, A.S., Carpenter, L.J., Evans, M.J., Fari, B.V.E., Heard, D.E., Hopkins, J.R., Lee, J.D., Moller, S.J., Lewis, A.C., Mendes, L., McQuaid, J.B., Oetjen, H., Saiz-Lopez, A., Pilling, M.J., and Plane, J.M.C.: Extensive halogen-mediated ozone destruction over the tropical Atlantic Ocean, Nature, 453, 1232-1235, 2008.

Sander, S.P., Golden, D.M., Kurylo, M.J., Moortgat, G.K., Wine, P.H., Ravishankara, A.R., Kolb, C.E., Molina, M.J., Finlayson-Pitts, B.J., Huie, R.E., and Orkin, V.L.: Chemical Kinetics and Photochemical Data for Use in Atmospheric Studies, Evaluation Number 15, Jet Propulsion Laboratory, Pasadena, CA (available at http://jpldataeval.jpl.nasa.gov/), 2006.

Sciare J., Baboukas, E., Kanakidous, M., Krischke, U., Belviso, S., Bardouki, H. and Mihalopoulos, N.: Spatial and temporal variability of atmospheric sulfur-containing gases and particles during the Albatross campaign, J. Geophys. Res., 105, 14433-14448, 2000.

Seinfeld, J.H. and Pandis, S.N.: Atmospheric chemistry and physics: from air pollution to climate change. 2nd ed. Wiley-Interscience. Hoboken, New Jersey, USA, 2006.

Shon Z.H., Davis, D., Chen, G., Grodzinsky, G., Bandy, A., Thornton, D., Sandholm, S., Bradshaw, J., Stickel, R., Chameides, W., Kok, G., Russell, L., Mauldin, L., Tanner, D., Eisele, F.: Evaluation of the DMS flux and its conversion to SO2 over the southern ocean. Atmos. Environ., 35, 159-172, 2001.

Simo R, Archer S D, Pedros-Alio C, Gilpin L, Stelfox-Widdicombe C E.: Coupled dynamics of dimethylsulfoniopropionate and dimethylsulfide cycling and the microbial food web in surface waters of the North Atlantic. Limnol Oceanogr, 47: 53-61, 2002.

Simo, R., and Dachs J.: Global ocean emission of dimethylsulfide predicted from biogeophysical data, Global Biogeochem. Cycles, 16(1.4), 1018, 2002.

Sievering, H., Cainey, J., Harvey, M., McGregor, J. Nichol, S., and Quinn, P.:
Aerosol non-sea-salt sulfate in the remote marine boundary layer under clear-sky and normal cloudiness conditions: Ocean-derived biogenic alkalinity enhances sea-salt sulfate production by ozone oxidation. J. Geophys. Res., 109, D19317, doi:10.1029/2003JD004315, 2004.

Stefels, J., and van Boekel, W.H.M.: Production of DMS from dissolved DMSP in axenic cultures of the marine phytoplankton species Phaeocystis sp. Mar. Ecol. Prog. Ser. 97: 11-18, 1993.

Sunda W., Kieber D.J., Kiene R.P., Huntsman S.: An antioxidant function for DMSP and DMS in marine algae. Nature, Vol. 418, p. 317-320, 2002.

Toole D. and Siegel D.A.: Light-driven cycling of dimethylsulfide (DMS) in the Sargasso Sea: closing the loop. Geophys. Res. Lett., Vol. 31, L09308, 2004.

Twomey, S.: Aerosols, clouds and radiation, Atmos. Environ. Part A, 25(1.11), 2435-2442, 1991.

Vallina, S.M., and Simó R.: Strong relationship between DMS and the solar radiation dose over the global surface ocean, Science, 315, 506, 508, 2007.

Wallington, T.J., Ellermann, T., and Nielsen, O.J.: Atmospheric chemistry of dimethylsulfide: UV spectra and self-reaction kinetics of $CH_3SCH_2$ and $CH_3SCH_2O_2$ radicals and kinetics of the reactions $CH_3SCH_2$ + $O_2$ $CH_3SCH_2O_2$ and $CH_3CH_2O_2$ + NO → $CH_3SCH_2O_2$ + $NO_2$. J. phys. Chem. 97, pp. 8442–8449, 1993.

Wanninkhof, R.H.: Relationship between wind speed and gas exchange over the ocean, J.Geophys. Res., 97, 7373-7382, 1992.

Wanninkhof, R., and McGillis, W.R.: A cubic relationship between air-sea CO2 exchange and wind speed, Geophys. Res. Lett., 26(1.13), 1889-1892, 1999.

Weber, R. J., McMurr y, P. H., Mauldin, R. L., Tanner, D. J., Eisele, F. L., Clarke, A. D., and Kapustin, V. N.: New particle formation in the remote troposphere: A comparison of observations at various sites, Geophys. Res. Lett., 26, 307–310, 1999.

Woodhouse, M. T., Carslaw, K. S., Mann, G. W., Vallina, S. M., Vogt, M., Halloran, P. R., and Boucher, O.: Low sensitivity of cloud condensation nuclei to changes in the sea-air flux of dimethyl-sulphide, Atmos. Chem. Phys., 10, 7545-7559, doi:10.5194/acp-10-7545-2010, 2010.

Woolf, D. K: Bubbles and their role in gas exchange, in The Sea Surface and Global Change, edited by R. Duce and P. Liss, pp. 173–205, Cambridge Univ. Press, NY, 1997.

# Chapter 2. Sea-to-air DMS Transfer Velocity

This chapter has been submitted to the *Journal of Geophysical Research* with the following tentative citation: Yang, M., Blomquist, B., Fairall, C., Archer, S., and Huebert, B.: Air-sea Exchange of Dimethylsulfide (DMS) in the Southern Ocean – Measurements from SO GasEx Compared to Temperate and Tropical Regions, *J. Geophys. Res.*, in revision, 2010.

**Abstract**

Dimethylsulfude (DMS), a biogenic sulfur gas produced in the surface ocean and constantly emitted to the marine atmosphere, has recently emerged as one of the key gases with which to directly quantify the air-sea transfer velocity ($k$). In the Southern Ocean Gas Exchange Experiment (SO GasEx), we measured atmospheric DMS concentration of 118±54 pptv (1 sigma), DMS sea-to-air flux of 2.9±2.1 μmoles $m^{-2}$ $day^{-1}$ by eddy covariance, and seawater DMS concentration of 1.6±0.7 nM. Dividing flux by the concurrent air-sea concentration difference yields the transfer velocity of DMS ($k_{DMS}$). Compared to previous open ocean measurements in the equatorial East Pacific, Sargasso Sea, Northeast Atlantic, and Southeast Pacific, $k_{DMS}$ in the Southern Ocean was lower mostly because of the cold surface water. Furthermore, we found that the Schmidt number normalization for waterside diffusivity does not account for all temperature effects in $k_{DMS}$. Higher solubility of DMS at a lower temperature results in greater airside control and less transfer of the gas by bubbles formed from breaking waves. We present here a normalization of $k_{DMS}$ for the temperature dependence in solubility, in addition to diffusivity. The final normalized DMS transfer velocity shows good agreement among

tropical and high latitude cruises, and is similar to *k* of less soluble gases such as carbon dioxide in low-to-moderate winds but significantly lower in high winds due to the reduced bubble-mediated transfer of DMS.

## 1. Introduction

Transfer of gases across the air-water interface has profound implications for the carbon and sulfur budgets in the marine atmosphere and biosphere. The sea-to-air transport of dimethylsulfide (DMS) is of particular interest because the gas is thought to influence climate through the production of sulfate aerosols that could serve as cloud condensation nuclei (Charlson et al., 1987). DMS is derived from phytoplankton in the surface seawater ($DMS_w$) and typically has a concentration of a few nM. Because of photochemical loss and dilution, the atmospheric DMS concentration ($DMS_a$) in the boundary layer is orders of magnitude lower than the Henry's Law equilibrium concentration. As a result, the flux of DMS is always positive (upward from the ocean surface) and is the largest natural source of reduced sulfur to the marine atmosphere (Lovelock et al., 1972). The substantial magnitude of the sea-to-air flux and the absence of other sources make it relatively easy to quantify the DMS transfer velocity ($k_{DMS}$):

$$k_{DMS} = Flux/(DMS_w - \alpha \cdot DMS_a) \qquad (2.1)$$

Here $\alpha$ is the dimensionless Ostwald solubility of the gas (adopted from Dacey et al. (1984) for DMS). The term inside of the parenthesis is the air-sea concentration difference that is the driving force for exchange; $\alpha \cdot DMS_a$ represents the waterside DMS concentration that would be in equilibrium with the bulk airside concentration.

Air-sea gas transfer is controlled by molecular and turbulent diffusion on the

waterside as well as airside. Close to the interface, turbulent transport diminishes and molecular diffusion dominates. With resistance on both sides of the boundary acting in series, the total transfer velocity of a gas ($k$) is a function of waterside transfer velocity ($k_w$) and airside transfer velocity ($k_a$):

$$k = [\frac{1}{k_w} + \frac{\alpha}{k_a}]^{-1} \quad (2.2)$$

For exchange of sparingly soluble gases, including carbon dioxide ($CO_2$), sulfur hexafluoride ($SF_6$), and helium (He), the molecular sub-layer on the waterside provides the greatest resistance. In contrast, exchange of highly soluble gases, such as methanol, is controlled by airside resistance, with water vapor representing complete airside control. DMS is intermediate in solubility, with $\alpha$ = 14.2 at 20 °C in seawater.

Since $k$ scales inversely to resistance, turbulence generated from wind stress ($\tau$) that thins the molecular sub-layers speeds up transfer. Because the 10-meter wind speed ($U_{10}$) is much easier to measure than $\tau$, most gas exchange parameterizations are based on $U_{10}$ only (Liss and Merlivat, 1986; Wanninkhof, 1992; Nightingale et al., 2000; Ho et al., 2006). However, these models that are derived from waterside controlled gases diverge significantly in high winds. From a more detailed consideration of the physics, Csanady (1990) theorized that $k$ has a linear dependence on the friction velocity ($u_*$), which is related to stress through the density of air ($\rho_a$): $\tau = \rho_a u_*^2$. Our observations of $k_{DMS}$ and $u_*$ in the Northeast Atlantic confirmed this linearity at moderate wind speeds (Huebert et al., 2010). However, this linear relationship might not hold in calm or heavy breaking wave conditions, when additional physical processes confound this simple picture of shear-driven direct exchange. When $U_{10}$ < ~2 m $s^{-1}$, buoyancy-driven free convection at the ocean surface may account for more transfer than wind shear (Soloviev and Schlüssel,

1994). Above ~7 m $s^{-1}$, whitecaps start to form on the sea surface. The additional surface area from air bubbles (Woolf, 1997) and the associated turbulent plume (Monahan and Spillane, 1984) can increase gas exchange. Insoluble gases partition readily into bubbles and should therefore show enhanced transfer in moderate-to-high winds. In contrast, a more soluble gas like DMS exhibits only modest bubble-mediated enhancement for wind speeds up to ~10 m $s^{-1}$ (Blomquist et al., 2006).

In the past several years, we have measured the sea-to-air flux of DMS by eddy covariance (EC) on five cruises in different oceanic environments (Fig. 2.1). Chronologically, they are 2003 Tropical Atmosphere Ocean (TAO) on the NOAA Ship *Ronald H. Brown*, 2004 Biocomplexity (hereinafter BIO) on the R/V *Steward Johnson*, 2007 Deep Ocean Gas Exchange Experiment (DOGEE) on the UK ship RRS *Discovery*, 2008 Southern Ocean Gas Exchange Experiment (SO GasEx) on *Ronald H. Brown*, and 2008 Vamos Ocean-Cloud-Atmosphere-Land Study Regional Experiment (VOCALS-REx, hereinafter VOCALS) on *Ronald H. Brown*. The location, time, DMS sea-to-air flux, seawater DMS concentration, and reference for each cruise are listed in Table 2.1.

While the environmental conditions of each cruise individually were not highly variable, together these five cruises encompass a large range in wind speed (1 ~ 21 m $s^{-1}$), sea surface temperature (SST, 2~30°C), and atmospheric boundary layer stability (statically unstable to stable), which is shown as histograms in Fig. 2.2. The higher winds, lower SST, and frequent occurrences of stable boundary layer set SO GasEx apart from other cruises. A compilation of $k_{DMS}$ from these projects allows us to assess our current understanding of gas exchange in an effort to improve existing models.

## 2. Experimental

### *2.1 Background on SO GasEx*

The Southern Ocean is characterized by sustained periods of high winds, low SST, and large seasonal cycles in biological productivity. Gas exchange between the ocean and atmosphere in the Southern Ocean plays an important role in the global climate through, for example, the sequestration of atmospheric $CO_2$ via production of polar bottom waters and through the role of DMS emissions in generation of atmospheric sulfate aerosols. SO GasEx was conceived as the third in a series of projects combining direct measurements of gas exchange with concurrent studies of related biological and physical processes, focused on the unique high wind conditions of the Southern Ocean (Ho et al., this issue a). SO GasEx included a $^3He/SF_6$ tracer patch study (Ho et al., this issue b), EC observations of $CO_2$ (Edson et al., this issue), and DMS (this paper). The measurements of atmospheric DMS concentration using an atmospheric pressure ionization mass spectrometer (APIMS) and DMS flux by EC are detailed recently by (Blomquist et al., 2010) and will not be described further here.

### *2.2 Measurements of Seawater DMS Concentration*

Seawater DMS ($DMS_w$) concentration near the surface was measured by a gas chromatograph (GC). For SO GasEx, $DMS_w$ was measured at ~10 minute intervals using a semi-continuous analytical system linked to an equilibration device. Seawater from the ship's clean water supply at ~5 m depth was passed through a membrane equilibrator (Liqui-Cel®, Extra-Flow 2.5 x 8) at ~400 mL $min^{-1}$. Nitrogen was passed through the equilibrator at a continuously monitored flow rate of 40 mL $min^{-1}$ and pressure of 150

kPa. DMS was trapped on an adsorbent (Carbopack-X, Sigma-Aldrich®) at -50 ºC and measured on a Varian 3800 GC equipped with a pulsed flame photometric detector (PFPD). The system was calibrated and sensitivity monitored hourly using a permeation device (Dynacal®, Vici Metronics Inc.) delivering 120 ng DMS $min^{-1}$ at 30 ºC. In DOGEE, $DMS_w$ was sampled every 7~10 min from a towed Fish at 1~2 m below the surface and quantified using a purge-and-cryogenic trap linked to a Varian 3800 GC with PFPD. A similar purge-and-trap method was used on the TAO and VOCALS projects, but at a lower frequency of every 15~30 minutes (Bates et al., 2000). The BIO cruise was a Lagrangian water mass study following a cyclonic and an anticyclonic eddy. $DMS_w$ was determined from the shallowest bin (~5 m) of CTD casts (Kiene and Service, 1991) and showed little variation as a result of the Lagrangian design. Limited inter-comparisons between samples manually collected at the surface and from the ship's clean seawater supply during DOGEE and SO GasEx suggest that there was no significant, systematic gradient in $DMS_w$ in the top 5 m of the water column in moderate winds. Nor was there a discernible difference in concentration caused by the different means of water sampling.

*2.3 Diffusivity Normalization on $k_{DMS}$*

The waterside diffusivity dependence of gas transfer can be described by the Schmidt number ($S_c$) as the ratio between kinematic viscosity ($\nu$) of seawater and molecular diffusivity ($D$), both functions of temperature and (to a lesser degree) salinity (Saltzman et al., 1993). To remove variance due to diffusivity, it is common to normalize transfer velocity measured at ambient conditions to a reference $S_c$ of 660:

$$k_{660} = k_{DMS}(660/S_c)^n \quad (2.3)$$

The exponent *n* is thought to vary from -2/3 for a rigid surface to -1/2 for a rough surface; we assume the latter for the open ocean. A Schmidt number of 660 corresponds to 20 °C for $CO_2$ and 27.2 °C for DMS in seawater. A relationship similar to (2.3) is also frequently used to account for diffusivity differences among gases, as in the derivation of $k_{660}$ for a specific gas of interest from $k_{660}$ of $^3He/SF_6$ obtained from deliberate tracer studies. The analysis below suggests this may lead to bias at moderate-to-high wind speeds when the gas of interest is much more soluble than that of the tracer gas.

Figure 2.3 shows time series of atmospheric and seawater DMS concentrations, DMS flux, 10-m wind speed, transfer velocity at ambient condition and normalized to $S_c$ of 660, as well as the DMS Schmidt number from SO GasEx. Elevated DMS flux clearly corresponded to higher $DMS_w$ at times, such as on March 14 and 24, but not always because of variable winds. Towards the end of the experiment, the ship encountered a storm while in transit to Uruguay. Wind speed briefly exceeded 20 m $s^{-1}$ and the surface water was much warmer (~14°C) during this period than what was typical of SO GasEx (~5°C). However, DMS flux and transfer velocity were not elevated, while $DMS_w$ was similar to earlier periods of the project.

## 3. Data Refinement and Normalization

### *3.1 Basic Data Filtering*

Uncertainty in $k_{660}$ hinges principally on the precision and sampling variability of the flux and $DMS_w$. There is substantial noise in EC flux observations that is independent of the measurement system. This scatter originates from sampling a

stochastic process (turbulence) over relatively short time scales where low frequency contributions to flux are poorly sampled. Even for a well-resolved scalar like water vapor, the sampling uncertainty of an hourly flux is on the order of 25% (Fairall et al., 2003). At a wind speed of ~8 m $s^{-1}$ and in a near-neutral boundary layer, Blomquist et al. (2010) showed that relative uncertainty in hourly DMS flux is on the order of ~30%. Uncertainty further increases when the boundary layer is stable, which is discussed in the next section. For a large number of hourly observations, however, precision in the mean flux estimate improves significantly. Here, we focus on eliminating conditions that might lead to nonrandom biases in the measurement.

From the lag correlation between $DMS_a$ and vertical wind velocity ($w$), we find a clear peak in correlation and a corresponding lag time of ~1.5 seconds (depending on the inlet length and flow rate) when the wind is from the bow sector. When the wind is coming from the stern quadrant, however, $DMS_a$ and $w$ show poor correlation due to severe airflow distortion by the ship's superstructure. For SO GasEx, three sonic anemometers were mounted on the foremast of the *Ronald H. Brown*, with one in the middle and two others ~1 m to the port and starboard sides. The DMS sampling inlet was located near the base of the middle anemometer. We limit relative wind direction to ±60° from the bow for the middle anemometer and -120° to 0° and 0° to 120° for the port and starboard anemometers, respectively. DMS fluxes are computed at 10-minute intervals from all three anemometers and averaged when two or more anemometers are in-sector. On all other cruises with a single anemometer, a limit in relative wind direction of ±60° from the bow is applied. Airflow distortions and complex vibrations can also occur when the ship is turning rapidly. Thus 10-minute flux segments when the range in gyro

heading exceeds 30 degrees are excluded from hourly averages.

In Fig. 2.4, hourly $k_{660}$ satisfying the above criteria from all five cruises are plotted vs. $U_{10}$, including the brief high wind speed period (>20 m $s^{-1}$) from SO GasEx. During this storm encounter, the sea was characterized by fully developed long swells and the measured $k_{DMS}$ was much lower than the trend extrapolated from intermediate winds. To date, we have not identified a measurement error responsible for the low $k_{DMS}$. There may be an environmental factor involved, but pending a more detailed analysis of this event, we will not consider these points further in this section.

To more clearly examine the trend in $k_{660}$ as a function of wind speed, we plot $k_{660}$ from the five cruises averaged to $U_{10}$ bins in Fig. 2.5. While overall $k_{660}$ increases with $U_{10}$, $k_{660}$ from tropical cruises such as TAO appears to be higher than that from the high latitude SO GasEx, particularly in high winds. A similar SST trend is observed by Marandino et al. (2009) in their synthesis of $k_{DMS}$ measurements. Also included in Fig. 2.5 is the $k_{DMS}$ curve computed from the NOAA COARE gas transfer model (discussed in detail below) using parameters $A$=1.3 and $B$=1.0 at 27.2 °C.

Another source of scatter in $k_{660}$ is the variability in discretely sampled $DMS_w$. When $DMS_w$ shows high temporal or spatial variability, uncertainty in the hourly mean waterside concentration increases; the location of $DMS_w$ measurement is also less likely to correspond to the flux footprint. For a measurement height of 18 m and at typical wind speeds, the flux footprint covers a region several hundred meters upwind of the ship under neutral or unstable conditions; the footprint can be much larger under stable conditions (Horst and Wiell, 1994). We address the variability in $DMS_w$ by setting a threshold of 0.25 for the relative standard error of the mean in the hourly $DMS_w$ for all

cruises except BIO, following Huebert et al. (2010).

*3.2 Effect of Atmospheric Stability*

The wind speed profile as a function of height depends on boundary layer stability. At a reference height of 10 meters, wind speed is related to wind stress through $u_*$ and the 10-m drag coefficient ($C_{D10}$): $u_* = C_{D10}^{1/2} U_{10}$. Adjusted to neutral condition, the relationship becomes $u_* = C_{D10n}^{1/2} U_{10n}$, where $C_{D10n}$ and $U_{10n}$ are stability-corrected. Logic follows that some of the scatter in the relationship between $k$ and $U_{10}$ is due to the effect of stability on the logarithmic wind speed profile, and may be reduced by using $U_{10n}$. We estimate $u_*$, $U_{10n}$, $z_0$ (roughness length), and $L$ (Monin-Obukhov length scale) from bulk meteorological variables using the NOAA COARE 3.0 bulk flux model (Fairall et al., 2003).

The stability of the atmospheric surface layer can be represented by the ratio $z/L$, with $z$ being the sensor height. The ratio $z/L$ depends on the air-sea temperature difference, and is a proxy for the relative contribution to turbulence generated by buoyancy and shear. A significantly positive $z/L$ implies a statically stable boundary layer, usually caused by warm air over cold water. A negative $z/L$ indicates statically unstable, as is typical of temperate and tropical regions. Under a near neutral condition, $z/L \approx 0$. Figure 2.6 shows DMS $k_{660}$ vs. $U_{10}$ and $U_{10n}$ for SO GasEx. The degree of scatter in $k_{660}$ is reduced when $U_{10n}$ is used, with the difference most noticeable in low-to-moderate winds where buoyancy-driven convection is more important. The coefficient of determination ($r^2$) for a linear relationship between $k_{660}$ and wind speed is improved from 0.51 to 0.56 with $U_{10n}$ instead of $U_{10}$.

Besides modifying the wind speed profile, static stability in the boundary layer increases uncertainty in the flux measurement (Blomquist et al., 2010). Stable conditions lead to suppression of turbulent eddies and possibly a shallow boundary layer. Strong, warm winds over a cooler ocean surface are often found in warm sectors of frontal passages. While damping of turbulence in these conditions may not be very significant due to the high surface shear, the boundary layer can become quite shallow. With all else being constant, a shallower boundary layer implies a steeper flux gradient, which results in a greater systematic underestimate of the true surface flux, as illustrated in Fig. 2.6 by the solid circles ($z/L > 0.05$). Hourly flux observations when $z/L > 0.05$ are hereafter omitted. This stability threshold is intended to remove conditions unfavorable for EC measurement and does not imply a cessation of turbulence. This filter removes about 30% of our observations from high latitude cruises (SO GasEx and DOGEE), while data from the tropical and temperate waters are largely unaffected. About 1100 hourly $k_{DMS}$ observations from all cruises remain following screening for $DMS_w$ and stability.

*3.3 Flux Corrections at High and Low Frequencies*

Some flux signal is lost at the lowest frequencies at 10-minute time intervals, and of the lowest frequencies that are measured, the sampling statistics are poor. Additional flux signal is lost at the highest frequencies due to an attenuation of small-scale fluctuations by the inlet system and the Nafion® air drier, which is needed to remove water from the ambient air and increase the sensitivity of the APIMS towards DMS. We partially correct hourly cospectra for high frequency inlet-attenuation based on an empirical frequency response function (a correction of a few percent, Blomquist et al.,

(2010)). An estimate for additional missing flux is obtained through comparison with a theoretical cospectral function for neutral conditions (Kaimal et al., 1972). Partially corrected cospectra are normalized to $DMS_w$ and $S_c$ = 660 and bin-averaged by relative wind speed ($U_R$). For each $U_R$ bin, the theoretical Kaimal function is fit to the observed data over a restricted frequency range (0.008~1 Hz). Measurement height and relative wind speed parameters in the fit are fixed to mean observed conditions. Within each bin, the difference in area between the fit and the observed cospectrum under the high and low frequency tails (0~0.005 Hz and 1~10 Hz) is an estimate of the missing flux. A cospectral correction factor ($F_C$) is computed as the ratio between the total corrected flux and the observed flux for each bin and fit to a polynomial as a function of $U_R$: $F_c = 1.165 - 0.020U_R + 0.001U_R^2$ for SO GasEx. The estimated correction to the flux is less than 5% for $U_R$ of 8~16 m $s^{-1}$, and on the order 10% for $U_R$ less than 5 or greater than 20 m $s^{-1}$. The magnitude of the correction varies somewhat among cruises because of variable sampling height, inlet length, flow rates, etc.

*3.4 Airside Resistance*

Airside resistance to exchange of sparingly soluble tracer gases is small and usually neglected. However, as the solubility ($\alpha$) of a gas increases with decreasing temperature, the airside resistance becomes more important. Rearranging (2.2), McGillis et al. (2000) defined the atmospheric gradient fraction $\gamma_a$ as the fraction airside contribution to total concentration difference: $\gamma_a = [1 + k_a(\alpha k_w)^{-1}]^{-1}$. For DMS, $\gamma_a$ is on the order of 0.05 at 20 °C, compared to only ~0.002 for the less soluble $CO_2$. Thus, the temperature dependence in airside resistance, which is not accounted for in (2.3), is more

significant for DMS than for $CO_2$. $k_{DMS}$ obtained from (2.1) represents the total transfer velocity. To account for all temperature effects when normalizing to $S_c$ = 660, the airside and waterside transfer velocity need to be specified and adjusted separately. Following McGillis et al. (2000), we estimate $k_a$ of DMS as $659U_{10n}(MW_{DMS}/MW_{H_2O})^{-1/2}$ (cm hr$^{-1}$), with *MW* representing molecular weight. To approximate $k_w$ a priori, we use the formulation from the NOAA COARE gas transfer model (cm hr$^{-1}$):

$$k_w = 360000u_*(\rho_w/\rho_a)^{-1/2}[h_w S_c^{1/2} + \kappa^{-1}\ln(0.5/\delta_w)]^{-1} + B(2450 f_{wh} G) \quad (2.4)$$

Here $\rho_w$ is the density of water, $\delta_w$ the waterside molecular sublayer thickness, $\kappa$ the von Karman's constant (0.4), and $h_w = 13.3/(A\phi)$. In $h_w$, $A$ is an empirical constant and tuned to 1.3 by Blomquist et al. (2006) using tropical EC measurements of DMS; $\varphi$ accounts for surface buoyancy flux enhancement of the transfer and only becomes important in wind speed less than ~2 m s$^{-1}$. The second term on the RHS of (2.4) is the parameterization of $k_b$ from Woolf (1997), where the whitecap fraction $f_{wh}$ = 3.84 x 10$^{-6}$ $U_{10}^{3.41}$ (Monahan and O'Muircheartaigh, 1980), and $G = \alpha^{-1}[1 + (14\alpha S_c^{-1/2})^{-1/1.2}]^{-1.2}$. $B$ is an empirical constant, to which we assign the provisional value of 1.0 (Blomquist et al., 2006).

At typical SO GasEx temperatures (~5 °C), $\gamma_a$ for DMS is about 0.10 at a wind speed of 15 m s$^{-1}$. The airside effect calculated here is smaller than was estimated by McGillis et al. (2000) for DMS because they used the parameterization from Wanninkhof (1992) for $k_w$, which significantly overestimates $k_{DMS}$ at high wind speeds. We can now estimate the ambient waterside transfer velocity of DMS from measured $k_{DMS}$: $k_w = k_{DMS}/(1-\gamma_a)$. Applying the Schmidt number normalization to $k_w$ yields $k_{w660}$. For consistency, the airside transfer should also be adjusted to 27.2 °C ($S_c$ = 660 for DMS),

such that the total normalized transfer velocity becomes:

$$k_{660} = [\frac{1}{k_{w660}} + \frac{\alpha_{660}}{k_a}]^{-1} \quad (2.5)$$

Here $\alpha_{660}$ represents the solubility of DMS at 27.2 °C (10.4). Compared to the $S_c$-only normalization specified by (2.3), separate treatment of the temperature dependence in waterside and airside transfer given by (2.5) increases $k_{660}$ from SO GasEx by ~4%.

After screening for $DMS_w$ variability as well as atmospheric stability, and accounting for temperature dependence in airside resistance, $r^2$ for a linear relationship between $k_{660}$ from (2.5) and $U_{10n}$ for all cruises is increased from 0.63 in Fig. 2.4 to 0.71 in Fig. 2.7. However, discrepancies in $k_{660}$ remain among different cruises, particularly in higher winds, which might be in part related to the temperature dependence in bubble-mediated transfer.

**4. Bubble-mediated Exchange and Solubility Normalization**

When waves break, air is trapped in water and entrained to depth of a few meters in the form of bubbles, which then rise and exchange gas with the surrounding water. The amount of a trace gas partitioning into air bubbles from the bulk water likely depends on both solubility and diffusivity. At lower temperatures, $\alpha$ increases and less gas is transferred from the bulk water to bubbles. The bubble component of $k_{DMS}$ should be normalized to a reference temperature separately from the interfacial component, which does not depend on $\alpha$. It is convenient to first estimate the interfacial component of gas exchange due to shear ($k_v$), ignoring buoyancy-driven exchange that is insignificant in moderate-to-high winds. An estimate for bubble-mediated transfer velocity ($k_b$) is then simply the difference between $k_w$ and $k_v$:

$$k_b = k_w - k_v = k_w - k_{v660}(660/S_c)^{1/2} = (k_{w660} - k_{v660})(660/S_c)^{1/2} \quad (2.6)$$

Here $k_{v660}$ is interfacial transfer velocity at $S_c$ = 660. We estimate $k_{v660}$ as a linear function of the tangential component of the friction velocity ($u_{*v}$) due to viscous wind shear (i.e. $k_{v660} = C_1 + C_2 u_{*v}$, as described below). To account for temperature effects, we normalize $k_b$ to $S_c$ = 660 using the $S_c$ and $\alpha$ dependence ($G$) described by the Woolf (1997) model for bubble-mediated exchange. Adding the interfacial component yields the solubility and diffusivity normalized waterside transfer velocity:

$k_{w660}' = k_{v660} + k_b(G_{660}/G)$, where $G_{660}$ is the Schmidt number-solubility dependence at 27.2 °C. We may then substitute $k_{w660}$' in place of $k_{w660}$ in (2.5) to yield the final normalized total transfer velocity ($k_{660}$'). While the procedure described above is simple, the justification and background require more detailed explanations, which will be covered in the remainder of this section.

*4.1 Quantifying the Interfacial Transfer Velocity*

From the two-layer model described by Liss and Slater (1974), physical processes that thin the diffusive sub-layers are conceptualized to enhance direct (interfacial) gas exchange through a reduction in resistance. Shear (viscous) stress from wind blowing tangentially to the sea surface is usually the most important of such processes, as it leads to micro-scale breaking of capillary waves and wavelets that are largely responsible for interfacial gas exchange (Frew et al., 2004). Surface renewal models from Csanady (1990) and Soloviev and Schlüssel (1994) predict that without bubbles, $k$ should be linearly related to $u_*$, consistent with our $k_{DMS}$ observations from DOGEE in moderate winds (Huebert et al., 2010).

In high winds ($U_{10}$ > ~10 m $s^{-1}$) and mature seas, the ocean surface transitions from micro-scale waves to the breaking of long gravity waves. As total surface stress grows with wind speed, an increasingly larger fraction is partitioned to wave stress, which includes momentum transfer into the ocean by breaking waves and form drag. While wave breaking can lead to more gas exchange via enhanced turbulence and bubble plume formation, increasing partition of total stress to form drag, which is a result of the pressure differential developed between the front and lee sides of large waves, may suppress micro-scale breaking (Banner et al., 1989) and potentially reduce the wind speed dependence of $k$. The net effect of these competing mechanisms on $k$ in high winds partly depends on gas solubility. Since wave stress does not significantly contribute to thinning of the diffusive sub-layer, a linear relationship between tangential friction velocity ($u_{*v}$) and interfacial transfer velocity ($k_v$) should be more general than that between $u_*$ and $k$ and hold true even in high winds, concurrent with the additional decrease in transfer resistance due to bubbles and whitecaps.

We determine $u_{*v}$ from the tangential component of wind stress. The COARE bulk flux algorithm follows Smith (1988) and partitions total roughness length as:

$$z_o = \varphi u_*^2 / g + 0.11\nu / u_* \qquad (2.7)$$

Here $\varphi$ is a fit to drag coefficient observations and $g$ is gravity. The first term on the RHS of (2.7) is due to waves, and the second due to smooth flow. From laboratory wind-wave studies, Banner and Peirson (1998) found that total stress in the smooth flow regime represents the upper limit for the tangential stress. Based on this result, Mueller and Veron (2009) (hereinafter MV09) estimate the 10-m tangential drag coefficient in neutral condition ($C_{D10,v}$) as a function of the smooth flow roughness length:

$$C_{D10\nu}{}^{1/2} = \kappa / \ln(10/(0.11\nu/u_{*\nu})) \quad (2.8)$$

Thus at a given wind speed, $u_{*\nu}$ can be computed iteratively: $u_{*\nu} = C_{D10\nu}{}^{1/2} U_{10n}$. The result of this partition of the total wind stress to the tangential and wave component is qualitatively similar to the alternate estimate by Soloviev and Schlüssel (1996) (hereinafter SS96), as shown in Fig. 2.8. SS96 use the Keulegan number defined by Csanady (1978) as the criterion for the transition to large-scale wave breaking: $Ke = u_{*w}{}^3 / g\nu$, where $u_{*w}$ is the waterside transfer velocity. Tangential stress is then estimated as a fraction of total stress: $(1 + Ke/Ke_{cr})^{-1}$, where $Ke_{cr}$ is the critical *Ke*, an empirically derived threshold dependent on wave age and speculatively set to 0.45 here for illustration. Tangential stress from SS96 varies with wave age, whereas $u_{*\nu}$ from MV09 does not (only the wave component does). We adopt the approach from MV09 because *Ke* is not required, as tangential stress is approximately independent of the specification of total drag coefficient (i.e. $u_*$ is not required to estimate $u_{*\nu}$).

Because of the increasing importance of wave stress with wind speed, $C_{D10\nu}$ decreases in high winds and $u_{*\nu}$ shows a slight downward curvature, with estimates from SS96 rolling off more. If $k_\nu$ follows $u_{*\nu}$ in high winds, it too should roll off slightly, which might not be apparent in observed total transfer of a sparingly soluble gas (e.g. $CO_2$) in high winds because the additional bubble-mediated exchange term overwhelms any suppression in interfacial exchange. However, for a soluble gas like DMS with a more modest bubble enhancement, the difference between $k_\nu$ and $k$ should be smaller. Indeed, if we plot observed $k_{DMS}$ vs. $u_*$, the trend would be best described as linear in moderate winds with a slight leveling off in high winds, qualitatively similar to the "wave attenuation" effect observed for DMS in the laboratory by Rhee et al. (2007). This roll

off suggests that the behavior of $k_{DMS}$ in high winds is related to reduced partition of total stress to the tangential component.

Let us now examine how $k_{w660}$ relates to $u_{*v}$ in different wind speed regimes for all cruises (Fig. 2.9). In the calmest conditions ($u_{*v}$ < ~0.1 m s$^{-1}$, corresponding to a wind speed of 2~3 m s$^{-1}$), the slope between $k_{w660}$ and $u_{*v}$ appears to be relatively flat, likely because buoyancy-driven convection is more important than wind shear at driving gas exchange. The slope steepens with increasing wind speeds; a linear fit from 2~6 m s$^{-1}$ yields an intercept ($C_1$) of -3.8 and a slope ($C_2$) of 69.7. We interpret the extrapolation of this fit to higher winds as interfacial transfer velocity ($k_{v660}$), which becomes less than the bin-average $k_{w660}$ above $u_{*v} \approx 0.2$ m s$^{-1}$ (a wind speed of 7~8 m s$^{-1}$, or the onset of whitecap formation). Subtracting $k_{v660}$ from $k_{w660}$ in moderate-to-high winds and removing the prior $S_c$ normalization yield an estimate of $k_b$ for DMS.

*4.2 Solubility Normalization of Bubble-mediated Exchange*

Normalizing $k_b$ to a reference temperature requires a model describing the $S_c$ and $\alpha$ dependence in bubbles. Scaling up from a single bubble model, Woolf (1997) parameterizes $k_b$ of $CO_2$ to be proportional to whitecap fraction ($f_{wh}$) and $G$. A linear relationship between $k_b$ and $f_{wh}$ was proposed by Monahan and Spillane (1984) and confirmed by laboratory results of *Asher et al*. (1996) with optically measured bubble plume coverage as the analog for $f_{wh}$. The term $G = \alpha^{-1}[1 + (14\alpha S_c^{-1/2})^{-1/1.2}]^{-1.2}$ contains the solubility and diffusivity dependence in $k_b$. Woolf (1997) identifies two asymptotic behaviors of $k_b$ at opposing limits of gas solubility. For an insoluble gas, $G$ approximately scales as $S_c^{-1/2}$. This implies the temperature dependence in solubility has

little effect on $k_b$ for gases like $SF_6$ and $CO_2$, such that the usual normalization to $S_c = 660$ is sufficient. For a very soluble gas, $G$ approaches $\alpha^{-1}$ and the $S_c$ dependence vanishes. For DMS at 5 °C, $\alpha = 28.3$ and $S_c = 2050$; the functional form of $G$ is close to $\alpha^{-1}$, with a weak $S_c$ dependence. Multiplying $k_b$ by the factor ($G_{660}/G$) yields the normalized bubble-mediated transfer velocity, which is then summed with the prior estimate of $k_{v660}$ to yield the final normalized waterside transfer velocity ($k_{w660}$'). For SO GasEx, the normalization to 27.2 °C increases $k_b$ by ~150%, or ~40% relative to $k_b$ adjusted using the $S_c$-only dependence. Together with interfacial exchange, $k_{w660}$' is ~6% greater than $k_{w660}$ in high winds. While the effect of this normalization appears to be small and only secondary in importance, for a larger $k_b$ (e.g. if $k_v$ rolls off more in high winds, as in SS96), the adjustment in $k_b$ would be correspondingly greater as well.

Keeling (1993) and Asher et al. (1996) describe different dependences on $S_c$ and $\alpha$ in bubble-mediated exchange than Woolf (1997). Keeling (1993) models $k_b$ based on bubble spectra photographically recorded in laboratory experiments designed to simulate wave breaking (Monahan and Zeitlow, 1969; Cipriano and Blanchard, 1981), with a range in bubble radius from ~0.03 mm to 4 mm. The author suggests that relatively large bubbles (>0.5 mm in radius) contribute significantly to $k_b$, which should scale roughly as $\alpha^{-0.3} S_c^{-0.35}$. Asher et al. (1996) measured the exchange of multiple gases in a tipping-bucket whitecap simulation tank. Following Memery and Merlivat (1985), Asher et al. (1996) separate $k_b$ to contributions from bubbles that dissolve in or equilibrate with the surrounding water before reaching the surface and ones that never equilibrate: $k_b = a\alpha^{-1} + b\alpha^{-0.37} Sc^{-0.18}$. Theoretically, small bubbles with long lifetimes tend to be dissolved or equilibrated; $k_b$ due to these bubbles should scale as $\alpha^{-1}$ (not limited by

diffusivity). On the other hand, large bubbles that rise rapidly have insufficient time to equilibrate with the bulk water before surfacing. Gas is exchanged between the bulk water and these large bubbles during their entire lifetime, implying a dependence on both $\alpha$ and $S_c$. For evasion and through a cleaned surface, Asher et al. (1996) estimate that gas exchange due to dissolving and equilibrating bubbles is orders of magnitude smaller than that due to non-equilibrating bubbles ($a$ = -1 x $10^{-4}$ and $b$ = 1.7 x $10^{-2}$, in units of m $s^{-1}$), suggesting that the overall functionality of $k_b$ for evasion is approximately $\alpha^{-0.37} S_c^{-0.18}$. If we assume a weaker solubility dependence in $k_b$ from Keeling (1993) or Asher et al. (1996), the temperature effect in $k_b$ will be smaller than what we have shown. Over the SST range of 5~27 °C, the formulation $\alpha^{-0.37} S_c^{-0.18}$ for DMS differs by a factor of ~1.8, whereas the Woolf (1997) formulation differs by a factor of ~2.5. Coincidentally, $S_c^{-0.5}$ for DMS over the same SST range also differs by a factor of ~1.8. Thus, using the formulation from Asher et al. (1996) to adjust $k_b$ leads to the essentially the same result as using the widely used $S_c$-only normalization.

The error caused by ignoring the temperature-solubility dependence in $k_b$ when normalizing transfer velocity to $S_c$ = 660 is most significant for gases of intermediate solubility. Using the COARE model, we can calculate the difference between $k_b$ ($G_{660}/G$) and $k_b$ $(660/S_c)^{-1/2}$ for a normalization from 5 °C to the temperature at which $S_c$ = 660 for a range of gases, and compute the relative error by dividing that difference by $k_{660}$. This is shown in Fig. 2.10 for DMS, $CO_2$, methyl iodide ($CH_3I$), and chloroiodomethane ($CH_2ClI$). In seawater, $S_c$ = 660 at 24.0 and 27.8 °C for $CH_3I$, and $CH_2ClI$; the respective $\alpha$ values are 3.6 and 18.8 (Archer et al., 2007). It is apparent that for very insoluble gases, the relative error in transfer velocity in high winds is near zero because the

temperature dependence of $G$ is similar to $S_c^{-1/2}$. Such is the case for $CO_2$ (Fig. 2.10), as well as $SF_6$, radon, and nitrous oxide (not shown). For soluble gases, the temperature dependence of $G$ diverges more from $S_c^{-1/2}$, but the magnitude of $k_b$ also decreases, so the error in total transfer velocity is negligible. It is transfer of gases with intermediate solubility, such as organosulfur compounds, that are affected the most by the temperature dependence in solubility. For example, applying the $S_c$ normalization to $CH_3I$ at SST = 5 °C underestimates $k_{660}$ by ~ 11% at a wind speed of 16 m $s^{-1}$.

## 5. Discussion

Replacing $k_{w660}$ in (2.5) with the $k_{w660}$' yields the final normalized total transfer velocity ($k_{660}$'), which is plotted in $U_{10n}$ bins for all five cruises in Fig. 2.11. Compared to Fig. 2.5, $k_{660}$' is greater than $k_{660}$ from (2.3) for the coldwater SO GasEx by ~7 cm $hr^{-1}$ at 15 m $s^{-1}$, whereas for the tropical TAO and BIO cruises, $k_{660}$' is slightly lower than $k_{660}$ at most wind speeds. To more clearly demonstrate the effects of filtering for $DMS_w$ variability and atmospheric stability, normalizing for temperature dependence in airside resistance, and adjusting for both $\alpha$ and $S_c$ dependence in $k_b$, Fig. 2.12(a) shows the difference between $k_{660}$ from (2.3) and COARE model estimate at 27.2 °C in $U_{10}$ bins; (b) shows the difference between final normalized $k_{660}$' and COARE estimate in $U_{10n}$ bins. The COARE gas transfer model estimate is used as a reference here for comparison. The divergence at high wind speeds shown in Fig. 2.12(a) illustrates the biases among cruises partly due to the residual temperature dependence not accounted for by (2.3). $k_{660}$' from all cruises show closer agreement with each other; at 9 m $s^{-1}$, the standard deviation of the bin-averages is 3.6 cm $hr^{-1}$ for $k_{660}$ and is reduced to 2.3 cm $hr^{-1}$

for $k_{660}$'. Table 2.2 contains the bin-average $k_{660}$ (from (2.5), accounting for temperature-solubility dependence in airside resistance, but not in bubbles) and $k_{660}$' of the five cruises, weighted by the number of points per bin for each cruise. Average $k_{DMS}$ from SO GasEx at ambient conditions and corresponding $u_*$ values in $U_{10n}$ bins from 1 to 15 m $s^{-1}$ are also presented.

We can now compare this average $k_{660}$' to previous observations of relatively insoluble gases and widely used wind speed-dependent parameterizations (Fig. 2.13). Based on measurements of $SF_6$ gas exchange in a lake and wind tunnel observations, Liss and Merlivat (1986) model *k* as three piece-wise linear functions with increasing slope at higher winds, representing distinctive regimes of smooth surface, rough surface (capillary waves), and breaking waves, respectively. From natural $^{14}C$ disequilibrium and the bomb $^{14}C$ inventory, Wanninkhof (1992) fits *k* with a quadratic function. From artificial injections of two volatile tracers ($^3He$ and $SF_6$) and one non-volatile tracer (spores) in the North Sea, Nightingale et al. (2000) report a parameterization of *k* that consists of both linear and quadratic dependences. Ho et al. (2006) fit a quadratic function to $^3He/SF_6$ measurements in the Southern Ocean. Based on EC observations of $CO_2$ during the GasEx I cruise in the North Atlantic (a $CO_2$ sink), Wanninkhof and McGillis (1999) suggested a cubic fit between *k* and wind speed. However, an equivalent study during the follow-up GasEx II cruise in the Equatorial Pacific (a $CO_2$ source) resulted in a much weaker wind speed dependence (McGillis et al. 2004). The authors attributed the GasEx II result to a limited wind speed range and strong diurnal heating.

Also shown in Fig. 2.13 are the $k_{660}$ curves from the COARE gas transfer model for DMS (*A*=1.3; *B*=1.0; SST=27.2 °C) and $CO_2$ (*A*=1.3; *B*=1.0; SST=20.0 °C).

Normalized for diffusivity, transfer velocities of waterside controlled gases due to buoyancy and shear are expected to be similar (Asher et al., 1996). Indeed, below 7~8 m $s^{-1}$, before the onset of whitecapping, $k_{660}$ of different waterside controlled gases are comparable. The exception is GasEx II (McGillis et al. 2004), which shows elevated $k_{660}$ in low winds. In higher winds, transfer velocity of DMS is significantly lower than that determined for $CO_2$ and from $^3He/SF_6$ due to the much higher solubility of DMS, and hence decreased partitioning into air bubbles. While a power law parameterization of $k$ as a function of wind speed might be adequate in application for one particular gas, it masks the complex physical mechanisms responsible for gas exchange in high winds and rough seas. To more accurately quantify the interfacial and bubble-mediated components of air-sea exchange, simultaneous high wind speed measurements of the transfer velocity of multiple gases with a large range of solubility will be needed.

In general, the COARE gas transfer model appears to predict DMS transfer velocity fairly well at the reference $S_c$. A better assessment of model performance is a comparison between the observed $k_{DMS}$ and modeled $k_{DMS}$ at ambient conditions, as normalization to a reference will introduce additional uncertainty due to assumptions in $S_c$ and $\alpha$. Such uncertainty amplifies when the SST is very different from 27.2 °C, as was the case for SO GasEx. Since temperature is a required input parameter for COARE 3.0 and the gas transfer parameterization for $k_b$ accounts for solubility and diffusivity effects, no adjustment on the model output is necessary for a direct comparison of $k_{DMS}$.

Figure 2.14 shows the hourly residual (observation minus model) in $k_{DMS}$ for all five cruises. The difference between the bin-average observation and model prediction is within ~2 cm $hr^{-1}$ across the wind speed range. In low winds, observation appears to be

less than the COARE prediction, which may be a result of measurement errors or model deficiencies. Relative uncertainty in the EC flux observations increases in low winds due to the lower signal to noise ratio and a shift of turbulent eddies towards lower frequencies that are less adequately sampled. Near surface gradients in $DMS_w$ are also more likely in calm conditions, which can lead to biases in $DMS_w$ measurements. With regard to the model, COARE uses the oceanic turbulent Richardson number and heat fluxes to determine the buoyancy contribution to gas exchange. Uncertainty in the critical turbulent Richardson number, an empirical constant that defines the threshold from free convection to forced convection, is an additional source of error. Overall, the discrepancy between observation and model at low winds should not greatly bias the predicted global mean flux because of the small magnitude of $k_{DMS}$ in calm conditions.

In moderate winds, observations and COARE prediction agree closely, implying that the empirical constant $A = 1.3$ for direct transfer is reasonable (the bin-average at 9 m $s^{-1}$ shows a small positive bias partly due to the several high $k_{DMS}$ points between 8~9 m $s^{-1}$). In high winds, the model prediction exceeds observation by ~10%, which could be due to an overestimation of bubble-mediated exchange (e.g. empirical constant $B$). Also, the model presently uses $u_*$ in the estimation of direct transfer; as $u_{*v}$ has a flatter curvature than $u_*$, using $u_{*v}$ would result in a smaller interfacial term in high winds. However, incorporating $u_{*v}$ in to the COARE model requires further tuning of empirical parameters $A$ and $B$. Such fitting is best done, if a universal relationship exists, with multiple gases of varying solubility, which is beyond the scope of this paper.

## 6. Conclusions

Over the past several years, we have measured the transfer velocity of DMS directly in five open ocean cruises at locations ranging from the tropics to the high latitudes. To limit the influence of measurement bias, we apply a number of quality control criteria based on relative wind direction, ship maneuvers, and atmospheric stability. To account for losses of flux signal at high and low frequencies due to inlet attenuation and limited sampling time, respectively, an approximate correction using the Kaimal cospectral function for neutral conditions is used, yielding a total correction of ~5% typically and ~10% for the highest and lowest relative wind speeds.

SO GasEx is unique for the low SST, high winds, and frequent occurrence of stable atmosphere. Normalized for diffusivity only, DMS transfer velocity from SO GasEx is still lower than those from warm water cruises. The solubility of DMS increases in low SST, which results in greater airside control and reduced bubble-mediated exchange. We demonstrate here adjustments accounting for these temperature effects, which yields improved agreement among DMS transfer velocity observations from five cruises. Compared to gas exchange observations of $CO_2$ and $SF_6$, normalized transfer velocity for DMS is similar at low-to-moderate wind speeds, where shear-driven interfacial exchange dominates. In high winds, however, DMS transfer trends significantly lower than transfer of other gases due to the solubility dependence in bubble-mediated exchange. Among widely used gas transfer parameterizations (e.g. Liss and Merlivat (1986), Wanninkhof (1992), Nightingale et al. (2000), Ho et al. (2006)), the physics-based NOAA COARE model shows the closest agreement with field observations of $k_{DMS}$.

In a recent review, Elliott (2009) summarizes gas transfer parameterizations for

DMS flux and examines the global distribution of DMS emissions with a planetary level sulfur cycle model. The author lists the discrepancies between generalized gas transfer parameterizations and recent eddy correlation flux measurements, and adopts a composite DMS transfer model based on formulations from Wanninkhof (1992) and Liss and Merlivat (1986) to account for the lower transfer at higher wind speeds compared to insoluble gases. At the time of the review by Elliot (2009), model validation with direct EC observations of DMS extended only to wind speeds of ~10 m $s^{-1}$ (Blomquist et al., 2006). Furthermore, provision for the computation of friction velocity within the ocean circulation model was not implemented, limiting the gas transfer representation to a simple dependence on wind speed. More recent $k_{DMS}$ observations, especially from SO GasEx, have extended the range of wind speed to 15 m $s^{-1}$. Results from this paper suggest that the dependence on SST in $k_{DMS}$ is more complex than previously assumed. For example, in high latitude regions characterized by low temperatures and high wind speeds, estimated $k_{DMS}$ from wind speed parameterizations will be biased high if only the Schmidt number normalization is used. For these reasons, the implementation of a physics-based gas transfer scheme similar to COARE 3.0 in planetary sulfur models is clearly desirable. In schemes that may already use bulk parameterizations of heat fluxes, the additional overhead to compute friction velocity and gas transfer velocity should be minimal.

The polar seas, especially the Southern Ocean, play a key role in the global sulfur cycle and atmospheric aerosol distribution through emissions of DMS (Gabric et al., 2004). The conclusions from Elliot (2009) with respect to an overestimate of polar DMS emissions by current sulfur cycle models seems justified based on the most recent field

observations of DMS transfer velocity at moderate-to-high wind speeds. However, the influence of wave fields and sea state on surface stress, and therefore on gas exchange, is not well parameterized by models, including COARE 3.0. If the anomalously low $k_{DMS}$ observations in very high winds from SO GasEx (Fig. 2.4) are found to be related to sea state, a further reduction in the net emission of DMS from polar seas may be warranted, but currently we must consider this issue unresolved.

**Acknowledgements**

We thank the National Oceanic and Atmospheric Administration for the primary support of this work through grant NA07OAR4310084 and the National Science Foundation for additional support through grants ATM-0241611 and ATM-0526341. We also thank NOAA project GC07-186 and NOAA's Health of the Atmosphere program. The participation of S.D. Archer in the Southern Ocean Gas Exchange Experiment was funded through the UK Natural Environment Research Council grant NE/F010656/1. Special thanks to J. Johnson and T. Bates (NOAA, Pacific Marine Environmental Laboratory) for seawater DMS measurements, R.M. Simpson, (University of Hawaii at Manoa) for instrument operation, and the crew of the *R/V Ronald H. Brown.*

## Tables

Table 2.1 Summary of cruises

| Cruise | Location | Time | Flux[1] | $DMS_w$[2] | Publication |
|---|---|---|---|---|---|
| TAO | Equatorial Pacific | Nov, 2003 | 7.1 (3.7) | 2.6 (0.8) | Huebert et al., 2004 |
| BIO | Sargasso Sea | Jul-Aug, 2004 | 6.2 (2.4) | 2.6 (0.4) | Blomquist et al., 2006 |
| DOGEE | Northeast Atlantic | Jun-Jul, 2007 | 5.2 (6.8) | 2.2 (2.4) | Huebert et al., 2010 |
| SO GasEx | Southern Ocean | Mar-Apr, 2008 | 2.9 (2.1) | 1.6 (0.7) | This work |
| VOCALS | Southeast Pacific | Oct-Nov, 2008 | 3.4 (1.9) | 2.8 (1.1) | Yang et al., 2009 |

1. Project mean DMS flux (1 sigma), μmoles $m^{-2}$ $day^{-1}$
2. Project mean seawater DMS concentration (1 sigma), nM

Table 2.2 Average DMS Transfer Velocity for SO GasEx and All Cruises

| $U_{10n}$, m $s^{-1}$ | $u_*$, m $s^{-1}$ | $k_{DMS}$, cm $hr^{-1}$ | $k_{660}$, cm $hr^{-1}$ | $k_{660}$', cm $hr^{-1}$ |
|---|---|---|---|---|
| 1 | 0.05 | - | 1.1 (0.1) | 1.1 (0.1) |
| 3 | 0.11 | 2.6 (0.4) | 2.8 (0.1) | 2.8 (0.1) |
| 5 | 0.17 | 3.8 (0.4) | 6.4 (0.1) | 6.4 (0.1) |
| 7 | 0.25 | 4.9 (0.5) | 10.7 (0.2) | 10.9 (0.2) |
| 9 | 0.33 | 6.6 (0.3) | 15.8 (0.4) | 16.3 (0.4) |
| 11 | 0.42 | 8.7 (0.3) | 19.2 (0.6) | 19.8 (0.6) |
| 13 | 0.52 | 10.1 (0.4) | 22.8 (0.8) | 23.4 (0.8) |
| 15 | 0.62 | 11.2 (0.7) | 26.2 (1.3) | 27.6 (1.4) |

$k_{DMS}$: bin-average from SO GasEx (standard error of the mean) at ambient conditions
$k_{660}$: bin-average from all cruises (standard error of the mean) from (2.5), without bubble normalization
$k_{660}$': bin-average from all cruises (standard error of the mean) with bubble normalization

**Figures**

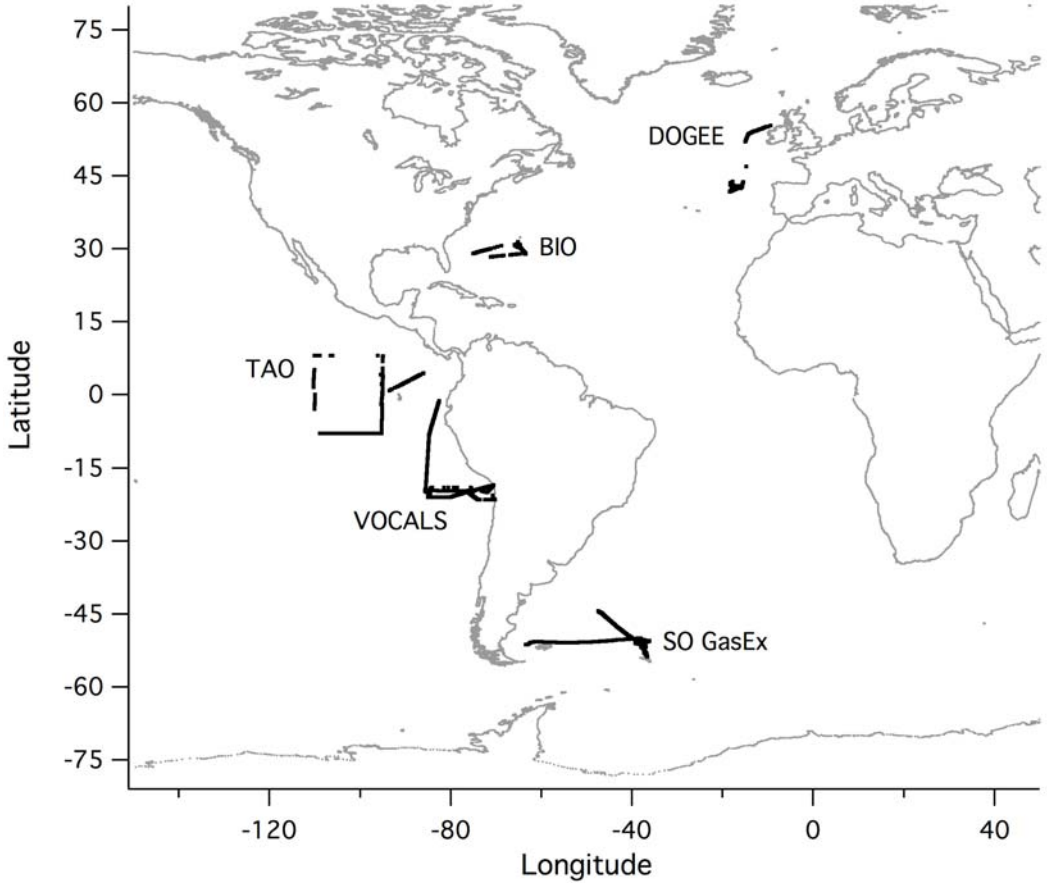


Figure 2.1 Map showing the five cruises from which DMS flux was measured directly with eddy covariance by U. Hawaii.

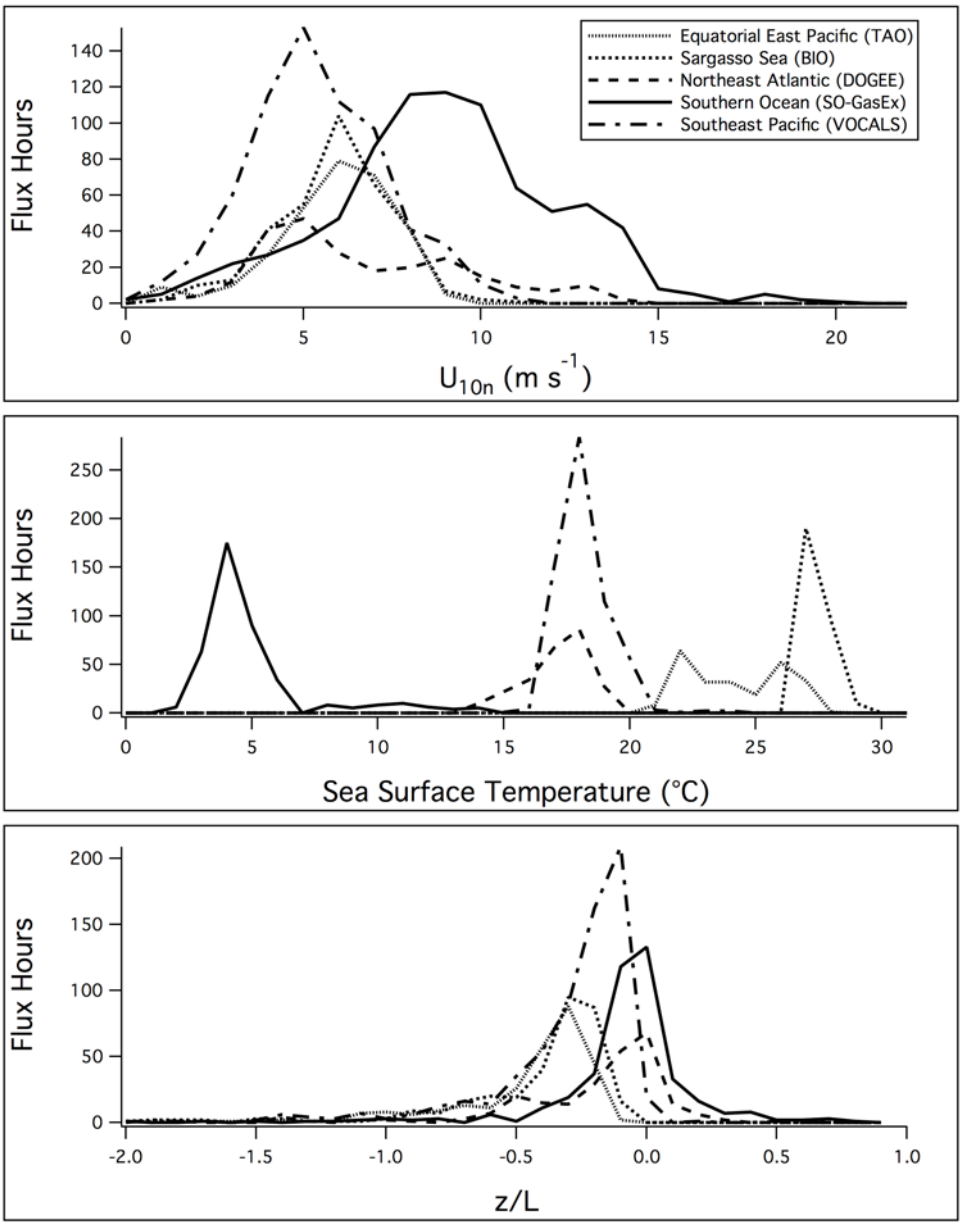


Figure 2.2 Histograms of 10-m neutral wind speed, SST, and stability parameter *z*/*L*. Tropical and temperate cruises were characterized by relative low wind speed, high SST, and unstable atmosphere. In SO GasEx, we encountered higher winds, lower SST, and more frequent occurrences of stable atmosphere.

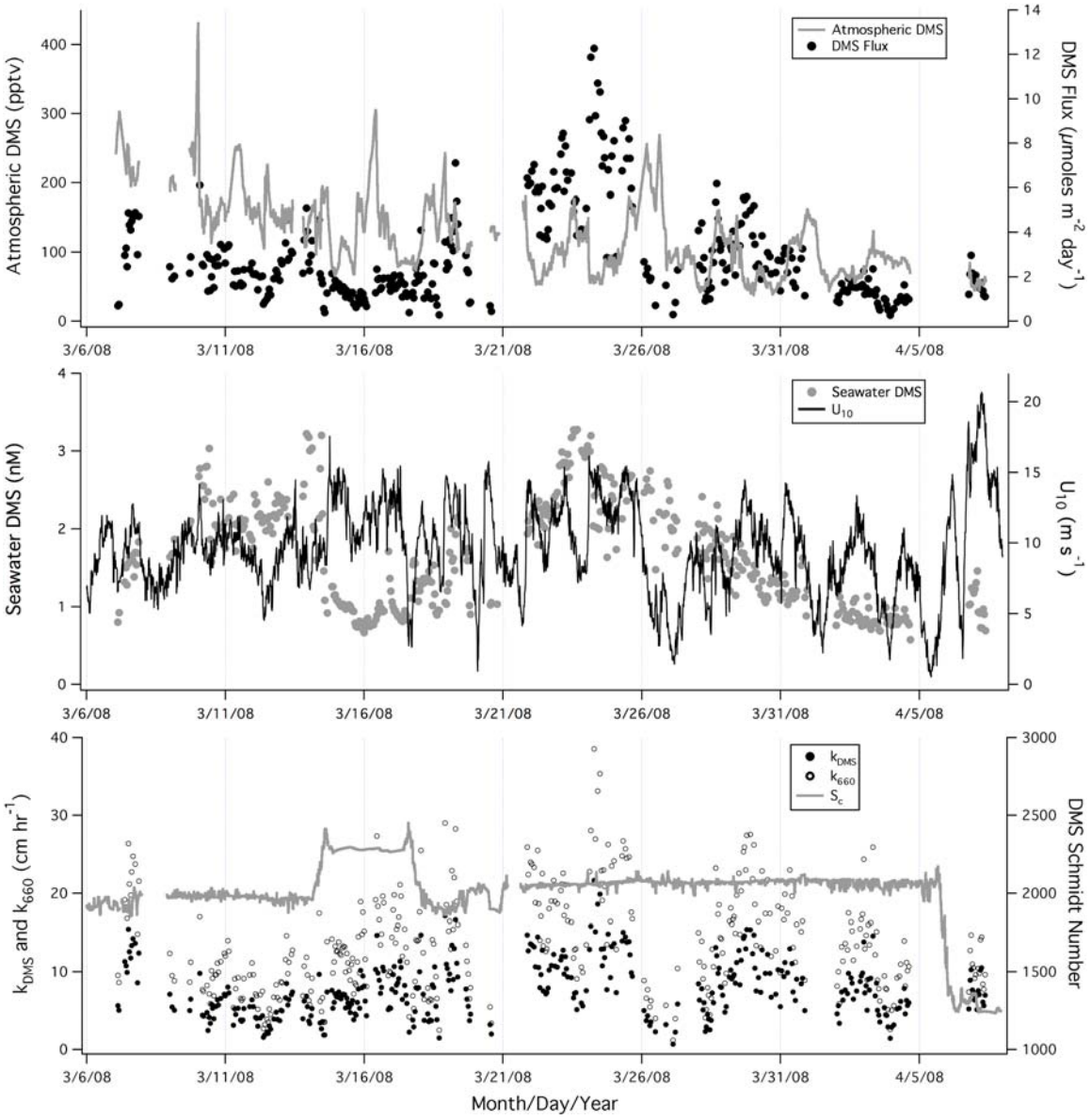


Figure 2.3 SO GasEx time series of atmospheric DMS concentration and flux (top); seawater DMS concentration and $U_{10}$ (middle); transfer velocity at ambient condition, normalized to $S_c$ = 660 as described in (2.3), as well as the DMS Schmidt number (bottom). Elevated DMS flux at times corresponded to higher seawater DMS concentration, such as on March 14 and 24. Near the end of the experiment, the ship encountered a storm while in transit to Uruguay. While wind speed briefly exceeded 20 m $s^{-1}$, DMS flux and transfer velocity were not elevated.

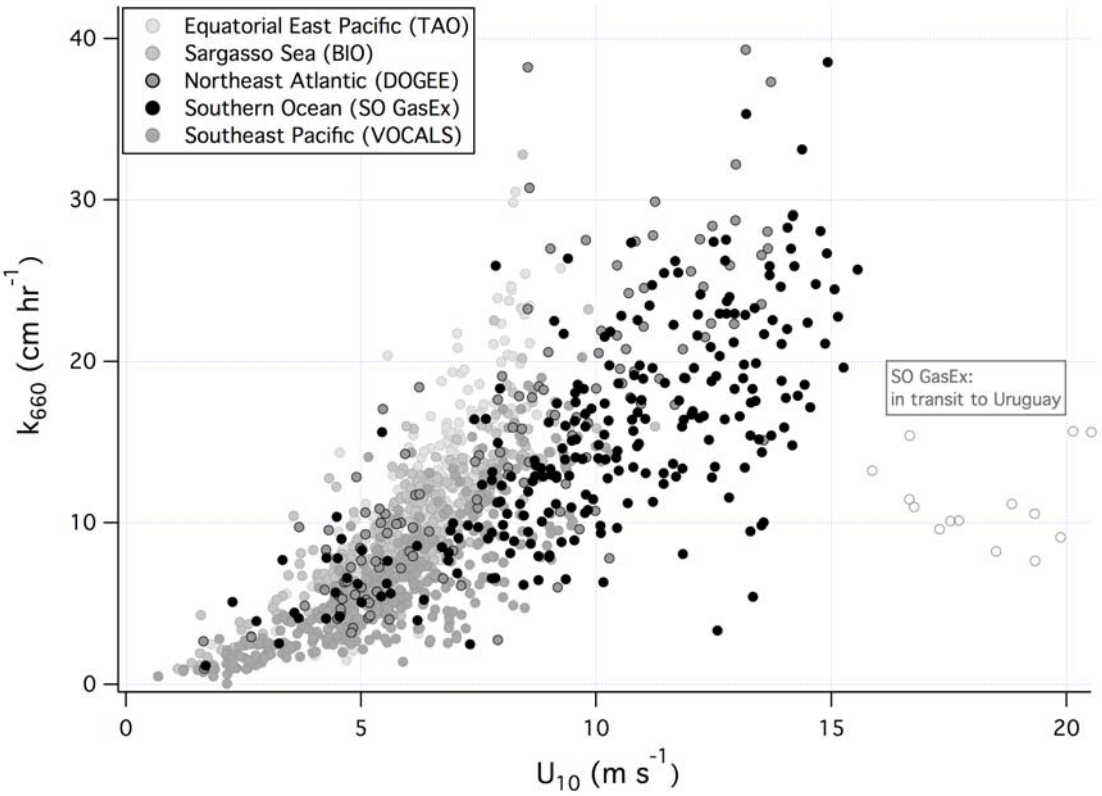


Figure 2.4 $k_{660}$ from (2.3) vs. $U_{10}$ from five cruises. The open circles in very high winds were from a storm in transit to Uruguay during SO GasEx. The $r^2$ for a linear relationship in the range of 0~16 m $s^{-1}$ is 0.63.

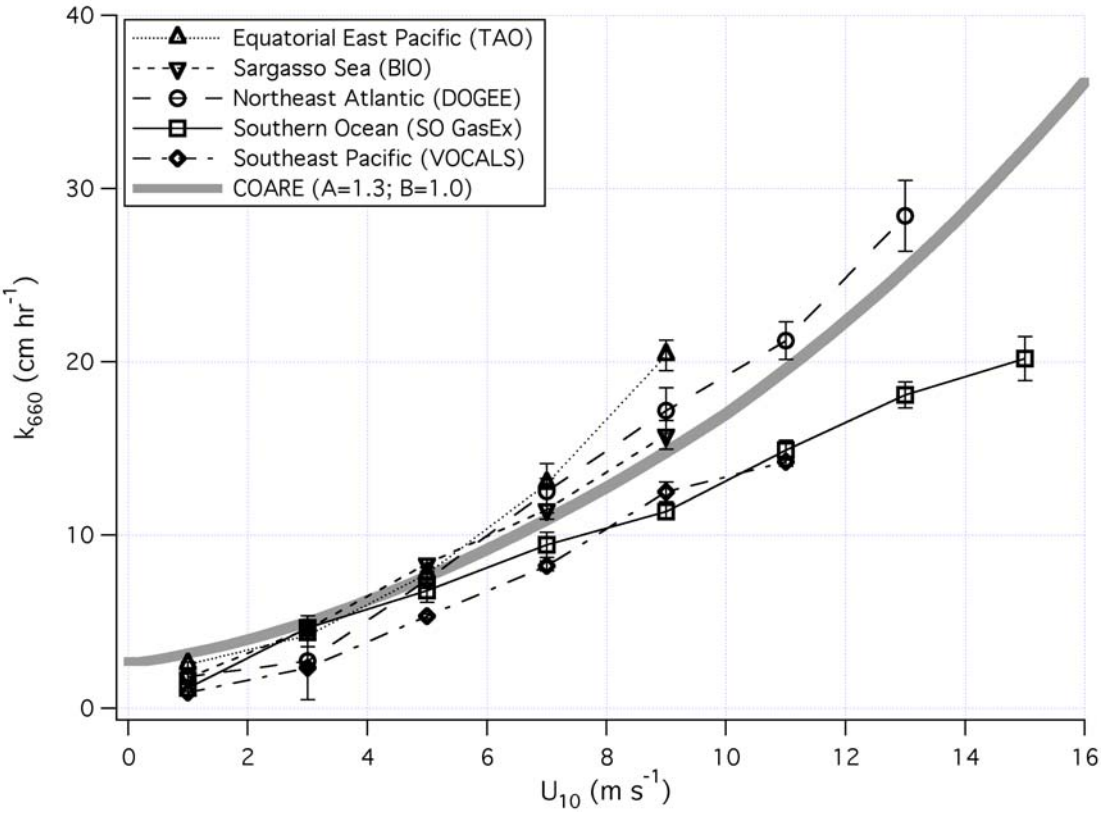


Figure 2.5 $k_{660}$ from (2.3) averaged to $U_{10}$ bins, along with the $k_{DMS}$ curve computed from the NOAA COARE gas transfer model (parameters $A$=1.3; $B$=1.0) at 27.2 °C ($S_c$ = 660 for DMS). Error bars correspond to standard errors of the mean within the bins. $k_{660}$ from SO GasEx clearly trends lower than $k_{660}$ from tropical cruises, such as TAO.

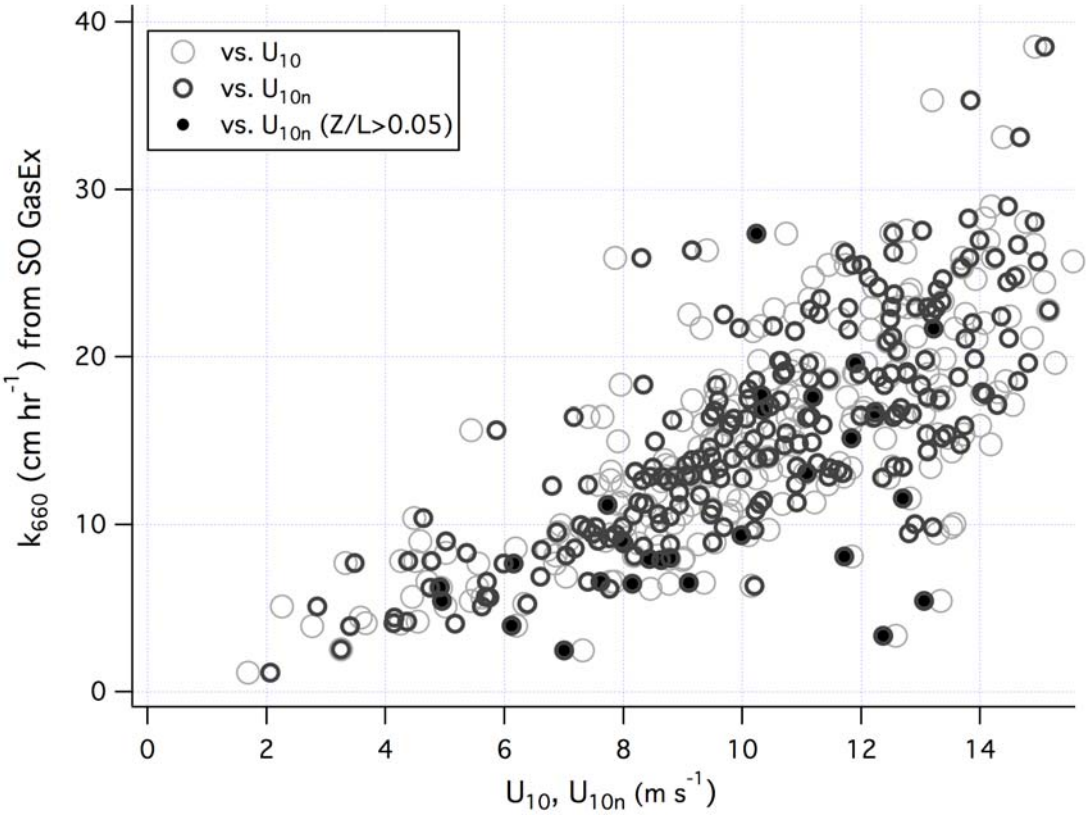


Figure 2.6 $k_{660}$ from (2.3) vs. $U_{10}$ and $U_{10n}$ from SO GasEx, with solid points indicating statically stable boundary layer ($z/L > 0.05$). The $r^2$ for a linear relationship between $k_{660}$ and wind speed is increased from 0.51 to 0.56 when $U_{10n}$ is used instead of $U_{10}$. In a more stable boundary layer, greater scatter and a potentially negative bias in $k_{660}$ are apparent.

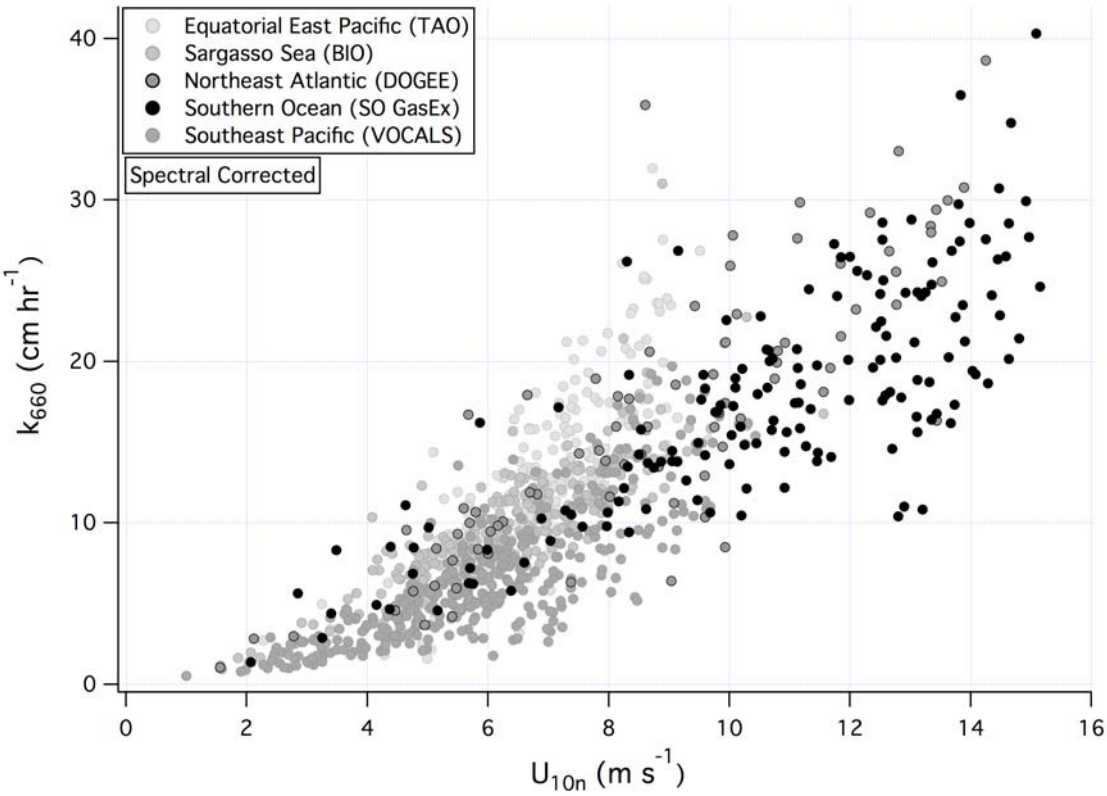


Figure 2.7 $k_{660}$ from (2.5) vs. $U_{10n}$ for all cruises. A spectral (Kaimal) correction has been applied to hours when $z/L < 0.05$, while hours when $z/L > 0.05$ are eliminated. Normalization for the temperature dependence in the airside resistance is included (Section 3.4). The $r^2$ for a linear relationship between $k_{660}$ and $U_{10n}$ for all cruises is increased from 0.63 in Fig. 2.4 to 0.71.

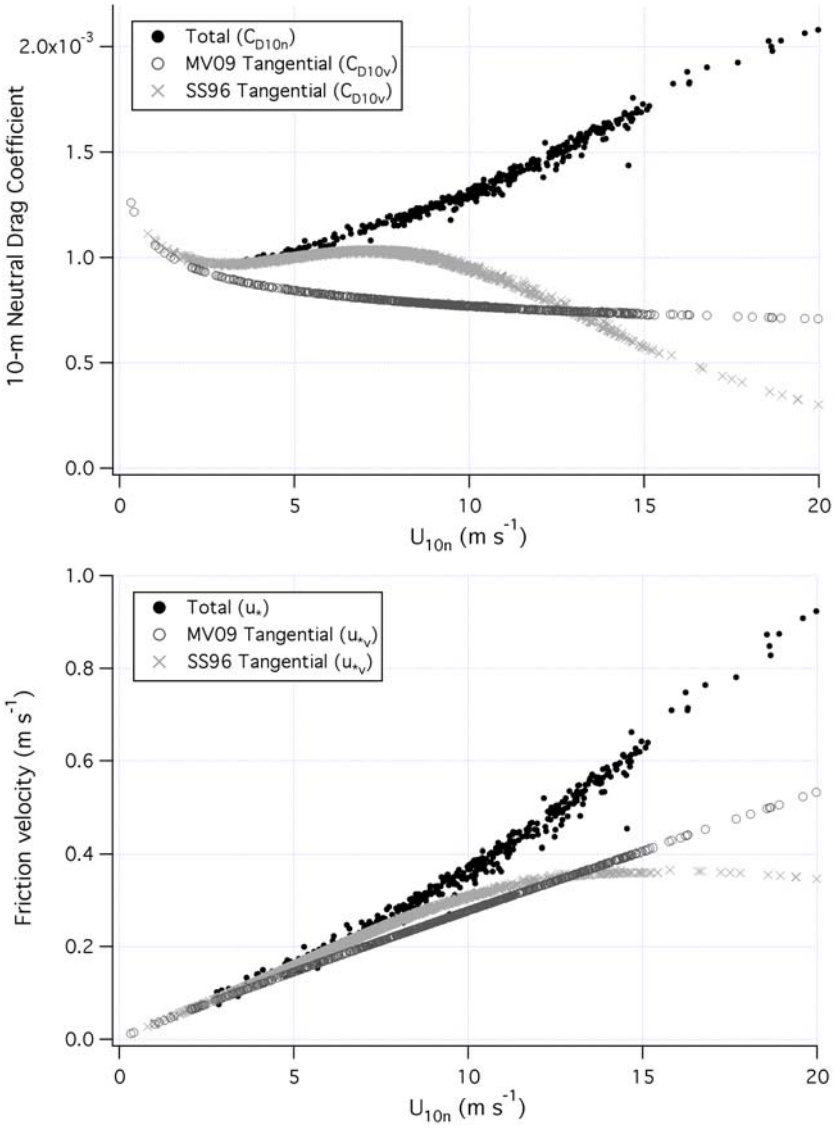


Figure 2.8 Partition of drag coefficient (top) and friction velocity (bottom) to tangential and wave components per *Mueller and Veron* (2009) (MV09) and *Soloviev and Schlüssel* (1996) (SS96). In high winds, departures in both parameters from total are due to increasing partition of total wind stress to wave stress. The SS96 approach results in a greater roll off in high winds for $u_{*v}$ than MV09; we adopt the latter because wave age is not required for the estimation of tangential stress.

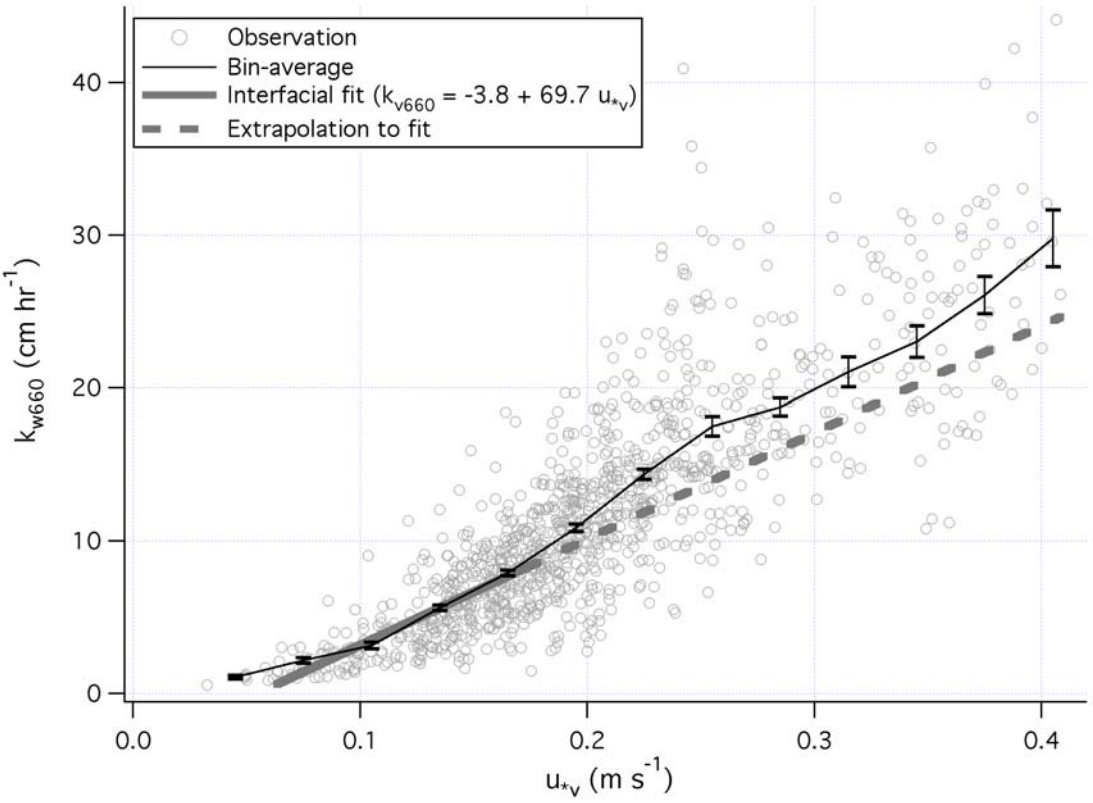


Figure 2.9 $k_{w660}$ vs. $u_{*v}$ for all cruises, with error bars corresponding to the standard errors of the mean within the bins. A linear fit in the low-to-moderate $u_{*v}$ range yields the proportionality for interfacial exchange. Bubble-mediated transfer is estimated as the difference between the extrapolation of the linear fit and total waterside transfer velocity.

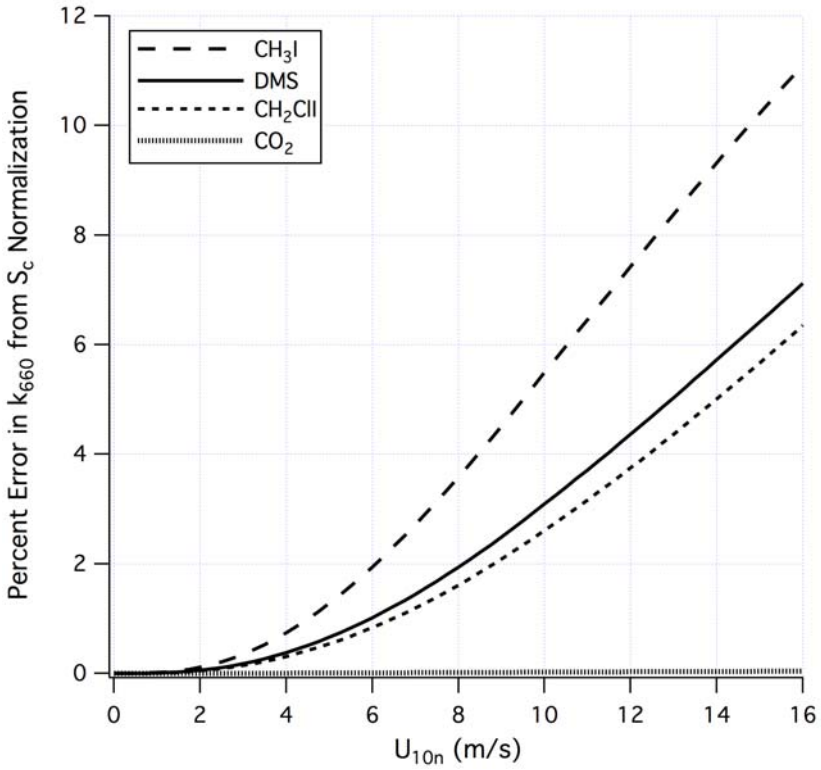


Figure 2.10 Relative error resulting from the application of the $S_c$-only normalization (2.3) for several trace gases from SST = 5 °C. Gases with intermediate solubility, such as $CH_3I$ and DMS, show the greatest bias, while the widely used $S_c$-only normalization appears to be adequate for less soluble gases like $CO_2$.

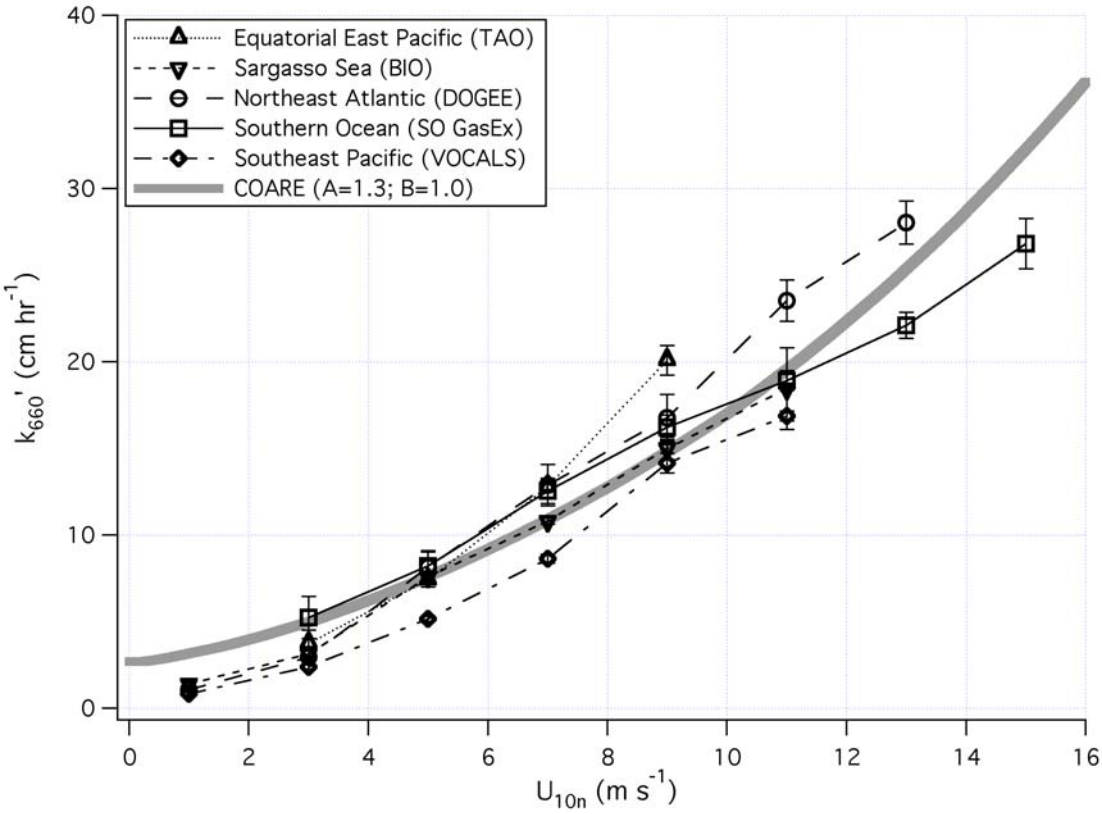


Figure 2.11 Bin-average of solubility normalized $k_{660}$' vs. $U_{10n}$, along with the estimate from COARE as a reference. Error bars correspond to standard errors of the mean within the bins. Compared to Fig. 2.5, transfer velocities from warm water cruises such as TAO and BIO are decreased slightly, whereas those from colder water cruises such as SO GasEx and VOCALS are adjusted upwards due to the temperature dependence in airside control and bubble-mediated transfer. At 9 m $s^{-1}$, the standard deviation among the five cruises is 3.6 cm $hr^{-1}$ in $k_{660}$ (Fig. 2.5), which is reduced to 2.3 cm $hr^{-1}$ in $k_{660}$'.

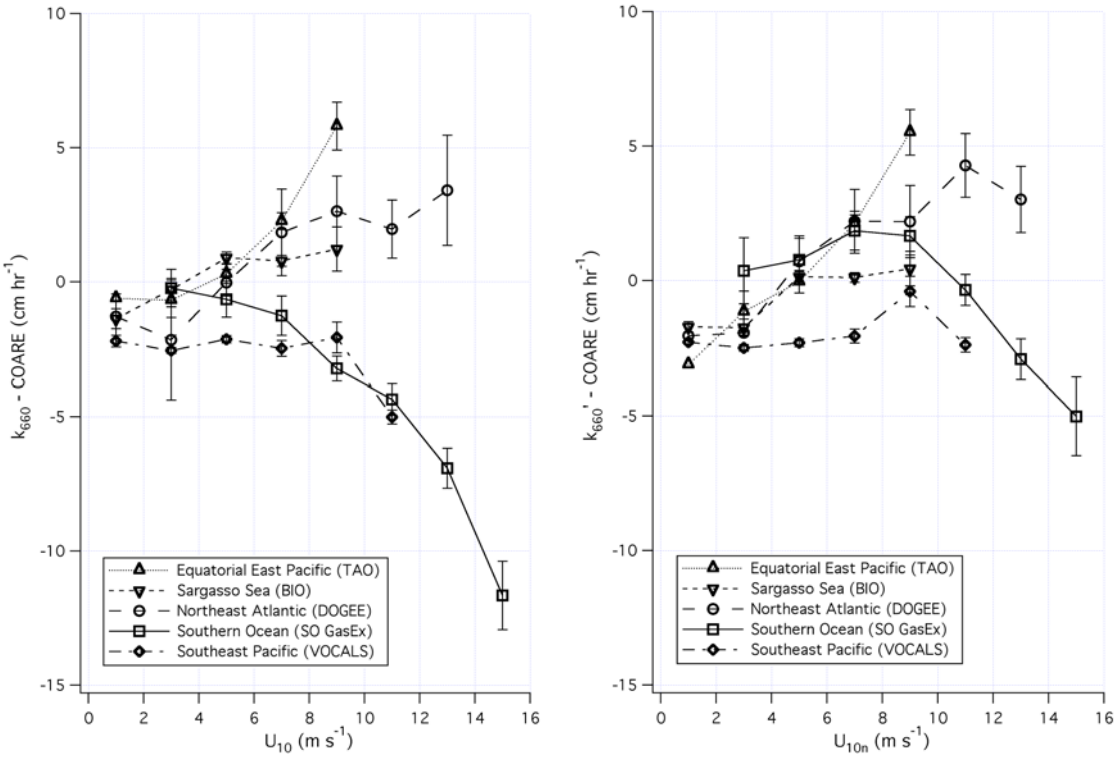


(a) (b)

Figure 2.12 (a) Difference between $k_{660}$ from (2.3) and COARE gas transfer model estimate at 27.2 °C in $U_{10}$ bins for all cruises, and (b) difference between final normalized $k_{660}$' and COARE estimate in $U_{10n}$ bins. Error bars correspond to standard errors of the mean within the bins. Filtering for $DMS_w$ variability and atmospheric stability, normalizing for temperature dependence in airside resistance, and adjusting for both solubility and $S_c$ dependence in $k_b$ results in closer agreement in transfer velocity among the five cruises. At 15 m $s^{-1}$, $k_{660}$' is about 7 cm $hr^{-1}$ higher than $k_{660}$ for SO GasEx.

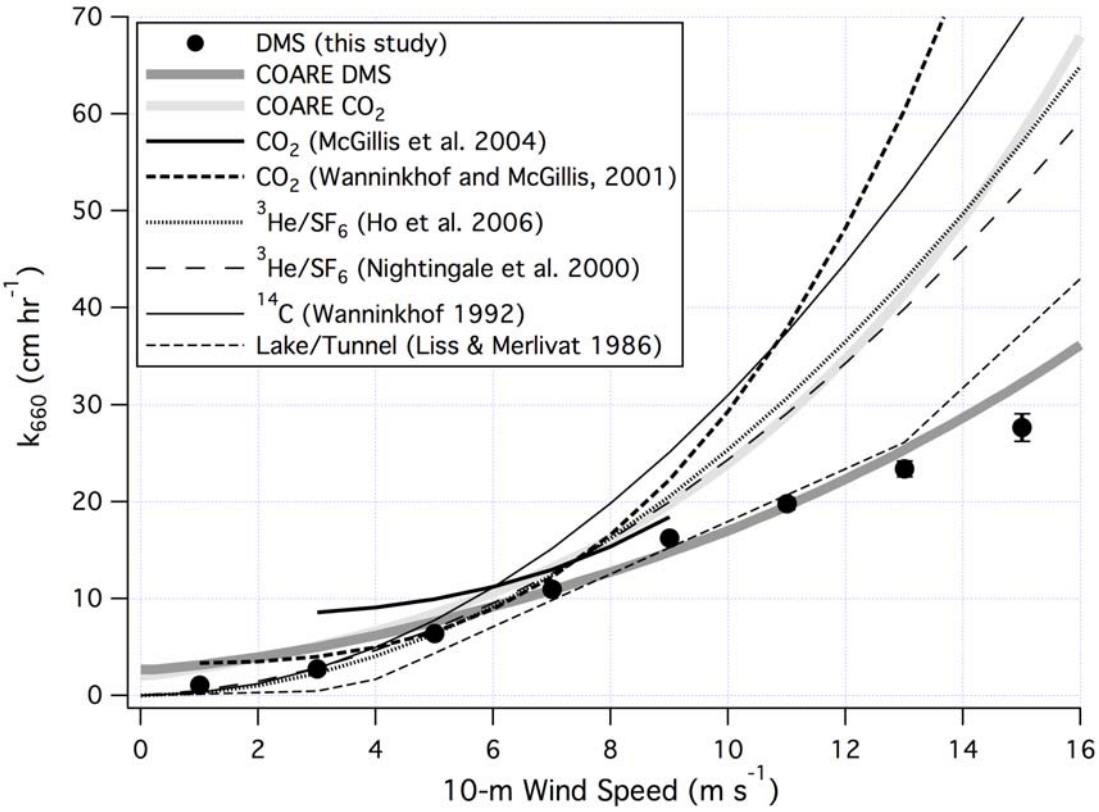


Figure 2.13 Comparison of DMS $k_{660}$' (average of all projects) with oft-used wind speed parameterizations derived from sparingly soluble gases. Transfer velocity of DMS is significantly lower in moderate to high winds than those of less soluble gases due to its much higher solubility, and thus reduced bubble mediated transfer.

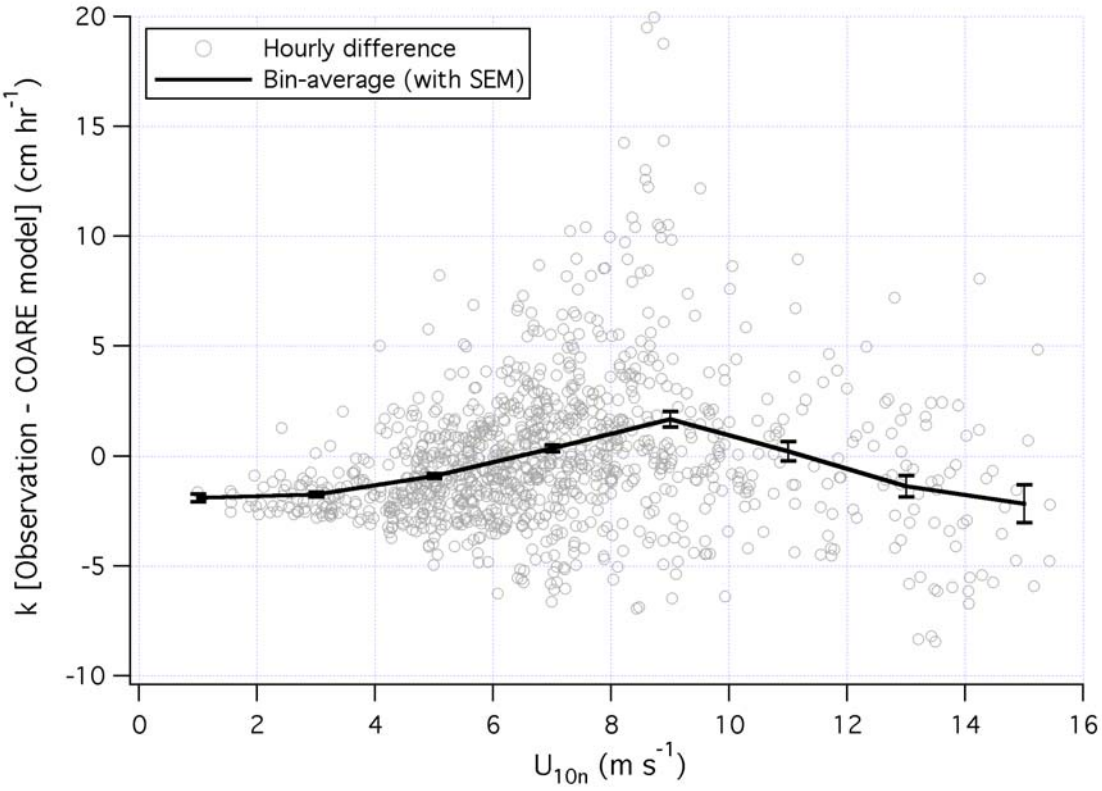


Figure 2.14 Difference between observed and COARE modeled $k_{DMS}$ at ambient conditions. The difference between the bin-average observation and model prediction is within ~2 cm $hr^{-1}$ across the wind speed range.

## References


Archer, S. D., Goldson, L. E., Liddicoat, M. I., Cummings, D. G., and Nightingale P. D. Marked seasonality in the concentrations and sea-to-air flux of volatile iodocarbon compounds in the western English Channel, J. Geophys. Res., 112, C08009, doi:10.1029/2006JC003963, 2007.

Asher, W.E., Karle, L.M., Higgins, B.J., Farley, P.J., Monahan, E.C., and Leifer I.S.: The influence of bubble plumes on air–water gas transfer velocities. J. Geophys. Res. 101, 12027–12041, 1996.

Bandy, A.R., Thornton, D.C., Tu, F.H., Blomquist, B.W., Nadler, W., Mitchell, G.M., and Lenchow D.H.: Determination of the vertical flux of dimethylsulfide by eddy correlation and atmospheric pressure ionization mass spectrometry (APIMS), J. Geophys. Res., 107(D24), 4743, doi:10.1029/2002JD002472, 2002.

Banner, M.L., Jones, I.S.F., and Trinder JC.: Wave number spectra of short gravity waves. J. Fluid. Mech., 198, 312–344, 1989.

Banner M.L., and Peirson W.L.: Tangential stress beneath wind-driven air-water interfaces, J. Fluid. Mech., 364, 115–145, 1998.

Bates, T. S., Quinn, P. K., Covert, D. S., Coffman, D. J., Johnson, J. E., and Wiedensohler A.: Aerosol physical properties and processes in the lower marine boundary layer: A comparison of shipboard sub-micron data from ACE-1 and ACE-2, Tellus, Ser. B, 52, 258–272, 2000.

Blomquist, B., Fairall, C.W., Huebert, B., Kieber D., and Westby, G.: DMS sea-air transfer velocity: Direct measurements by eddy covariance and parameterization based on the NOAA/COARE gas transfer model, Geophys. Res. Lett., 33(7), 10.1029/2006GL025735, 2006.

Blomquist, B. W., Huebert, B. J., Fairall, C. W., and Faloona, I. C.: Determining the sea-air flux of dimethylsulfide by eddy correlation using mass spectrometry, Atmos. Meas. Tech., 3, 1-20, doi:10.5194/amt-3-1-2010, 2010.

Charlson, R.J., Lovelock, J.E., Andreae, M.O., and Warren S.G.: Oceanic phytoplankton, atmospheric sulfur, cloud albedo and climate, Nature, 326, 655-661, 1987.

Cipriano, R. J. and Blanchard D.C.: Bubble and aerosol spectra produced by a laboratory 'breaking wave.' J. Geophys. Res., 86, 8085–8092, 1981.

Csanady, G.T.: Turbulent interface layers. J. Geophys. Res. 83, 2329–2342, 1978.

Csanady, G.T: The role of breaking wavelets in air-sea gas transfer, J. Geophys. Res., 95, 749–759, 1990.

Dacey, J.W.H., Wakeham, S.G., and Howes B.L.: Henry's law constants for dimethylsulfide in freshwater and seawater, Geophys. Res. Lett., 11, 10, 991–994, 1984.

Edson, J. B., Fairall, C. W., Bariteau, L., Helmig, D., Zappa, C. J., Cifuentes-Lorenzen, A., McGillis, W. M., Pezoa, S, and Hare J. E. (this issue): Eddy-Covariance Measurement of CO2 Gas Transfer Velocity during the 2008 Southern Ocean Gas Exchange Experiment (SO GasEx): Wind Speed Dependency, J Geophy. Res.

Edson, J.B., Hinton, A.A., Prada, K.E., Hare, J.E., and Fairall C.W.: Direct covariance flux estimates from mobile platforms at sea, J. Atmos. Oceanic Technol., 15, 547–562, 1998.

Elliott, S.:, Dependence of DMS global sea-air flux distribution on transfer velocity and concentration field type, J. Geophys. Res., 114, G02001, doi:10.1029/2008JG000710. 2009.

Fairall, C.W., Bradley, E.F., Hare, J.E., Grachev, A.A., and Edson, J.B.: Bulk parameterization of air-sea fluxes: Updates and verification for the COARE algorithm, J. Climate, 16, 571–591, 2003.

Frew, N. M., et al., Air-sea gas transfer: Its dependence on wind stress, small-scale roughness, and surface films, J. Geophys. Res., 109, C08S17, doi:10.1029/2003JC002131, 2004.

Gabric, A. J., Simo, R., Cropp, R. A., Hirst, A. C., and Dachs J.: Modeling estimates of the global emission of dimethyl sulfide under enhanced greenhouse conditions, Global Biogeochem. Cycles, 18, GB2014, doi:10.1029/2003GB002183, 2004.

Ho, D., Law, C.S., Smith, M.J., Schlosser, P., Harvey, M., and Hill, P.: Measurements of air-sea gas exchange at high wind speeds in the Southern Ocean: Implications for global parameterizations. Geophys. Res. Lett., Vol. 33, L16611, doi:10.1029/2006GL026817, 2006.

Ho, D. T., Sabine, C. L., Hebert, D., Ullman, D. S., Wanninkhof, R., Strutton, P. G., Hamme, R. C., Hales, B., Edson, J. B., and Hargreaves B. R. (this issue a): Southern Ocean Gas Exchange Experiment: Setting the Stage, J Geophy. Res.

Ho, D. T., Wanninkhof, R., Schlosser, P., Ullman, D. S., Hebert, D., and Sullivan K. F. (this issue b): Gas transfer velocities measured with 3He/SF6 during the Southern Ocean Gas Exchange Experiment, J Geophy. Res.

Horst, T.W., and Weil J.C.: How Far is Far Enough? The Fetch Requirements for Micrometeorological Measurement of Surface Fluxes. J. Atmos. Oceanic Tech., 11, 1018-1025, 1994.

Huebert, B., Blomquist, B., Yang, M., Archer, S., Nightingale, P., Yelland, M., Stephens, J., Pascal, R., and Moat, B.: Linearity of DMS Transfer Coefficient with Both Friction Velocity and Wind Speed in the Moderate Wind Speed Range, Geophys. Res. Lett., 37, L01605, doi:10.1029/2009GL041203, 2010.

Kaimal, J., Wyngaard, J., Izumi, Y., and Cot ´e O.: Spectral characteristics of surface layer turbulence, Q. J. Roy. Metor. Soc., 98, 563–589, 1972.

Keeling, R.F.: On the role of large bubbles in air–sea gas exchange and supersaturation in the ocean. J. Mar. Res. 51, 237–271, 1993.

Kiene, R.P., and Service, S.K.: Decomposition of dissolved DMSP and DMS in estuarine waters: dependence on temperature and substrate concentration, Mar. Ecol. Prog. Ser., 76, p.1-11, 1991.

Liss, P.S., and Merlivat, L.: Air-sea gas exchange rates: Introduction and synthesis, in The Role of Air-Sea Interactions in Geochemical Cycling, edited by p.Buat-Menard, pp. 113-129, D.Reidel, Hingham, MA, 1986.

Liss, P.S., and Slater P.G.: Flux of Gases across the air-sea interface, Nature, 247, 181–184, 1974.

Lovelock, J.E., Maggs, R.J., and Rasmussen R.A.: Atmospheric dimethyl sulphide and the natural sulphur cycle. Nature, 237, No. 5356, 452–453, 1972.

Marandino, C. A., De Bruyn, W.J., Miller, S.D., and Saltzman E.S.: Open ocean DMS air/sea fluxes over the eastern South Pacific Ocean, Atmos. Chem. Phys., 9, 345–356, 2009.

McGillis, W.R., Dacey, J.W.H., Frew, N.M., Bock, E.J., and Nelson, R.K.: Water-air flux of dimethylsulfide, J. Geophys. Res., 105, NO. C1, 1187–1193, 2000.

McGillis, W. R., et al.: Air-sea CO2 exchange in the equatorial Pacific, J. Geophys. Res., 109, C08S02, doi:10.1029/2003JC002256, 2004.

Monahan, E.C., and O'Muircheartaigh I.G.: Optimal power-law description of oceanic whitecap coverage on wind speed, J. Phys. Ocean., 10, 2094–2099, 1980.

Monahan, E.C., and Spillane M.C.: The role of whitecaps in air-sea gas exchange, in Gas Transfer at Water Surfaces, edited by G.H. Jirka and W. Brutsaert, pp. 495–504, D. Reidel, Norwell, MA, 1984.

Monahan, E. C. and Zeitlow C. R.: Laboratory comparisons of fresh-water and salt-water whitecapes. J. Geophys. Res., 74, 6961–6966, 1969.

Mueller J.A., and Veron F.: Nonlinear Formulation of the Bulk Surface Stress over Breaking Waves: Feedback Mechanisms from Air-flow Separation. Boundary-Layer Meteoro., 130(1): 117–134, doi 10.1007/s10546-008-9334-6, 2009.

Nightingale, P.D., Malin, G., Law, C.S., Watson, A.J., Liss, P.S., Liddicoat, M.J., Boutin J., and Upstill-Goddard R.C.: In situ evaluation of air-sea gas exchange using novel conservative and volatile tracers, Global Biogeochem. Cycles, 14, 373–387, 2000.

Rhee, T.S., Nightingale, P.D., Woolf, D.K., Caulliez, G., Bower, P., and Andreae M.O.: Influence of energetic wind and waves on gas transfer in a large wind-wave tunnel facility, J. Geophys. Res., 112, C05027, doi:10.1029/2005JC003358, 2007.

Saltzman, E. S., King, D. B., Holmen, K., and Leck C.: Experimental determination of the diffusion coefficient of dimethylsulfide in water, J. Geophys. Res., 98, 16,481–16,486, 1993.

Smith, S. D.: Coefficients for sea surface wind stress, heat flux, and wind profiles as a function of wind speed and temperature, J. Geophys. Res., 93, 15,467–15,472, 1988.

Soloviev, A. and Schlüssel P.: Parameterization of the cool skin of the ocean and of the air-ocean gas transfer on the basis of modeling surface renewal. J. Phys. Ocean., 24, 1339–1346, 1994.

Soloviev, A.V., Schlüssel P.: Evolution of cool skin and direct air-sea gas transfer coefficient during daytime, Boundary-Layer Meteoro., 77, 45–68, 1996.

Wanninkhof, R.H.: Relationship between wind speed and gas exchange over the ocean, J.Geophys. Res., 97, 7373-7382, 1992.

Wanninkhof, R.H., Asher, W.E., Ho, D.T., Sweeney, C., McGillis W.R.: Advances in Quantifying Air-Sea Gas Exchange and Environmental Forcing, Annual Review of Marine Science 1 2009, 213–244, 2009.

Wanninkhof, R., and McGillis, W.R.: A cubic relationship between air-sea CO2 exchange and wind speed, Geophys. Res. Lett., 26(13), 1889-1892, 1999.

Woolf, D. K: Bubbles and their role in gas exchange, in The Sea Surface and Global Change, edited by R. Duce and P. Liss, pp. 173–205, Cambridge Univ. Press, NY, 1997.

Yang, M., Blomquist, B.W., and Huebert B.J.: Constraining the concentration of the hydroxyl radical in a stratocumulus-topped marine boundary layer from sea-to-air eddy covariance flux measurements of dimethylsulfide, Atmos. Chem. Phys., 9, 9225–9236, 2009.

# Chapter 3. Oxidation of DMS by the Hydroxyl Radical

This chapter is published in the journal *Atmospheric Chemistry and Physics* in 2009 with the following complete citation: Yang, M., Blomquist, B., and Huebert, B.: Constraining the concentration of the hydroxyl radical in a stratocumulus-topped marine boundary layer from sea-to-air eddy covariance flux measurements of dimethylsulfide, *Atmos. Chem. Phys.*, 9, 9225-9236, 2009. The article may be found at http://www.atmos-chem-phys.org/9/9225/2009/acp-9-9225-2009.html.

## Abstract

The hydroxyl radical (OH) is an important oxidant in the troposphere due to its high reactivity and relative abundance. Measuring the concentration of OH in situ, however, is technically challenging. Here we present a simple method of estimating an OH-equivalent oxidant concentration ("effective OH") in the marine boundary layer (MBL) from the mass balance of dimethylsulfide (DMS). We use shipboard eddy covariance measurements of the sea-to-air DMS flux from the Vamos Ocean-Cloud-Atmosphere-Land Study Regional Experiment (VOCALS-REx) in October and November of 2008. The persistent stratocumulus cloud-cover off the west coast of South America and the associated strong inversion between MBL and the free troposphere (FT) greatly simplify the dynamics in this region and make our budget estimate possible. From the observed diurnal cycle in DMS concentration, the nighttime entrainment velocity at the inversion is estimated to be 4 mm $sec^{-1}$. We calculate 1.4(±0.2) x $10^6$ OH molecules $cm^{-3}$ from the DMS budget, which represents a monthly effective concentration and is well within the range of previous estimates. Furthermore, when

linearly proportioned according to the intensity of solar flux, the resultant diel OH profile, together with DMS surface and entrainment fluxes, enables us to accurately replicate the observed diurnal cycle in DMS (correlation coefficient over 0.9). The nitrate radical ($NO_3$) is found to have little contribution to DMS oxidation during VOCALS-REx. An upper limit estimate of 1 pptv of bromine oxide radical (BrO) would account for 30% of DMS oxidation and lower the OH concentration to $1.0 \times 10^6$ OH molecules $cm^{-3}$. Our effective OH estimate includes the oxidation of DMS by such radicals.

### 3.1 Introduction

While non-reactive towards the major constituents of the atmosphere, the hydroxyl radical (OH) is the principal oxidizing free radical in the troposphere for trace species (Levy, 1971). The primary source of OH is the reaction between water vapor and excited atomic oxygen ($O(^1D)$); the latter is a product of the photo-dissociation of ozone ($O_3$) by photons between 290 and 320 nm. Reduction of the hydroperoxy radical ($HO_2$) by nitrogen oxide (NO), and to a lesser degree by $O_3$, contributes to the recycling of OH (Donahue and Prinn, 1990). OH reacts readily with most trace gases and is often regenerated during the process, resulting in sustained OH concentrations on the order of $10^6$ molecules $cm^{-3}$ globally (Prinn et al., 1995; Spivakowsky et al., 2000). The radical is consumed primarily by reacting with carbon monoxide (CO), but it also reacts with sulfur dioxide ($SO_2$), nitrogen dioxide ($NO_2$), and a wide range of hydrocarbons. Models predict higher OH concentrations for the tropics and for the southern hemisphere. The former is attributed to higher humidity and solar fluxes that promote $O_3$ dissociation; the

latter is presumably due to less CO south of the equator (a result of lower anthropogenic emissions; Seinfeld and Pandis, 2006).

Due to the transient nature of the radical, measuring OH in situ was not possible until the last two decades, when specialized instruments based on absorption, fluorescence, and mass spectroscopy were developed (e.g. Mount, 1992; Hard et al., 1984; Eisele and Tanner, 1991). However, direct observations of this radical cannot be made in all field experiments (such as during VOCALS-REx). Even when in situ OH measurements are available, they might not represent a temporal or regional average, which is of importance to large-scale models.

Alternatively, global and regional distributions of OH are often estimated by measuring chemicals with known lifetimes that are exclusively consumed by this radical, such as methyl chloroform (Prinn et al., 1992). Here we follow a similar approach and use a budget analysis of naturally-derived atmospheric dimethylsulfide (DMS) to constrain the equivalent OH concentration in a clean, stratocumulus-capped marine boundary layer.

Dimethylsulfide ($CH_3SCH_3$) in the open ocean ($DMS_w$) is derived exclusively from phytoplankton. Due to photochemical destruction and rapid dilution, the atmospheric concentration of DMS is always orders of magnitude lower than the expected Henry's law equilibrium concentration with $DMS_w$. Consequently, DMS gas always effluxes from the surface ocean and is the largest source of reduced sulfur to the atmosphere (Lovelock et al., 1972). The substantial magnitude of the flux and the lack of other sources make DMS an ideal gas with which to study air-sea exchange. In the atmosphere, DMS is principally oxidized by OH to form $SO_2$, dimethylsulfoxide

(DMSO) and methane sulfonic acid (MSA). $SO_2$ may be oxidized further to form sulfate, which contributes to aerosol growth and formation of cloud condensation nuclei (CCN). The coverage and lifetime of marine clouds formed from these CCN affect the earth's radiative balance and may in turn be linked to biological production in the ocean (Charlson et al., 1987; Kloster et al., 2006).

The oxidation of DMS by OH proceeds through two separate pathways: the hydrogen-atom abstraction at a methyl group that subsequently leads to mostly $SO_2$:

$$CH_3SCH_3 + OH\cdot \xrightarrow{k1} CH_3SCH_2\cdot + H_2O \quad (3.1)$$

and the OH addition to the sulfur atom that can lead to a wider range of products, including DMSO and MSA:

$$CH_3SCH_3 + OH\cdot \xrightarrow{k2} CH_3\dot{S}(OH)CH_3 \quad (3.2)$$

The abstraction pathway is favored under high temperatures; the Arrhenius form for this rate constant is $k_1 = 1.1 \times 10^{-11} \exp(-240/T)$, equating to $4.9 \times 10^{-12}$ $cm^3$ $molec^{-1}$ $sec^{-1}$ at 298 K. The addition pathway is favored under low temperatures; this oxygen ($O_2$) and temperature dependent rate constant is best represented by $k_2 = 1.0 \times 10^{-39} [O_2] \exp(5820/T) / \{1+5.0 \times 10^{-30} [O_2]\exp(6280/T)\}$ (Sander et al., 2006). At 298 K, about 80% of the oxidation of DMS goes through the abstraction pathway; the two pathways are about equal at 285 K (Stickel et al., 1993, Wallington et al., 1993).

Other oxidants, including nitrate and halogen radicals, may also consume DMS. The nitrate radical ($NO_3$) is produced from the reaction between $NO_2$ and $O_3$. The DMS-$NO_3$ reaction is several times slower than the DMS-OH reaction. Unlike OH, $NO_3$ can only have an appreciable concentration at night because it is photolyzed rapidly during the day. Studies from Equatorial Christmas Island showed that in the remote Pacific, the

contribution to DMS loss from $NO_3$ is less than a few percent due to the low levels of $NO_x$ ($NO + NO_2$) away from anthropogenic activities (Davis et al., 1999; Chen et al., 2000). The same studies also suggested that the DMS-chlorine reaction, while still very poorly understood, accounts for no more than 5~10% to the oxidation of DMS. Other authors (e.g. Sciare et al., 2000) have found OH and $NO_3$ to be inadequate in explaining their observed DMS losses, and speculated that the naturally derived bromine oxide (BrO) might be another significant DMS oxidant.

The aforementioned Christmas Island experiments demonstrated a clear diurnal cycle of DMS in the MBL (Bandy et al., 1996; Davis et al., 1999). While the supply of DMS to the boundary layer via air-sea exchange is continuous, destruction of DMS principally takes place during the sunlit hours, when OH is available. As a result, DMS starts to increase from its daily minimum just before sunset and builds up through the night until just after sunrise, at which time photolysis causes DMS to decrease until the next cycle. This diurnal cycle in DMS can be altered in a pollution-influenced marine environment where anthropogenically produced $NO_x$ level is higher, as nighttime oxidation of DMS by $NO_3$ can be comparable in magnitude to daytime oxidation by OH (Yvon et al., 1996).

The equivalent OH we estimate here from VOCALS-REx is an effective concentration, the concentration of OH that would cause the same rate of DMS loss as if OH were the only oxidant. In all likelihood, our effective OH is slightly higher than the actual OH concentration, since it includes minor contributions from the other oxidants.

The VOCALS-REx experiment took place in October and November of 2008 in the Southeast Pacific, off the west coast of Chile and Peru

(http://www.eol.ucar.edu/projects/vocals/). The experiment aimed to address the interactions among the ocean, atmosphere, and clouds in this tightly coupled regional climate system. The Andes mountain range to the east forces strong winds parallel to the coast. Ekman transport results in coastal upwelling of cold, nutrient-rich waters, which leads to stability in the lower troposphere. The warm, dry air over the cool water surface, together with the large-scale subsidence from the Hadley Cell, creates a widespread and persistent stratocumulus cloud deck (Bretherton et al., 2004). These thin, low-lying, and hence radiatively-cooling clouds form from CCN aerosols. While anthropogenic emissions dominate the coastal region, a significant fraction of CCN likely originates from DMS-derived sulfate in the clean marine environment offshore. From time to time, hundred-kilometer sized openings (which can be observed from satellites) form in the stratocumulus cloud-deck and advect with the mean wind. These features have been coined "pockets of open cells" (POCs) and are hypothesized to be related to removal of CCN by drizzle from the air (Stevens et al., 2003). To further our understanding in this phenomenon, we need to look at the origin and fate of the CCN-precursors, including DMS and its oxidants.

A stratocumulus marine boundary layer is characterized by vigorous mixing due to the intense longwave radiative cooling at the cloud-top (Lilly 1968). Air entrains down from the FT, which is balanced by a deepening of the MBL and wind divergence. The strong inversion in effect caps the MBL, confining surface-borne scalars like DMS. Therefore, a stratocumulus region such as the Southeast Pacific can be viewed as a natural analog to a box model, with clearly defined inputs and outputs. These simplified conditions enable us to estimate the effective OH concentration from mass balance.

### 3.2 Experimental and Methods

The National Oceanographic and Atmospheric Administration (NOAA) ship *Ronald H. Brown (RHB)* was deployed in the Southeast Pacific from approximately October 24$^{th}$ to November 30$^{th}$, 2008. In addition to retrieving and maintaining the Woods Hole Oceanographic Institute's Stratus buoy at 85°W and 20°S, a number of E-W transects were made at latitudes between 18.5°S and 21.5°S to survey eddies and upwelling features. The edges of such eddies are often associated with higher levels of biological productivity, hence more $DMS_w$ (T. Bates, P. Matrai: unpublished data). In the same general time frame, multiple aircraft, including the National Science Foundation (NSF)/National Center for Atmospheric Research (NCAR) C-130, repeatedly flew westward from its base station in Arica, Chile to the stratocumulus region offshore. The anthropogenic influence was minimal away from the coast, with average CO, $O_3$, and $SO_2$ concentrations of 65 ppbv, 30 ppbv, and 25 pptv, respectively, typical of a clean MBL. Most of the research flights were designed to survey the 20°S cross-section and study the formation and development of POCs.

During the experiment, two nearly identical atmospheric pressure ionization mass spectrometers (APIMS) were used to measure DMS on board of *RHB* and the C-130, the distinction being that the instrument at sea was sampling at a high rate of 20 Hz to quantify the sea-to-air flux, whereas the one aloft was measuring concentration every 10 seconds. The measurement of DMS by the APIMS with isotopically labeled standard technique has been described previously (Bandy et al., 2002; Huebert et al., 2004;

Blomquist et al., 2006). Most recently, Blomquist et al. (2009) discussed in great details about the instrument setup, flux processing, data refinement, and uncertainty estimates.

We estimate the OH-equivalent oxidant concentration from the budget analysis of DMS. The conservation equation for any chemical species, *S*, in the marine boundary layer is represented as (with the overbar representing an average in time/space):

$$\frac{\partial \overline{S}}{\partial t} + \overline{u}\frac{\partial \overline{S}}{\partial x} + \frac{\partial \overline{S'w'}}{\partial z} = P - L \qquad (3.3)$$

The first term on the left represents the time rate of change in the concentration of *S*. The second term is the horizontal advection of *S* due to gradients along the mean wind (*u*). The third term is the flux divergence, the difference between vertical fluxes at the bottom and top of the box model. Local (chemical) production and loss of *S* are represented by *P* and *L*, respectively, on the right side of the conservation equation.

As described in the previous section, DMS fluxes upwards from the surface ocean to the stratocumulus-topped MBL, where it is oxidized (principally by OH), diluted by DMS-free air entrained from the FT, and transported horizontally. DMS is not produced chemically, so $P = 0$. Therefore the chemical loss due to oxidation can be calculated by closure if we know the DMS surface flux, entrainment flux, horizontal advection, and the time rate of change.

### *3.2.1 Surface Flux of DMS*

On the ship, the inlet of our mass spectrometer was located at 18 m above the water surface on the jackstaff, where flow-distortion due to the ship's superstructure is minimized. A precisely known amount of the triply-deuterated DMS standard was continuously injected at the inlet and combined with a high ambient air flow. The DMS

concentration was determined from the ratio between the ambient and standard DMS mass spectrometer signals. Relative wind speeds, acceleration, and rotation in three axes were recorded at the same frequency as the DMS by a Gill Sonic anemometer and a Systron-Donner Motionpak accelerometer, respectively. Ship's motion was removed from relative winds to get true winds following Edson et al., (1998). To obtain surface flux ($F_0$) via eddy covariance, DMS concentration was correlated with the vertical wind velocity ($w$) in the form of $F_0 = \overline{DMS'w'}$ (primes here denote deviations from the means). Flux was initially computed in ten-minute segments that overlapped by 50%. To remove times when sampling conditions were unfavorable, any ten-minute segment with relative wind direction more than 90 degrees off the bow or gyro heading changing by over 10 degrees (ship maneuvering) was screened out. The remaining "good" segments were averaged to hourly values.

Time-series of 18-m DMS concentration and flux from the *RHB* are shown in Fig. 3.1, with campaign means (±standard deviations) of 57±(26) pptv and 3.4 (±1.9) μmoles $m^{-2}$ $day^{-1}$, respectively. Also shown are true wind speed and direction from the sonic anemometer at the same height. The wind direction hardly varied, almost always coming from the South/Southeast (150°). We limit our averaging to offshore observations only (73°W ~ 86°W and 18°S ~ 22°S, hereinafter 'the VOCALS region'). Near-shore data were not included in the averaging due to anthropogenic influence as well as heterogeneities in the atmospheric DMS field caused by spikes in $DMS_w$ on the edges of localized coastal eddies.

Even with the ship steaming at up to 12 knots, the classic sinusoidal diurnal cycle in DMS is clearly visible on a number of days (Fig. 3.2). This observation implies a

widespread horizontal homogeneity over the region with limited meso-scale variability. Continental influence, which is usually associated with high levels of $NO_x$, and thus high $NO_3$, was minimal.

*3.2.2 Boundary Layer Structure*

We determined the boundary layer structure during VOCALS-REx from shipboard radiosonde launches every six hours. Figure 3.3 shows a time series of temperature contours from the soundings, with the dark line indicating the inversion immediately above the stratocumulus cloud deck. Over the course of more than a month, the structure of the MBL was relatively constant, with an average temperature of 13˚C. In addition to radiosondes, a W-band radar (24 m range gate, 50 m pulse length) from the ship measured cloud top height continuously. On average, the stratocumulus cloud top varied from ~1350 m near dawn to ~1200 m near dusk, suggesting a greater entrainment rate in the nighttime. Inversion heights determined from radiosondes are nearly identical with the cloud top estimates from the W-band radar (S. de Szoeke, personal communication).

We used DMS concentration from the C-130 aircraft ($DMS_{C130}$) to infer the distribution of the scalar within the MBL and exchange with the FT. Figure 3.4 shows a typical profile of the lower troposphere during VOCALS-REx. $DMS_{C130}$ decreased gradually with altitude within the MBL and rapidly dropped to near-zero above the stratocumulus cloud-top in the FT. Across the thin inversion layer of only a few tens of meters, the changes in dew point and potential temperature were usually of the order of 20 and 10 K, respectively.

When the MBL is shallow and well mixed, scalars with long lifetimes are thought to be homogeneously distributed vertically. DMS in the boundary layer is emitted from the ocean surface and diluted by entrainment above; with a mixing time in the MBL (~1 hour) much shorter than its lifetime (1~2 days, estimated later), DMS concentration at the top of the MBL is usually only a few pptv lower than at the surface (Faloona et al., 2005). However, this difference was more significant in the VOCALS region, where the average inversion height was 1.3 km. Figure 3.5 shows the mean profile from the C-130 during the campaign. Altitude was normalized to the inversion height ($z_i$). $DMS_{C130}$ aloft was normalized to the concentration from the lowest leg at ~30 m ($DMS_{C130,0}$). On average, $DMS_{C130}$ immediately below the inversion was ~80% of the concentration near the surface, exhibiting a linear decrease with height. We linearly regressed $DMS_{C130}/DMS_{C130,0}$ against $z/z_i$ in the MBL ($r^2 = 0.8$). The fraction of DMS at height $z$ relative to the surface value can then be parameterized as $1 - \alpha (z/z_i)$, where $\alpha = 0.2$ represents the "decoupling" parameter. This formulation of the MBL structure is similar to what is used in Wood and Bretherton (2004).

*3.2.3 Advective Flux of DMS*

In VOCALS-REx, DMS concentration and flux measured from the ship show increasing trends away from the coast due to generally greater $DMS_w$ concentration and higher wind speeds offshore (Fig. 3.6). The ratio between DMS flux and concentration, however, was nearly constant with longitude. Bin-averaged inversion heights from radiosondes and 18-m wind speeds within the latitude range of 20±2°S are also plotted on

the same figure. The boundary layer was deeper offshore (~1.5 km at 85°W) than at the coast (~1.1 km), as is typical of this region.

We estimated the advective flux of DMS from the horizontal gradient computed from shipboard DMS concentration. Using multi-variate linear regression, DMS averaged to daily means (to remove diel variability) was regressed against Lat and Lon. The fitting coefficients were -2 pptv °Lon$^{-1}$ and -1 pptv °Lat$^{-1}$, with higher DMS towards the West/Southwest (Fig. 3.7). For an average wind speed of 6 m sec$^{-1}$ from 150°, multiplying the zonal and meridional winds (-3 and 5 m sec$^{-1}$, respectively) by the DMS gradient gave an advection of 0.04 pptv hr$^{-1}$. Integrating over the 1.3 km column led to an advective flux of only 0.05 μmoles m$^{-2}$ day$^{-1}$, less than 1% of the DMS sea-to-air flux. Advection was small because the mean wind direction was largely orthogonal to the horizontal DMS gradient; we set it to zero hereafter.

*3.2.4 Entrainment Velocity*

To calculate the entrainment flux of DMS, we need to know the entrainment velocity ($\omega_e$) at the inversion. While $\omega_e$ was not directly measured during VOCALS-REx, we can estimate it from the observed nighttime increase in shipboard DMS concentration. To account for the dilution effect from changing MBL depth, we integrate DMS concentration from the ship to the depth of MBL using the vertical gradient determined from Section 2.2, resulting in column concentration, $\langle DMS \rangle$, in units of μmoles m$^{-2}$.

The vertically integrated form of (3.3) is shown in (3.4), with the advection and production terms now dropped out. Now every term is in units of flux:

$$\frac{\partial\langle\overline{DMS}\rangle}{\partial t} = F_0 - \omega_e(DMS_{z_i^-} - DMS_{z_i^+}) - k_{PFO}\langle\overline{DMS}\rangle \quad (3.4)$$

The term on the left side of (3.4) is the time rate of change. The last term on the right represents the local loss of DMS, which has been expanded to the product of $k_{PFO}$ (a pseudo first order reaction rate constant) and DMS column concentration. We have separated flux divergence into the first and second terms on the right hand side of (3.4), representing the DMS fluxes at the ocean surface and inversion, respectively. The entrainment flux is formulated as the entrainment velocity, $\omega_e$, multiplied by the concentration jump across the inversion (Lilly, 1968), with subscripts $z_i^-$ and $z_i^+$ denoting just below and above $z_i$. The concentration just below the inversion can be approximated from the 18-m concentration by the fraction (1 - $\alpha$). Taking the concentration above the inversion to be zero, (3.4) thus simplifies to:

$$\frac{\partial\langle\overline{DMS}\rangle}{\partial t} = F_0 - \omega_e(1-\alpha)DMS - k_{PFO}\langle\overline{DMS}\rangle \quad (3.5)$$

The nighttime build up of DMS column concentration appears to be linear with time (Fig. 3.8). The slope over these hours approximately represents the time rate of change in ⟨DMS⟩, which includes the flux divergence plus any nocturnal chemical loss. There is no OH at night, and we assume the $NO_3$ reaction to be insignificant (this assumption is validated in the last section); the loss term thus drops out. From hour 1 to 10 UTC (or 20:00 to 05:00 local time), we calculated a time rate of change in ⟨DMS⟩ of 2.6 μmoles $m^{-2}$ $day^{-1}$. The mean nighttime surface flux obtained by eddy covariance was 3.2 μmoles $m^{-2}$ $day^{-1}$. The nighttime entrainment flux thus needs to be 0.6 μmoles $m^{-2}$ $day^{-1}$ to balance the budget, requiring $\omega_e$ = 4 mm $sec^{-1}$.

The entrainment velocity derived above is only a nighttime value, and might not be representative of the climatological mean since there was possibly diurnal modulation of the inversion height. Shortwave heating of cloud top stabilizes the MBL and tends to reduce entrainment during the day, while longwave cooling at night may enhance entrainment. Off the coast of California, where stratocumulus clouds are also prevalent, eddy covariance flux measurements of three conserved scalars (DMS, $O_3$, and total water) immediately above and below the inversion indicated a range of 1.2~7.2 mm $sec^{-1}$ for $\omega_e$, with higher values at night (Faloona et al., 2005). Using a mixed-layer approach, Caldwell et al. (2005) found a 6-day average $\omega_e$ of 4±1 mm $sec^{-1}$ during the East Pacific Investigation of Climate (EPIC) stratocumulus cruise in 2001. Combining satellite observations with National Centers for Environmental Prediction (NCEP) reanalysis, Wood and Bretherton (2004) determined an $\omega_e$ of 2~6 mm $sec^{-1}$ in the tropical and subtropical east Pacific, with a likely value of 4 mm $sec^{-1}$ in the VOCALS region. While our estimated nighttime $\omega_e$ could theoretically be an over-estimate of the diurnal average, 4 mm $sec^{-1}$ appears to be a reasonable value compared to previous results. We show later that our calculated effective OH concentration is not very sensitive to the choice of $\omega_e$, because reaction with OH represents a far greater removal term for DMS than dilution due to entrainment. At the limit of zero for $\alpha$ (i.e. no decoupling in DMS), $\omega_e$ is lowered to 3 mm $sec^{-1}$, still within the range of previous estimates.

### *3.2.5 Estimating Effective OH*

From the clear diurnal cycles and near-constant flux to concentration ratio in the project averages (Fig. 3.2 and Fig. 3.6), diurnally averaged DMS field in the MBL

appears to be approximately constant in space and time over the duration of the project. We thus assume DMS to be in a steady-state on that scale.

For the purpose of this derivation we first assume that the oxidation of DMS is solely due to reactions with OH. The pseudo first-order rate constant $k_{PFO}$ in (3.5) is expressed as $k_{OH}$, the total second order rate constant of the DMS-OH reaction ($k_{OH} = k_1 + k_2$), multiplied by the concentration of OH. With an average MBL temperature of 13˚C during VOCALS-REx, we calculate $k_{OH}$ to be 7.9 x $10^{-12}$ $cm^3$ $molec^{-1}$ $sec^{-1}$, with the abstraction pathway accounting for 60% of the total oxidation.

Rearranging and expanding (3.5) with no time rate of change leads to:

$$OH = \frac{F_0 - \omega_e(1-\alpha)DMS}{\left\langle \overline{DMS} \right\rangle k_{OH}} \tag{3.6}$$

Using $\omega_e$ = 4 mm $sec^{-1}$ and $\alpha$ = 0.2, we find an effective OH concentration of 1.4 x $10^6$ molec $cm^{-3}$ for VOCALS-REx, somewhat higher than the estimated global average possibly due to high water content and solar radiation and low anthropogenic influence in this region. From PEM-Tropics A and B, which took place during September/October of 1996 and March/April of 1999, respectively, Olsen et al. (2001) showed that OH ranged from 1.4~1.8 x $10^6$ molec $cm^{-3}$ in the latitude range of 10S~30S and in the lowest 2 km, with higher values in the austral spring. The PEM-Tropics experiments did not extend into the stratocumulus region, however, where solar flux is lowered by 10~20% relative to the normal trade wind cumulus regime. An effective OH concentration of 1.4 x $10^6$ molec $cm^{-3}$ implies a lifetime of 1.1 days for DMS with respect to OH in the MBL, well within the range of previous estimates of 0.5~2 days (e.g., Wine et al., 1981; Hynes et al., 1986).

Allowing for a substantial uncertainty of ±2 mm $sec^{-1}$ in the entrainment velocity

(due to diel variability, for example), the relative error in the calculated OH concentration is only ~12% because dilution due to entrainment is small compared to photochemical loss. The potential of $\omega_e$ being biased high implies that our calculated OH might be an underestimate (though this could be partially compensated by the our assumption that OH is the only DMS oxidant). At a limit of $\alpha = 0$, OH is lowered to $1.2 \times 10^6$ molec $cm^{-3}$. The uncertainties in the inversion heights from radiosoundes and the W-band were about 25 m (S. de Szoeke, personal communication, 2009). Assuming an absolute uncertainty of 2 mm $sec^{-1}$ for $\omega_e$ and 0.1 for $\alpha$, the propagated absolute uncertainty for the equivalent OH concentration is ~0.2 molecules $cm^{-3}$, or 15%. One apparent benefit of estimating OH from the DMS flux and concentration is that both measurements are made by the same instrument; any calibration uncertainty in the instrument (such as flow rate or standard concentration) is thus negated, not affecting the final outcome.

### 3.3 Discussion

The above OH estimate is an average value over a month. In reality, OH is only produced during the day when photochemistry is possible; the radical is consumed completely when there is no light. The next logical step is to approximate the diel variation in OH, which has pronounced impacts on the cycling of sulfur species in the MBL, from DMS to $SO_2$ to sulfate.

#### *3.3.1 Diel Variability in OH*

To approximate the diel profile of OH, we need to know the sources and sinks of the $HO_x$ (OH + $HO_2$) system because the OH : $HO_2$ ratio is usually a steady-state constant

(Faloona et al. 2000). To a first order, the availability solar flux, and hence the ozone photolysis frequency, $JO(^1D)$, limits OH production since the subsequent reaction between $O(^1D)$ and water vapor is rapid. OH can also be recycled from $HO_2$ by reaction with NO and $O_3$. As for the sinks of $HO_x$, both the self-reaction of $HO_2$ and OH + $HO_2$ (when $NO_x$ is low) represent quadratic loss in $HO_x$. In a high $NO_x$ environment, the OH + $NO_2$ reaction is the major sink and a linear loss for $HO_x$.

We can approximate the dependence of steady-state OH concentration on solar flux as $JO(^1D)^b$, with the exponent *b* being $NO_x$-dependent. When $NO_x$ is high, OH relates linearly to $JO(^1D)$ because $HO_2$ becomes less important (e.g. Holland et al., 1998). When $NO_x$ is low, OH is formed by the reaction with water vapor as well as from recycling of $HO_2$ by $O_3$ (and NO, if any), while the loss of $HO_x$ is largely quadratic. Overall *b* likely takes on a value between 0.5 and 1. Berresheim et al. (2003) found that $b = 0.68$ off the coast of Crete in the Mediterranean, where the mean $NO_2$ mixing ratio was 0.4 ppbv. While there was no direct measurements of $NO_x$ during VOCALS-REx, in situ observations from 10S~30S during PEM-Tropics A and B yielded 5~10 pptv of $NO_x$ in the lowest 2 km (Olson et al., 2001). Schultz et al. (1999) showed that in the tropical South Pacific, the median $NO_x$ level was only 4 pptv in the lowest 2 km. Thus VOCALS likely falls in the low $NO_x$ regime and one may expect *b* to be less than 1.

We first binned solar flux measured by the shipboard radiometer in the VOCALS region to the time of day, which expectedly resulted in a smooth curve with peak insolation at ~17:00 UTC. Not knowing the exact value of *b*, hourly hydroxyl concentrations ($OH_t$) were proportioned as linear and square root functions of the solar flux, with the diel average of the radical constrained by $1.4 \times 10^6$ molecules $cm^{-3}$. The

radical peaked at ~5 x $10^6$ molecules $cm^{-3}$ in the linear case and ~4 x $10^6$ molecules $cm^{-3}$ in the square root case (with a broader distribution). While this method seems rather simplistic compared to photochemical models containing many photoactive species, the general shape of our derived diel OH profile agrees fairly well with previous direct observations in the tropical/subtropical Pacific basin (e.g. Davis et al., 2001; Mauldin et al., 2001). As another comparison to our effective OH estimate from DMS, we use photolysis rates of $O_3$ and hydrogen peroxide ($H_2O_2$) predicted from the NCAR Tropospheric Ultraviolet and Visible (TUV) Radiation Model (http://cprm.acd.ucar.edu/Models/TUV/), reaction rate between $O_3$ and $HO_2$, and destruction rate due to CO, methane, hydrogen gas, $O_3$, $H_2O_2$, and $HO_2$ from Sander et al. (2006) to calculate the expected OH concentration. The TUV estimates photolysis rates based on time, latitude, longitude, and oxidant field, and accounts for clouds and aerosol scattering using climatological reflectivity from the Total Ozone Mapping Spectrometer (TOMS). The model yielded a noontime OH concentration of ~6 x $10^6$ molecules $cm^{-3}$, which is ~20% higher than our daytime peak in the linear scenario but likely within the range of uncertainties.

*3.3.2 Reproducing the Diurnal Cycle of DMS*

The oxidation of DMS in the atmosphere has been modeled previously given an estimate of OH (Shon et al., 2001; Nowak et al., 2001). Using a similar approach and building upon (3.5), the surface DMS concentration at time *t* can be written as:

$$\left\langle \overline{DMS} \right\rangle_t = \left\langle \overline{DMS} \right\rangle_{t-1} + F_{0,t-1} - \omega_e (1-\alpha) DMS_{t-1} - k_{PFO,t-1} \left\langle \overline{DMS} \right\rangle_{t-1} \quad (3.7)$$

For simplicity, we used the average $\omega_e$ of 4 mm $sec^{-1}$, neglecting any potential diel variation in the entrainment velocity. The implied DMS diurnal variation is not very sensitive to the choice of $\omega_e$ for the same reason as in Section 2.5.

We first equated, $k_{PFO,t}$, the pseudo first order reaction rate constant of DMS, simply to $k_{OH}$ $OH_t$, with $OH_t$ being the time-dependent radical concentration calculated from Section 3.1. Figure 3.9(a) shows the diel cycle of OH approximated as a linear function of solar flux, DMS column concentration calculated from (3.7), as well as the observation. Figure 3.9(b) shows the same calculation except OH was approximated as a square root function of solar flux. It is apparent that the calculated DMS agrees closer with the observation when the dependence on solar flux, and hence $JO(^1D)$, is linear. In the square root case, implied DMS does not decrease as rapidly as observed after sunrise because the OH distribution is too broad. The linear dependence might come as a surprise given the expectedly low level of $NO_x$; this might be due to chemistry that are not considered or well understood. In the next section we explore the importance of nitrate and bromine oxide radicals in DMS oxidation, and see whether we can further improve the fit to the observed diurnal cycle.

### *3.3.3 DMS Oxidation by $NO_3$ and BrO*

The rate constant of the DMS-$NO_3$ reaction can be represented by $k_{NO3} = 1.9 \times 10^{-13} \exp(500/T)$, giving $1.0 \times 10^{-12}$ $cm^3$ $molec^{-1}$ $sec^{-1}$ at 298 K (Sander et al., 2006). Studies from Allan et al. (2000) in the relatively clean MBL at Mace Head suggested that the nocturnal level of the nitrate radical hovers on the order of a pptv, with reaction with

DMS being its most important loss mechanism. Platt and Heintz (1994) estimated a globally averaged concentration of 3 pptv for $NO_3$.

Uncertain about how much $NO_3$ was present in the Southeast Pacific, we apportioned the total oxidative loss of DMS to fractions due to $NO_3$ and OH′ (the prime denotes the 'actual' OH concentration, assuming a linear dependence on solar flux). For example, if 10% of DMS oxidation was due to $NO_3$, the ratio between diurnal averaged $k_{NO3}$ $NO_3$ and $k_{OH}$ OH′ should be 1:9. To crudely mimic the diel variation in $NO_3$, we assume its nighttime level to be twice the diurnal average and the daytime concentration to be zero. In reality, $NO_3$ might not achieve steady-state through out the night (Allan et al., 2000). We arrived at the closest least-square fit between observed and calculated DMS (correlation coefficient exceeding 0.9) when 99% of DMS oxidation is due to OH, as any additional $NO_3$ would degrade the fit; this corresponds to less than 0.005 pptv of $NO_3$. In all likelihood, low levels of $NO_x$ and $O_3$ were limiting the production of $NO_3$ during VOCALS-REx.

The rate constant of the DMS-BrO reaction can be represented by $k_{BrO} = 1.4 \times 10^{-14} \exp(950/T)$, yielding $3.4 \times 10^{-13}$ $cm^3$ $molec^{-1}$ $sec^{-1}$ at 298 K (Sander et al., 2006). Read et al. (2008) measured BrO with differential optical absorption spectroscopy (DOAS) at Cape Verde in the tropical Atlantic Ocean. They found an average BrO concentration over 2 pptv during the day and zero at night, with a diurnal profile resembling a 'top hat' distribution.

During VOCALS-REx, with a similar DOAS technique, no significant BrO was detected, with ~1 pptv being the upper limit daytime peak concentration (R. Volkamer, personal communication, 2009). The same instrument also detected ~1 pptv of iodine

oxide (IO), a level insignificant towards DMS oxidation due to its much lower reactivity. If we crudely approximate the diurnal profile of BrO with a square root dependence on solar flux, 1 pptv of daytime maximum BrO implies a diel average concentration just under 0.4 pptv. This upper limit concentration of BrO would account for ~30% of total DMS oxidation; the OH concentration would then need to be reduced to $1.0 \times 10^6$ molecules $cm^{-3}$. The shape of implied DMS from (3.7) with this allocation of oxidants is not significantly different from what is shown in Fig. 3.9(a). Therefore from the implied DMS diurnal cycle alone, it is difficult to assess whether 1 pptv of BrO is too high. Our OH-equivalent oxidant concentration may still include other DMS oxidants, such as $NO_3$ and BrO.

### 3.4 Conclusions

We have demonstrated that a month-long average OH-equivalent oxidant concentration in a stratocumulus-capped marine boundary layer can be derived from the sea-to-air flux and concentration of DMS measured from a ship with a simple mass balance method. From aircraft profiles during VOCALS-REx, DMS concentration appeared to decrease linearly with altitude in the MBL due to decoupling. On average, DMS immediately below the inversion was ~80% of the surface concentration. DMS concentration in the MBL displayed the classic sinusoidal diurnal cycle, in which daily maxima and minima were found to be just after sunrise and just before sunset, respectively, as a result of the continuous build up via air-sea exchange and daytime consumption by photochemistry. From the nighttime build up of DMS column concentration, we estimated an entrainment velocity of 4 mm $sec^{-1}$ from the difference

between the time rate of change and the observed surface flux. The advective flux of DMS was found to be insignificant because the horizontal gradient in DMS was largely perpendicular to the mean wind direction. The calculated OH concentration of 1.4 (±0.2) x $10^6$ molecules $cm^{-3}$ from the DMS budget equation agrees well with previous estimates, and represents a regional OH-equivalent oxidant concentration. Actual OH will be less by the extent that other DMS oxidants, such as nitrate- and halogen- radicals, react with DMS. The applicability of this approach of estimating the equivalent-OH concentration hinged on the stationarity and horizontal homogeneity of the region over a long enough time scale. Areas with much greater mesoscale variability or additional source and sink terms will complicate the budget analysis.

We fitted the OH-equivalent oxidant concentration as both linear and square root functions of the observed solar flux averaged to the time of day. Using the resultant diel profiles in OH, the mean observed DMS surface flux, and an entrainment velocity of 4 mm $sec^{-1}$, we were able to accurately replicate the observed diurnal cycle of DMS in the MBL. Despite the expected low $NO_x$ concentration, a linear relationship between OH and solar flux, and hence $JO(^1D)$, yielded a better fit between observed and implied diurnal cycles (correlation coefficient over 0.9) than a square root relationship. The nitrate radical was considered in the DMS oxidation and found to be unimportant in VOCALS-REx. We cannot rule out BrO as a possible oxidant, however. An upper limit estimate of 1 pptv of BrO (daytime peak) would account for 30% of total DMS oxidation, lowering our effective OH to 1.0 x $10^6$ molecules $cm^{-3}$.

**Acknowledgement**

We thank the National Science Foundation for support of this work through grant ATM-0241611 and ATM-0526341. Aircraft thermodynamic data and gas concentrations were provided by NCAR/EOL under sponsorship of the NSF. Aircraft DMS data was provided by Drexel University. Special thanks to C.W. Fairall, NOAA, S. de Szoeke, Oregon State University, R. Volkamer, University of Colorado at Boulder, S. Conley, University of California, Davis, R.M. Simpson, University of Hawaii at Manoa, and the crew of the *R/V Ronald H. Brown.*

**Figures**

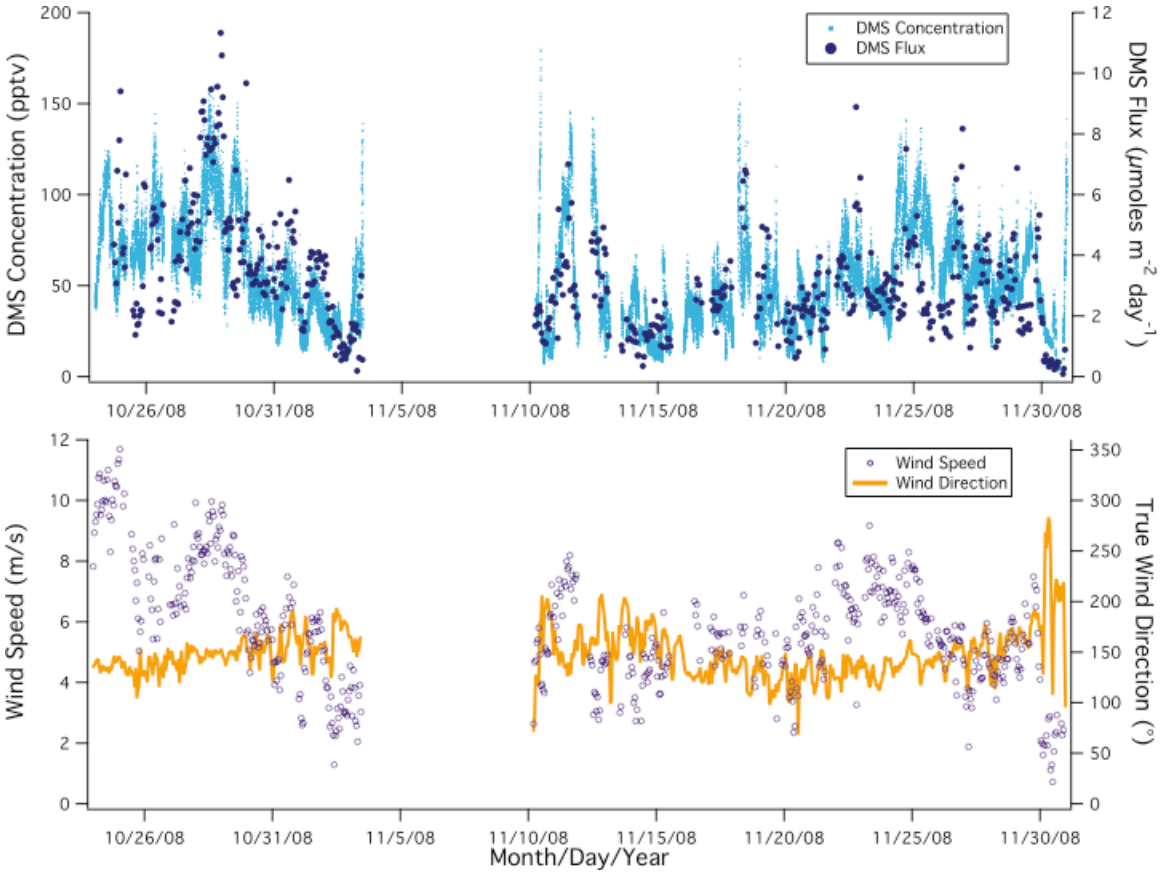


Figure 3.1 Time-series of DMS concentration and surface flux (top), and true wind speed and direction (bottom) from the *RHB* during VOCALS-REx. Elevated DMS flux usually corresponded to spikes in $DMS_w$ on the edges of localized eddies and high winds. The wind was consistently from the S/SE.

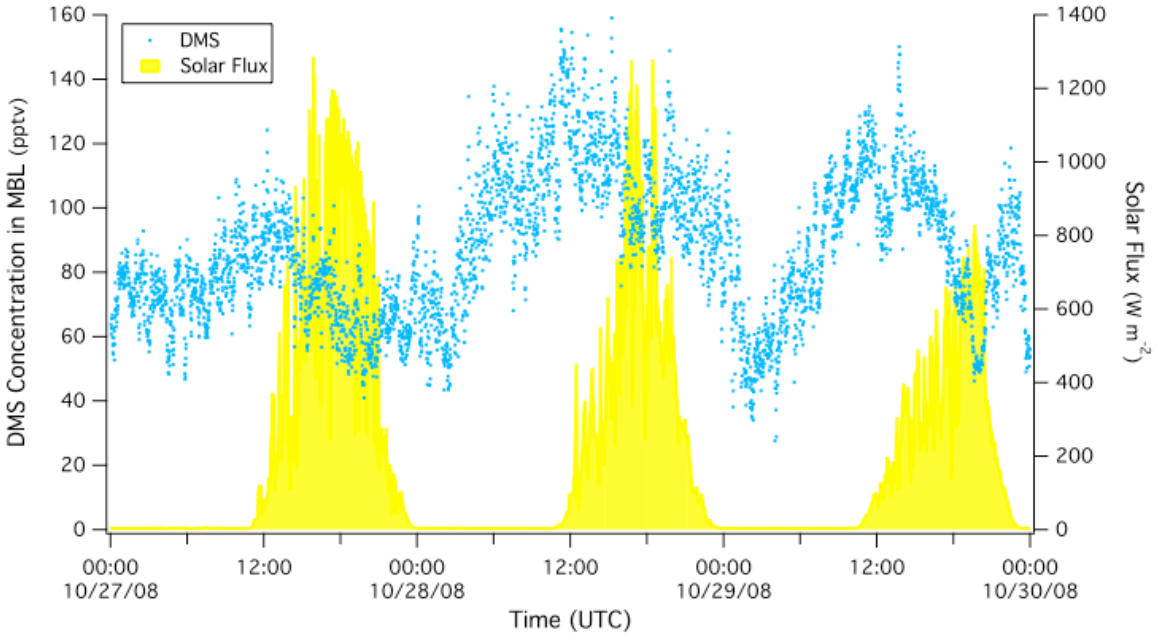


Figure 3.2 Examples of diurnal cycles in DMS concentration observed from the *RHB*, along with solar flux measured from a shipboard radiometer. Maxima and minima in DMS were usually observed just after sunrise and just before sunset, respectively, as a result of continuous build up of the gas via air-sea exchange and daytime photochemistry.

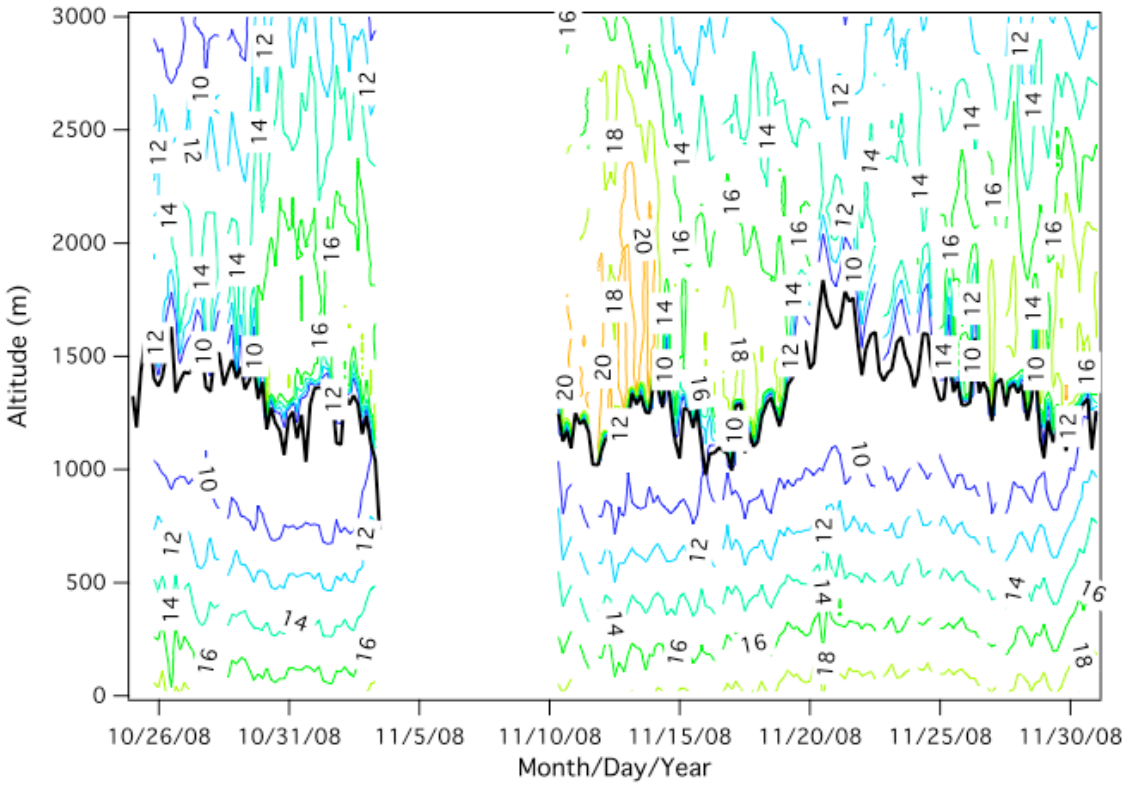


Figure 3.3 Time-series of temperature contours from the radiosondes from the *RHB*, with the dark line indicating the inversion. Over a ~monthly timescale, the trend in the depth of the MBL along the E-W transect was relatively constant, deeper offshore (e.g. Oct 26$^{th}$ and Nov 20$^{th}$) than near the coast (e.g. Nov 3$^{rd}$ and Nov 10$^{th}$). The average temperature was 13 ºC in the middle of the MBL.

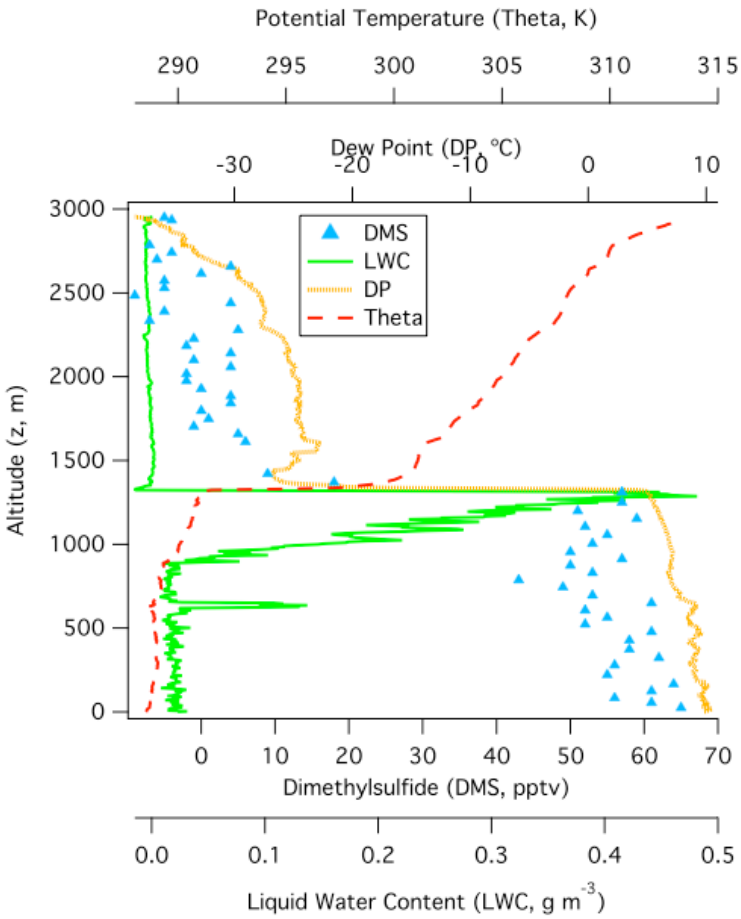


Figure 3.4 A typical profile of the lower troposphere determined from the C-130 (12:24~12:35 UTC on Oct 25th during Research Flight No. 5). $DMS_{C130}$ decreased linearly with altitude in the MBL (the lower ~1300 m in this profile) and dropped to zero in the FT. A strong inversion atop the stratocumulus cloud deck (indicated by high liquid water content) was defined by sharp gradients in dew point and potential temperature.

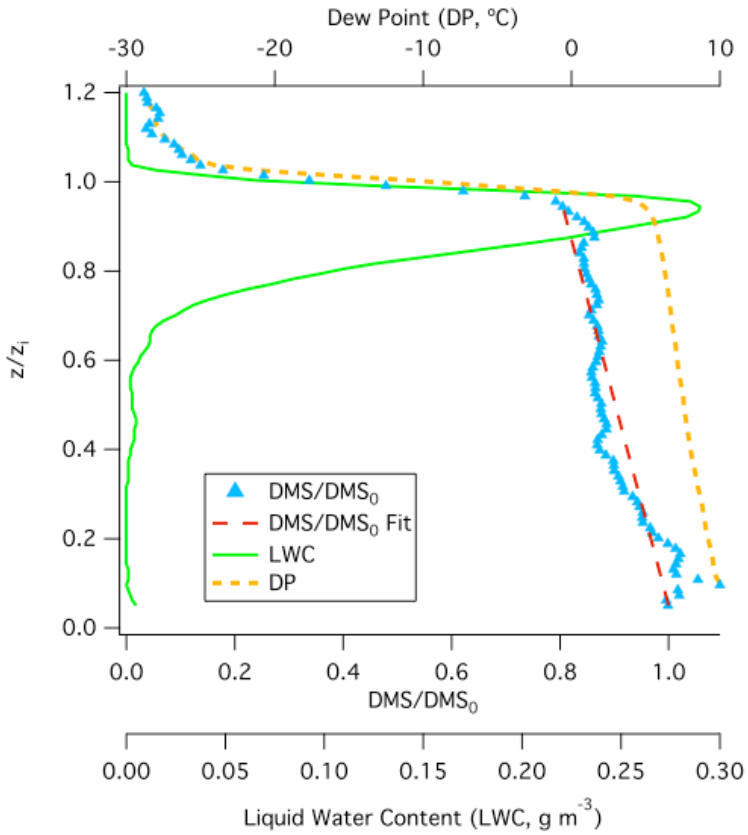


Figure 3.5 Averaged profile from the C-130 with altitude normalized to the inversion height and $DMS_{C130}$ normalized to concentration from the lowest leg. Concentration at height $z$ is related to the near-surface concentration by the parameterization $1 - \alpha\,(z/z_i)$, with $\alpha$ being the DMS "decoupling" parameter and on average equaling to 0.2.

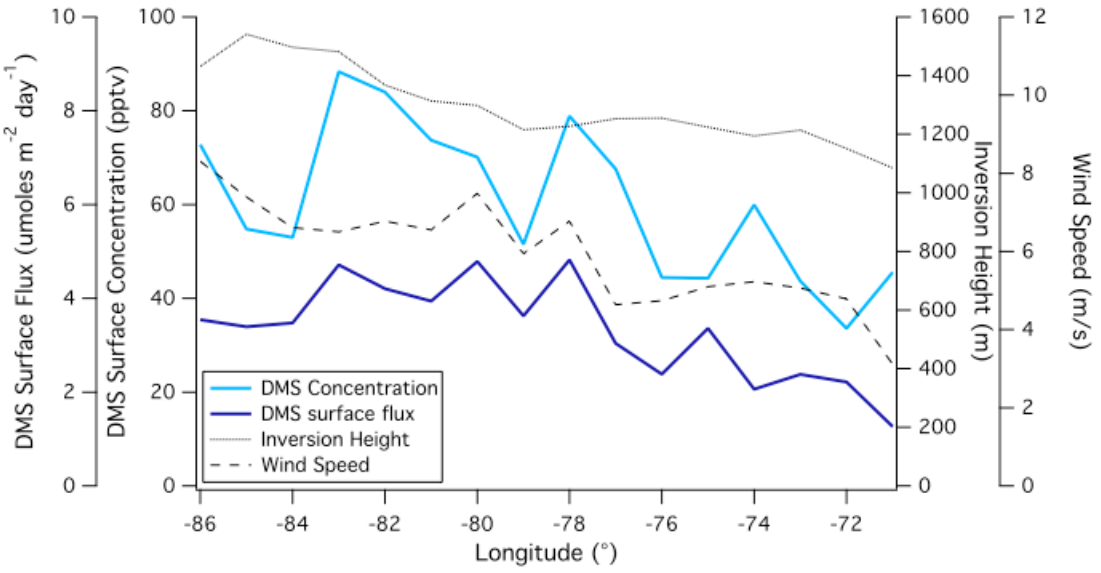


Figure 3.6 VOCALS averages of atmospheric DMS concentration and surface flux from the *RHB* in the latitude range of 20±2°S, as well as wind speed and inversion height. The ratio between DMS flux to concentration was largely constant, suggesting minimal time rate of change in the DMS field on a monthly timescale. Both the boundary layer height and wind speed were greater offshore.

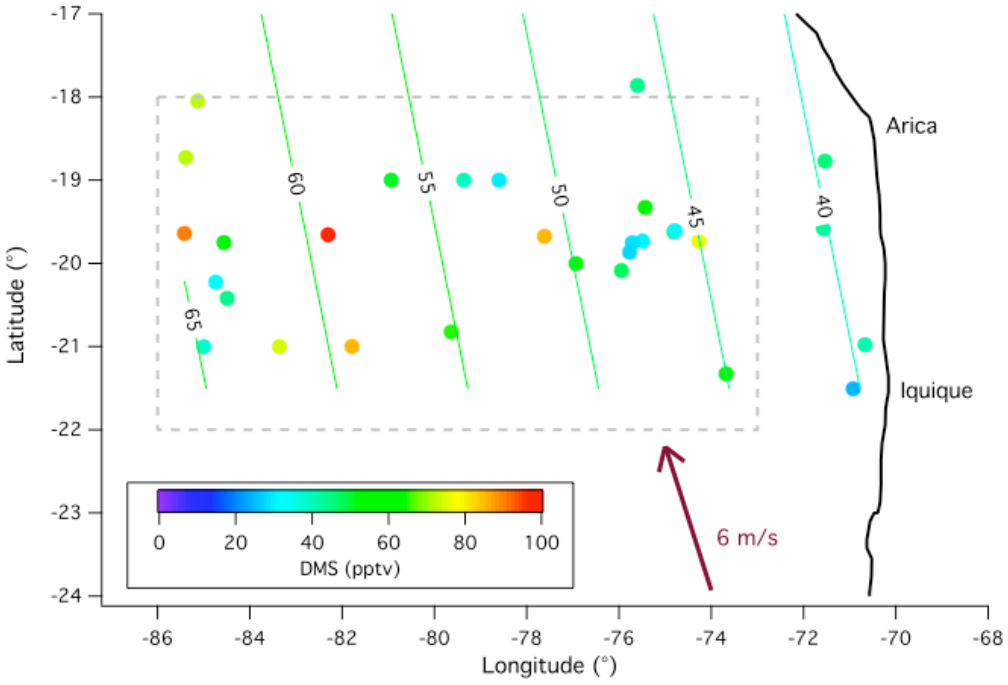


Figure 3.7 Multi-regression of daily DMS concentration from the *RHB* (colored circles) vs. Lat and Lon. Contours from the regression analysis show a gradient in DMS concentration that is orthogonal to the mean wind vector. The advective flux was thus minimal. The box with dashed lines defines the "VOCALS region."

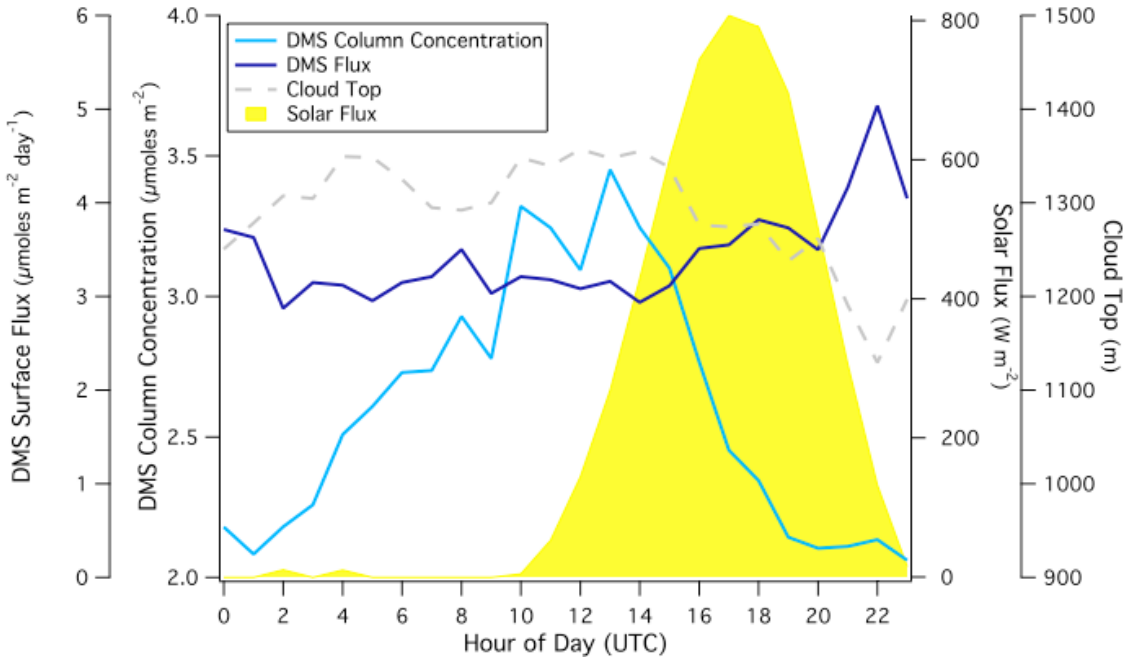


Figure 3.8 DMS surface flux, column concentration, shortwave radiation, and cloud top measured from the *RHB* in the VOCALS region averaged to the time of day. The nighttime increase in DMS column concentration was approximately linear, enabling us to estimate an entrainment velocity of 4 mm $sec^{-1}$.

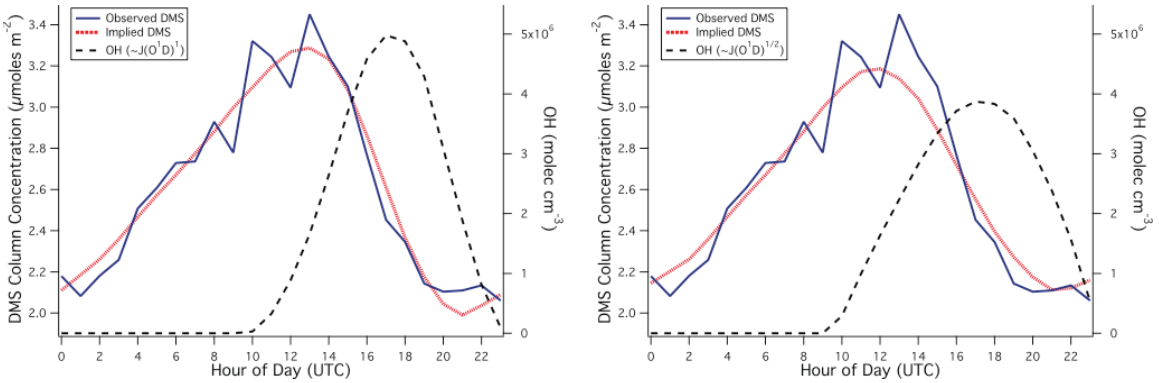


Figure 3.9 Observed and implied DMS diurnal cycle: a) with OH linearly proportional to the solar flux; b) with OH proportional to the square root of the solar flux. A linear relationship between OH and solar flux yielded a better fit to the DMS diurnal cycle, despite the expected low $NO_x$ concentration. To investigate the importance of other oxidants, the OH-equivalent oxidant concentration was apportioned to OH, $NO_3$ and BrO. Even a minuscule amount of $NO_3$ was found to degrade the fit between the implied and observed DMS. BrO cannot be distinguished from OH based on the DMS diurnal cycle. For VOCALS-REx, the maximum DMS oxidation due to BrO was estimated to be 30%.

## References


Bandy, A.R., Thornton, D.C., Blomquist, B.W., Chen, S., Wade, T.P., Ianni, J.C., Mitchell, G.M., and Nadler, W.: Chemistry of dimethylsulfide in the equatorial Pacific atmosphere, Geophys. Res. Lett., 23(7), 741–744, 1996.

Bandy, A.R., Thornton, D.C., Tu, F.H., Blomquist, B.W., Nadler, W., Mitchell, G.M., and Lenchow, D.H.: Determination of the vertical flux of dimethylsulfide by eddy correlation and atmospheric pressure ionization mass spectrometry (APIMS), J. Geophys. Res., 107(D24), 4743, doi:10.1029/2002JD002472, 2002.

Bates, T.S., Quinn, P.K., Covert, D.S., Coffman, D.J., Johnson, J.E., and Wiedensohler, A.: Aerosol physical properties and processes in the lower marine boundary layer: A comparison of shipboard sub-micron data from ACE-1 and ACE-2, Tellus, Ser. B, 52, 258 – 272, 2000.

Blomquist, B. W., Huebert, B. J., Fairall, C. W., and Faloona, I. C.: Determining the sea-air flux of dimethylsulfide by eddy correlation using mass spectrometry, Atmos. Meas. Tech., 3, 1-20, doi:10.5194/amt-3-1-2010, 2010.

Blomquist, B., Fairall, C.W., Huebert, B., Kieber D., and Westby, G.: DMS sea-air transfer velocity: Direct measurements by eddy covariance and parameterization based on the NOAA/COARE gas transfer model, Geophysical Research Letters, 33(7), 10.1029/2006GL025735, 2006.

Berresheim, H., Plass-Dulmer, C., Elste, T., Mihalopoulos, N., and Rohrer, F.: OH in the coastal boundary layer of Crete during MINOS: Measurements and relationship with ozone photolysis, Atmospheric Chemistry and Physics, 3, 639-649, 2003.

Bretherton, C. S., and Pincus, R.: Cloudiness and marine boundary layer dynamics in the ASTEX Lagrangian experiments. Part I:Synoptic setting and vertical structure, J. of Atmos. Sci., 52, 2707-2723, 1995.

Bretherton, C.S., Uttal, T., Fairall, C.W., Yuter, S.E., Weller, R.A., Baumgardner, D., Comstock, K., Wood, R. and Rag, G.B.: The EPIC 2001 stratocumulus study, Bulletin of the American Meteorological Society, 85 (7), 967-977, 2004.

Caldwell, P., Bretherton, C.S., and Wood, R.: Mixed-Layer Budget Analysis of the Diurnal Cycle of Entrainment in Southeast Pacific Stratocumulus. Journal of the Atmospheric Sciences: Vol. 62, No. 10, pp. 3775–3791, 2005.

Charlson, R.J., Lovelock, J.E., Andreae, M.O. and Warren, S.G.: Oceanic phytoplankton, atmospheric sulfur, cloud albedo and climate, Nature, 326, 655-661, 1987.

Chen, G., Davis, D.D. Kasibhatla, P., Bandy, A.R., Thornton D.C., Huebert, B.J., Clarke, A.D., Blomquist, B.W.: A study of DMS oxidation in the tropics: comparison of Christmas Island field observations of DMS, $SO_2$, and DMSO with model simulations. Journal of Atmospheric Chemistry, 37, 137-160, 2000.

Davis, D., Grodzinsky, G., Chen, G., Crawford, J., Eisele, F., Mauldin, L., Tanner, D., Cantrell, C., Brune, W., Tan, D., Faloona, I., Ridley, B., Montzka, D., Walega, J., Grahek, F., Sandholm, S., Sachse, G., Vay, S., Anderson, B., Avery, M., Heikes, B., Snow, J., O'Sullivan, D., Shetter, R., Lefer, B., Blake, D., Blake, N., Carroll, M., and Wang, Y.: Marine latitude/altitude OH distributions: Comparison of Pacific Ocean observations with models, J Geophys Res-Atmos, 106, 32691-32707, 2001.

Davis, D., Chen, G., Bandy, A., Thornton, D., Eisele, F., Mauldin, L. Tanner, D. Lenschow, D., Fuelberg, H., Huebert, B., Heath, J., Clarke, A., and Blake, D.: Dimethylsulfide oxidation in the equatorial Pacific: comparison of model simulations with field observations for DMS, $SO_2$, $H_2SO_4$(g), MSA(g), MS, and NSS. Journal of Geophysical Research, Vol 104, NO. D5, 5765-5784, 1999.

Donahue, N., and Prinn, R.: Nonmethane hydrocarbon chemistry in the remote marine boundary layer, J. Geophys. Res., 95, 18,387- 18,411, 1990.

Edson, J.B., Hinton, A.A., Prada, K.E., Hare, J.E., and Fairall, C.W.: Direct covariance flux estimates from mobile platforms at sea, *J. Atmos. Oceanic Technol.*, 15, 547-562, 1998.

Eisele, F. L., and Tanner, D. J.: Ion assisted tropospheric OH measurement, J. Geophys. Res., 96, 9295-9308, 1991.

Faloona, I., Lenschow, D., Campos, T., Stevens, B., van Zanten, M., Blomquist, B., Thornton, D., Bandy, A., and Gerber, H.: Observations of Entrainment in Eastern Pacific Marine Stratocumulus Using Three Conserved Scalars. J. Atmos. Sci., 62, 3268–3285, 2005.

Faloona, I., Tan, D., and Fuelberg, H.: Observations of $HO_x$ and its relationship with $NO_x$ in the upper troposphere during SONEX, J. Geophys. Res., 105, 3771-3784, 2000.

Hard, T.M., O'Brien, R.J., Chan, C.Y., and Mehrabzadeh, A.A.: Tropospheric free radical determination by FAGE, Environ. Sci. Technol., 18, 768-777, 1984.

Holland, F., Aschmutat, U., Heßling, M., Hofzumahaus, A., and Ehhalt, D.H.: Highly time resolved measurements of OH during POPCORN using laser-induced fluorescence spectroscopy, J. Atmos. Chem., 31, 205-225, 1998.

Huebert, B.J., Blomquist, B.W., Hare, J.E., Fairall, C.W., Johnson, J.E., and Bates, T.S.: Measurement of the sea-air DMS flux and transfer velocity using eddy correlation, Geophys. Res. Lett., 31, L23113, doi:10.1029/2004GL021567, 2004.

Hynes, A.J., Wine, P.H., and Semmes, D.H.: Kinetics and mechanisms of OH reactions with organic sulfides. Journal of Physical Chemistry 90, 4148-4156, 1986.

Kloster, S., Feichter, J., Maier-Reimer, E., Six, K.D., Stier, P., and Wetzel, P.: DMS cycle in the marine ocean-atmosphere system - a global model study, Biogeosciences **3**(1): 29-51, 2006.

Levy, H.I.: Normal Atmosphere: Large Radical and Formaldehyde Concentrations Predicted, Science, 173, 141-143, 1971.

Lilly, D. K.: Models of cloud-topped mixed layers under a strong inversion. Quart. J. Roy. Meteor. Soc., 94, 292–309, 1968.

Lovelock, J.E., Maggs, R.J., and Rasmussen, R.A.: Atmospheric dimethyl sulphide and the natural sulphur cycle. Nature, 237, No. 5356, 452-453, 1972.

Mauldin, R.L., Eisele, F.L., Cantrell, C.A., Kosciuch, E., Ridley, B.A., Lefer, B., Tanner, D. J., Nowak, J.B., Chen, G., Wang, L., and Davis, D.: Measurements of OH aboard the NASA P-3 during PEM-Tropics B, J. Geophys. Res., 106, 32657-32666, 2001.

Mount, G.H., The measurement of tropospheric OH by long-path absorption, 1. Instrumentation, J. Geophys. Res., 97, 2427-2444, 1992.

Nowak, J. B., Davis, D.D., Chen, G., Eisele, F.L., Mauldin III, R.L., Tanner, D.J., Cantrell, C., Kosiuch, E., Bandy, A., Thorton, D., and Clarke, A.: Airborne observations of DMSO, DMS, and OH at marine tropical latitudes, Geophys. Res. Lett., 28(11), 2201–2204, 2001.

Olson, J.R. Crawford, J.H., Davis, D.D., Chen, G., Avery, M.A., Barrick, J.D.W., Sachse, G.W., Vay, S.A., Sandholm, S.T., Tan, D., Brune, W.H., Faloona, I.C., Heikes, B.G., Shetter, R.E., Lefer, B.L., Singh, H.B.,

Talbot, R.W., and Blake, D.R.: Seasonal differences in the photochemistry of the South Pacific: A comparison of observations and model results from PEM-Tropics A and b, J. Geophys. Res., 106 (D23), 32749-32766, 2001.

Platt, U., and Heintz, F.: Nitrate radicals in tropospheric chemistry, Isr. d. Chem., 34, 289-300, 1994.
Prinn, R, Cunnold, D., Simmonds, P., Alyea, F., Boldi, R., Crawford, A., Fraser, P., Gutzler, D., Hartley, D., Rosen, R., and Rasmussen, R.: Global Average Concentration and Trend for Hydroxyl Radicals Deduced From ALE/GAGE Trichloroethane (Methyl Chloroform) Data for 1978–1990, J. Geophys. Res., 97(D2), 2445–2461, 1992.

Prinn, R.G., Weiss, R.F., Miller, B.R., Huang, J., Alyea, F.N., Cunnold, D.M., Fraser, P.J., Hartley, D.E., and Simmonds, P.G.: Atmospheric trends and liftetime of $CH_3CCl_3$ and global OH concentrations, Science, 269, 187-192, 1995.

Read, K.A., Mahajan, A.S., Carpenter, L.J., Evans, M.J., Fari, B.V.E., Heard, D.E., Hopkins, J.R., Lee, J.D., Moller, S.J., Lewis, A.C., Mendes, L., McQuaid, J.B., Oetjen, H., Saiz-Lopez, A., Pilling, M.J., and Plane, J.M.C.: Extensive halogen-mediated ozone destruction over the tropical Atlantic Ocean, Nature, 453, 1232-1235, 2008.

Russell, L. M., Lenschow, D. H., Laursen, K.K., Krummel, B., Siems, S.T., Bandy, A.R. Thornton, D.C., Bates, T.S.: Bidirectional mixing in an ACE 1 marine boundary layer overlain by a second turbulent layer, J. Geophys. Res., 103, 16,411-16,432, 1998.

Sander, S.P., Golden, D.M., Kurylo, M.J., Moortgat, G.K., Wine, P.H., Ravishankara, A.R., Kolb, C.E., Molina, M.J., Finlayson-Pitts, B.J., Huie, R.E., and Orkin, V.L.: Chemical Kinetics and Photochemical Data for Use in Atmospheric Studies, Evaluation Number 15, Jet Propulsion Laboratory, Pasadena, CA (available at http://jpldataeval.jpl.nasa.gov/), 2006.

Seinfeld, J.H. and Pandis, S.N.: Atmospheric chemistry and physics: from air pollution to climate change. 2nd ed. Wiley-Interscience. Hoboken, New Jersey, USA, 2006.

Sciare J., Baboukas, E., Kanakidous, M., Krischke, U., Belviso, S., Bardouki, H. and Mihalopoulos, N.: Spatial and temporal variability of atmospheric sulfur-containing gases and particles during the Albatross campaign, J. Geophys. Res., 105, 14433-14448, 2000.

Shon, Z.H, Davis, D., Chen, G., Grodzinsky, G., Bandy, A., Thornton, D., Sandholm, S., Bradshaw, J., Stickel, R., Kok, G., Mauldin, L., Tanner D., and Eisele, F.: Evaluation of the DMS Flux and its Conversion in $SO_2$ Over the Southern Ocean, Atmospheric Environment, 35, 159-172, 2001.

Shultz M.G., Jacob, D.J., Wang, Y., Logan, J.A., Atlas, E.L., Blake, D.R., Blake, N.J., Bradshaw, J.D., Fenn, M.A., Flocke, F., Gregory, G.L., Heikes, B.G., Sachse, G.W., Sandholm, S.T., Shetter, R.E., Singh, H.B., Talbot, R.W.: On the origin of tropospheric ozone and $NO_x$ over the tropical South Pacific, J. Geophys. Res. 104, 5829-5843, 1999.

Spivakowsky, C.M., Logan, A.J., Montzka, S.A., Balkanski, Y.J., Foreman-Fowler, M., Jones, D.B.A., Horowitz, L.W., Fusco, A.C., Brenninkmeijer, C.A.M., Prather, M.J., Wofsy, S.C., McElroy, M.B.: Three dimensional climatological distribution of tropospheric OH: Update and evaluation, J. Geophys. Res., 105, 8931-8980, 2000.

Stevens, B, Lenschow, D.H., Vali, G., Gerber, H., Bandy, A., Blomquist, B., Brenguier, J.L., Bretherton, C.S., Burnet, F., Campos, T., Chai, S., Faloona, I., Friesen, D., Haimov, S., Laursen, K., Lilly, D.K., Loehrer, S.M., Malinowski, S.P., Morley, B., Petters, M.D., Rogers, D.C., Russell, L., Savic-Jovcic, V., Snider, J.R., Straub, D., Szumowski, M.J., Takagi, H., Thornton, D.C., Tschudi, M., Twohy, C., Wetzel, M., and van Zanten, M.C.: Dynamics and Chemistry of Marine Stratocumulus -- DYCOMS-II, 2003: Bull. Amer. Meteorol. Soc., 84, 579-593, 2003.

Stickel R.E., Zhao, Z., and Wine, P.H.: Branching ratios for hydrogen transfer in the reactions of OD radicals with $CH_3SCH_3$ and $CH_3SC_2H_5$. Chem. Phys. Lett. 212, pp. 312–318, 1993.

Wallington, T.J., Ellermann, T., and Nielsen, O.J.: Atmospheric chemistry of dimethylsulfide: UV spectra and self-reaction kinetics of $CH_3SCH_2$ and $CH_3SCH_2O_2$ radicals and kinetics of the reactions $CH_3SCH_2$ + $O_2$ $CH_3SCH_2O_2$ and $CH_3CH_2O_2$ + NO → $CH_3SCH_2O_2$ + $NO_2$. J. phys. Chem. 97, pp. 8442–8449, 1993.

Wine, P.H., Kreutter, N.M., Gump, C.A., Ravishankara, A.R.: Kinetics of OH reactions with the atmospheric sulfur compounds $H_2S$, $CH_3SH$, $CH_3SCH_3$, $CH_3SSCH_3$. Journal of Physical Chemistry 85, 2660-2665, 1981.

Wood, R., and Bretherton, C.S.: Boundary Layer Depth, Entrainment, and Decoupling in the Cloud-Capped Subtropical and Tropical Marine Boundary Layer. J. Climate, 17, 3576–3588, 2004.

Yvon, S.A., Plane, J.M.C., Nien, C.-F., Cooper, D.J. and Saltzman, E.S.: The interaction between the nitrogen and sulfur cycles in the polluted marine boundary layer, J Geophys. Res., 101, 1379-1386, 1996.

# Chapter 4. Cycling of $SO_2$ and $SO_4^{2-}$ in the Marine Atmosphere

This chapter will be submitted to the journal *Atmospheric Chemistry and Physics* with the following tentative citation: Mingxi Yang, Huebert, B. Blomquist, B., Howell, S., Shank, L., McNaughton, C., Kapustin, V., Clarke, A., Hawkins, L. Russell, L., Covert, D., Johnson, J. Bates, T., Quinn, P., Zagorac, N., Bandy, A., deSzoeke, S., Zuidema, P., Tucker, S. A. Brewer, W.: Atmospheric Sulfur Cycling in the Southeast Pacific – Longitudinal Distribution, Diel Variability, and New Particle Formation Observed from VOCALS-REx, *Atmos. Chem. Phys*.


**Abstract**

Dimethylsulfide (DMS) emitted from the ocean is a natural precursor gas for sulfur dioxide ($SO_2$) and non-sea-salt sulfate aerosols ($SO_4^{2-}$), which affect cloud formation in the marine atmosphere. During the VAMOS-Ocean-Cloud-Atmosphere-Land Study Regional Experiment (VOCALS-REx) in October and November of 2008, a variety of instrumentation platforms were deployed in the Southeast Pacific off the coast of Chile and Peru to study the linkage between aerosols and stratocumulus clouds. We present here observations from the NOAA Ship *Ronald H. Brown* and the NSF/NCAR C-130 aircraft along ~20°S from the coast (70°W) to a remote marine region (85°W). While $SO_4^{2-}$ and $SO_2$ concentrations were distinctly elevated in the coastal marine boundary layer (MBL) due to anthropogenic influence (~800 and 80 pptv, respectively), their concentrations rapidly decreased offshore (~100 and 25 pptv). Compared to the mass entrainment fluxes of $SO_4^{2-}$ and $SO_2$ from the free troposphere (0.5±0.3 and 0.3±0.2

μmoles $m^{-2}$ $day^{-1}$), the sea-to-air DMS flux (3.8±0.1 μmoles $m^{-2}$ $day^{-1}$) remained the predominant source of sulfur mass to the MBL. In-cloud oxidation was found to be the most important mechanism for $SO_2$ removal (2.1±0.4 μmoles $m^{-2}$ $day^{-1}$) and in situ $SO_4^{2-}$ production. Surface $SO_4^{2-}$ concentration in the remote region displayed pronounced and unexpected diel variability, increasing rapidly in the first few hours after sunset and then decaying for the rest of the diurnal cycle. We theorize that the increase in $SO_4^{2-}$ was due to nighttime coupling of the MBL that mixed down cloud-processed air, while sporadic precipitation scavenging and daytime decoupling were responsible for the subsequent decline in $SO_4^{2-}$.

Nucleation of new particles was surprisingly common in the remote region of VOCALS-REx, as observed on both the aircraft and the ship. Often associated with precipitation events and pockets of open cells (POCs), these new particle formation events likely took place in the cloud outflow region, where the preexisting aerosol surface area was low due to scavenging and the reactive gas concentrations were high. The low anthropogenic influence in the remote region and ample DMS concentration suggest that the source of sulfuric acid vapor for nucleation was likely natural.

### 4.1 Introduction

The ocean is the largest source of natural reduced sulfur gas to the atmosphere, most of which is in the form of dimethylsulfide (DMS), a volatile organic compound produced from phytoplankton. The annual global sea-to-air DMS emission is estimated to be 15~33 Tg S (Kettle and Andreae, 2000), depending on the gas exchange and wind

speed parameterization. In the atmosphere, DMS is principally oxidized by the hydroxyl radical (OH) to a number of products, including sulfur dioxide ($SO_2$). In addition to DMS oxidation, $SO_2$ is formed from fossil fuel combustion and biomass burning and removed from the MBL through deposition to the ocean surface and oxidative reactions in the gas and aqueous phase. Gas phase oxidation of $SO_2$ by OH and subsequent reactions with water vapor ($H_2O_{(g)}$) yield sulfuric acid vapor ($H_2SO_{4(g)}$), which usually condenses upon preexisting aerosol surfaces and increases sulfate aerosol ($SO_4^{2-}$) mass. Under infrequent, specific conditions, $H_2SO_{4(g)}$ may undergo gas-to-particle nucleation and form numerous new nm-sized $SO_4^{2-}$ aerosols, which then grow by condensation and coagulation.

Generally the oxidation of $SO_2$ in the aqueous phase, which can take place in cloud water or in sea-salt aerosols by hydrogen peroxide ($H_2O_2$) at low pH and with ozone ($O_3$) at high pH, is much faster than in the gas phase. Aqueous oxidation of $SO_2$ also leads to $SO_4^{2-}$ aerosols, which are termed non-sea-salt-$SO_4^{2-}$ to differentiate from sulfate originated in seawater. These aerosols from oxidative reactions typically make up the bulk of the submicron (fine) aerosol mass, causing the fine mode to be acidic. Sea-salt aerosols formed from wave breaking account for the majority of the supermicron (coarse) number as well as total aerosol mass, and tend to be more basic than the fine mode because of the initial alkalinity of seawater (pH~8.1) and its carbonate buffering capacity. Due to dissolution of $CO_2$ and other acids, cloud water typically has a pH under 5 (Chameides, 1984), which makes $H_2O_2$ the principal oxidant of $SO_2$ in cloud. Hegg (1985) suggested cloud processing to be the most important mechanism for the conversion from $SO_2$ to $SO_4^{2-}$. Because the reaction rate between $SO_2$ and $O_3$ is greatly accelerated at high pH

(Hoffmann, 1986), some authors postulated $O_3$ oxidation in sea-salt aerosols to be an important sink of $SO_2$ and source of $SO_4^{2-}$ mass (Sievering et al., 1991; Faloona et al., 2010). However, both the uptake of $SO_2$ and the production of $SO_4^{2-}$ increase the acidity of the sea-salt, making the $O_3$ reaction self-limiting.

In addition to affecting atmospheric chemistry, $SO_4^{2-}$ aerosols are climatically important because they alter the global radiative balance directly by scattering light (Charlson et al. 1992) and indirectly by controlling the optical properties, areal extent, and lifetimes of clouds via the formation of cloud condensation nuclei (CCN). At a certain level of water vapor supersaturation, aerosols larger than a critical size and with a soluble composition (e.g. $SO_4^{2-}$) act as CCN and activate to form cloud droplets. Pruppacher and Klett (1997) estimated a supersaturation level of ~0.35% for typical marine clouds with an updraft velocity of ~1 m $s^{-1}$, corresponding to a critical diameter of approximately 70~80 nm for activation. In a remote marine environment where CCN represent a large fraction of the aerosol number, a gap in this size range in the number distribution is often observed, which has been coined the 'Hoppel minimum' (Hoppel et al., 1986). Aerosols smaller than the critical diameter are unactivated and sometimes called Aitken particles, while aerosols larger than the critical diameter have been activated and grown into the accumulation mode (0.1~1 um).

Charlson et al. (1987) coined the 'CLAW' hypothesis, which postulated a negative feedback loop from enhanced phytoplankton growth and DMS efflux in a warming climate leading to a decrease in incident radiation (and hence cooling) due to greater albedo of marine clouds from more $SO_4^{2-}$ derived CCN. With liquid water content

unchanged, more CCN should increase the cloud droplet number concentration and reduce the mean droplet size, which lead to more reflective and possibly longer living clouds. The effects of naturally derived $SO_4^{2-}$ on clouds are expected to be greatest in areas deprived of CCN (Twomey, 1991), such as over the remote ocean in the relatively pristine Southern Hemisphere.

The Southeast Pacific is a region characterized by large-scale subsidence associated with subtropical anticyclonic flow, coastal upwelling of cold water driven by Ekman transport, and a large stratocumulus cloud deck capped by a strong inversion layer (Bretherton et al., 2004). The stratocumulus topped MBL is shallow near the coast (~ 1 km) with more broken clouds. Away from shore, the MBL deepens with thicker clouds and more extensive precipitation in the form of drizzle. Satellite observations show frequent hundred-kilometer sized openings in the stratocumulus cloud deck. Termed "pockets of open cells" (POCs), these features persist for a timescale of a day and advect with the mean wind (Stevens et al., 2005). The geographical gradient in cloud properties as well as the formation and evolution of POCs likely depend on the availability of aerosols that can act as CCN and suppress drizzle, and drizzle that in turn removes said aerosols. The coastal regions of Chile and Peru are characterized by pollution emissions of $SO_4^{2-}$ and $SO_2$ from fossil fuel consumption and processing of copper ores. Because the prevailing wind direction at the surface is S/SE along the Andes mountain range, anthropogenic influence decreases quickly away from shore, where a greater contribution to the $SO_4^{2-}$ burden and larger fraction of CCN likely originate from DMS.

In this paper, we will report the longitudinal and vertical distributions of $SO_2$ and $SO_4^{2-}$ measured from a ship and an aircraft during Vamos Ocean-Cloud-Atmosphere-Land Study Regional Experiment (VOCALS-REx). Two examples of new particle nucleation observed in the MBL will be discussed. Following up on the DMS budget presented in Yang et al. (2009), we will estimate the budgets of $SO_2$ and $SO_4^{2-}$ using a mass balance approach in the remote region of the Southeast Pacific. The conservation equation for any chemical species, *S*, in the MBL is represented in (4.1), with the overbar representing an average in time and/or space:

$$\frac{\partial \overline{S}}{\partial t} + \overline{u}\frac{\partial \overline{S}}{\partial x} + \frac{\partial \overline{S'w'}}{\partial z} = P - L \qquad (4.1)$$

The terms on the LHS are the time-rate of change in the concentration of *S*, horizontal advection of *S* due to gradients along the mean wind, and vertical flux divergence, respectively. In situ production and loss of *S* are represented by *P* and *L* on the RHS of the conservation equation.

**4.2 Experimental**

During VOCALS-REx, the National Oceanographic and Atmospheric Administration (NOAA) research vessel *Ronald H. Brown* (*RHB*) made multiple transects between the coastal city of Arica at 70°W and the remote marine region near the Woods Hole Oceanographic Institution (WHOI) Improved Meteorology (IMET) moored buoy at 20°S, 85°W. The ship sailed in two legs: Leg 1 from Panama to the IMET buoy and then to Arica (Oct. 20~Nov. 3), and Leg 2 from Arica to near 85°W and back to Arica (Nov. 10~Dec. 11). In addition to surveying several eddies, *RHB* stationed at 85°W and 75°W

for over 24 hours to more closely observe diel cycles.

The National Science Foundation (NSF)/National Center for Atmospheric Research (NCAR) aircraft C-130 flew 14 research flights (RF) out of Arica between Oct. 15 and Nov. 15. Out of the 14 flights, eight were dedicated to survey the 20°S line to as far as 86°W, four were designed to study the structures and evolution of POCs, and two were parallel to the coast in the N-S direction between 20°S and 30°S for examining continental influence. For the 20°S surveying flights, the aircraft typically flew 10-minute level legs near the surface, in the mid MBL, at cloud level, and above clouds. Sounding profiles from the surface to ~4 km were frequently performed.

*4.2.1 RHB*

The measurement of airside DMS by an atmospheric pressure ionization mass spectrometer (APIMS) during VOCALS-REx is outlined by Yang et al., (2009). DMS was sampled from the mast of the ship (18 m) along with instantaneous winds and ship motions at a high rate of 20 Hz, which allowed for the eddy covariance computation of the DMS sea-to-air flux. Instrument design, flux computation, and error analysis are detailed by Blomquist et al. (2010). Seawater DMS was taken from the ship's non-toxic water supply at ~5.5 m below the ocean surface, extracted by a purge-and-trap method, and analyzed by gas chromatography with a sub-nM detection limit (Bates et al., 2000).

Aerosol chemical compositions and size distributions were measured by the Pacific Marine Environmental Laboratory through an isokinetic inlet on the forward deck of the ship. Submicron and supermicron aerosols were collected on a two-stage multi-jet cascade impactor (50% aerodynamic cutoff diameters of 1.1 and 10 μm) over 2~23

hours. In addition to providing gravimetric mass, collected aerosols were analyzed for soluble concentrations of sodium ($Na^+$), potassium ($K^+$), calcium ($Ca^{2+}$), magnesium ($Mg^{2+}$), ammonia ($NH_4^+$), methane sulfonic acid ($MSA^-$), chloride ($Cl^-$), bromide ($Br^-$), nitrate ($NO_3^-$), sulfate, and oxalate ($Ox^{2-}$) using ion chromatography (Bates et al., 2008). A coating of silicon grease on the first impaction stage prevented bouncing of large particles. Non-sea-salt- $SO_4^{2-}$ and $Cl^-$ deficit were calculated by subtracting sea-salt sulfate and $Cl^-$ components from aerosol concentrations. An Aerodyne quadrupole aerosol mass spectrometer (Q-AMS) was used to continuously measure submicron particulate concentrations of $SO_4^{2-}$, $NO_3^-$, $NH_4^+$, and organic matter with detection limits of 0.02, 0.02, 0.15, and 0.16 $\mu g\ m^{-3}$ respectively (Hawkins et al., 2010). The AMS measured non-refractory aerosols (those vaporizing at 600°C), thus excluded mineral dust, elemental carbon, and sea-salt. The AMS sulfate measurements agreed exceptionally well with collocated submicron filter measurements of $SO_4^{2-}$ and showed a high degree of correlation with integrated submicron aerosol volume. The number concentration of aerosols greater than ~13 nm (CN) was measured by a TSI 3010 condensation particle counter (CPC). Aerosols greater than ~5 nm (UFCN) were measured by a TSI 3025 ultrafine CPC and a water based TSI counter. Aerosol size distributions from 0.02~10 μm were obtained by a merging spectra from a differential mobility particle sizer (DMPS) and an aerodynamic particle sizer (APS) at a regulated RH of 60% (Bates et al., 2008). Aerosol scattering and ozone ($O_3$) were measured by a 3-channel TSI 3563 nephelometer and a Thermo Environmental Instruments Model 49C ozone analyzer.

Vertical structures of temperature and humidity were determined from radiosonde launched several times a day from the ship by the NOAA Earth System Research Laboratory (de Szoeke et al., 2008). During the second half of VOCALS-REx, cloud fraction and cloud top height were determined from a W-band radar. Rain rate was measured by a shipboard optical rain gauge; but considering the difficulty with quantifying drizzle, the measurement should be viewed as qualitative. The mixed layer height (MLH) from the surface was determined by a High Resolution Doppler Lidar (2 μm) from velocity variance (turbulence) profiles and aerosol backscatter gradient (Tucker et al. 2009). Liquid water path ($L_{WP}$), or the amount of liquid water integrated over the MBL column, was estimated using a microwave radiometer by University of Miami (Zuidema et al., 2009).

*4.2.2 C-130*

$SO_2$ was measured at 1 Hz using an APIMS by Drexel University following the method described in detail by Thornton et al., (2002). An isotopically labeled $^{34}SO_2$ was mixed with ambient air at the inlet, enabling the calculation of the ambient concentration of $SO_2$ from the ratio between ambient and labeled species. Both DMS and $SO_2$ on the C-130 were sampled from backward facing inlets, which should not be affected by cloud droplets. Thus within clouds, measurements of those gases represent interstitial concentrations.

The University of Hawaii aerosol instruments were typically located behind a low turbulence inlet (LTI) (Huebert et al., 2004). Breaking up of cloud droplets upon collision on the wall of the inlet caused a cloud shattering artifact, or an increase in the

measured number of particles. By excluding such incidents, aerosol data at cloud level were biased towards cloud free regions. A high resolution time-of-flight AMS on the C-130 measured aerosol concentration of $SO_4^{2}$, $NO_3^{-}$, $NH_4^{+}$, and organic matter. As with the AMS on the ship, the AMS on the C-130 sampled with a near-unity efficiency for aerosols up to ~0.8 μm in diameter and excluded large particles.

Aerosol size distributions from diameters of 0.01 to 10 μm were obtained by merging spectra from a radial differential mobility analyzer (RDMA, 0.01~0.20 μm), a TSI long differential mobility analyzer (LDMA, 0.10~0.50 μm), a PMS laser optical particle counter (OPC, 0.12~8.0 μm), and a TSI 3321 aerodynamic particle sizer (APS, 0.78~10.0 μm) (Howell et al., 2006). Measured at near ambient pressure and cabin temperatures, the sample air was dried to a RH of ~20% by mixing with desiccated air to remove water from aerosols. Direct comparisons between the distributions measured on the C-130 and *RHB* can only be qualitative in nature because of the different sampling strategies and airspeeds. At the dried environment of C-130 measurements, MBL aerosols had most likely undergone efflorescence and been approximately halved in diameters, whereas the already dry FT aerosols remained largely unchanged. The *RHB* distributions, on the other hand, were measured at ~60% RH, closer to the ambient RH of ~70% and above the humidity threshold for efflorescence; the measured diameters were thus only ~10% smaller than ambient diameters. Moreover, the lowest size cut was lower for the C-130 distribution (10 nm) than for the RHB distribution (20 nm); thus more small particles were detected by the instruments aflight. For the coarse mode, the isokinetic inlet on the ship had a higher sampling efficiency than the LTI on the aircraft.

Bulk cloud water was collected by Colorado State University with an Airborne Cloud Collector, which had a 50% size cut diameter of 8 μm and thus collected most cloud drops but excluded small, unactivated aerosols (K. Beam, personal communication, 2010). Cloud water was analyzed for pH, S(IV) by absorbance, peroxides by fluorescence, anions and cations by ion chromatography. Aqueous concentrations in μM can be converted to mixing ratios using cloud liquid water content.

Inversion heights ($Z_i$) determined based on potential temperature and dew point gradients from the C-130 sounding showed excellent agreement with those determined from potential temperature profiles from shipboard radiosondes. Because $Z_i$ varied both with longitude and with the time of day, to average vertical distributions, altitude ($Z$) is normalized to $Z_i$, with $Z/Z_i$ =1 indicating the inversion. For FT averages along 20°S, only observations within 1 km above $Z_i$ are included.

### 4.3 Observations

To evaluate the relative importance of natural and pollution sulfur sources, we separate the VOCALS-REx sampling area longitudinally to the 'coastal' region (70°W ~ 73°W) and 'offshore' region (73°W ~ 86°W). We further isolate the 'remote' region (78°W ~ 86°W) from the offshore region. Figure 4.1 shows a map of the *RHB* cruise track color-coded by the DMS sea-to-air flux; the dotted and solid lines indicate the offshore and remote regions. This stratification is based on aircraft observation of CO and shipboard measurement of radon, both indicators of continental influence. The lowest MBL CO concentration was found west of 78°W at ~62 ppbv; CO increased to ~73 ppbv near the coast, corresponding to elevated $SO_4^{2-}$ concentrations. Hawkins et al.

(2010) showed that the concentration of radon (a radioactive decay product of uranium in rocks and soil) in the remote marine region was approximately half of the value by the coast. Three-day back trajectories by those authors showed that east of 75°W, airmasses had been previously in contact with land south of the VOCALS-REx sampling area, near the Chilean capital Santiago. In contrast, west of 78°W, air had originated from the remote South Pacific. Figure 4.2 show a typical 20°S survey flight by the C-130 (RF 03 on Oct 21). The flight track is color-coded by $SO_2$ concentration, with marker size corresponding to $SO_4^{2-}$. The aircraft encountered more polluted air in two flights south of ~22°S, closer to Santiago, as well as on RF 14. Greater continental influence was also observed on the *RHB* north of ~15°S, closer to Peru. For our '20°S' averages, we limit the latitudinal range to 18°S ~ 22°S and exclude RF 14 from C-130 statistics. Because the aircraft usually took off from Arica in the early morning, reached 80~85°W at around sunrise, and returned to shore in the afternoon, spatial and temporal biases were inherent. We will thus mostly rely on ship observations for diel cycles and aircraft observations for vertical structures.

### *4.3.1 Mean Concentrations: Coastal vs. Marine*

It was hypothesized prior to VOCALS-REx that coastal upwelling of cold, nutrient rich water stimulates growth of phytoplankton, which leads to more seawater DMS and atmospheric DMS by the shore than in the remote region. We only observed enhanced seawater DMS in isolated pockets near the coast. More often high seawater DMS was associated with the edge of an eddy or near a front between two water masses, where temperature and salinity changed markedly. On average along 20°S, seawater

DMS was not substantially different between the coastal and the remote regions. Higher atmospheric DMS concentration and sea-to-air flux were observed away from the coast principally as a result of higher wind speed. At the same air-sea concentration difference in DMS (dictated by the seawater concentration), a higher wind speed generally leads to a greater transfer velocity, and hence more DMS flux out of the ocean.

Project average concentrations of DMS, $SO_2$ and $SO_4^{2-}$ along 20°S and in the MBL and FT are shown in Fig. 4.3. Pollution emission was unquestionably the major source of sulfur mass near shore, with $SO_2$ and $SO_4^{2-}$ concentrations elevated at ~80 and ~800 pptv in the MBL, respectively. Moving offshore towards the remote region, $SO_2$ and $SO_4^{2-}$ decreased rapidly to 'background' levels. $SO_2$ varied from flight to flight but was relatively well mixed with a mean (standard deviation) MBL concentration of ~25 (15) pptv, about 40% of the DMS concentration. We show later that the relatively low concentration of $SO_2$ in the MBL was likely due to processing of air by stratocumulus clouds. $SO_4^{2-}$ was exceedingly variable horizontally and vertically, which in part explains the difference between the averaged MBL concentrations from the *RHB* 118 (85) pptv and C-130 60 (60) pptv in the remote MBL. While generally not very variable with mean remote FT concentrations of ~26 and ~40 pptv, respectively, $SO_2$ and $SO_4^{2-}$ were occasionally elevated immediately above the clouds, as was CO. CO in the FT had a range of 67~77 ppbv, with higher concentrations suggesting sporadic long distance transport of pollution-influenced air. Due to the lack of precipitation, both $SO_2$ and $SO_4^{2-}$ aerosols can have much longer lifetimes in the FT (a few weeks) than in the MBL (a few days), enabling them to be transported from continental sources to offshore regions.

$O_3$ averaged 26 and 52 ppbv in the offshore MBL and FT, respectively. MBL $O_3$ displayed a diurnal variability qualitatively similar to that of DMS. $O_3$ built up at night as a result of entrainment from the FT, whereas during the day, photochemical and heterogeneous reactions outpaced entrainment and led to a steady decrease in $O_3$. Dry deposition to ocean surface represents a small but continuous sink for $O_3$ at all times. As with the DMS budget (Yang et al., 2009), we can estimate the entrainment velocity ($\omega_e$) by balancing the nighttime $O_3$ build up with entrainment and deposition fluxes, assuming no chemical source and loss at night. Assuming a deposition velocity of 0.01 cm $s^{-1}$ (derived from eddy covariance measurements of $O_3$ during the Stratus 06 cruise in the same region, J. Hare, personal communication, 2010), we calculate a nighttime $\omega_e$ of ~6 mm $s^{-1}$, higher than $\omega_e$ = 4 mm $s^{-1}$ that was derived from the DMS budget. Using a higher deposition velocity would require a greater $\omega_e$ to balance the $O_3$ time-rate-of-change. However, unlike the E-W orientated horizontal gradient in DMS, $O_3$ was generally higher in the north (~30 ppbv at 19°S) than in the south (~20 ppbv at 21°S), implying a gradient along the mean wind direction. Thus the advective flux of $O_3$ could be substantial and complicate the interpretation of $\omega_e$ from the $O_3$ budget.

*4.3.2 Vertical Distributions*

Lilly (1968) first theorized that longwave radiative cooling at the cloud-top causes convective instability and generates turbulence in a stratocumulus capped MBL. Liquid water content ($L_{WC}$) averaged 0.2 g $m^{-3}$ in the ~300 m deep stratocumulus clouds during VOCALS-REx. Immediately above the cloud deck, a strong inversion layer separates the

MBL from the stable, dry, and relatively quiescent FT. With jumps of 10 and 20 K in potential temperature and dew point over a few tens of meters, the inversion layer confines surface-derived scalars to the MBL. Turbulence at the inversion irreversibly entrains air from the FT into the MBL, with the rate of entrainment varying with radiative fluxes at the stratocumulus cloud-top. At night, longwave cooling causes greater convective instability, more turbulent mixing in the MBL, and increased entrainment. In VOCALS-REx, mixed layer height measured by the shipboard lidar indicated a coupled (well-mixed) MBL at night. During the day, shortwave heating of the cloud-top partially suppresses turbulence, which reduces entrainment, causing the surface layer and the upper MBL to become decoupled (Nicholls, 1984). Evaporative cooling from falling drizzle droplets may further affect the coupling of the MBL. Lidar measurements showed that the velocity variance in the MBL was ~50% lower during the daytime, with the mixed layer height (MLH) only reaching 60~70% of $Z_i$ in the remote region, generally below the stratocumulus cloud bottom but above the lifting condensation level (LCL). While a cloud base well above the LCL is usually thought to indicate decoupling, the MLH measurement provides more direct information on the degree of mixing. Turbulence was still present, but more intermittent above the MLH. The extent of decoupling also depends on the MBL depth; as the MBL deepens further to the west (~1.6 km at 85°W) from the coast (~1 km at 70°W), the frequency and degree of decoupling increase.

Near the surface (e.g. at the ship's level), the concentration of a tracer produced from the upper MBL or entrained from the FT and lost to the ocean surface may decrease during the day due to decoupling that shuts off the source above. Such would be the case

for $O_3$, and for $SO_4^{2-}$ if most of it were produced in clouds. In contrast, surface concentration of a tracer with an oceanic source, such as DMS, may increase faster during the decoupled daytime without considering chemical loss. The mean C-130 vertical profiles of temperature, dew point, potential temperature, liquid water content, CO, $O_3$, $SO_4^{2-}$, and $SO_2$ in the remote region are shown in Fig. 4.4. $SO_2$ and $SO_4^{2-}$ concentrations appeared reduced at cloud level (~18 and 30 pptv), likely in part to due in-cloud oxidation and scavenging by clouds when measurements were taken near cloud outflow regions. Figure 4.5 shows the mean aerosol size distributions (number, surface area, and volume) at ~20% RH from the C-130 in the remote region, stratified by the normalized altitude ($Z/Z_i$). The low and mid MBL distributions were similar, with the Hoppel minimum at ~70 nm indicating cloud processing. The upper MBL distribution was biased towards cloud free and POC regions, as cloud shattering compromised measurements inside of clouds. The above cloud distribution was a superposition of two modes: a 30 nm mode associated with low CO (< ~64 ppbv) and an 80 nm mode associated with high CO (> ~74 ppbv). The former can be seen as a 'background' distribution, whereas the latter is indicative of long distance transport of pollution.

*4.3.3 Precipitation*

Marine clouds usually undergo many activation-evaporation cycles before aerosols and cloud droplets are deposited to the sea surface as rain. From C-130 radar and lidar measurements, Bretherton et al. (2010) estimated a mean cloud-base drizzle rate of 1~2 mm $day^{-1}$ over the entire VOCALS project, with 80-90% evaporating before

reaching the surface, agreeing with previous estimates (Bretherton et al. 2004). An array of measurements from the *RHB* and C-130 all indicated that precipitation was more likely in the late evening to early morning. Cloud fraction determined from the shipboard radiosondes averaged over 90% between midnight and sunrise and decreased to 20~30% in the afternoon. $L_{WP}$ determined from the shipboard ceilometer peaked above 150 g $m^{-2}$ over the same time span, more than three times the afternoon value (Fig. 4.6). The optical rain gauge on the ship detected sporadic precipitation events with some rates over ~1 mm $hr^{-1}$, but typically at a lower value of ~0.2 mm $hr^{-1}$. Precipitation was more intense and frequent offshore, with most of the detectable rain events taking place during Leg 1 and west of 80ºW.

*4.3.4 Diurnal Cycles*

$SO_4^{2-}$ concentration measured by the AMS on the *RHB* displayed large diel variability, as exemplified by the period from Oct. 28 to 31 when the ship was steaming eastward at 11 knots from 85ºW to 75ºW (Fig. 4.7). $SO_4^{2-}$ increased from 20~30 pptv to over 150~300 pptv over the first few hours after sunset, peaking at around 0400 UTC (1 am local), with $O_3$ showing a similar trend. $SO_4^{2-}$ then declined over the rest of the day, with the sharpest decrease in the early morning, when the frequency and intensity of drizzle peaked. Precipitation with rates of ~0.3 mm $hr^{-1}$ were recorded on the ship at night and during the day on Oct. 28 and 29. The MBL alternated between being coupled at night and decoupled during the day, as evidenced from the difference between the $Z_i$ and MLH. The rapid nighttime increase in $SO_4^{2-}$ is in contrast with previous measurements in the Equatorial Pacific (Huebert et al. 1996), which shows a daytime

building up of $SO_4^{2-}$ from $SO_2$ oxidation by OH. Moreover, the observed build up in $SO_4^{2-}$ is much too fast to be caused by any chemical mechanisms alone. As $O_3$ was increasing at the same time, the most likely explanation evokes a source of $SO_4^{2-}$ in the upper MBL, such as the in-cloud oxidation of $SO_2$. This source did not add to the surface concentration in the daytime due to decoupling of the MBL. As the MBL became re-coupled after sunset, air rich in $SO_4^{2-}$ was mixed downwards, increasing the surface concentration. Precipitating droplets that evaporate while falling might have sped up the transport of $SO_4^{2-}$ from cloud level to the surface. Unfortunately, per flight plans, the C-130 did not sample the remote region at this time of the day to offer any direct evidence.

The observed diel variability in $SO_4^{2-}$ is consistent with size distribution measurements on the *RHB*, which are stratified according to the time of day in Fig. 4.8. In the remote region, the greatest accumulation mode was measured in the evening (2200~0600 UTC), whereas the coarse mode appeared to be the largest in the late afternoon (1400~2200 UTC), presumably due to high winds that generate more sea-salt aerosols.

*4.3.5 New Particle Nucleation*

During the day, $H_2SO_{4(g)}$ formed from the OH oxidation of $SO_2$ usually condenses on the surfaces of preexisting aerosols and grows them to larger sizes. The total $SO_4^{2-}$ aerosol mass is increased by this process, but the aerosol number remains largely unchanged. Under specific conditions (usually high $H_2SO_{4(g)}$ and $H_2O_{(g)}$ and low aerosol surface area), however, $H_2SO_{4(g)}$ may undergo gas-to-particle conversion and nucleate new nm-sized particles, resulting in a sudden and dramatic increase in the number

concentration (Weber et al., 1999). These freshly formed particles grow by condensation of vapor and coagulation by Brownian motion to a detectable size of ~3 nm in minutes to an hour (Weber et al., 1999) and to 10 nm with in a few hours (Hegg et al., 1992). Nucleation events have been observed in clean air high in the free troposphere (Clarke 1998b), near cloud outflow regions (Hegg et al., 1990; Perry and Hobbs, 1994), in the remote marine boundary layer (Hoppel et al., 1994), and adjacent to a region of precipitation (Clarke et al., 1998a).

In VOCALS-REx, nucleation events were detected on numerous occasions on both the C-130 and *RHB* as evidenced by elevated concentrations of small particles. On the aircraft, we categorize recent nucleation events by a greater abundance of particles with diameter (at 20% RH) under 30 nm relative to over 30 nm; these events are averaged for the remote region and plotted in Fig. 4.5. The number of particles from 10~30 nm was 390 $cm^{-3}$ at times of recent nucleation, much higher than the low MBL average under normal conditions (87 $cm^{-3}$); the submicron and total aerosol surface areas (3.4 and 5.0 $\mu m^2$ $cm^{-3}$, respectively) were significantly reduced during nucleation compared to normal (17.1 and 22.7 $\mu m^2$ $cm^{-3}$). The coarse distributions were similar between recent nucleation and the upper MBL, consistent with the idea that new particle formation occurred near cloud level. C-130 profiles also showed enhanced small particles at cloud level that were volatile. Clouds scavenge aerosols, and also pump moisture and aerosol precursor gases into the surroundings. In the outflow region, elevated actinic flux enhances OH and hence $H_2SO_{4(g)}$ production. Mixing of cloud outflow air devoid of particles and adjacent air rich in $H_2O_{(g)}$ and $H_2SO_{4(g)}$ creates an ideal condition for nucleation (Clarke et al, 1998a). CO during these recent nucleation events was very low

at ~61 ppbv, similar to the remote MBL concentration, suggesting that the source of $H_2SO_{4(g)}$ was likely natural.

On the *RHB*, we identify times of recent nucleation by looking for high UFCN:CN ratio and greater relative abundance of particles under 35 nm diameter (at 60% RH) from size distributions. As UFCN and CN represented aerosol numbers greater than ~5 and ~13 nm respectively, the difference between the two correspond to recently nucleated aerosols in the size range of 5~13 nm. The mean distribution for recent new particle formation in the remote region is plotted in Fig. 4.8. For these nucleation events, the number of particles in 20~35 nm range was 250 $cm^{-3}$, much higher than 40 $cm^{-3}$ normally; the submicron and total surface areas were 10.4 and 25.5 $\mu m^2$ $cm^{-3}$, respectively, as compared to the typical 23.5 and 37.8 $\mu m^2$ $cm^{-3}$. While the coarse mode during nucleation was much smaller compared to normal in the C-130 distributions, this distinction was not observed in the distributions from the *RHB*. The ship was likely detecting particles recently nucleated at cloud level that had been subsequently mixed down to the surface.

Two examples of recent nucleation events observed on the *RHB* are shown as time-series in Fig. 4.9 and Fig. 4.10. The first took place on Oct. 24, when the ship was near 85ºW and 16ºS and steaming south at 11 knots. The submicron particle area decreased quickly from ~20 $\mu m^2$ $cm^{-3}$ to ~13 $\mu m^2$ $cm^{-3}$ by 0500 UTC (2 am local time), when we began to detect small particles. Over 3 hours (a distance of 60 km), the number of particles in the 5~13 nm range was consistently 200~300 $cm^{-3}$. The ship likely encountered a different airmass at 0800 UTC, coinciding with a precipitation event; the

wet scavenging of nucleation mode aerosols is very efficient due to diffusion. Further evidence of freshly formed particles, albeit less dramatic, can be seen in few hours following 0900, as the aerosol surface area continued to decline. Interestingly, our detection of recent nucleation occurred largely in the absence of light, or $H_2SO_{4(g)}$ production (sunrise was not until 1000 UTC). Given the brief lifetime of $H_2SO_{4(g)}$ due to its low volatility, the gas-to-particle conversion had likely taken place in the daytime of Oct. 23 rather than during 0500~0800 UTC of Oct. 24. The relatively high temperature and low RH on Oct. 24 were also not favorable for in situ nucleation. Lacking $H_2SO_{4(g)}$ for condensation, the recently formed particles grew very slowly in the nighttime from coagulation alone such that many of them were still under 13 nm by 0800 UTC. With the ship closer to land at 16ºS than at 20ºS, radon was ~30% higher during this period than in the VOCALS remote region. Thus we cannot rule the possibility that the source of $H_2SO_{4(g)}$ for nucleation and condensational growth was partly anthropogenic.

For our second example of nucleation, the ship was largely stationed at 85ºW and 20ºS on Oct. 27 (Fig. 4.10). Geostationary Satellite (GOES) images showed that a pocket of open cell (POC) was advecting over the area from approximately 0800 to 2200 UTC. CN steadily decreased from ~600 $cm^{-3}$ at 1000 UTC to ~100 $cm^{-3}$ by 1600 UTC, along with an increase in $O_3$. As $O_3$ started to decrease at 1700 UTC, both CN and UFCN increased rapidly in a few bursts until 1900 UTC, with a number concentration of ~250 $cm^{-3}$ in the 5~13 nm size range. The water mixing ratio also increased during these bursts of new particles, suggesting that the ship was in the downdraft region of the clouds and nucleation took place near cloud level. The submicron particle surface area was very

low compared to normal, likely in part due to precipitation scavenging. The surface area actually increased from 2 to 8 $\mu m^2$ $cm^{-3}$ while CN decreased, which was a result of the dramatic loss of very small particles due to preferentially enhanced scavenging and growth of the accumulation mode by condensation and coagulation. Light drizzle events were visually observed on multiple occasions, as was the formation of new stratus clouds. Liquid water path, air temperature, RH, and dew point all showed periodicity on a timescale of ~30 minutes, which may be reflecting intermittent turbulence and cell structures. Measurements from the shipboard lidar also indicated decoupling, as at 1700 UTC the ~700 m deep MLH was only about half of $Z_i$. Similar to cloud scavenging, precipitation removes aerosols and can create favorable conditions for nucleation. As this recent nucleation event was observed in the early afternoon when the actinic flux peaked, there should be ample in situ production of $H_2SO_{4(g)}$, so that the gas-to-particle conversion likely took place recently in the POC. Both $SO_4^{2-}$ and radon were very low, while DMS peaked over 100 pptv for this day, suggesting that the source of $H_2SO_{4(g)}$ was most likely natural. Interestingly, the seawater DMS concentration was ~50% higher in the POC, where the solar flux was also ~30% higher, compared to the closed-cell (cloudy) days before and after.

### 4.4 Discussion

We focus our budget calculations on the remote region to examine the natural cycling of sulfur in the marine atmosphere. In the following sections, we will first briefly introduce and approximate each of the rates in the budget equations of $SO_2$ and $SO_4^{2-}$. At

the end, initiated with observations, we will calculate the diurnal cycles of $SO_2$ and $SO_4^{2-}$ based on those rates and adjust the least certain terms if necessary to achieve steady state mass balance. Through multi-variate fitting, Yang et al. (2009) showed that the horizontal gradient in atmospheric DMS concentration mostly lay in the E-W direction, orthogonal to the prevailing wind along the Andes (~150°); the advective flux of DMS was thus negligible. While DMS was not measured in the upwind region of the Southeast Pacific during the campaign, previous observations of seawater DMS in the South Pacific (e.g. Lee et al., 2010) were similar to those measured during VOCALS-REx, implying that the biogenic sulfur source strength in the upwind region was likely not very different. Analogous multi-variate analysis of $SO_2$ and $SO_4^{2-}$ concentrations in the remote MBL over the entire project resulted in similarly small advective fluxes on average because gradients in $SO_2$ and $SO_4^{2-}$ were also largely longitudinal. We will therefore ignore advection in our budgets below.

*4.4.1 Sulfur Dioxide Budget*

Observations from the Equatorial Pacific first demonstrated a quantitative anti-correlation between DMS and $SO_2$ as a result of the oxidation of DMS by the OH radical (Bandy et al., 1996). During the day, $SO_2$ is produced from DMS faster than it is photochemically destroyed in the MBL. Thus it is no surprise that MBL $SO_2$ concentration from the C-130 was greater during the day than at night in the remote region in VOCALS-REx. But due to the temporal and spatial biases, the aircraft observations might not accurately represent the actual diurnal profile of $SO_2$. It is thus informative to examine the budget of $SO_2$ by integrating (4.1) from the surface to the

inversion height. The angular brackets denote column integrals, with every term now in units of flux (e.g. μmoles $m^{-2}$ $day^{-1}$):

$$\frac{\partial\left\langle\overline{SO_2}\right\rangle}{\partial t} = F_{SO_2,0} - F_{SO_2,Zi} + \left\langle P_{SO_2}\right\rangle - \left\langle L_{SO_2,OH}\right\rangle - \left\langle L_{SO_2,cloud}\right\rangle - \left\langle L_{SO_2,aero}\right\rangle \quad (4.2)$$

The term on the LHS of (4.2) is the time-rate-of-change in column concentration. The flux divergence is separated into the first and second terms on the RHS, representing the $SO_2$ flux at the ocean surface (deposition) and at the inversion (entrainment). $P_{SO2}$ is in situ production of $SO_2$ from DMS, while the last three terms represent losses due to OH, in clouds, and in aerosols, respectively.

*4.4.1.1 $SO_2$ Dry Deposition*

The surface flux, or the dry depositional loss, of $SO_2$ to the ocean may be related to the $SO_2$ concentration near the surface ($[SO_{2,0}]$) and a deposition velocity ($V_{dep}$):

$$F_{SO_2,0} = -V_{dep}[SO_{2,0}] \quad (4.3)$$

The seawater concentration is irrelevant here for the air-sea exchange of $SO_2$ due to its high reactivity in the seawater (Fairall et al., 2007). At a typical VOCALS-REx wind speed of 6 m $s^{-1}$, models based on atmospheric resistance predict $V_{dep} \approx 5$ mm $s^{-1}$ (Wesely and Hicks, 1977; Fairall et al., 2007). Aircraft eddy covariance measurements from a recent Equatorial project yielded a somewhat lower $V_{dep}$ of 3~4 mm $s^{-1}$ at this wind speed (Faloona et al. 2010). With $V_{dep}$ = 4±1 mm $s^{-1}$ and $[SO_{2,0}]$ = 35 pptv, dry deposition flux was 0.6±0.1 μmole $m^{-2}$ $day^{-1}$, or 0.4±0.1 pptv $hr^{-1}$ for a 1.3 km deep MBL. We will show later that dry deposition was a minor term in the $SO_2$ budget, such that the uncertainty in $V_{dep}$ does not significantly alter our conclusions.

*4.4.1.2 $SO_2$ Entrainment*

The entrainment of $SO_2$ may be formulated as the entrainment velocity, $\omega_e$, multiplied by the concentration jump in $SO_2$ across the inversion (Lilly, 1968), with $Z_i^-$ and $Z_i^+$ indicating below and above $Z_i$:

$$F_{SO_2,zi} = \omega_e\{[SO_{2,Z_i^-}] - [SO_{2,Z_i^+}]\} \quad (4.4)$$

From the nighttime budget analysis of DMS in the offshore region, Yang et al. (2009) estimated an $\omega_e$ of ~4 mm $s^{-1}$, same as the diel mean estimated from climatological and mixed-layer models for this region (Wood and Bretherton, 2004; Caldwell et al. 2005). Using the Weather and Research Forecast model and solving for the change of MBL depth over time, Rahn and Garreaud (2010) estimated a similar mean $\omega_e$ value as the residual for VOCALS-REx.

With a mean of ~25 pptv from the C-130, the concentration of $SO_2$ in the remote MBL was higher in the day (30~50 pptv) than before sunrise (~20 pptv) due to DMS oxidation. The concentration at cloud level was reduced to ~18 pptv, likely due to a combination of in-cloud oxidation and incorporation of FT air by entrainment. At ~26 pptv, $SO_2$ in the FT likely originated from long distance transport of natural or anthropogenic emissions. Using a mean $\omega_e$ of 4 mm $s^{-1}$ and the concentration jump between the FT and the cloud level (26 and 18 pptv), entrainment increased MBL $SO_2$ concentration at an approximate rate of 0.1 μmole $m^{-2}$ $day^{-1}$, or ~0.1 pptv $hr^{-1}$.

However, as entrainment is a unidirectional process, the 'mass flux' of $SO_2$ mixed into the MBL from the FT does not depend on the concentration below the inversion.

Multiplying 4±2 mm $s^{-1}$ by the FT concentration then yields a $SO_2$ mass flux of ~0.3 ±0.2 μmole $m^{-2}$ $day^{-1}$, all of which would be converted to $SO_4^{2-}$ aerosols, mostly in clouds as we will show later.

*4.13. $SO_2$ Production from DMS*

In the marine boundary layer (MBL), DMS is principally oxidized through the reaction with the hydroxyl radical (OH) in two separate pathways: H-atom abstraction and OH-addition (Yin et al., 1990). The abstraction channel is favored at high temperatures and essentially all leads to $SO_2$, while the addition channel is favored at low temperatures and leads to methane sulfonic acid (MSA), dimethylsulfoxide (DMSO), and also $SO_2$. From DMS budget, Yang et al. 2009 estimated an effective OH concentration of 1.4±0.2 x $10^6$ OH molecules $cm^{-3}$ on a diel mean, peaking at ~5 x $10^6$ OH molecules $cm^{-3}$ at noontime. Representing the conversion efficiency from DMS to $SO_2$ as $\gamma$, the in situ production of $SO_2$ is the DMS flux divergence multiplied by $\gamma$, or:

$$\left\langle P_{SO_2} \right\rangle = \gamma(k_{OH+DMS}[OH]\left\langle \overline{DMS} \right\rangle) \quad (4.5)$$

Here $k_{OH+DMS}$ is the total second order rate constant of the DMS-OH reaction (sum of the abstraction and addition channels). At an average MBL temperature of ~13˚C during VOCALS-REx, $k_{OH} \approx 7.9 \times 10^{-12}$ $cm^3$ $molec^{-1}$ $sec^{-1}$, with the abstraction pathway accounting for 60% of the total oxidation (Sander et al., 2006). The coefficient $\gamma$ typically ranges from 0.6~0.9, and is recommended to be 0.7(±0.2) by Faloona (2009).

MSA largely resides in the particulate phase; in VOCALS-REx, most of the MSA was found in the fine mode according to filter measurements. Since MSA is entirely

produced from DMS whereas $SO_4^{2-}$ can have both natural and anthropogenic origins, the MSA:$SO_4^{2-}$ ratio can be used to infer the natural contribution to the sulfur burden. In the Southern Hemisphere, a strong correlation was observed between the submicron MSA:$SO_4^{2-}$ ratio and DMS emission (Bates et al. 1992). The submicron MSA:$SO_4^{2-}$ ratio in this study varied between 0.04~0.15 and very closely followed DMS concentration (Fig. 4.11). The ratio was high when DMS peaked and was the lowest at the coast. In an environment free of anthropogenic influence, a higher MSA:$SO_4^{2-}$ ratio may also be interpreted to indicate greater importance of the addition channel of DMS oxidation (Yin et al., 1990). The mean ratio for the fine mode (0.08) and total (0.11) during VOCALS-REx were higher than in the tropical Pacific (R. Simpson, personal communication, 2010) likely in part because of the lower temperature in the Southeast Pacific. If MSA was the only other major oxidation product of DMS besides $SO_2$, and if all of the $SO_4^{2-}$ was formed from DMS, assuming equal lifetime for MSA and $SO_4^{2-}$ due to precipitation scavenging, a MSA:$SO_4^{2-}$ ratio of 0.1 implies $\gamma \approx 0.9$. Accounting for DMSO, the other major product from the addition channel but not measured during the campaign, would reduce $\gamma$. Using a range of 0.7~0.9 in $\gamma$ led to a diel average $SO_2$ gas phase production of 2.2~2.8 μmoles $m^{-2}$ $day^{-1}$, or 1.8~2.3 pptv $hr^{-1}$. In midday, the $SO_2$ production rate from DMS peaked at 7.5~9.7 μmoles $m^{-2}$ $day^{-1}$, or 6.1~7.8 pptv $hr^{-1}$.

*4.4.1.4 $SO_2$ Gas Phase Oxidation*

The rate of daytime oxidation of $SO_2$ by OH is:

$$\left\langle L_{SO_2,OH} \right\rangle = k_{OH+SO_2}[OH]\left\langle \overline{SO_2} \right\rangle \quad (4.6)$$

The second order rate constant between OH and $SO_2$, $k_{OH+SO2}$, is about 9.6 x $10^{-13}$ $cm^3$ $molec^{-1}$ $sec^{-1}$ at ~13˚C (Sander et al., 2006). At a $SO_2$ concentration of 35 pptv, the diel loss rate was 0.22 μmoles $m^{-2}$ $day^{-1}$, or 0.17 pptv $hr^{-1}$. The greatest $SO_2$ loss occurred at a rate of 0.9 μmoles $m^{-2}$ $day^{-1}$, or 0.7 pptv $hr^{-1}$, not during midday, but in the late afternoon.

*4.4.1.5 $SO_2$ Aqueous Phase Oxidation – In Cloud*

$SO_2$ may be removed from the MBL by reacting with $H_2O_2$ and $O_3$ in cloud droplets or in sea-salt aerosols. With extensive cloud coverage in the Southeast Pacific, in-cloud oxidation of $SO_2$ is expected to be a major source of $SO_4^{2-}$ mass. Figure 4.12 shows $SO_2$ concentration in the MBL vs. liquid water content ($L_{WC}$) for the offshore region. Compared to the concentration below cloud or in the clear sky MBL, the interstitial $SO_2$ concentration was reduced to ~18 pptv, with perhaps slightly higher concentration during the day than at night. In an aqueous solution, $SO_2$ is equilibrated to $SO_2.H_2O$, $HSO_3^-$, and $SO_3^{2-}$ (together S(IV)) and the equilibrium reactions are pH dependent:

$$[SO_2 \cdot H_2O] = H_{SO_2}[SO_2] \tag{4.7a}$$

$$[HSO_3^-] = \frac{K_{s1}[SO_2 \cdot H_2O]}{[H^+]} = \frac{H_{SO_2}K_{s1}[SO_2]}{[H^+]} \tag{4.7b}$$

$$[SO_3^{2-}] = \frac{K_{s2}[HSO_3^-]}{[H^+]} = \frac{H_{SO_2}K_{s1}K_{s2}[SO_2]}{[H^+]^2} \tag{4.7c}$$

The Henry's coefficient $H_{SO2}$ =1.23 M $atm^{-1}$ as well as equilibrium constants $K_{s1}$=1.3x$10^{-2}$ M and $K_{s2}$=6.6x$10^{-8}$ M at 298 K are all higher at lower temperatures with $-\Delta H/R$ of 3135, 1960, and 1495 K, respectively (Hoffmann and Calvert, 1985). $K$ at the ambient

temperature is related to the equilibrium constant at 298 K ($K_{298}$) by the relationship $K = K_{298}\exp[-\Delta H/R\,(1/T - 1/298)]$).

In the remote region, with an average cloud water $H_2O_2$ concentration of 65 μM (~0.9 ppbv in gas phase), stoichiometrically there was enough oxidant to oxidize all of the S(IV) to $SO_4^{2-}$. Bulk cloud water measurements showed mean $SO_4^{2-}$ concentration of ~45 μM in the remote region, which for $L_{WC} \approx 0.2$ g m$^{-3}$ converts to ~200 pptv, somewhat higher than the below cloud concentration. S(IV), on the other hand, was barely detectable in cloud water. Cloud water had an average pH of 4.2 (typically 3.5~6), consistent with the ensemble mean pH of 4.3 in stratocumulus droplets from a recent a survey of measurements over the last twenty years (Faloona, 2009). At this pH, $HSO_3^-$ is the predominant S(IV) species.

Ignoring mass transfer limitation, the loss rate of S(IV), and hence the production rate of $SO_4^{2-}$, by reaction with $H_2O_2$ is taken from Martin and Damschen, (1981) [M s$^{-1}$]:

$$-\frac{d[S(IV)]_{H_2O_2}}{dt} = k_{H_2O_2}[H^+][H_2O_2][HSO_3^-] \tag{4.8a}$$

$$k_{H_2O_2} = \frac{2.1\times10^6}{0.1+[H^+]} \tag{4.8b}$$

The rate constant $k_{H2O2}$ is in units of M$^{-2}$ s$^{-1}$ and decreases at lower temperatures with $-\Delta H/R = -3650$ (Maahs, 1983). The reaction is largely pH insensitive because the pH dependences in the equilibrium of $HSO_3^-$ and in the $H_2O_2$ reaction cancel. With a gas phase $SO_2$ concentration of 25 pptv, cloud water $H_2O_2$ concentration of 65 μM, and pH of 4.2, the instantaneous loss rate of S(IV) due to $H_2O_2$ is 7.2 x 10$^{-10}$ M s$^{-1}$. An alternate reaction rate, which is about three times higher than the one from Martin and Damschen (1981), was presented by Hoffmann and Calvert (1985). We demonstrate later that this

alternate rate appears to be unrealistically high from the perspective of the steady state mass balance of $SO_2$. However, the large discrepancy in this reaction rate contributes to the uncertainty of our budget estimates.

The loss rate of S(IV) by reaction with $O_3$ [M $s^{-1}$] is:

$$-\frac{d[S(IV)]_{O_3}}{dt} = (k_{O_{3,0}}[SO_2 \cdot H_2O] + k_{O_{3,1}}[HSO_3^-] + k_{O_{3,2}}[SO_3^{2-}])[O_3] \quad (4.9)$$

where $k_{O3,0}$, $k_{O3,1}$, and $k_{O3,2}$ are 2.4 x $10^4$, 3.7 x $10^5$, and 1.5 x $10^9$ $M^{-1}$ $S^{-1}$ at 298 K, respectively (Hoffmann, 1986). Because $k_{O3,2}$ is orders of magnitude higher than the other two reactions, the overall reaction rate approximately varies inversely with the square of $[H^+]$ and is greatly enhanced at high pH when there is more $SO_3^{2-}$. At the average cloud pH and gas phase concentrations of 26 ppbv and 25 pptv for of $O_3$ and $SO_2$, the instantaneous loss rate of S(IV) due to $O_3$ is ~4 x $10^{-12}$ M $s^{-1}$, two orders of magnitude slower than the $H_2O_2$ reaction.

The aqueous phase oxidation rate of S(IV) in cloud [M $s^{-1}$] can be converted to an equivalent gas phase equivalent rate of $SO_2$ loss [pptv $hr^{-1}$] using $L_{WC}$:

$$L_{SO_2,cloud} = 3.6 \times 10^9 L_{WC} RT(-\frac{d[S(IV)]_{H_2O_2}}{dt} - \frac{d[S(IV)]_{O_3}}{dt}) \quad (4.10)$$

$R$ is the gas constant (0.082 atm L $K^{-1}$ $mole^{-1}$), and $T$ is the average cloud temperature (~282 K). With 25 pptv of $SO_2$, 65 μM (~0.9 ppbv) of $H_2O_2$, and $L_{WC}$ of 0.2 g $m^{-3}$, $L_{SO2,cloud}$ is 12 pptv $hr^{-1}$ (48% $hr^{-1}$). On average including the $O_3$ reaction affects the in-cloud oxidation rate insignificantly.

However, using the instantaneous $d$[S(IV)]/d$t$ (i.e. assuming an open system) to budget $SO_2$ loss over time will certainly lead to an overestimation. In a more realistic closed system, the concentration of the limiting oxidant decreases significantly as

reaction proceeds, and so will $d$[S(IV)]/d$t$. To calculate $SO_2$ depletion as a function of time in cloud over an hour, we start with an initial $SO_2$ concentration of 25 pptv, $H_2O_2$ concentration of 0.9 ppb, $L_{WC}$ of 0.2 g $m^{-3}$, and temperature of 282 K. For simplicity, since there is more than sufficient $H_2O_2$ to oxidize all of the $SO_2$ and this reaction is largely pH-independent, a constant pH of 4.2 and an $O_3$ concentration of zero are used. Assuming rapid equilibration between the gas phase and aqueous phase (i.e. no mass transfer limitation), at a given minute gas phase $SO_2$ is computed by subtracting $L_{SO2,cloud}$ / 60 from $SO_2$ from the previous minute. Aqueous concentration of $H_2O_2$ is updated by subtracting $d$[S(IV)]/d$t$ x 60 from the previous time step and equilibrating with the gas phase. As seen in Fig. 4.13, 9.3 pptv (37%) of $SO_2$ is consumed after an hour in cloud, which is 0.8 times the rate calculated from the open system, while the excess $H_2O_2$ is only decreased slightly.

From large eddy simulations (LES), Feingold et al. (1998) showed that for a stratocumulus capped MBL, a parcel of air is in clouds for on average ~15 minutes in an hour, or 25% of the time. From Fig. 4.13, 2.8 pptv of $SO_2$ (~11%) is oxidized to $SO_4^{2-}$ after 15 minutes in cloud, or 1.9 pptv if we account for the mean cloud fraction of ~0.67. The $SO_2$ formation rate from DMS is 1.8~2.3 pptv $hr^{-1}$ (for $\gamma$ of 0.7~0.9) on a diel average. Adding of ~0.1 pptv $hr^{-1}$ due to entrainment and subtracting dry deposition of 0.4 pptv $hr^{-1}$ and OH loss of ~0.2 pptv $hr^{-1}$ leaves a daily residual of 1.3~1.8 pptv $hr^{-1}$. Thus the approximated loss rate of $SO_2$ in clouds appears comparable to the production rate. If using the much higher rate constant of the $SO_2$-$H_2O_2$ reaction from Hoffmann and Calvert (1985) instead, the in-cloud oxidation of $SO_2$ would far exceed $SO_2$ production from DMS, which is unrealistic and inconsistent with observations. Lacking other

evidence, the rate constant from Martin and Damschen (1981) appears to be more applicable for VOCALS-REx.

In addition to the uncertainty in the $SO_2$-$H_2O_2$ rate constant, the calculation above might be subject to caveats due to the simplifications with respect to mass transfer and reaction time in cloud. Mass transfer from interstitial air to a cloud droplet involves diffusion in the gas phase, interfacial transfer from the gas phase to the aqueous phase, and diffusion in the aqueous phase. If the rate of the chemical reaction is faster than any of those steps, a gradient in concentration develops away from the interface and the reaction becomes limited by the rate of mass transfer. Schwartz (1988) showed that even for 30 μm diameter cloud droplets, in-cloud reaction between $SO_2$ and $H_2O_2$ does not appear to be limited by mass transfer. The typical mean cloud droplet radius was 10~15 μm in the VOCALS-REx remote region from MODIS images. However, calculations assuming instantaneous equilibrium between gas and aqueous phases should still be considered upper limits. For simplicity, we applied a mean in-cloud residence time instead of a distribution of cloud residence times. We could also account for the times inside and outside of clouds by using the mean $L_{WC}$ for the entire MBL (~0.06 g $m^{-3}$), which is similar to multiplying the cloud level mean $L_{WC}$ of 0.2 g $m^{-3}$ by 25%.

Zhang et al. (1999) modeled the depletion of $SO_2$ within a single cloud pass using LES coupled with chemistry. For the case of low $SO_2$ (excess oxidants) and typical cloud pH, they showed that $H_2O_2$ reaction dominates over the $O_3$ reaction due to the orders of magnitude higher aqueous $H_2O_2$ concentration. While our calculated depletion of $SO_2$ is slower than what was simulation by Zhang et al. (1999) because they used the $H_2O_2$ rate constant from Hoffmann and Calvert (1985), qualitatively the results are

similar. Those authors also suggested that $SO_4^{2-}$ produced by the oxidation of $H_2O_2$ is evenly distributed across the drop-size spectrum and tends to broaden the processed CCN spectrum, which can enhance coalescence and hence drizzle. From our calculation, it appears that in-cloud oxidation was enough to account for essentially all of the $SO_2$ loss, which would render other sinks insignificant. Nevertheless, we will look at the oxidation of $SO_2$ in sea-salt aerosols for the sake of completeness.

*4.4.1.6 $SO_2$ Aqueous Phase Oxidation – In Sea-salt Aerosols*

As alluded to previously, the oxidation of $SO_2$ by $O_3$ only becomes important at pH > ~6. While aerosol pH was not directly measured during VOCALS-REx, we can get a sense for the acidity of the aerosol phase by looking at bulk filter measurements on the *RHB*. From ion balance of aerosols, the anion:cation molar equivalent ratio averaged 1.38 for the submicron mode away from shore, implying acidic aerosols. As 60~70% of the total aerosol surface area was submicron near the ocean surface, the fine mode was acidic due to the uptake of $SO_2$, $SO_4^{2-}$, etc. The anion:cation ratio peaked above 2.3 (most acidic) when the ship was near the coast, where $SO_4^{2-}$ and $NO_3^-$ levels from pollution were elevated. This longitudinal pattern in acidity is in agreement with shipboard AMS measurements of submicron $SO_4^{2-}$ and $NH_4^+$ (Fig. 4.14). $SO_4^{2-}$ in aerosols is typically titrated by ammonium ($NH_4^+$), which can have continental and marine sources (Zhuang and Huebert, 1996), to form ammonium bisulfate ($NH_4HSO_4$) and ammonium sulfate ($(NH_4)_2SO_4$), depending on the extend of neutralization. Beyond ~80°W, the $SO_4^{2-}$:$NH_4^+$ molar ratio was close to the full neutralization limit of 1:2 for $(NH_4)_2SO_4$, with additional acidic components likely from nitric and organic acids. That

the fine mode was not very acidic in the remote region might be due to the frequent wet removal by drizzle. Near the coast, the $SO_4^{2-}$:$NH_4^+$ ratio exceeded 1:1 (the ratio for $NH_4HSO_4$) due to high anthropogenic emission of acidic species.

In the supermicron mode, the anion:cation ratio averaged 1.03 away from shore, less acidic than in the fine mode partly because the alkalinity of sea-salt and the carbonate buffer could initially slow down the increase in acidity from the uptake of acidic vapors. A coarse mode with pH less than 7 can also be inferred from chloride deficit calculations, which is included in Fig. 4.11. Sulfuric and nitric acid vapors react with sea-salt aerosols that are initially rich in sodium chloride, forming hydrochloric acid, which is vaporized to the atmosphere and results in increased acidity and reduced $Cl^-$ in reacted sea-salt (e.g. Keene et al., 1990; McInnes et al., 1994). In the offshore region, a small $Cl^-$ deficit of -0.1 μg $m^{-3}$ was observed in the coarse mode. A greater deficit of -0.9 μg $m^{-3}$ was seen near the coast again because of pollution, as evidenced by the much higher aerosol scattering at 550 nm. With low aerosol calcium through out the entire project (0.1 μg $m^{-3}$), the less acidic coarse mode offshore than near the coast was due to lower uptake of acidic species rather than a titration with alkaline dust materials.

We estimate the upper limit sea-salt oxidation rate of $SO_2$ in an analogous fashion to in-cloud oxidation (4.10). The cloud $L_{WC}$ is replaced with the integrated supermicron aerosol mass concentration derived from the *RHB* size distribution, which averaged ~8 μg $m^{-3}$. At a pH of 6.0, the $SO_2$ reaction with $O_3$ is a couple orders of magnitude faster than the reaction with $H_2O_2$. With gas phase $O_3$ and $SO_2$ concentrations of 26 ppbv and 25 pptv, respectively, the instantaneous loss rate of S(IV) due to $O_3$ is ~1.2 x $10^{-8}$ M $s^{-1}$, implying a sea-salt $SO_2$ oxidation rate less than 0.01 pptv $hr^{-1}$, negligible compared to dry

deposition, gas phase oxidation, and in-cloud oxidation. At a higher pH of 6.5, the oxidation rate of $SO_2$ in sea-salt is increased to 0.08 pptv $hr^{-1}$, but still less than half of the gas phase oxidation rate. By neglecting mass transfer and keeping the pH constant, the calculation above represents an overestimation because in real sea-salt aerosols, $SO_4^{2-}$ production and uptake $SO_2$ by diffusion (which could be rate limiting) would acidify the aerosols eventually even with the carbonate buffer, slowing down further $O_3$ reaction. The insignificance of $O_3$ oxidation from the perspective of MBL $SO_2$ budget is consistent with the observation that only 5~6% of the total non-sea-salt $SO_4^{2-}$ was found in the coarse mode during VOCALS-REx per filter measurements. Moreover, this percentage was relatively insensitive to longitude, whereas the pH of sea-salt aerosols likely differed substantially from near shore to the remote marine region, suggesting that mechanisms other than $SO_2$ oxidation (e.g. direct uptake of $H_2SO_4$) was responsible for $SO_4^{2-}$ to exist in the coarse mode.

*4.4.1.7 $SO_2$ Budget Summary*

To more accurately calculate the sources and sinks of $SO_2$, we look at their time-evolutions over the course of a day and compare the implied $SO_2$ diurnal cycle with observations. From (2.2), omitting sea-salt oxidation, the column integrated concentration of $SO_2$ at time *t* can be written as:

$$\left\langle \overline{SO_2} \right\rangle_t = \left\langle \overline{SO_2} \right\rangle_{t-1} + (F_{SO_2,0})_{t-1} - (F_{SO_2,Zi})_{t-1} + \left\langle P_{SO_2} \right\rangle_{t-1} - \left\langle L_{SO_2,OH} \right\rangle_{t-1} - \left\langle L_{SO_2,cloud} \right\rangle_{t-1} \qquad (4.11)$$

The last five terms on the RHS represent time-integrated rates from the previous time step. C-130 Observations of $SO_2$ in the remote region were available in the hours of 0800~2000 UTC. We initialize our calculation with the column integrated concentration

at 0900 UTC (6 am local) because that was approximately the time when the aircraft reached the west most location (80~85°W) on most 20°S survey flights. Compared to other hours, observations from 0900 to 1300 UTC should be subject to the least amount of bias because the aircraft usually stayed in the same general area. The DMS diurnal cycle is calculated as in Yang et al. (2009) for the remote region and used to estimate $SO_2$ production assuming conversion efficiencies of 0.7 and 0.9 from DMS to $SO_2$. The loss rates of $SO_2$ are largely first order (i.e. dependent on the $SO_2$ column concentration) and updated at each hour. Over one diel cycle, we consider the budget closed when $SO_2$ column concentration at the end of the calculation matches that at the beginning under the assumptions of steady state and stationarity.

In Yang et al. (2009), a constant entrainment velocity of 4 mm $s^{-1}$ was used for simplicity because entrainment was a small term in the DMS budget. From direct measurements of DMS, $O_3$, and water vapor fluxes, Faloona et al. (2005) estimated higher $\omega_e$ at night in the stratocumulus region off the coast of California due to greater radiatively driven turbulence and cloud coverage than during the day, consistent with findings from Bretherton et al. (2004) in the Southeast Pacific. We can crudely approximate the diel variability in $\omega_e$ for VOCALS-REx by linearizing $\omega_e$ with cloud fraction at each hour relative to the mean cloud fraction (0.67), which leads to 6 mm $s^{-1}$ at night and 2 mm $s^{-1}$ during the day. As seen in Fig. 4.15, entrainment, deposition, and gas phase OH oxidation are all minor losses of $SO_2$. In-cloud oxidation, the largest sink for $SO_2$, is estimated using a fixed $H_2O_2$ concentration of 65 μM and constant pH of 4.2 (i.e. an open system). The concentration of $SO_2$ below the inversion is adjusted from the implied time dependent MBL $SO_2$ concentration using the observed gradient from C-130

profiles. The aqueous concentration of S(IV) is equilibrated with the cloud level $SO_2$ mixing ratio. Instead of using $L_{WC}$ from the C-130 and approximating the time parcels spend in clouds, we use the liquid water path ($L_{WP}$) determined from the ship, which accounted for both cloudy and clear air conditions. For $\gamma = 0.9$, we find that the in-cloud oxidation loss term needs to be multiplied by a coefficient of 0.43 to balance the diel budget of $SO_2$. This coefficient is necessary for two reasons. First is the overestimation of in-cloud oxidation from using an open system as opposed to the more realistic closed system; the latter is not trivial to simulate over a diel cycle. Secondly, we calculate in-cloud oxidation based on implied $SO_2$ concentration at cloud level, which has both MBL and FT sources. For the cloud-processing term in the budget of MBL $SO_2$ concentration, only $SO_2$ originated from the MBL and lost in clouds should be included. For the lower $\gamma$, the in-cloud oxidation term needs to be further reduced. We see in Fig. 4.15 that the implied $SO_2$ cycle matches well with observations up to 1300 UTC (a few hours after sunrise). Comparison worsens for the subsequent hours, which is likely in part due to the large spatial variability of the C-130 observations as the aircraft was then often profiling or transiting. The major rates in the MBL $SO_2$ budget are summarized in Table 4.1 with both choices of $\gamma$.

### *4.4.2 Sulfate Budget*

From a island-based experiment in the Equatorial Pacific, Huebert et al. (1996) measured a clear diurnal cycle in $SO_4^{2-}$ aerosols. $SO_4^{2-}$ built up slowly during the day and peaked near sunset, consistent with photochemical production from $SO_2$. Dilution due to entrainment of FT air was mostly responsible for the nighttime $SO_4^{2-}$ decline. In

contrast to the diurnal trend shown by Huebert et al. (1996), $SO_4^{2-}$ during VOCALS-REx was the lowest in the late afternoon, increased rapidly for the first several hours after sunset, peaked at 0400 UTC (1 am local), decreased steadily and leveled off over the rest of the diurnal cycle. As with $SO_2$, we first look at the magnitudes of the different terms in the MBL integrated $SO_4^{2-}$ budget:

$$\frac{\partial\left\langle \overline{SO_4^{2-}} \right\rangle}{\partial t} = F_{SO_4^{2-},0,dry} + F_{SO_4^{2-},0,wet} - F_{SO_4^{2-},Zi} + \left\langle P_{SO_4^{2-}} \right\rangle \quad (4.12)$$

The term on the LHS is the time-rate of change. The first three terms on the RHS are dry deposition to the surface, wet deposition due to precipitation, and entrainment at the inversion, respectively. The last term represent in situ production of $SO_4^{2-}$ from $SO_2$. Similar to DMS profiles shown in Yang et al. (2009), average vertical profiles of $SO_4^{2-}$ showed a slightly decreasing concentration with height in the MBL, which can be approximated as a function of $Z/Z_i$ and $\alpha = 0.2$; the latter is the 'decoupling' parameter derived from the profile of DMS. We thus adjust the surface $SO_4^{2-}$ concentration by $1 - 0.5\ \alpha$ for the column integration. During the decoupled daytime, as $SO_4^{2-}$ above the MLH might be different from that within the MLH, this adjustment is rather crude, but represents our current best estimate in the absence of continuous measurements of $SO_4^{2-}$ above the MLH.

*4.4.2.1 $SO_4^{2-}$ Dry Deposition*

The surface flux of $SO_4^{2-}$ is related to the concentration near the surface ($[SO_4^{2-}{}_{,0}]$):

$$F_{SO_4^{2-},0,dry} = -\int_0^\infty V_{aero}(D)[SO_4^{2-},_0(D)]dD \quad (4.13)$$

The deposition velocity of particles, $V_{aero}$, is a strong function of particle size ($D$). Coarse particles deposit orders of magnitude faster due to gravitational settling than accumulation mode particles. At less than 0.02 μg $m^{-3}$ (~5 pptv), only ~5% of the total non-sea-salt $SO_4^{2-}$ was found in the coarse mode in the offshore region per filter measurements. Aside from the oxidation of $SO_2$ on sea-salt, which we have shown to be insignificant, other potential mechanisms for transferring $SO_4^{2-}$ to the coarse mode might be direct uptake of $H_2SO_{4(g)}$ or through drizzle. If precipitating droplets evaporate before falling to the surface, as was the case 80~90% of the time, aerosols would be returned to the MBL, but likely at greater sizes than before being scavenged. While little $SO_4^{2-}$ was measured in the coarse mode, the enhanced $V_{aero}$ of supermicron aerosols suggests that it is still possible for dry deposition to be a noticeable sink for $SO_4^{2-}$. Lacking size distributed $SO_4^{2-}$ information, we rely on shipboard APS aerosol size distribution and coarse $SO_4^{2-}$ mass from filter measurements.

The deposition velocity of coarse aerosols as a function of size is estimated using the model from Slinn and Slinn (1980), with wet diameters adjusted from measured diameters at 60% RH to the ambient RH according to the sea-salt growth curve (Howell et al., 2006). Integrating the mass distribution over supermicron sizes yields a concentration that agrees well with supermicron gravimetric mass from filter measurements (~8 μg $m^{-3}$), of which ~0.5% was non-sea-salt $SO_4^{2-}$. To approximate size resolved $SO_4^{2-}$, we apply this percentage uniformly to the supermicron mass distribution (i.e. assuming coarse $SO_4^{2-}$ has the same relative distribution as sea-salt aerosols).

Previous impactor measurements in the remote Pacific showed that most of the coarse $SO_4^{2-}$ is present at 2~3 μm, or towards the smaller end of the supermicon spectrum (R. Simpson, personal communication, 2010), whereas the distribution of sea-salt tends to be broader. Allocating more $SO_4^{2-}$ to the larger end of the supermicon spectrum, where the deposition velocity is much higher, could thus overestimate deposition flux.

At the upper size cutoff of the APS (10 μm at 60% RH, or ~11 μm at ambient RH), $V_{aero}$ peaks at ~0.2 cm $s^{-1}$. Multiplying the approximated $SO_4^{2-}$ distribution by the size dependent $V_{aero}$ and summing over supermicron sizes leads to a mean surface flux of merely ~0.002 μmoles $m^{-2}$ $day^{-1}$. Even with a ten-fold higher $V_{aero}$, the resultant deposition flux would still be only ~10% of the $SO_4^{2-}$ production rate from the gas phase oxidation of $SO_2$, and orders of magnitude lower than other terms in the $SO_4^{2-}$ budget, consistent with the estimate from Rodhe (1978) that the residence time of $SO_4^{2-}$ is much longer than that of $SO_2$ with respect to dry deposition. This result is unsurprising because the vast majority of the $SO_4^{2-}$ mass was found in the accumulation mode, where dry deposition is very slow.

*4.4.2.2 $SO_4^{2-}$ Entrainment*

The entrainment of $SO_4^{2-}$ is calculated similarly to that of $SO_2$ (4.4). From average C-130 profiles, with a $SO_4^{2-}$ concentration below the inversion ~40 pptv less than above, entrainment diluted the MBL at a rate of 0.5(±0.3) μmole $m^{-2}$ $day^{-1}$, or 0.4(±0.2) pptv $hr^{-1}$. The 20~30 pptv of $SO_4^{2-}$ observed at cloud level was biased towards clear sky, cloud outflow, and POC regions, thus not representative of $SO_4^{2-}$ concentration below the

inversion. As with $SO_2$, considering the mass flux of $SO_4^{2-}$ at the inversion to be only proportional to the FT concentration (~40 pptv, which did not vary much diurnally), entrainment added 0.5(±0.3) μmole $m^{-2}$ $day^{-1}$ of $SO_4^{2-}$ to the MBL. Together with the mass flux of $SO_2$ of 0.3(±0.2) μmoles $m^{-2}$ $day^{-1}$, the upper limit contribution of anthropogenic sulfur mass from the FT to the MBL is 0.8(±0.4) μmoles $m^{-2}$ $day^{-1}$, ~20% of the DMS sea-to-air flux.

*4.4.2.3 $SO_4^{2-}$ Production*

The in situ production rate of $SO_4^{2-}$ is derived from the loss rate of $SO_2$ and includes both gas and aqueous phase oxidations.

$$\left\langle P_{SO_4^{2-}} \right\rangle = \left\langle P_{SO_4^{2-},OH} \right\rangle + \left\langle P_{SO_4^{2-},cloud} \right\rangle \tag{4.14}$$

To balance the $SO_2$ budget in the MBL (4.12), 2.1 μmoles $m^{-2}$ of $SO_2$ needs to be oxidized in cloud over the entire day, from which we excluded the in-cloud oxidation of $SO_2$ originated from the FT (to $SO_4^{2-}$). Considering the additional FT $SO_2$ contribution, 4.0 μmoles $m^{-2}$ of $SO_4^{2-}$ was produced in-cloud over the entire day.

*4.24. $SO_4^{2-}$ Wet Deposition*

Because of its high water solubility, $SO_4^{2-}$ is readily taken up in clouds, particularly for aerosols above the critical size for activation. Coalescence of cloud droplets form precipitation, which removes aerosols both scavenged in-cloud and collected in the column of air below while falling. Figure 4.16 shows $SO_4^{2-}$ vs. rain rate reaching the surface ($P_d$) measured by the shipboard optical rain gauge, color-coded by

longitude. The heaviest precipitation events (> 1 mm $hr^{-1}$) occurred west of 80°W and were associated with the lowest $SO_4^{2-}$. The average $P_d$ of 0.01 mm $hr^{-1}$ in the remote region (including non-precipitating periods) is consistent with the typical cloud bottom drizzle rate of ~1.5 mm $day^{-1}$ with 15% reaching the surface estimated from radars and lidars by Bretherton et al. (2010). The wet deposition flux of $SO_4^{2-}$ is the sum of below cloud scavenging and in-cloud scavenging (first and second terms on the RHS below):

$$F_{SO_4^{2-},0,wet} = F_{SO_4^{2-},0,BC} + F_{SO_4^{2-},0,IC} \tag{4.15}$$

The below cloud scavenging rate of $SO_4^{2-}$ by droplets that reach the surface depends on the average MBL concentration:

$$F_{SO_4^{2-},0,BC} = -\Lambda_{BC}[SO_4^{2-}]H_{BC} \tag{4.16}$$

Here $\Lambda_{BC}$ is the below cloud scavenging coefficient of $SO_4^{2-}$, which depends on rain rate and the collection efficiency; the latter is a complex function of the droplet and aerosol size distributions. Andronache (2003) showed that small drizzle droplets are more efficient at scavenging aerosols than larger rain droplets. Scavenging by falling droplets is particularly efficient for coarse particles (by impaction) and for nuclei mode particles (by Brownian motion). In contrast, accumulation size particles lie in the 'scavenging well' and have the lowest efficiency. From Seinfeld and Pandis (2006), for typical drizzle diameter of 0.2 mm and 200~300 nm aerosols (mean diameter for $SO_4^{2-}$ mass), the below cloud scavenging coefficient is about 0.01 $hr^{-1}$ for a rain rate of 1 mm $hr^{-1}$. Thus we estimate $\Lambda_{BC}$ [$hr^{-1}$] as 0.01 ($P_d$ / 1). For a well-mixed MBL, $H_{BC}$ is the height from the surface to the bottom of a precipitating cloud, which we equate to *MLH*. This approximation should be valid for the nighttime when the MBL was coupled and

shipboard lidar sensed up to the cloud bottom; it is less robust during the decoupled daytime, but because precipitation did not reach the surface as frequently then, uncertainty from using $H_{BC}$ should be fairly small. From (4.16), we calculate a below cloud $SO_4^{2-}$ wet removal of 0.006 μmole $m^{-2}$ $day^{-1}$ on average and ~0.1 μmole $m^{-2}$ $day^{-1}$ for heavy rain events.

Most of the wet removal of $SO_4^{2-}$ was due to in-cloud scavenging. When cloud forms in a rising air parcel, $SO_4^{2-}$ aerosols mostly become cloud droplets (nucleation scavenging) and are later removed by precipitation; a minor fraction of $SO_4^{2-}$ remains cloud interstitial aerosols. ten Brink et al. (1986) found very low levels of aerosol $SO_4^{2-}$ in cloud interstitial air compared to cloud-free air, suggesting a high efficiency for the scavenging of $SO_4^{2-}$ by cloud droplets. The in-cloud scavenging of $SO_4^{2-}$ is formulated similarly to below cloud scavenging, but with in-cloud scavenging coefficient ($\Lambda_{IC}$) and concentration integrated to $Z_i$:

$$F_{SO_4^{2-},0,IC} = -\Lambda_{IC}\left\langle \overline{SO_4^{2-}} \right\rangle \tag{4.17}$$

Okita et al. (1996) found a bulk scavenging efficiency of 0.5 $P_d^{\,0.74}$ $hr^{-1}$ from $SO_4^{2-}$ measurements over the Sea of Japan during a winter monsoon. Following the concepts of in-cloud scavenging from Scott (1982) and constrained by bulk precipitation measurements from the Eastern United States, Andronache (2004) parameterized the in-cloud scavenging efficiency of $SO_4^{2-}$ using a Marshall and Palmer (1948) precipitation size distribution: 1.26 $P_d^{\,0.78}$ $hr^{-1}$. Utilizing at the moment the parameterization from Okita et al. (1996), the in-cloud scavenging loss would be ~1.2 μmole $m^{-2}$ $day^{-1}$ and over 25 μmole $m^{-2}$ $day^{-1}$ for the heaviest precipitation events.

*4.4.2.5 $SO_4^{2-}$ Budget Summary*

To explain the $SO_4^{2-}$ observations from the ship, we first calculate the expected diel cycle of $SO_4^{2-}$ with sources and sinks discussed above assuming a well-mixed MBL. Omitting dry deposition, the column integrated concentration of $SO_4^{2-}$ at time *t* can be written as:

$$\left\langle \overline{SO_4^{2-}} \right\rangle_t = \left\langle \overline{SO_4^{2-}} \right\rangle_{t-1} - (F_{SO_4^{2-},Zi})_{t-1} + \left\langle P_{SO_4^{2-}} \right\rangle_{t-1} - \left\langle L_{SO_4^{2-},wet} \right\rangle_{t-1} \quad (4.18)$$

Shipboard $SO_4^{2-}$ measurements were taken in the remote region during Oct. 24~30 and Nov. 16~17. We initiate our calculation with the observation at 0000 UTC and compute over one diel cycle. To quantify the average effect of episodic rainfall, the mean precipitation rate of 0.01 mm $hr^{-1}$ is proportioned linearly with the relative cloud fraction, as done with $\omega_e$. We found that an in-cloud scavenging coefficient of 1.0 $P_d^{\,0.74}$ $hr^{-1}$, which is between the parameterizations from Okita et al. (1996) and Andronache (2004), results in a balance between the source and sink terms. As seen in Fig. 4.17, being proportional to $L_{WP}$, the in-cloud oxidation of $SO_2$ peaks in the early morning, which is largely offset by wet deposition that also peaks at the same time when cloud fraction was the highest and precipitation the most intense. Without clouds, gas phase oxidation is responsible for the slow daytime build up of $SO_4^{2-}$, which then decreases at night due to increased entrainment, similar to the observed trend from Huebert et al. (1996). However, the processes discussed above do not capture the observed diel trend in VOCALS-REx (note that we could have started our calculation at any initial value, but

would still not obtain a rapid increase in $SO_4^{2-}$ from 0000 to 0400 UTC and decline afterwards).

The observation that surface $O_3$ (which had a FT source) always increased along with $SO_4^{2-}$ in the early evening suggests that the main source of $SO_4^{2-}$ spike was from above. High levels of $SO_4^{2-}$ were not usually observed in the remote FT, which leaves the upper MBL to be the more likely source, with $SO_4^{2-}$ produced from in-cloud oxidation of $SO_2$. During the day, due to the decoupling of the MBL, $SO_4^{2-}$ generated in cloud could be concentrated in the upper MBL and not mixed down to the surface. The re-coupling of the MBL after sunset would mix down this air rich in $SO_4^{2-}$, causing a spike in measured concentration. $SO_4^{2-}$ was then depleted by wet deposition over the rest of diurnal cycle, with the most rapid loss in the early morning. To test this hypothesis, instead of adding in-cloud $SO_2$ oxidation to the $SO_4^{2-}$ budget continuously as in (4.17), we sum the in-cloud $SO_2$ oxidation over the entire day and incorporate it to MBL $SO_4^{2-}$ budget only during the first four hours after sunset. The daily production of $SO_4^{2-}$ in cloud amounted to 4.0 μmoles $m^{-2}$, similar to the increase observed from 0000 to 0400 UTC in the column integrated concentration. Thus we add 1 μmole $m^{-2}$ of $SO_4^{2-}$ to each of these four hours and re-calculate the $SO_4^{2-}$ budget with this sudden $SO_4^{2-}$ input (Fig. 4.18). As wet depositional loss is first order, the large amount of $SO_4^{2-}$ added initially is adequately depleted over the rest of the diurnal cycle and the implied diel variability is qualitatively similar to observations. The major rates in the MBL $SO_4^{2-}$ budget are included in Table 1.

A refinement to the one layer box model utilized here for our diel calculations would be to solve the upper and lower parts of the MBL separately in the decoupled daytime; at night the two layers would join to become one as the MBL re-couples. However, not knowing the exchange between the upper and lower parts of the MBL during the day (which may be examined by eddy covariance) makes the implementation of such a dynamical model difficult for the time being.

### 4.5 Conclusions

In order to evaluate the effects of anthropogenic sulfur inputs to the atmosphere, we must first understand the natural background cycles. In VOCALS-REx, multiplatform observations and the relatively simple dynamics of the stratocumulus capped marine boundary layer allowed us estimate the sources and sinks of DMS, $SO_2$, and $SO_4^{2-}$ aerosols. The sea-to-air flux of DMS (3.8±0.4 μmoles $m^{-2}$ $day^{-1}$), rather than entrainment of mostly anthropogenically produced $SO_2$ and $SO_4^{2-}$ (0.8±0.4 μmoles $m^{-2}$ $day^{-1}$), was the predominant source of sulfur mass in the remote region of the Southeast Pacific. Accounting for dilution due to entrainment (0.7±0.3 μmoles $m^{-2}$ $day^{-1}$), the remaining DMS was oxidized by OH to mostly $SO_2$. The $SO_2$ production rate from DMS was calculated to be 2.2~2.8 μmoles $m^{-2}$ $day^{-1}$ using a DMS to $SO_2$ conversion of 0.7~0.9, peaking at 7.5~9.7 μmoles $m^{-2}$ $day^{-1}$ in midday. From our implied diel cycle calculations ($\gamma = 0.9$), entrainment slightly increased the MBL $SO_2$ concentration at a rate of 0.05±0.02 μmoles $m^{-2}$ $day^{-1}$, while dry deposition decreased $SO_2$ at a rate of 0.6±0.1 μmoles $m^{-2}$ $day^{-1}$. The gas phase oxidation by OH to $H_2SO_{4(g)}$ (then to $SO_4^{2-}$) was about

0.2 μmoles $m^{-2}$ $day^{-1}$ on a diel average, peaking at 0.9 μmoles $m^{-2}$ $day^{-1}$ in the afternoon. The largest $SO_2$ loss term was the in-cloud oxidation to $SO_4^{2-}$ at 2.1±0.5 μmoles $m^{-2}$ $day^{-1}$, which appears to balance the $SO_2$ budget and implies other potential removal mechanisms were insignificant. With a slightly acidic aerosol coarse mode, our order of magnitude calculation of $SO_2$ oxidation by $O_3$ in sea-salt using measured aerosol size distribution yielded a negligible rate. Entrainment diluted MBL $SO_4^{2-}$ at a rate of 0.5±0.3 μmoles $m^{-2}$ $day^{-1}$, while dry deposition represented an insignificant sink for $SO_4^{2-}$ because little non-sea-salt $SO_4^{2-}$ mass was present in the supermicron mode. The $SO_4^{2-}$ produced from $SO_2$ was largely removed by wet deposition to the ocean surface.

Diurnally, the implied $SO_2$ cycle shows a maximum in concentration at around sunset due to oxidation of DMS by OH and minimum just after sunrise as a result of in-cloud oxidation, with dry deposition being a continuous loss term. This diel variation is anticorrelated with that of DMS, consistent with previous observations in the remote Pacific. The $SO_4^{2-}$ diel cycle observed on the ship appeared to be mostly due to boundary layer dynamics and the intricately connected in-cloud $SO_2$ oxidation and drizzle. $SO_4^{2-}$ produced in cloud was confined to near cloud level during the daytime, when the upper and lower parts of the MBL were often decoupled. As increased turbulence re-coupled the MBL after nightfall, the large amount of $SO_4^{2-}$ built up in the upper MBL was mixed downwards, increasing the concentration at the surface. After peaking in the middle of the night, $SO_4^{2-}$ steadily declined and leveled off for the rest of the day due to wet removal. Drizzle, more frequent in the remote region than near shore, was also more

intense from late night to early morning than in the afternoon. Overall, $SO_2$ had a lifetime of just over half a day, while $SO_4^{2-}$ had a lifetime of ~1.5 days.

Recent particle nucleation events were observed on numerous occasions in the MBL from the aircraft as well as on the ship during VOCALS-REx. Such events occurred when $H_2SO_{4(g)}$ production was likely high and available aerosol surface areas were low due to cloud or precipitation scavenging, such as in a POC. Given the ample production rate of $H_2SO_{4(g)}$ from naturally derived $SO_2$ and low levels of pollution indicators during times of recent nucleation, it is possible that DMS remained not only the most important precursor gas to $SO_4^{2-}$ aerosol mass in the remote Southeast Pacific, but also a significant source for new aerosol number.

**Acknowledgement**

We thank the National Science Foundation for support of this work through grant ATM-0241611 and ATM-0526341. Aircraft thermodynamic data and ancillary gas concentrations were provided by NCAR/EOL under sponsorship of the NSF (http://data.eol.ucar.edu/master_list/?project=VOCALS). PMEL data were downloaded from http://saga.pmel.noaa.gov/data/download.php?cruise=VOCALS. Special thanks to C.W. Fairall, R.M. Simpson, University of Hawaii at Manoa, and the crew of the *R/V Ronald H. Brown.*

## Tables

Table 4.1 Diel averaged rates in MBL concentration budgets of DMS, $SO_2$, and $SO_4^{2-}$

| **DMS** | μmole $m^{-2}$ $day^{-1}$ | pptv $hr^{-1}$ | % $day^{-1}$ |
|---|---|---|---|
| Sea-to-air Flux | 3.81±0.38 | 3.09±0.31 | 118±12 |
| Entrainment | -0.66±0.33 | -0.54±0.27 | -20±10 |
| Loss to OH | -3.15±0.50 | -2.56±0.41 | -97±16 |

| | $\gamma = 0.9$ | | | $\gamma = 0.7$ | | |
|---|---|---|---|---|---|---|
| **$SO_2$** | μmole $m^{-2}$ $day^{-1}$ | pptv $hr^{-1}$ | % $day^{-1}$ | μmole $m^{-2}$ $day^{-1}$ | pptv $hr^{-1}$ | % $day^{-1}$ |
| Prod. from DMS | 2.84±0.45 | 2.30±0.37 | 158±25 | 2.21±0.35 | 1.79±0.29 | 134±21 |
| Entrainment | 0.05±0.02 | 0.04±0.02 | 3±1 | 0.06±0.03 | 0.05±0.03 | 4±2 |
| Dry Deposition | -0.56±0.14 | -0.45±0.11 | -31±8 | -0.51±0.13 | -0.41±0.10 | -31±8 |
| Loss to OH | -0.22±0.03 | -0.18±0.02 | -12±2 | -0.20±0.03 | -0.16±0.02 | -12±2 |
| Loss to Clouds | -2.10±0.48 | -1.70±0.39 | -117±26 | -1.56±0.38 | -1.27±0.31 | -95±23 |
| **$SO_4^{2-}$** | μmole $m^{-2}$ $day^{-1}$ | pptv $hr^{-1}$ | % $day^{-1}$ | μmole $m^{-2}$ $day^{-1}$ | pptv $hr^{-1}$ | % $day^{-1}$ |
| Prod. from $SO_2$ | 4.02±0.89 | 3.26±0.72 | 75±16 | 3.32±0.70 | 2.70±0.57 | 62±13 |
| Entrainment | -0.51±0.26 | -0.41±0.21 | -9±5 | -0.28±0.14 | -0.23±0.11 | -5±3 |
| Wet Deposition | -3.51±0.92 | -2.85±0.75 | -65±17 | -3.04±0.72 | -2.47±0.58 | -56±13 |

Positive (negative) indicate increases (decreases) in MBL concentrations.
$SO_2$ and $SO_4^{2-}$ rates are calculated with two separate DMS to $SO_2$ conversion efficiencies, 0.9 and 0.7.
Percent daily rates are calculated with respect to observed (DMS and $SO_4^{2-}$) or implied ($SO_2$) daily mean concentrations.
Errors for entrainment, dry deposition, and $SO_2$ oxidation are estimated from uncertainty in $\omega_e$, $V_{dep}$, and [OH], with errors for other rates propagated under 95% confidence.

**Figures**

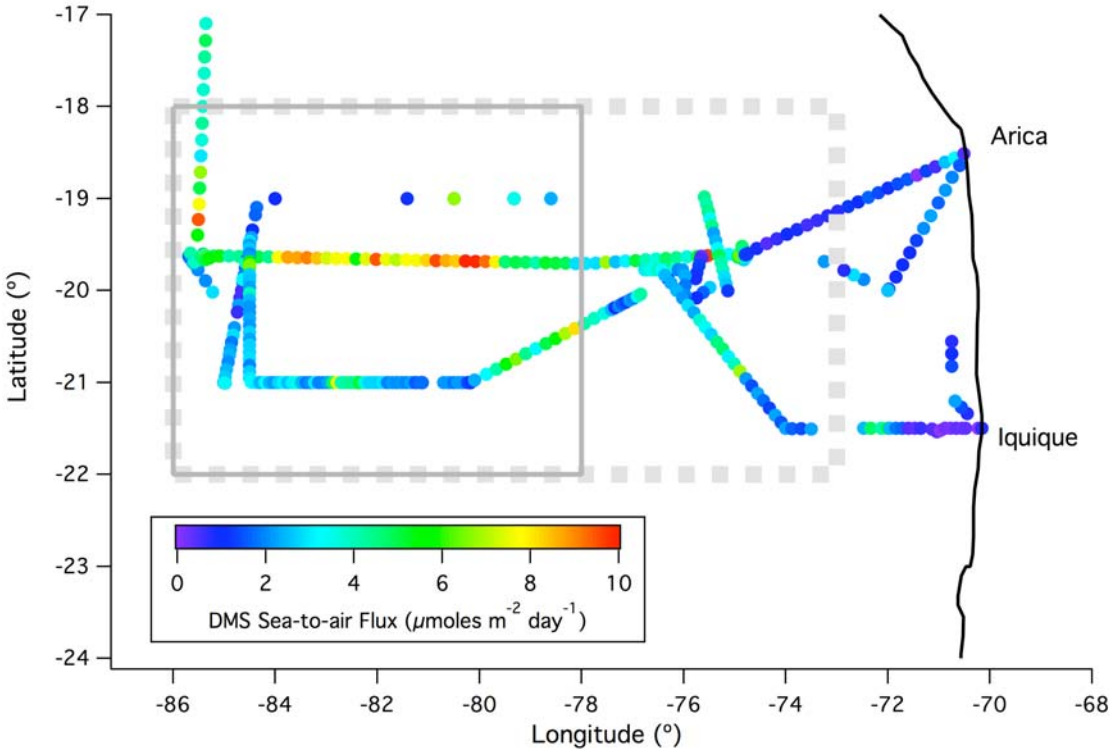


Figure 4.1 VOCALS-REx cruise track color-coded by the DMS sea-to-air flux measured with eddy covariance. Flux was higher offshore mostly as a result of higher wind speed. Seawater DMS concentration was variable and elevated in isolated areas mostly associated with fronts and eddies, but showed no general longitudinal trend. The dotted and solid boxes indicate the VOCALS 'offshore' and 'remote' regions, respectively.

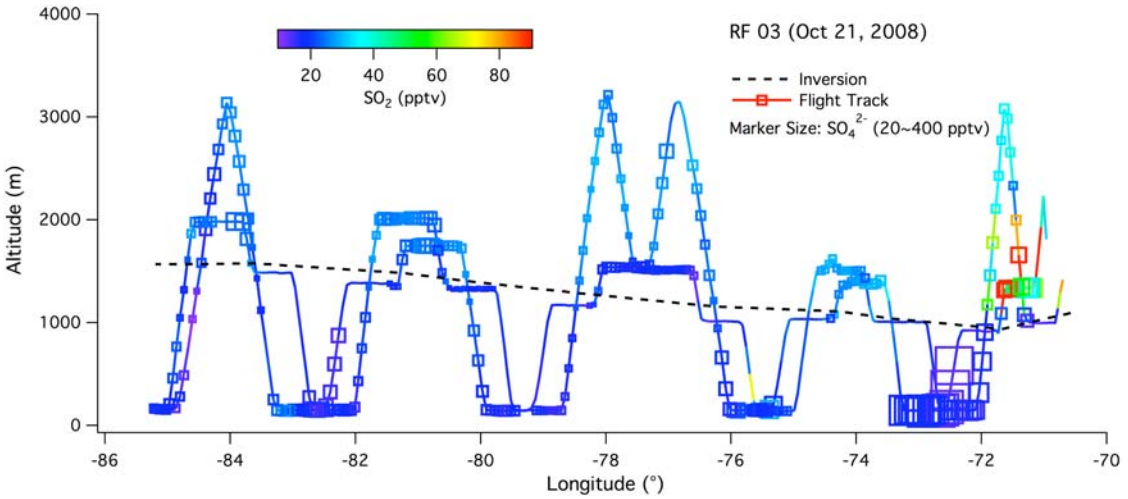


Figure 4.2 A typical 20°S Survey flight by the C-130 (RF 03), with color indicating $SO_2$ concentration and marker size representing aerosol $SO_4^{2-}$ concentration. Both sulfur species showed higher concentrations near the coast than offshore. Also shown is the inversion height derived from C-130 profiles, which increased with distance away from shore. Level legs were typically flown near the surface, below the stratocumulus cloud deck, and above cloud, with occasional profiles to higher altitudes.

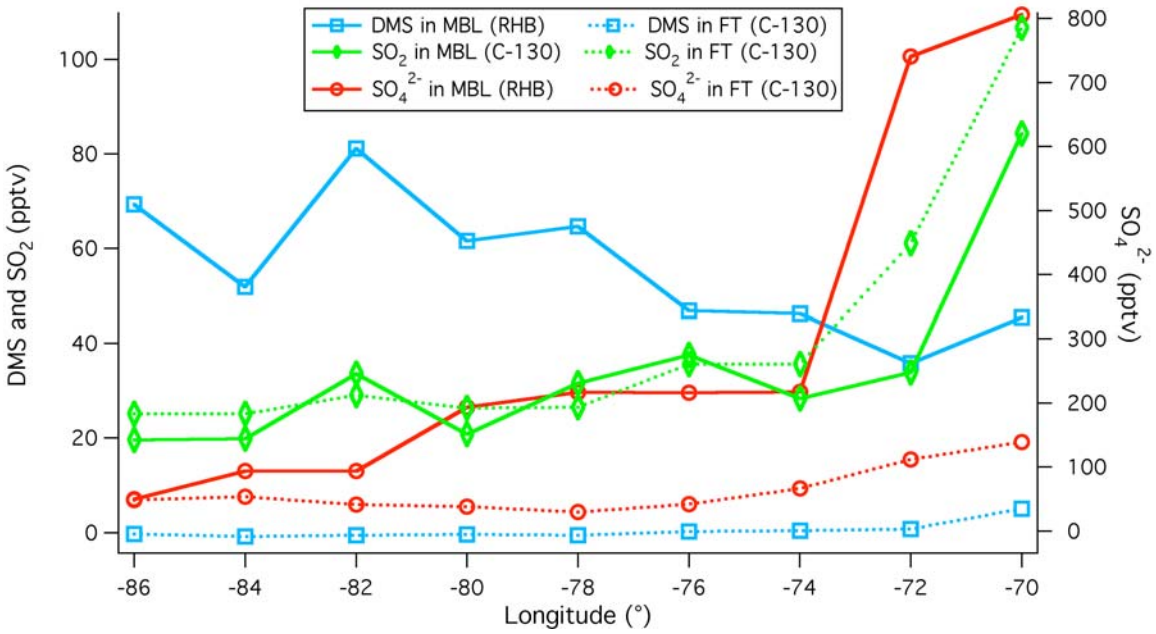


Figure 4.3 Longitudinal trends in the atmospheric concentrations of DMS, $SO_2$, and $SO_4^{2-}$ along 20(±2)°S in the MBL and FT (project averages). $SO_2$ and $SO_4^{2-}$ were significantly elevated near shore due to pollution, and rapidly decreased away from shore, where DMS was higher. In the remote atmosphere, the sea-to-air DMS flux accounted for about three quarters of the MBL sulfur burden, with the rest due to the entrainment of $SO_2$ and $SO_4^{2-}$.

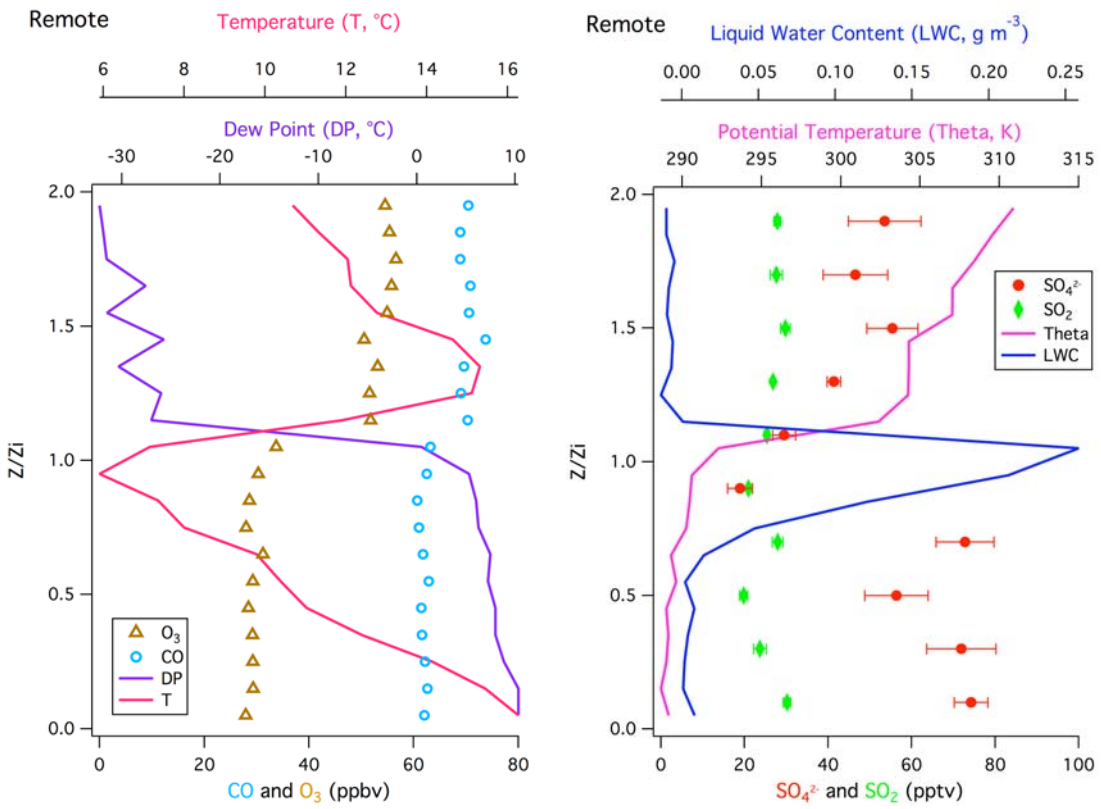


(a) (b)

Figure 4.4 (a) Averaged vertical profiles of temperature, dew point, CO, and $O_3$; (b) $SO_4^{2}$, $SO_2$ (with standard error of the mean), potential temperature, and liquid water content vs. altitude normalized to the inversion height. CO and $O_3$ concentrations were consistently greater above the sharp inversion ($Z/Z_i = 1$), while $SO_4^{2-}$ was greater below the inversion. Both $SO_2$ and $SO_4^{2-}$ (cloud free air and interstitial concentrations) were reduced at cloud level, most likely due to cloud processing and scavenging.

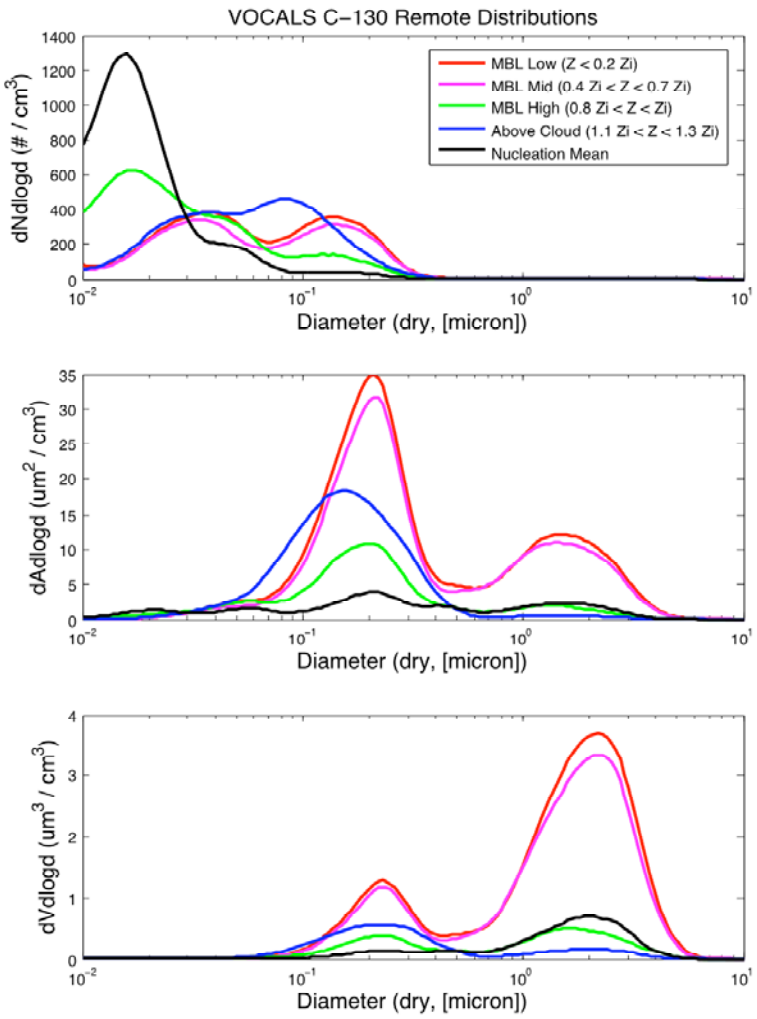


Figure 4.5 Mean VOCALS C-130 remote particle number, surface area, and volume distributions at different normalized altitudes. While the mid-MBL distribution was similar to the surface distribution, the upper MBL distribution was much reduced, likely as a result of cloud scavenging and MBL decoupling. The above cloud distribution was a superposition of two modes, with the ~30 nm mode corresponding to low CO and the ~80 nm mode corresponding to high CO. Also shown is the distribution identified by high concentrations of recently nucleated small particles and typically characterized with reduced surface area.

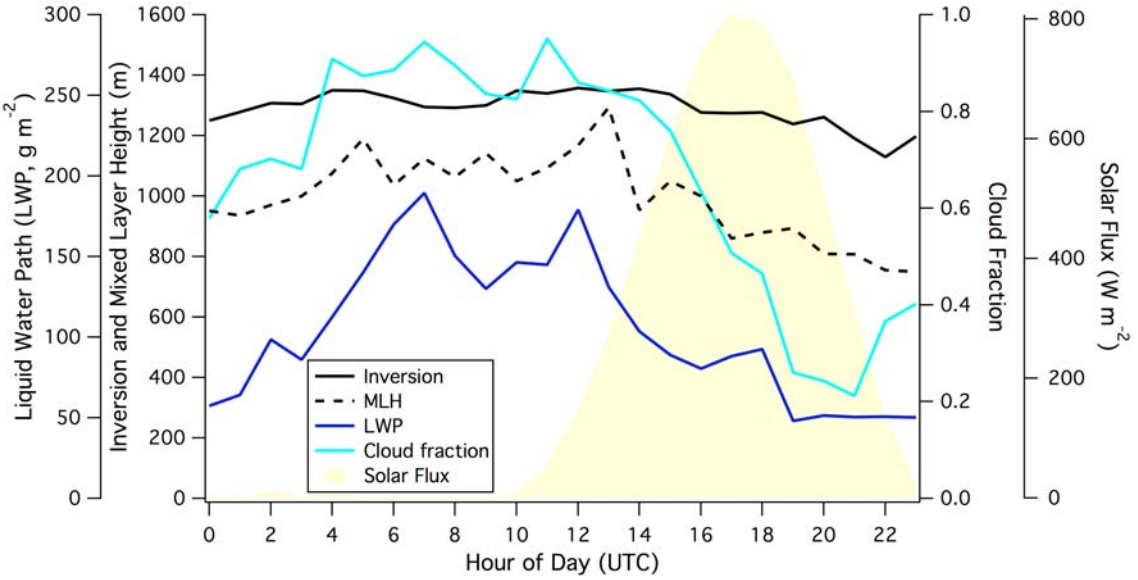


Figure 4.6 Diel cycles in inversion height, mixed layer height, liquid water path, and cloud fraction in the VOCALS offshore region. All of these variables were greater at night than during the day mostly due to the diel variability in the radiative properties associated with the stratocumulus cloud deck.

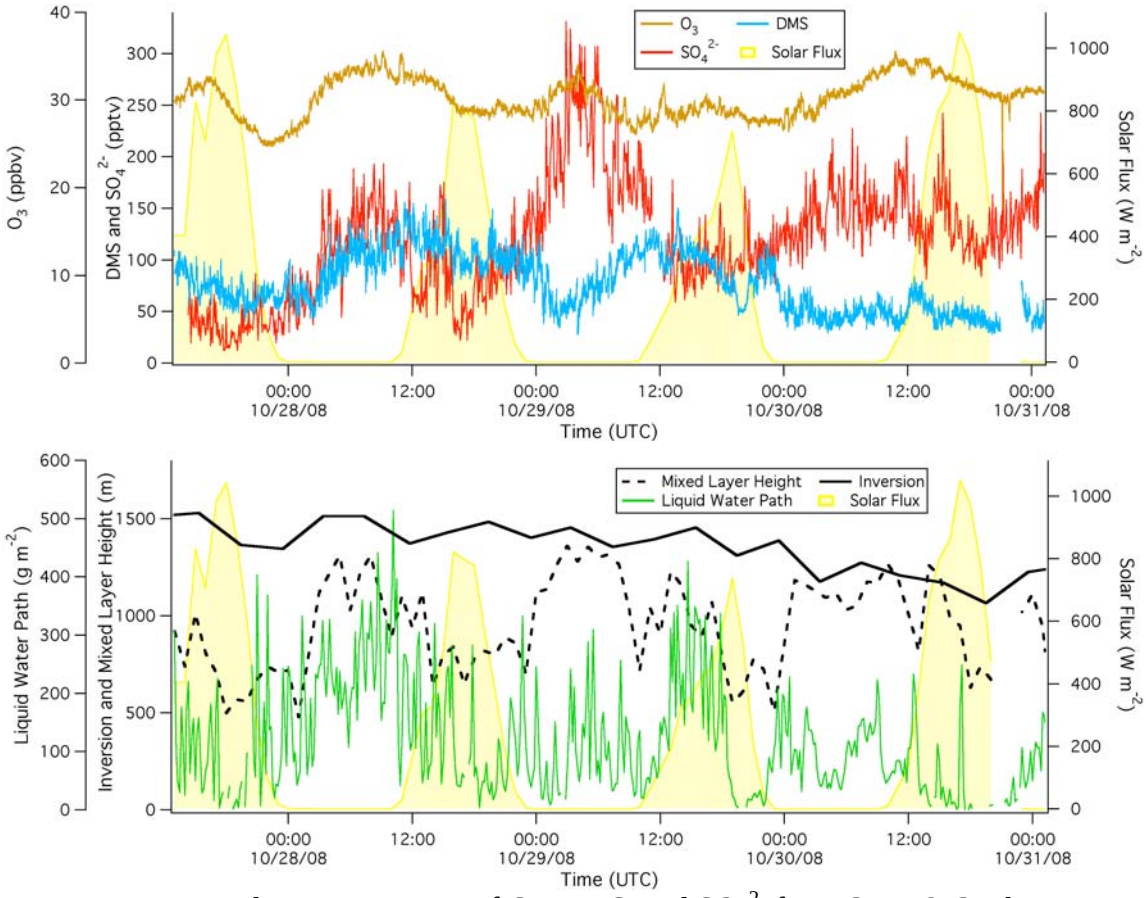


Figure 4.7 Top panel: concentrations of $O_3$, DMS, and $SO_4^{2-}$ from Oct. 28~31; bottom panel: liquid water path, mixed layer height, and inversion height for the same period. Unlike what photochemistry predicts, $SO_4^{2-}$ frequently decreased during the day and peaked at night, as did $O_3$. MLH approached $Z_i$ at night, suggesting a well-mixed MBL, whereas during the day MLH was only ~1/2 of $Z_i$, indicating decoupling. The nighttime increase in $SO_4^{2-}$ was likely due to MBL coupling and in-cloud production of $SO_4^{2-}$.

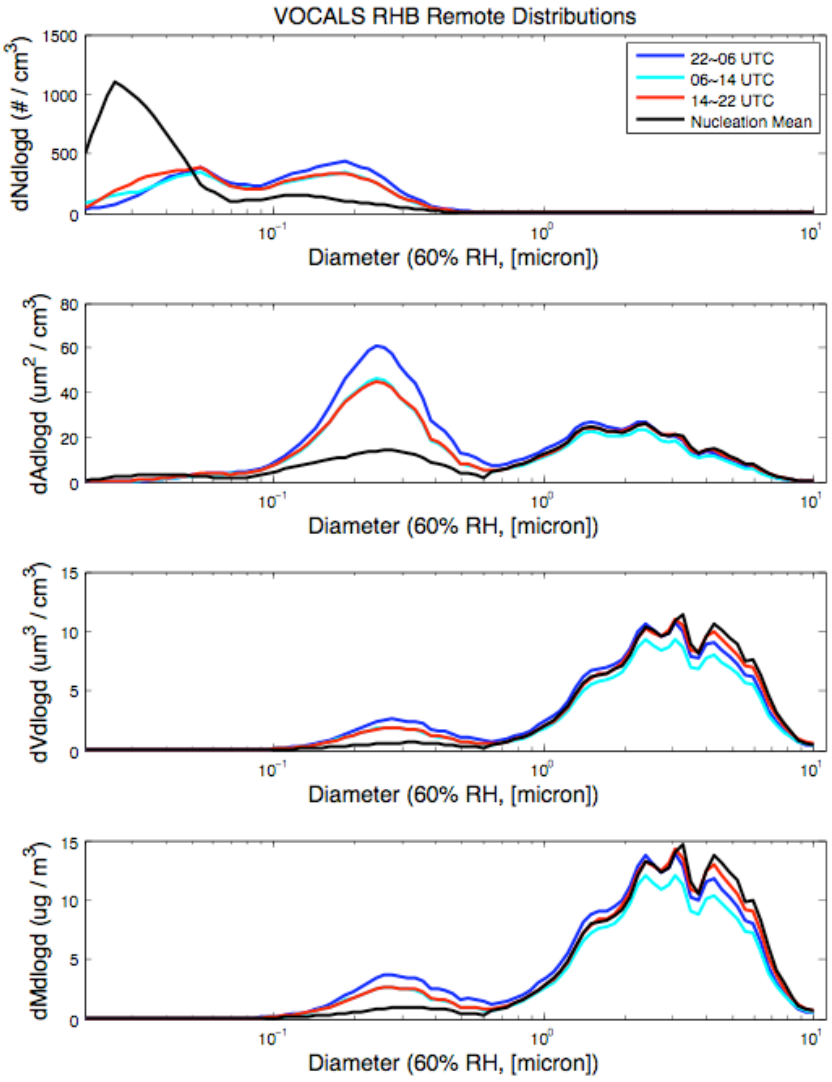


Figure 4.8 Mean VOCALS RHB particle number, surface area, volume, and mass distributions stratified by the time of day in the remote region. The accumulation mode (dominated by $SO_4^{2-}$) was clearly the largest between near sunset to a few hours before sunrise (2200~0600 UTC), consistent with the observed increase in $SO_4^{2-}$ by the shipboard AMS. The coarse mode (dominated by sea-salt) appeared to be largest in the afternoon (1400~2200 UTC) likely as a result of higher wind speed. Also shown is the distribution characterized by high concentrations of recently nucleated small particles and low aerosol surface area.

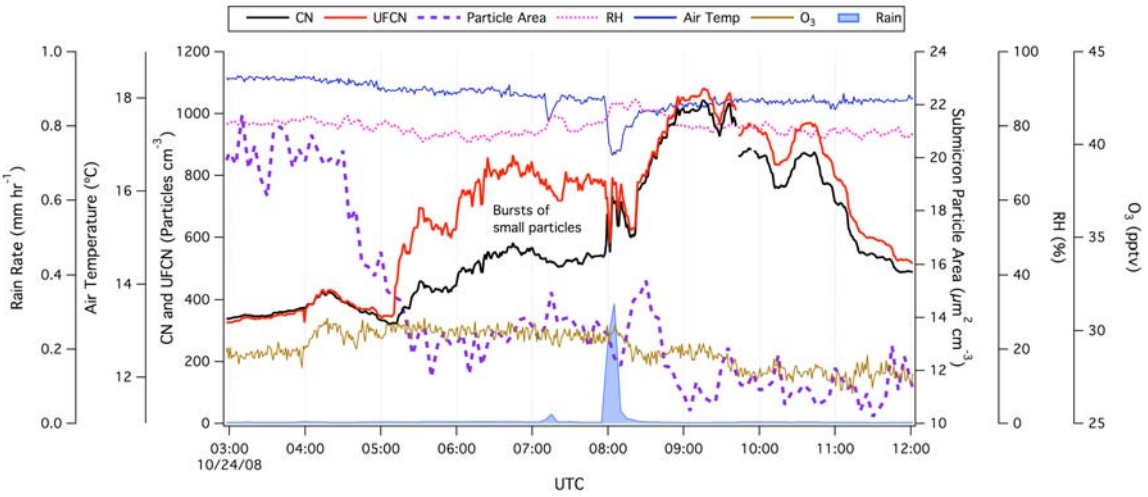


Figure 4.9 Recent nucleation event observed on the night of Oct. 24, when the ship was near 85ºW and 16ºS and steaming south at 11 knots. The submicron particle area decreased drastically from ~20 $\mu m^2$ $cm^{-3}$ to ~13 $\mu m^2$ $cm^{-3}$ by 0500 UTC (2 am local time), when the number of particles in the 5~13 nm range increased to 200~300 $cm^{-3}$. Assuming the airmass stayed the same, a precipitation event at 0800 UTC appeared to scavenge essentially all of these small particles. Due to the short lifetime of $H_2SO_{4(g)}$, the gas-to-particle conversion had likely taken place in the daytime of Oct. 23 rather than during 0500~0800 UTC of Oct. 24. Without $H_2SO_{4(g)}$ for condensational growth, the nucleation model particles grew very slowly in the nighttime such that many of them were still under 13 nm by the morning.

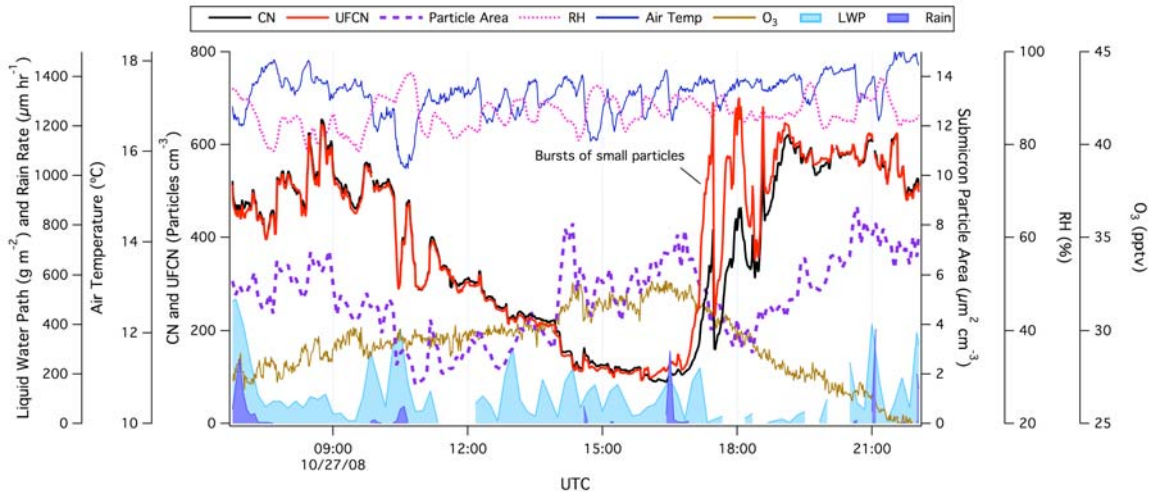


Figure 4.10 Recent nucleation event observed on Oct. 27, when the ship was stationed at 85ºW and 20ºS. The beginning and the end of the time series roughly corresponded to the leading and trailing edges of a POC, as determined from GOES images. CN steadily decreased from ~600 $cm^{-3}$ at 0900 UTC to ~100 $cm^{-3}$ by 1600 UTC, along with an increase in $O_3$. As $O_3$ started to decrease at 1700 UTC, both CN and UFCN increased rapidly in a few bursts, with a difference of ~250 $cm^{-3}$ between the two number concentrations. The submicron particle surface area was very low (2~8 $\mu m^2$ $cm^{-3}$), likely in part due to frequent light drizzle events. Liquid water path, air temperature, and RH all showed periodicity on a timescale of ~30 minutes, which may be reflecting the intermittent turbulence and cell structures in the decoupled MBL.

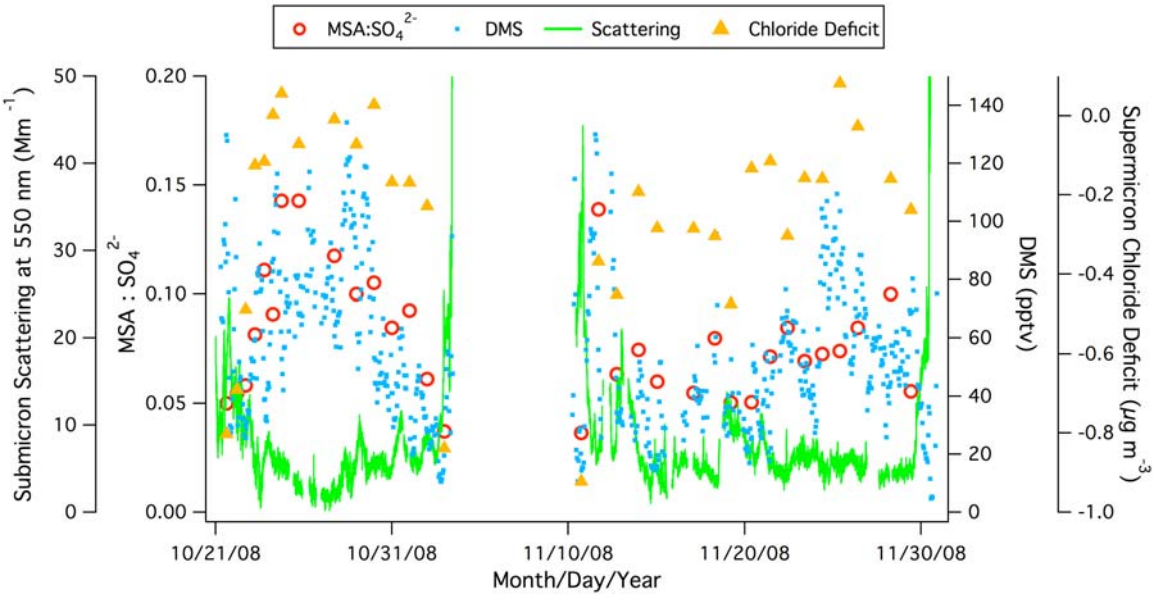


Figure 4.11 Time-series of submicron $MSA:SO_4^{2-}$ ratio and scattering at 550 nm, DMS, and supermicron chloride deficit. The $MSA:SO_4^{2-}$ ratio follows closely to DMS concentration, providing another evidence that DMS was the most important sulfur source away from the coast and also implying that the lifetimes of these sulfur species were similar. Chloride deficit was the largest near the coast, where pollution emission of acidic aerosols (sulfate and nitrate) were the highest, as evidenced by the high scattering.

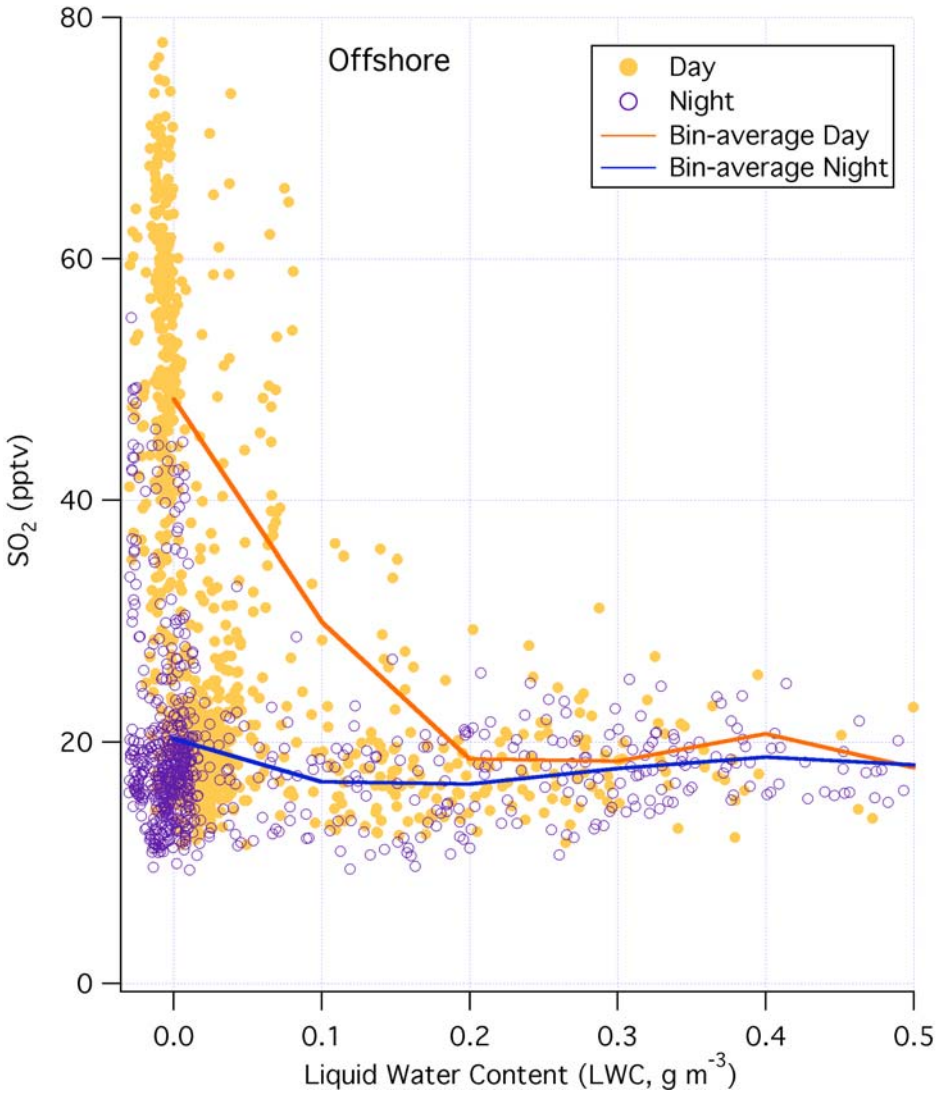


Figure 4.12 $SO_2$ concentration below the inversion vs. liquid water content from the C-130 for the VOCAL offshore region, stratified to daytime and nighttime. Higher $SO_2$ during the day was due to DMS oxidation. Above 0.2 g $m^{-3}$ (mean $L_{WC}$ for the stratocumulus clouds), $SO_2$ was reduced to ~18 pptv as a result of in-cloud oxidation. The interstitial $SO_2$ might be slightly higher during the day due to the initially higher MBL concentration.

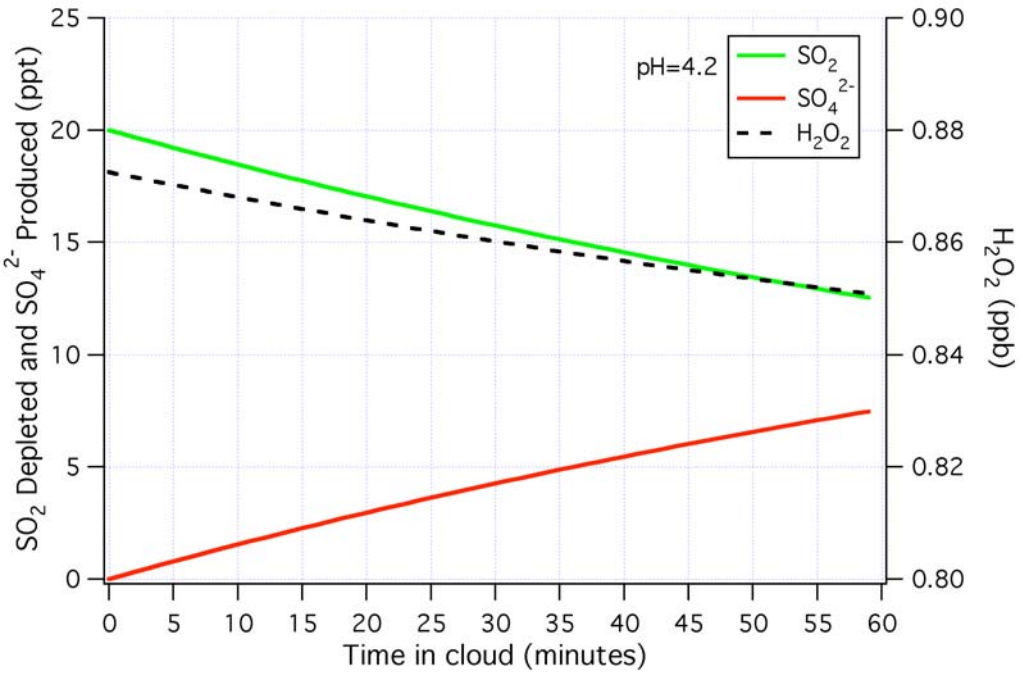


Figure 4.13 Calculated oxidation of $SO_2$ to sulfate in cloud due to $H_2O_2$ in a closed system. Initial concentrations were set to 20 pptv and 65 μM (~0.9 ppb) for $SO_2$ and $H_2O_2$. The liquid water content and pH were fixed at 0.2 g $m^{-3}$ and 4.2, respectively. After ~15 minutes (typical in cloud residence time), 11% of the $SO_2$ is converted to $SO_4^{2-}$, leaving an interstitial concentration $SO_2$ of ~18 pptv.

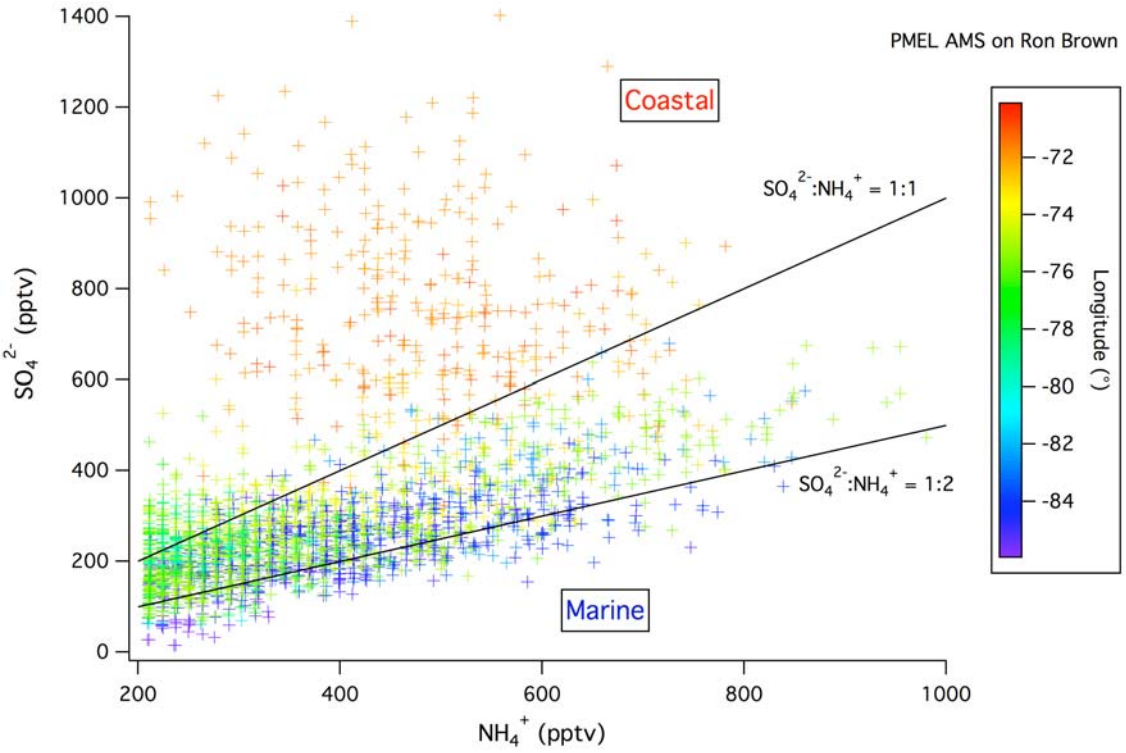


Figure 4.14 $SO_4^{2-}$ vs. $NH_4^+$ from the shipboard AMS, color-coded by longitude. The $SO_4^{2-}$: $NH_4^+$ ratio lies close to the theoretical full neutralization limit of 1:2 for ammonium sulfate in the remote marine region. Closer to the coast, the ratio exceeds 1:1 (for ammonium bisulfate) due to pollution emission.

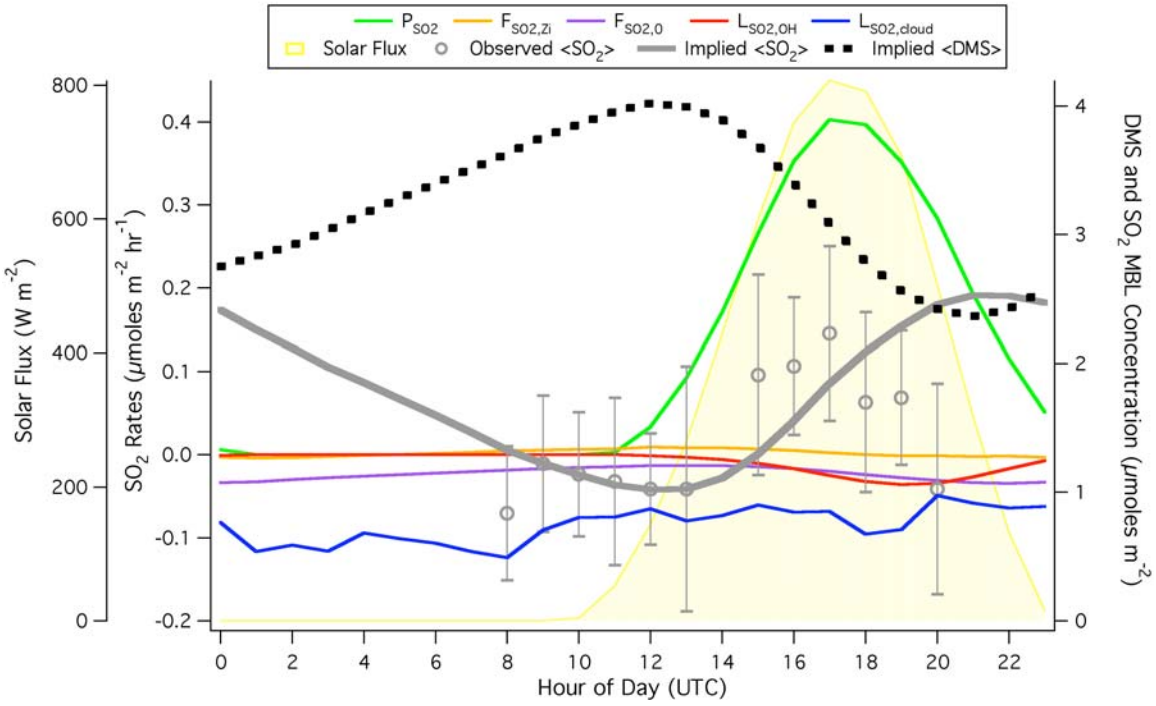


Figure 4.15 Implied $SO_2$ diel cycle, with oxidation from DMS being the principal source and in-cloud oxidation as the main sink. The implied cycle agrees well with observations (error bars correspond to standard deviation within hour bins) until 1500 UTC, with measurements in the subsequent hours likely subject to greater spatial bias.

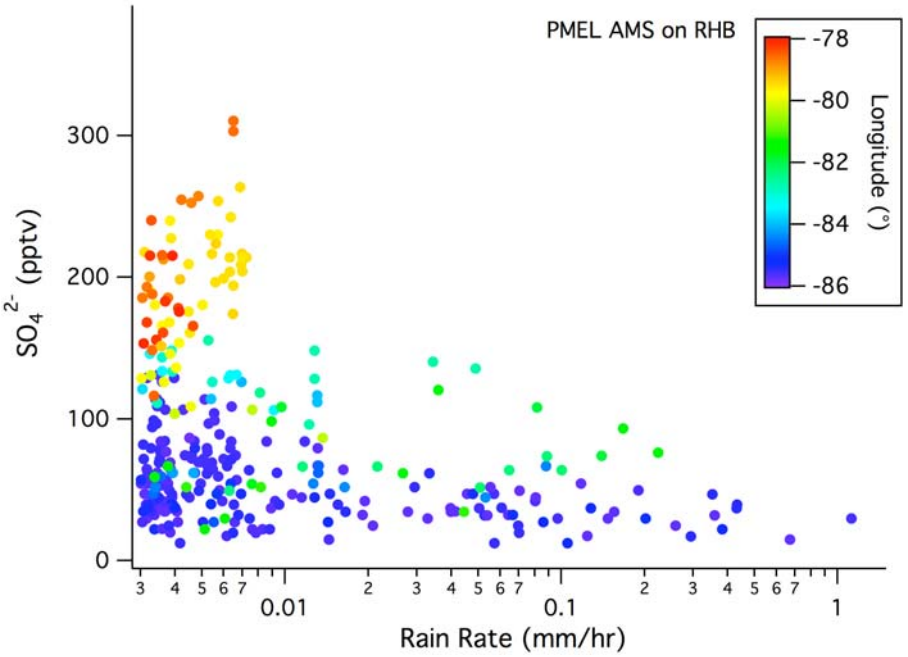


Figure 4.16 *RHB* $SO_4^{2-}$ concentration vs. rain rate from an optical rain gauge, color-coded by longitude. While there was clearly a longitudinal trend in $SO_4^{2-}$, the lowest concentration at 85°W corresponded to high rain rates, suggesting efficient precipitation scavenging.

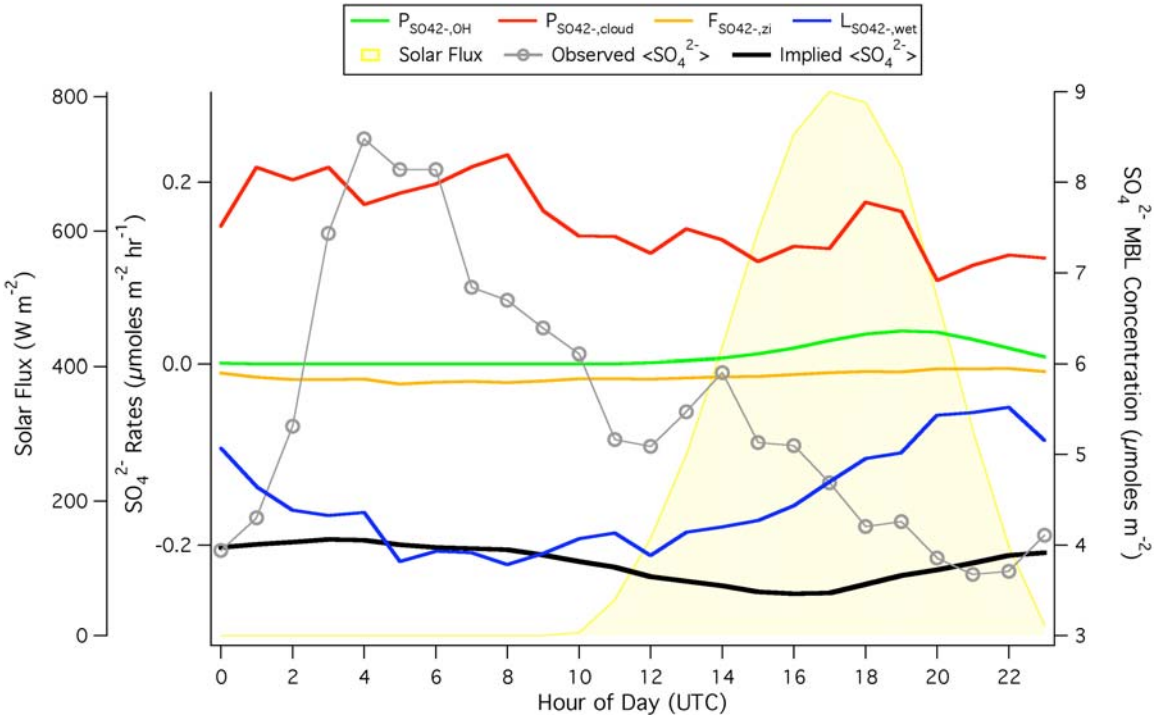


Figure 4.17 Implied $SO_4^{2-}$ cycle assuming a well-mixed MBL, with calculation initiated with the observation at 0000 UTC. The in-cloud production term is largely offset by wet deposition, with gas phase oxidation by OH accounting for the small increase in $SO_4^{2-}$ towards the end of the day. While the source and sink terms appear to balance, the observed diel cycle in $SO_4^{2-}$ is not captured by this calculation.

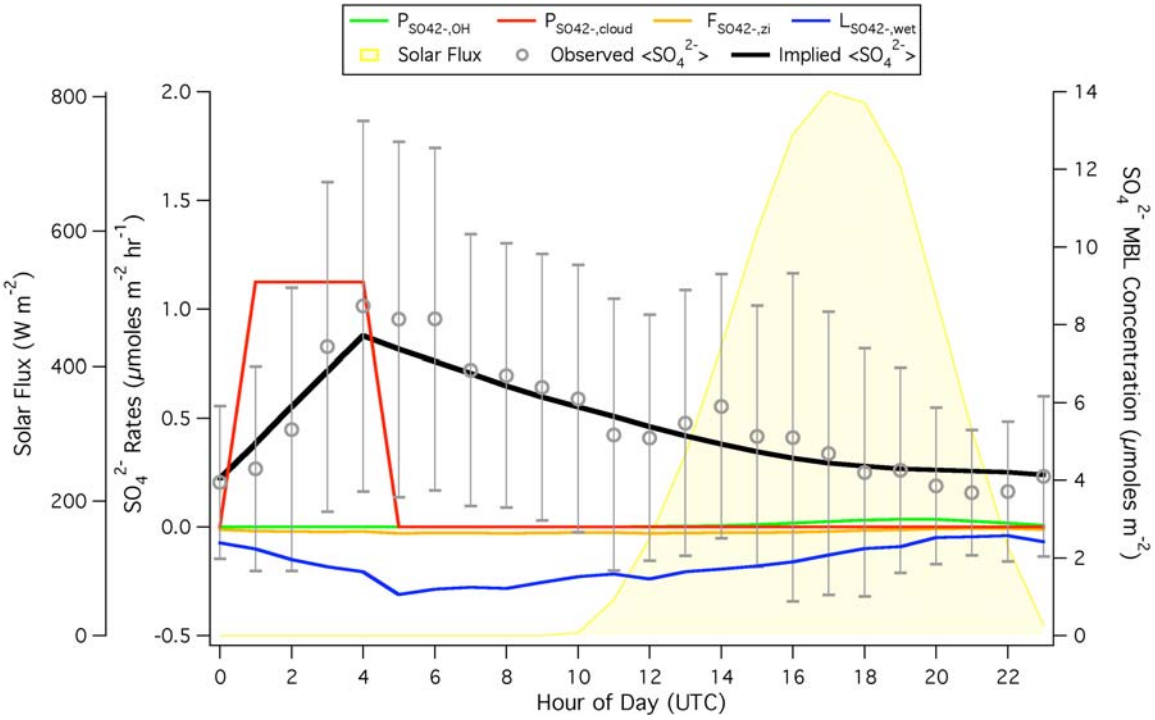


Figure 4.18 Implied $SO_4^{2-}$ cycle assuming a well-mixed MBL at night and decoupled MBL during the day. $SO_4^{2-}$ produced in-cloud is summed over the entire day and only added to the MBL budget over the first four hours after sunset as the MBL re-coupled. Initiated with the observation at 0000 UTC, the implied cycle qualitatively agrees with shipboard observations (error bars correspond to standard deviation within hour bins).

## References


Andronache, C.: Estimated variability of below-cloud aerosol removal by rainfall for observed aerosol size distributions, Atmos. Chem. Phys., 3, 131-143, doi:10.5194/acp-3-131-2003, 2003.

Andronache, C.: Estimates of sulfate aerosol wet scavenging coefficient for locations in the Eastern United States, Atmos. Environ., 38, 6, P 795-804, ISSN 1352-2310, DOI: 10.1016/j.atmosenv.2003.10.035, 2004

Bandy, A.R., Thornton, D.C., Blomquist, B.W., Chen, S., Wade, T.P., Ianni, J.C., Mitchell, G.M., and Nadler W.: Chemistry of dimethyl sulfide in the equatorial Pacific atmosphere, Geophys. Res. Lett., 23(7), 741–744, doi:10.1029/96GL00779, 1996.

Bates, T.S., Lamb, B.K., Guenther, A., Dignon, J. and Stoiber, R.E.: Sulfur emissions to the atmosphere from natural sources. J. Atmos. Chem. 14: 315-337, 1992.

Bates, T.S., Quinn, P.K., Covert, D.S., Coffman, D.J., Johnson, J.E., and Wiedensohler, A.: Aerosol physical properties and processes in the lower marine boundary layer: A comparison of shipboard sub-micron data from ACE-1 and ACE-2, Tellus, Ser. B, 52, 258 – 272, 2000.

Bates, T. S., Quinn, P.K., Coffman, D., Schulz, K., Covert, D.S., Johnson, J.E., Williams, E.J., Lerner, B.M., Angevine, W.M., Tucker, S.C., Brewer, W.A., Stohl, A.: Boundary layer aerosol chemistry during TexAQS/GoMACCS 2006: Insights into aerosol sources and transformation processes, J. Geophys. Res., 113, D00F01, doi:10.1029/2008JD010023, 2008.

Bretherton, C.S., Uttal, T., Fairall, C.W., Yuter, S.E., Weller, R.A., Baumgardner, D., Comstock, K., Wood, R. and Rag, G.B.: The EPIC 2001 stratocumulus study, Bulletin of the American Meteorological Society, 85 (7), 967-977, 2004.

Bretherton, C. S., Wood, R., George, R. C., Leon, D., Allen, G., and Zheng, X.: Southeast Pacific stratocumulus clouds, precipitation and boundary layer structure sampled along 20 S during VOCALS-REx, Atmos. Chem. Phys. Discuss., 10, 15921-15962, doi:10.5194/acpd-10-15921-2010, 2010.

Blomquist, B. W., Huebert, B. J., Fairall, C. W., and Faloona, I. C.: Determining the sea-air flux of dimethylsulfide by eddy correlation using mass spectrometry, Atmos. Meas. Tech., 3, 1-20, doi:10.5194/amt-3-1-2010, 2010.

Caldwell, P., Bretherton, C.S., and Wood, R.: Mixed-Layer Budget Analysis of the Diurnal Cycle of Entrainment in Southeast Pacific Stratocumulus. Journal of the Atmospheric Sciences: Vol. 62, No. 10, pp. 3775–3791, 2005.

Chameides, W.L.: The photochemistry of a remote marine stratiform cloud, J. Geophys. Res. 89(D3), 4739–4755, doi:10.1029/JD089iD03p04739, 1984.

Charlson, R.J., Lovelock, J.E., Andreae, M.O., and Warren S.G.: Oceanic phytoplankton, atmospheric sulfur, cloud albedo and climate, Nature, 326, 655-661, 1987.

Charlson, R.J., and H. Rodhe, 1982: Factors controlling the acidity of rainwater, Nature, 295, 683-685.
Charlson, R.J., Schwartz, S.E., Hales, J.M., Cess, R.D., Coakley, J.A. Jr., Hansen, J.E., and Hoffman, D.J.: Climate forcing by anthropogenic aerosols, Science, 255, 423-3430, 1992.

Clarke, A.D., Davis, D., Kapustin, V.N., Eisele, F., Chen, G., Paluch, I., Lenschow, D., Bandy, A.R., Thornton, D., Moore, K., Mauldin, L., Tanner, D., Litchy, M., Carroll, M.A., Collins, J., Albercook, G.: Particle nucleation in the tropical boundary layer and its coupling to marine sulfur sources. Science, 282, 89-92, 1998a.

Clarke, A.D., Varner, J.L., Eisele, F. Mauldin, R.L., Tanner, D., and Litchy, M.: Particle production in the remote marine atmosphere: Cloud outflow and subsidence during ACE 1, J. Geophys. Res., 103(D13), 16,397–16,409, doi:10.1029/97JD02987, 1998b.

de Szoeke, S.P., Fairall, C.W., and Pezoa, S.: Ship Observations of the Tropical Pacific Ocean along the Coast of South America. Journal of Climate, 22, 458-464, 2008.

Fairall, C. W., Helmig, D., Ganzeveld, L., and Hare, J.: Water-side turbulence enhancement of ozone deposition to the ocean, Atmos. Chem. Phys., 7, 443-451, doi:10.5194/acp-7-443-2007, 2007.

Faloona, I. Sulfur processing in the marine atmospheric boundary layer: A review and critical assessment of modeling uncertainties, Atmos. Environ., 43, 18, 2841-2854, ISSN 1352-2310, DOI: 10.1016/j.atmosenv.2009.02.043 2009.

Faloona, I., Conley, S., Blomquist, B., Clarke, A., Kapustin, V., Howell, S., Lenschow, D.H., Bandy, A.: Sulfur dioxide in the tropical marine boundary layer: dry deposition and heterogeneous oxidation observed during the Pacific Atmospheric Sulfur Experiment. J. Atmos. Chem., doi: 10.1007/s10874-010-9155-0, 2010.

Faloona, I., Lenschow, D., Campos, T., Stevens, B., van Zanten, M., Blomquist, B., Thornton, D., Bandy, A., and Gerber, H.: Observations of Entrainment in Eastern Pacific Marine Stratocumulus Using Three Conserved Scalars. J. Atmos. Sci., 62, 3268–3285, 2005.

Feingold, G., Kreidenweis, S., and Zhang, Y.: Stratocumulus processing of gases and cloud condensation nuclei 1. Trajectory ensemble model, J. Geophys. Res., 103(D16), 19527-19542, 1998.

Hawkins, L.N., Russell, L.M., Covert, D.S., Quinn, P.K., and Bates T.S.: Carboxylic acids, sulfates, and organosulfates in processed continental organic aerosol over the southeast Pacific Ocean during VOCALS-REx 2008, J. Geophys. Res., 115, D13201, doi:10.1029/2009JD013276, 2010.

Hegg, D.A.: The importance of liquid-phase oxidation of $SO_2$ in the troposphere. J. Geophys. Res., 20, 3773-377, 1985.

Hegg, D.A., Covert, D.S., and Kapustin, V.N., Modeling a case of particle nucleation in the marine boundary layer, J. Geophys. Res., 97(D9), 9851-9857, 1992.

Hegg, D.A., Radke, L.F., and Hobbs, P.V.: Particle production associated with marine clouds, J. Geophys. Res., 95(D9), 13,917–13,926, doi:10.1029/JD095iD09p13917, 1990.

Hoffmann, M. R.: On the Kinetics and Mechanism of Oxidation of Aquated Sulfur Dioxide by Ozone, Atmos. Environ. 20, 1145-1154, 1986.

Hoffmann, M.R., and Calvert, J.G.: Chemical transformation modules for Eulerian acid deposition models, Volume 2, The Aqueous-Phase Chemistry, EPA/600/3-85/017. U.S. Environmental Protection Agency, Research Triangle Park, N.C., 1985.

Hoppel, W. A., Frick, G.M. Fitzgerald, J.W., and Larson R.E.: Marine boundary layer measurements of new particle formation and the effects nonprecipitating clouds have on aerosol size distribution, J. Geophys. Res., 99(D7), 14,443–14,459, doi:10.1029/94JD00797, 1994.

Hoppel, W.A., Frick, G.M., Larson, R.E.: Effect of nonprecipitating clouds on the aerosol size distribution in the marine boundary layer. Geophys. Res. Lett., 13(2), 125–128, doi:10.1029/GL013i002p00125, 1986.

Howell, S.G., Clarke, A.D., Shinozuka, Y., Kapustin, V., McNaughton, C.S., Huebert, B.J., Doherty, S.J., and Anderson, T.L.: Influence of relative humidity upon pollution and dust during ace-Asia: Size distributions and implications for optical properties. J. Geophys. Res. Atmos. 111(D6), D06205.

doi:10.1029/2004JD005759, 2006.

Huebert, B.J., Howell, S.G., Covert, D., Bertram, T., Clarke, A., Anderson, J.R., Lafleur, B.G., Seebaugh, W.R., Wilson, J.C., Gesler, D., Blomquist, B., Fox, J: PELTI: Measuring the Passing Efficiency of an Airborne Low Turbulence Aerosol Inlet. Aerosol Sci. and Tech., 38,803-826, 2004.

Huebert, B.J., Wylie, D.J., Zhuang, L., Heath, J.A.: Production and loss of methanesulfonate and non-sea salt sulfate in the equatorial Pacific marine boundary layer. *Geophys. Res. Lett.*, 23, 737-740, 1996.

Keene, W.C., Pszenny, A.A.P., Jacob, D.J., Duce, R.A., Galloway, J.N., Schultz-Tokos, J.J., Sievering, H., Boatman, J.F.: The geochemical cycling of reactive chlorine through the marine troposphere. Global Biogeochem. Cycles., 4, 407- 430, 1990.

Kettle, A.J. and Andreae, M.O.: Flux of dimethylsulfide from the oceans: a comparison of updated data sets and flux models. J. Geophys. Res., 105(D22), 26,793–26,808, doi:10.1029/2000JD900252, 2000.

Lee, G., Park, J., Jang, Y., Lee, M., Kim, K., Oh, R., Kim, D., Yi, H., Kim, T.: Vertical variability of seawater DMS in the South Pacific Ocean and its implication for atmospheric and surface seawater DMS, Chemosphere, 78, 8, P. 1063-1070, ISSN 0045-6535, DOI: 10.1016/j.chemosphere.2009.10.054, 2010.

Lilly, D. K.: Models of cloud-topped mixed layers under a strong inversion. Quart. J. Roy. Meteor. Soc., 94, 292–309, 1968.

Maahs, H.G.: Sulfur dioxide/water equilibrium between 0° and 50°: An examination of data at low concentrations, in Heterogeneous Atmospheric Chemistry, edited by D.R. Schryer, p 187-195, AGU, Washington, D.C., 1983.

Marshall, J.S. and Palmer, W.M.: The distribution of raindrop with size. Journal of Meteorology 5, 165–166, 1948.

Martin, L. and Damschen, D.E., Aqueous oxidation of sulfur dioxide by hydrogen peroxide at low pH, Atmos. Environ., 15, 9, 1981, 1615-1621, ISSN 0004-6981, DOI: 10.1016/0004-6981(81)90146-3, 1981.

McInnes, L.M., Covert, D.S., Quinn, P.K., Germani, M.S.: Measurements of chloride depletion and sulfur enrichment in individual sea-salt particles collected from the remote marine boundary-layer. J. Geophys. Res., 99(D4), 8257–8268, doi:10.1029/93JD03453, 1994.

Nicholls, S.: The dynamics of stratocumulus: aircraft observations and comparisons with a mixed layer model, Q. J. Roy. Meteorol. Soc., 110, 783–820, 1984.

Okita, T., Hara, H., Norio F.: Measurements of atmospheric $SO_2$ and $SO_4^{2-}$, and determination of the wet scavenging coefficient of sulfate aerosols for the winter monsoon season over the sea of Japan, Atmos. Environ., 30, 22, P, 3733-3739, ISSN 1352-2310, DOI: 10.1016/1352-2310(96)00090-8, 1996.

Perry, K.D., and Hobbs, P.V., Further evidence for particle nucleation in clear air adjacent to marine cumulus clouds, J. Geophys. Res., 99(D11), 22,803–22,818, doi:10.1029/94JD01926, 1994.

Pruppacher, H. R. and Klett, J. D.: Microphysics of Clouds and Precipitation, 2nd edition, Kluwer Academic Publishers, Dordrecht, 954, 15938, 1997.

Rahn, D. A. and Garreaud, R.: Marine boundary layer over the subtropical southeast Pacific during VOCALS-REx – Part 1: Mean structure and diurnal cycle, Atmos. Chem. Phys., 10, 4491-4506, doi:10.5194/acp-10-4491-2010, 2010.

Rodhe, H.: Budgets and turn-overtimes of atmospheric sulfur compounds, Atmos. Environ., 12, 671-680, 1978.

Sander, S.P., Golden, D.M., Kurylo, M.J., Moortgat, G.K., Wine, P.H., Ravishankara, A.R., Kolb, C.E., Molina, M.J., Finlayson-Pitts, B.J., Huie, R.E., and Orkin, V.L.: Chemical Kinetics and Photochemical Data for Use in Atmospheric Studies, Evaluation Number 15, Jet Propulsion Laboratory, Pasadena, CA (available at http://jpldataeval.jpl.nasa.gov/), 2006.

Schwartz, S.E.: Mass transport limitation to the rate of in-cloud oxidation of $SO_2$: reexamination in the light of new data, Atmos. Environ., 22, 2491-2499, 1988.

Scott, B.C.: Theoretical estimates of the scavenging coefficient for soluble aerosol particles as a function of precipitation type, rate and altitude. Atmos. Environ.,16, 1753–1762, 1982.

Seinfeld, J.H. and Pandis, S.N.: Atmospheric chemistry and physics: from air pollution to climate change. 2nd ed. Wiley-Interscience. Hoboken, New Jersey, USA, 2006.

Sievering, H., Cainey, J., Harvey, M., McGregor, J. Nichol, S., and Quinn, P.:
Aerosol non-sea-salt sulfate in the remote marine boundary layer under clear-sky and normal cloudiness conditions: Ocean-derived biogenic alkalinity enhances sea-salt sulfate production by ozone oxidation. J. Geophys. Res., 109, D19317, doi:10.1029/2003JD004315, 2004.

Slinn, S.A., and Slinn, W.G.N.: Predictions for particle deposition on natural waters. Atm. Environ., 14, 1013-1016, 1980.

Stevens, B., Vali, G., Comstock, K., Wood, R., VanZanten, M., Austin, P. H., Bretherton, C. S., and Lenschow, D. H., Pockets of Open Cells (POCs) and Drizzle in Marine Stratocumulus, Bull. Am. Meteor. Soc., 86, 51–57, 2005.

ten Brink, H.M., Schwartz, S.E. Daum, P.H., Efficient scavenging of aerosol sulfate by liquid-water clouds, Atmos. Environ., 21, 9, 2035-2052, ISSN 0004-6981, DOI: 10.1016/0004-6981(87)90164-8, 1986.

Thornton, D.C., Bandy, A.R., Tu, F.H., Blomquist, B.W., Mitchell, G.M., Nadler, W., and Lenschow, D.H.: Fast airborne sulfur dioxide measurements by atmospheric pressure ionization mass spectrometry (APIMS). J. Geophys. Res. Atmos. 107(D22), 4632, doi:10.1029/2002JD002289, 2002.

Tucker, S., Senff, C.J., Weickmann, A.M., Brewer, W.A., Banta, R.M., Sandberg, S.P., Law, D.C., Hardesty, R.M.: Doppler Lidar Estimation of Mixing Height Using Turbulence, Shear, and Aerosol Profiles. J. Atmos. Oceanic Technol., 26, 673–688. 2009.

Twomey, S.: Aerosols, clouds and radiation, Atmos. Environ. Part A, 25(11), 2435-2442, 1991.
Weber, R. J., McMurr y, P. H., Mauldin, R. L., Tanner, D. J., Eisele, F. L., Clarke, A. D., and Kapustin, V. N.: New particle formation in the remote troposphere: A comparison of observations at various sites, Geophys. Res. Lett., 26, 307–310, 1999.

Wesely, M.L. and Hicks, B.B.: Some factors that affect deposition rates of sulfur-dioxide and similar gases on vegetation. J. Air Pollut. Control Assoc. 27(11), 1110–1116, 1977.

Yang, M., Blomquist, B.W., and Huebert B.J.: Constraining the concentration of the hydroxyl radical in a stratocumulus-topped marine boundary layer from sea-to-air eddy covariance flux measurements of dimethylsulfide, Atmos. Chem. Phys., 9, 9225–9236, 2009.

Wood, R., and Bretherton, C.S.: Boundary Layer Depth, Entrainment, and Decoupling in the Cloud-Capped Subtropical and Tropical Marine Boundary Layer. J. Climate, 17, 3576–3588, 2004.

Yin, F., Grosjean, D., and Seinfeld, J.: Photooxidation of dimethylsulfide and dimethyldisulfide, I, Mechanism development, J.Atmos. Chem., 11, 309-364, 1990.

Zhang, Y., Kreidenweis, S., and Feingold G.: Stratocumulus processing of gases and cloud condensation nuclei 2. Chemistry sensitivity analysis, J. Geophys. Res., 104(D13), 16061-16080 1999.

Zhuang, L., and B. J. Huebert, B.: Lagrangian analysis of the total ammonia budget during Atlantic Stratocumulus Transition Experiment/Marine Aerosol and Gas Exchange, J. Geophys. Res., 101(D2), 4341–4350, doi:10.1029/95JD02467, 1996.

Zuidema, P., Painemal, D., de Szoeke, S., Fairall, C.: Stratocumulus Cloud-Top Height Estimates and Their Climatic Implications. Journal of Climate, 22, 4652-4666, 2009.